STUTTGARTER BEITRÄGE ZUR PRODUKTIONSFORSCHUNG

PHILIPP TEMPEL

Dynamics of Cable-Driven Parallel Robots with Elastic and Flexible, Time-Varying Length Cables

Universität Stuttgart

Fraunhofer IPA

STUTTGARTER BEITRÄGE ZUR PRODUKTIONSFORSCHUNG BAND 94

Philipp Tempel

Dynamics of Cable-Driven Parallel Robots with Elastic and Flexible, Time-Varying Length Cables

FRAUNHOFER VERLAG

Kontaktadresse:
Fraunhofer-Institut für Produktionstechnik und Automatisierung IPA, Stuttgart
Nobelstraße 12, 70569 Stuttgart
Telefon 07 11/9 70-11 01
info@ipa.fraunhofer.de; www.ipa.fraunhofer.de

STUTTGARTER BEITRÄGE ZUR PRODUKTIONSFORSCHUNG

Titelbild: © Deutscher Pavillon Expo Milano 2015/Jacopo Bianchini

Bibliografische Information der Deutschen Nationalbibliothek
Die Deutsche Nationalbibliothek verzeichnet diese Publikation in der Deutschen Nationalbibliografie; detaillierte bibliografische Daten sind im Internet über www.dnb.de abrufbar.
ISSN: 2195-2892
ISBN (Print): 978-3-8396-1536-2

D 93

Zugl.: Stuttgart, Univ., Diss., 2019

Druck: Mediendienstleistungen des Fraunhofer-Informationszentrum Raum und Bau IRB, Stuttgart
Für den Druck des Buches wurde chlor- und säurefreies Papier verwendet.

© by FRAUNHOFER VERLAG, 2019
Fraunhofer-Informationszentrum Raum und Bau IRB
Postfach 80 04 69, 70504 Stuttgart
Nobelstraße 12, 70569 Stuttgart
Telefon 07 11 9 70-25 00
Telefax 07 11 9 70-25 08
E-Mail verlag@fraunhofer.de
URL http://verlag.fraunhofer.de

Dynamics of Cable-Driven Parallel Robots with Elastic and Flexible, Time-Varying Length Cables

Von der Fakultät Konstruktions-, Produktions- und Fahrzeugtechnik
der Universität Stuttgart zur Erlangung der Würde eines
Doktoringenieurs (Dr.-Ing.) genehmigte Abhandlung

vorgelegt von

Philipp Tempel

aus Stuttgart

Hauptberichter:	PD Dr.-Ing. Andreas Pott
Mitberichter:	Prof. Dr. Bernard Haasdonk
	Marc Gouttefarde, Ph.D.
	Prof. Dr. ir. habil. Remco I. Leine
Tag der mündlichen Prüfung:	19. Juli 2019

Institut für Steuerungstechnik der Werkzeugmaschinen und
Fertigungseinrichtungen der Universität Stuttgart.

2019

All models are wrong.
But some are useful.

George E. P. Box
1976, Journal of the American
Statistical Association
(Box 1976)

Abstract

Cable-driven parallel robots are a special class of parallel manipulators with prismatic rigid-link actuators replaced by flexible and elastic fiber cables. However, this in nature simple replacement of motion and force transmitting components, results in drastic implications on the kinematics and dynamics of such robots. Not only are cables noticeably lighter than their rigid-link counterparts, but they are also more elastic and flexible which becomes very apparent when spanning a cable between two points: cable sag is induced by the cable's own weight, a behavior that cannot be compensated for completely. Incommodiously, these two properties—elasticity and flexibility—of fiber cables makes operating cable-driven parallel robots more involved than anticipated from their rigid-link counterparts and is still an active research field. In this thesis, particular focus is placed on the dynamics of cable-driven parallel robots under explicit consideration of cables and their spatial and axial dynamics.

For the purpose of designing and controlling cable robots, we derive a full multibody model of cable robots describing spatial cable motion by means of Cosserat rod theory. Borrowed from classical mechanics, Cosserat rods capture large elastic deformations such as strain and bending allowing for describing motion of cables in space. The equations of motion are discretized using Rayleigh-Ritz's approach to turn the continuum "cable" into a finite-dimensional model. Reference for evaluation of the cable and robot model are classical beam theory much like well-established methods of cable robot kinetostatics and of cable force distribution calculations. Numerical results of the robot dynamics are obtained with an energy and momentum conserving mechanical integrator for constrained multibody systems.

Axial stress-strain dynamics of fiber cables show hysteretic and nonlinear behavior which cannot be represented by a purely linear spring. We propose theoretically and investigate experimentally an analogous model based on multiple springs and dampers, that captures hysteretic behavior and stress relaxation

well. Its elastic and viscous material parameters are estimated using transfer function identification.

Both contributions provide valid models for further considerations in modeling, simulation, and control of cable-driven parallel robots.

Keywords: parallel mechanism, cable-driven parallel robot, kinetostatics, forward dynamics, cable dynamics

Zusammenfassung

Parallele Seilroboter sind eine spezielle Ausführung paralleler Manipulatoren, bei denen prismatische Antriebe durch elastische und flexible Kunststofffaserseile ersetzt werden. Das Ersetzen der bewegungs- und kraftübertragenden Komponenten impliziert jedoch drastische Auswirkungen auf Kinematik und Dynamik der Roboter. Seile sind nicht nur spürbar leichter als prismatische Antriebe, sie sind auch elastischer und flexibler, was sich beim Spannen eines Seils zwischen zwei Punkten zeigt: Seildurchhang durch Eigengewicht des Seils ist unvermeidbar. Beide Eigenschaften — Elastizität und Flexibilität — von Faserseilen machen den Betrieb von Seilrobotern herausfordernder als von Manipulatoren mit starren Antrieben bekannt. In dieser Arbeit wird besonderer Fokus auf die Dynamik paralleler Seilroboter gelegt, unter expliziter Berücksichtigung der Seile und ihrer räumlichen und axialen Dynamik.

Für Entwurf und Steuerung dieser Roboter wird ein vollständiges Mehrkörpermodell aus Plattform und Seilen hergeleitet, welches die räumliche Seilbewegung durch die Cosserat-Balkentheorie beschreibt. Auf Basis dieser Theorie der klassischen Mechanik können große elastische Verformungen wie Dehnung und Biegung beschrieben werden, was ein Formulieren der Seilbewegung im Raum ermöglicht. Bewegungsgleichungen werden mittels Rayleigh-Ritz-Ansatz diskretisiert, um das Kontinuum "Seil" in eine endlich-dimensionale Form zu überführen. Referenzmodell zur Bewertung der Güte des Seil- und Robotermodells ist die klassische Balkentheorie ebenso wie etablierte Methoden der Roboterkinetostatik und der Seilkraftverteilungsalgorithmen. Numerische Ergebnisse der Roboterdynamik erfolgt mit einem energie- und impulserhaltenden mechanischen Integrator für Mehrkörpersysteme.

Die axiale Seildynamik, d. h. Kraft und Dehnung, von Kunststofffaserseilen zeigt hysteretisches und nichtlineares Verhalten auf, das durch eine rein lineare Feder nicht dargestellt werden kann. Ein analoges Kraftdehungsmodell wird auf Basis experimenteller Untersuchungen entwickelt, welches auf mehreren Federn und Dämpfern basiert und das hysteretische Verhalten und die auftretende

Spannungsrelaxation gut erfasst. Elastische und viskose Materialparameter werden durch die Identifikation der Übertragungsfunktion bestimmt.

Beide Beiträge liefern gültige Modelle zum Einsatz in der Modellierung, Simulation und Steuerung paralleler Seilroboter.

Stichwörter: Parallelroboter, parallele Seilroboter, Kinetostatik, Vorwärtsdynamik, Seildynamik

Acknowledgements

First and foremost, I want to thank my doctoral advisor Andreas Pott for laying the foundations of my work and for enriching conversations upon which my research and personal development could thrive. Without his accurate review and good mentorship, many weekends of tedious works would not have been avoided as he kept making sure I stay focused and on track not losing sight of the big goal. He has shown his trust in my work even at an early stage when giving me the opportunity of going to Gwangju, South Korea, as a visiting researcher of only four months of experience. These two months in Gwangju were the best hands-on training I have ever had giving me the needed experience to also tackle practical challenges of cable robots. Contributing to the universal exposition Expo 2015 in Milan, Italy, under Andreas' supervision was a once in a lifetime opportunity and an exciting application propelling cable robots into the public. In the same breath, I want to thank everyone involved with the Expo cable robot, with special emphasis on thanking Ingo Kaske (Milla&Partner GmbH), Ulrich Kunkel (E^3 Engineering & Education for Entertainment), Stephan Brinkert (ASM Steuerungstechnik GmbH), Helwig Fülling, Stephan Hückinghaus, and Frank Mettner (all Fülling & Partner Ingenieurgesellschaft mbH), and lastly my immediate academic peers, Peter Eberhard and Fabian Schnelle (both ITM, University of Stuttgart). Regardless of his workload, Andreas always found time to assist and mentor me, and I am privileged for having had the opportunity to work with him.

Secondly, I want to thank my immediate superior at the department, Armin Lechler, for providing me with the tools, opportunity, and trust to indulge myself in this research, but who also established an environment of fostering research and critical thinking and acclaim. Thirdly, I am obliged to thank the SimTech Cluster of Excellence at the University of Stuttgart and its leadership and administrative team who enabled and expelled an interdisciplinary research cluster in which my project was imbedded. To add to that, I would like to thank the German Research Foundation (DFG) for financial support of the project

within the Cluster of Excellence in Simulation Technology (EXC 310/2) at the University of Stuttgart.

Thanks to the SimTech Cluster, I was entitled to being a visiting researcher at the Laboratoire d'Informatique, de Robotique et de Microélectronique de Montpellier (LIRMM) under the proficient supervision of Marc Gouttefarde. Despite his finishing his French Habilitation *Habilitation á diriger des recherches* during my stay, he took the time to introduce to me a till then mostly unknown family of cable robots—hanging cable robots like CoGiRo. Marc and his peers Pierre-Elie Herve and Olivier Tempier have helped me understand the specifics of this type of cable robot and helped me perform experiments for our successful contribution to inertia parameter estimation of suspended cable robots.

I should mention my immediate peers at Fraunhofer IPA, Valentin Schmidt, Philipp Miermeister, and Werner Kraus, who were outstanding role models, especially during the first year in which I was a half-baked researcher. To my closest colleagues and fast friends, whom I've learned to appreciate not only for their knowledge and wisdom, but also for making long nights and long weekends at the department a romp of a time, I extend my hand in gratitude. Fruitful discussions with you have also provided for the opportunity for me to develop my keen wit, yet, at the same time, helped me not get lost in too many details and all the nitty-gritty. The friendships I have developed rank amongst my most cherished possessions and, as such, I will strive to contribute my share to retaining them in the future, despite great distances that will inevitably develop. A grateful appreciative Thank You must also be expressed to all non-scientific members of the department implying administrative, mechanical and electrical workshops. There may not be any direct contribution of yours to this work, yet without administrative, financial, mechanical, or electrical expertise of yours, some questions may still be unanswered as of today. Gratitude may be expressed toward my students who contributed to the findings presented in this thesis over the years.

Ultimately, my time at the department would not have been possible if it hadn't been for my parents' emboldening me in taking this opportunity and channeling my capabilities and strengths toward the ultimate goal of enriching science and research with my contribution, lest we forget their emotional support

throughout the years. Last but not least, thank you to my friends whose love and encouragement made me get through even the most frustrating times and for showing forbearance with me throughout all of these years.

Deeply,

Philipp Tempel Stuttgart, 28th November 2019

Table of Contents

List of Figures

List of Tables

List of Symbols

Symbol	Description	Unit
$\boldsymbol{\varphi}$	Angular positions of servo motors.	rad
A_i	Point denoting i-th cable anchor on the frame.	
B_i	Point denoting i-th cable anchor on the platform.	
C_i	Point denoting i-th cable corrected leave point on the frame.	
$\boldsymbol{a}_i$	Vector denoting i-th cable anchor A_i on the frame.	m
$\boldsymbol{b}_i$	Vector denoting i-th cable anchor B_i on the platform.	m
$\boldsymbol{c}_i$	Vector denoting i-th cable corrected leave point C_i on the frame.	m
$\boldsymbol{a}$	Angular acceleration of a physical body in space.	$\mathrm{m/s^2}$
$\boldsymbol{p}$	Angular position of a physical body in space, usually given through a set of orientation parameters such as Euler angles η_{Eul}, Tait-Bryan angles η_{TB}, or quaternions $\boldsymbol{\Theta}$	m
$\boldsymbol{v}$	Angular velocity of a physical body in space.	m/s
T	Arbitrary point on a physical body.	
$\boldsymbol{\beta}$	Geometrical measure of deformation representing the relative displacement of a slender structural element subjected to an external load applied perpendicularly to an axis of the element.	

Symbol	Description	Unit
Δ	Absolute cable elongation i.e., change of length given through $\Delta = L - L_{\mathrm{o}}$.	m
f	Scalar cable force with which it acts on its surrounding or by which it is being tensed.	N
$\boldsymbol{F}$	Directed vector of cable force.	N
$\boldsymbol{u}$	Normalized directed vector of cable force such that $\|\boldsymbol{u}\| \equiv 1$.	N
$\boldsymbol{f}_{\sim}$	Distribution of cable forces for static or dynamic balancing of the mobile platform.	N
$\boldsymbol{f}$	Vector of all m scalar cable forces such that $\boldsymbol{f} = [f_1, \ldots, f_m]^{\top}$.	N
L	Scalar length of a cable, usually referring to the unstrained cable length if not denoted differently by the subscript index.	m
$\boldsymbol{L}$	Vector of all m scalar cable lengths such that $\boldsymbol{L} = [L_1, \ldots, L_m]^{\top}$.	m
$\boldsymbol{\varrho}$	Position of an arbitrary point T with respect to the the body's center of mass.	m
κ	Measurement of the failure of a curve to be a straight line, given through $\kappa = (\|\boldsymbol{\gamma}' \times \boldsymbol{\gamma}''\|)/(\|\boldsymbol{\gamma}'\|^3)$.	
$\boldsymbol{\gamma}$	Arbitrary curve given in space defined as function of its unitary path coordinate abscissae $\boldsymbol{\gamma} = \boldsymbol{\gamma}(\xi)$.	
$\boldsymbol{B}$	Binormal to the curve $\boldsymbol{\gamma}$ given through $\boldsymbol{B} = (\boldsymbol{\gamma}' \times \boldsymbol{\gamma}'')/(\|\boldsymbol{\gamma}' \times \boldsymbol{\gamma}''\|)$.	

Symbol	Description	Unit
$\boldsymbol{N}$	Normal to the curve $\boldsymbol{\gamma}$ given through $\boldsymbol{T} = (\boldsymbol{\gamma}' \times (\boldsymbol{\gamma}'' \times \boldsymbol{\gamma}'))/(\|\boldsymbol{\gamma}' \times (\boldsymbol{\gamma}'' \times \boldsymbol{\gamma}')\|)$.	
$\boldsymbol{T}$	Tangent to the curve $\boldsymbol{\gamma}$ given through $\boldsymbol{T} = \boldsymbol{\gamma}'/\|\boldsymbol{\gamma}'\|$.	
n	Number of degrees of a freedom of a physical body; can be subdivided into translational degrees of freedom n_{T} and rotational degrees of freedom n_{R}.	
n_{R}	Number of rotational degrees of a freedom of a physical body.	
n_{T}	Number of translational degrees of a freedom of a physical body.	
$\overline{\nabla}$	Discrete form of the vector differential operator ∇	
i	Electric current; rate of flow of electric charge past a point or region.	A
u	Voltage, difference in electric potential between two points.	V
T	Energy held by an object because of its motion.	J
U	Energy held by an object because of its position relative to other objects, stresses within itself, its electric charge, or other factors.	J
$\boldsymbol{h}$	Fictitious force, also called pseudo force, d'Alembert force or inertial force, are forces that appear to act on a mass whose motion is described using a non-inertial frame of reference, such as an accelerating or rotating reference frame.	[N, N m]

Symbol	Description	Unit
f	Force, any interaction that, when unopposed, will change the motion of an object.	N
$\boldsymbol{g}$	Holonomic constraints of a constrained multibody system.	
$\boldsymbol{J}$	Moment of inertia, also known as angular mass or rotational inertia, of a rigid body is the quantity that determines the torque needed for a desired angular acceleration about a rotational axis.	$\mathrm{kg\,m^2}$
$\boldsymbol{\Theta}$	Joint coordinates of a given platform pose.	
$\boldsymbol{\Phi}_{(.)}$	Mapping of the kinematics problem, either inverse kinematics $\boldsymbol{\Phi}_{\mathrm{IK}}$ or direct kinematics $\boldsymbol{\Phi}_{\mathrm{DK}}$.	
$\boldsymbol{\lambda}$	Lagrange (underdetermined) multipliers in constrained multibody dynamics; can be understood as fictitious forces ensuring satisfaction of holonomic constraints.	
$\boldsymbol{a}$	Linear acceleration of a physical body in space.	$\mathrm{m/s^2}$
$\boldsymbol{p}$	Linear position of a physical body in space.	m
$\boldsymbol{v}$	Linear velocity of a physical body in space.	m/s
$\boldsymbol{M}$	Spatial mass matrix of a physical body given as composed of linear inertia matrix and angular inertia matrix.	kg
m	Scalar mass; a property of physical bodies and measure of their resistance to acceleration when a net force is applied.	kg

Symbol	Description	Unit
ω	Natural frequency, also known as eigenfrequency; frequency at which a system tends to oscillate in the absence of any driving or damping force.	rad/s
$\Delta\boldsymbol{x}$	Iteration step in Newton-Raphson method of the root-finding problem.	
η	Tuple of parameters used to define an orientation transformation.	
η_{Eul}	Tuple of Euler parameters $\eta_{\text{Eul}} = \langle\alpha;\beta;\gamma\rangle$.	
η_{TB}	Tuple of Euler parameters $\eta_{\text{TB}} = \langle\Phi;\Theta;\Psi\rangle$.	
λ	Path coordinate along the abscissae of a geometric curve with $\lambda \in [0, s]$ where s be the arc length of the curve.	
ξ	Path coordinate along the abscissae of a geometric curve normalized with respect to the arc length i.e., $\lambda \in [0, 1]$.	
$\hat{\boldsymbol{y}}$	Platform pose composed of platform linear position $\boldsymbol{r}$ and platform angular postiion $\boldsymbol{R}_{\text{P}}$ reading $\hat{\boldsymbol{y}} = \langle\boldsymbol{r};\boldsymbol{R}_{\text{P}}\rangle$.	$[\text{m}, (\cdot)]$
p	Degree of a polynomial; highest of the degrees of its monomials (individual terms) with non-zero coefficients.	
$\boldsymbol{\Theta}$	Quaternion vector defined as $\boldsymbol{\Theta} = [\Theta_0, \Theta_1, \Theta_2, \Theta_3]$ where Θ_0 is the real part of the quaternion.	
r	Actuator redundancy of a parallel mechanism calculated by $r = n - m$.	

Symbol	Description	Unit
$\boldsymbol{e}$	Residual i.e., the error in a result. By example, suppose we want to find x such that $f(x) = b$. With the approximation x_0 of x, the residual is then $b - f(x_0)$ whereas the error is $x - x_0$.	
I	Second moment of area, a geometrical property of an area reflecting distribution of its points with regard to an arbitrary axis.	m^4
$\boldsymbol{\Pi}$	Matrix of n_Π shape functions for the discrete displacement of a curve in 3-dimensional space as function of unitary path coordinate ξ i.e., $\boldsymbol{\Pi}(\xi) \in \mathbb{R}^{3\times 3\,n_\Pi}$.	
h	Step size used in fixed step-size numerical integration.	s
$\boldsymbol{\varepsilon}$	Geometrical measure of deformation representing the relative displacement between particles in a physical material body.	
$\boldsymbol{\sigma}$	Internal forces that neighboring particles of a continuous material exert on each other.	Pa
$\boldsymbol{A}^\top$	Structure matrix of a cable robot, which is the transpose of the conventional inverse kinematics Jacobian $\boldsymbol{A}^\top = \mathrm{D}\,\boldsymbol{\Phi}_{\mathrm{IK}}^\top$.	
ϵ	Threshold value for stopping root-finding algorithms.	
$\boldsymbol{\tau}$	Torque, moment, moment of force, or "turning effect"; the rotational equivalent of a linear force.	N m
τ	Measurement of the failure of a curve to be planar, given through $\tau = (\boldsymbol{\gamma}' \bullet (\boldsymbol{\gamma}'' \times \boldsymbol{\gamma}'''))/(\|\boldsymbol{\gamma}' \times \boldsymbol{\gamma}''\|^2)$.	
ϱ	Unit density of a physical body.	$\mathrm{kg/m}^3$

Symbol	Description	Unit
η	Modulus of viscosity. A high modulus of viscosity means the material or liquid will not flow easily—imagine syrup—while a low modulus of viscosity means the material or liquid will flow easily—imagine water or gasoline.	$\mathrm{kg/(m\,s)}$
β_w	Wrapping angle of the cable on its guiding pulley.	rad
$\boldsymbol{w}$	External wrench on the mobile platform, composed of gravitational wrench $\boldsymbol{w}_\mathrm{G}$ and process wrench $\boldsymbol{w}_\mathrm{O}$.	$[\mathrm{N}, \mathrm{N\,m}]$
E	Young's modulus of elasticity describing resistance against uniaxial stress in the direction of deformation. A high modulus of elasticity means the material or fluid requires large deformation forces—imagine steel—while a low modulus of elasticity means the material or fluid requires only small deformation forces—imagine a rubber band.	$\mathrm{kg/(m\,s^2)}$

Notation

Notation	Description
$\boldsymbol{M}$	Matrix quantities are, if not introduced otherwise, written in uppercase bold math font.
$\boldsymbol{x}$	Vector quantities are, if not introduced otherwise, written in lowercase bold math font.
x	Scalar quantities are, if not introduced otherwise, written in lowercase light math font.
$(\cdot)_{rc}$	r-th row, c-th column component of matrix $(\cdot)$.
$(\cdot)_{r}$	r-th component of vector $(\cdot)$.
$\boldsymbol{a} \times \boldsymbol{b}$	Cross product, or vector product, of two linearly independent vectors $\boldsymbol{a}, \boldsymbol{b} \in \mathbb{R}^3$, defined as $\boldsymbol{a} \times \boldsymbol{b} = \|\boldsymbol{a}\| \, \|\boldsymbol{b}\| \, \boldsymbol{n} \sin\theta$ where θ is the angle between $\boldsymbol{a}$ and $\boldsymbol{b}$ and $\boldsymbol{n}$ is a vector perpendicular to both $\boldsymbol{a}$ and $\boldsymbol{b}$.
$\boldsymbol{a} \bullet \boldsymbol{b}$	Dot product, or scalar product, of two vectors $\boldsymbol{a} \in \mathbb{R}^k$ and $\boldsymbol{b} \in \mathbb{R}^k$ defined as $\boldsymbol{a} \bullet \boldsymbol{b} = \boldsymbol{a}^\top \boldsymbol{b} = \sum_{j=1}^{k} \boldsymbol{a}_j \, \boldsymbol{b}_j$.
${}^{\mathrm{F}}(\cdot)$	Frame of reference of vector or matrix $(\cdot)$ e.g., ${}^{\mathrm{F}}\boldsymbol{x}$ is $\boldsymbol{x}$ given in coordinates of $\mathcal{K}_{\mathrm{F}}$, ${}^{\mathrm{O}}\boldsymbol{x}_i$ is $\boldsymbol{x}_i$ given in coordinates of $\mathcal{K}_{\mathrm{O}}$; if the frame of reference pre-superscript is omitted, the world frame $\mathcal{K}_{\mathrm{O}}$ is assumed.
$(\cdot)_{\mathrm{C}}$	Index for a cable quantity.
$(\cdot)_{\mathrm{DK}}$	Index for direct kinematics or forward kinematics.

Notation	Description
$(\cdot)_{\mathrm{D}}$	Index for a drum quantity.
$(\cdot)_{\mathrm{FD}}$	Index for forward dynamics.
$(\cdot)_{\mathrm{ID}}$	Index for inverse dynamics.
$(\cdot)_{\mathrm{IK}}$	Index for inverse kinematics.
$(\cdot)_{\mathrm{O}}$	Index for an operation process quantity.
$(\cdot)_{\mathrm{P}}$	Index for a platform quantity (not to be confused with $(\cdot)_{\mathrm{Rr}}$).
$(\cdot)_{\mathrm{Rr}}$	Index for a roller or pulley quantity (not to be confused with $(\cdot)_{\mathrm{P}}$).
$(\cdot)_{\mathrm{R}}$	Index for a rotational quantity.
$(\cdot)_{\mathrm{SM}}$	Index for a servo motor i.e., drive train quantity.
$(\cdot)_{\mathrm{T}}$	Index for a translational quantity.
$(\cdot)_{\mathrm{W}}$	Index for a winch quantity.
$\bar{x}$	Mean value of variable x used in its for of the arithmetic mean of a set of data $x_1, x_2, \ldots, x_n$ such that $\bar{x} = 1/n \sum_l^n x_l$.
$\tilde{x}$	Median of variable x, defined such that it separates a data sample into a higher half and lower half of values.
$\cdot\mathrm{R}\cdot\mathrm{T}$	Classification scheme of cable robots depending on the number of DOF of the mobile platform where T stands for translational and R stands for rotational degrees of freedom (DOFs), respectively.

Notation	Description
$\|\cdot\|_p$	p-norm (also called ℓ_p-norm) of vector $\boldsymbol{v} \in \mathbb{R}^k$ with $p \geq 1$ given by $\|\boldsymbol{v}\|_p = \left(\sum_{j=1}^{k} \|\boldsymbol{v}_j\|^p\right)^{1/p}$. If p is omitted, we assume $p \equiv 2$.
$\mathrm{D}_x(\cdot)$	Differential operator denoting partial derivative of its succeeding argument with respect the denoted subscript i.e., $\mathrm{D}_x(\cdot) = \frac{\partial(\cdot)}{\partial x}$.
$p_{x\,\%}$	Value that a given percentage x of data or observations of a group of observations fall under. The 20th percentile gives the value below of which 20 % of all observations are located.
$[\cdot]_\times$	Skew-symmetric cross product matrix of vector $(\cdot) \in \mathbb{R}^3$ satisfying $[\cdot]_\times \boldsymbol{a} = (\cdot) \times \boldsymbol{a}$. In fact, the cross product skew-symmetric matrix is the Plücker matrix of line $(\cdot)$.
$\dot{(\cdot)}$	First total-derivative with respect to time of scalar or vector $(\cdot)$ such that $\dot{(\cdot)} = \frac{\mathrm{d}(\cdot)}{\mathrm{d}t}$.
$\ddot{(\cdot)}$	Second total-derivative with respect to time of scalar or vector $(\cdot)$ such that $\ddot{(\cdot)} = \frac{\mathrm{d}^2(\cdot)}{\mathrm{d}t^2}$.
$(\cdot)^\top$	Transpose of vector or matrix $(\cdot)$ such that $(\cdot)_{rc}^\top = (\cdot)_{cr}$.
$(\cdot)^\mathsf{H}$	Hermitian transpose (also called conjugate transpose) which is obtained by taken the transpose $\boldsymbol{A}^\top$ of matrix $\boldsymbol{A}$ and then complex conjugating each entry i.e., $\boldsymbol{A}^\mathsf{H} = (\overline{\boldsymbol{A}})^\top = \overline{\boldsymbol{A}^\top}$. If $\boldsymbol{A} \in \mathbb{R}$, then $\boldsymbol{A}^\mathsf{H} = \boldsymbol{A}^\top$.
σ_x^2	Variance is defined as the expectation of a random variable's squared deviations from its mean. More coherently, variance describes how far (random) data are spread from their mean value.

Notation	Description
$\langle(\cdot);(\cdot);\ldots;(\cdot)\rangle$	Set of vectors of matrices of unequal size that cannot be concatenated but ought be thought of as representing one common entity.

Acronyms

Acronyms	Description
ALF	augmented Lagrangian formulation
BDF	backward differentiation formulae
BG material	Burgers material
BSM	Baumgarte stabilization method
CAD	computer-aided design
CDPR	cable-driven parallel robot
CPM	coordinate partitioning method
CRPM	completely restrained positioning mechanism
DAE	differential-algebraic equation
DOF	degree of freedom
FDP	forward dynamics problem
FKP	forward kinematics problem
FRPM	fully restrained positioning mechanism
GGL	Gear-Gupta-Leimkuhler
GKV material	generalized Kelvin material
GMW material	generalized Maxwell material
IDP	inverse dynamics problem
IKP	inverse kinematics problem

Acronyms	Description
IRPM	incompletely restrained positioning mechanism
KV material	Kelvin–Voigt material
LQG	linear–quadratic–Gaussian controller
LQR	linear–quadratic regulator
MP	motion pattern
MW material	Maxwell material
NURBS	non-uniform rational B-spline
ODE	ordinary differential equation
PDE	partial differential equation
PI controller	proportional-integral controller
PID controller	proportional-integral-derivative controller
PM	penalty method
RRPM	redundantly restrained positioning mechanism
SDE	spring-damper element
SLM	standard Lagrange multipliers method
SLS material	standard linear solid material
SNAE	system of nonlinear algebraic equations
UHMWPE	ultra-high-molecular-weight polyethylene
ZR material	Zener material

Chapter 1

Introduction

Before introducing the mathematical and mechanical fundamentals of cable-driven parallel robots in the next chapter, the following pages will show the concepts and benefits of cable-driven, or cable-actuated, mechanisms as well as their key distinction to other mechanisms such as conventional parallel manipulators and robots. Following that, an overview of state-of-the-art research and state-of-the-art applications in the field of cable-driven mechanisms, in particular focusing on cable-driven parallel robots, will be given. Inferring from the state of the art, shortcomings of current knowledge and research on cable-driven parallel robots will be given, focusing particularly on the dynamics formulations of such systems. Concluding from this overview, the thesis focus with assumptions and simplifications made will be presented and given in very short terms. To round off the chapter, notable applications of cable-driven parallel robots and academic demonstrators will be shown.

Cable-driven mechanisms[1] have been known to mankind for many millennia since cables were one of the first things men used in mooring and fastening objects. There is evidence dating cables back to 17 000 BC, while the Egyptians were probably the first to use cables as tools for erecting buildings like the Great Pyramid of Giza. While the materials used in manufacturing cables have changed from water reeds, grass, leather, and animal hair to more modern materials like steel or even synthetic fibers like Aramid/Kevlar or Dyneema (similar to Aramid, yet made of so-called ultra-high-molecular-weight polyethylene (UHMWPE) fiber), their basic usage principle has not changed much: On the one end, a

[1] With synonyms *wire*- or *tendon*-driven or based mechanisms.

Table 1.1: Yield strengths and unit densities of different materials. Yield strength refer to a single fiber or strand of the material.

Material	Yield Strength / GPa	Density / $\mathrm{kg\,m^{-3}}$
Piano wire	2	7800
Steel high-strength alloy ASTM A514	0.690	7800
Aramid (Kevlar)	3.620	1440
Aluminum alloy 2014-T6	0.400	2700
UHMWPE (Dyneema®)	0.020	970
Bone	104—121	—

cable is attached to a spooling device, most usually a rotating drum, on the other end, the cable is attached to an object that is to be manipulated. By changing the cable's length, the object can be moved; however, care needs to be taken as cables can only exert tensile forces i.e., they can only pull on whatever they are connected to, resulting in a unilateral motion of the manipulated object. Adding a second cable to the opposite side moving antagonistic to the first cable, we are now able to move the object in one dimension. Adding more and more cables, ideally always in antagonistic pairs of two, we can increase the number of controllable DOFs from one to up to six. Then, we are able to position an object in space in virtually arbitrary orientation and position since we control all six DOFs—three translational and three rotational. By adding a control system to the equation and automating synchronized motion of the winches, we obtain a cable-driven mechanism.

The most well-known representatives of cable-driven mechanisms are probably cranes and the so-called Skycam (Cone 1985) and its competing products CableCam and Spidercam. All systems use four cables guided from a winch over a series of pulleys toward the camera cage attached to the distal end. By changing cable lengths, the camera moves over the field of soccer, football, or baseball stadia giving the audience a bird's-eye view of the happenings on the field. Such perspectives cannot be achieved using conventional boom lift camera cranes as their operational space is very limited due to limitations arising from structural instabilities. Cable-driven systems like Skycam, on the other hand, make great use of the advantages of cable-driven systems: reduced inertia stemming from

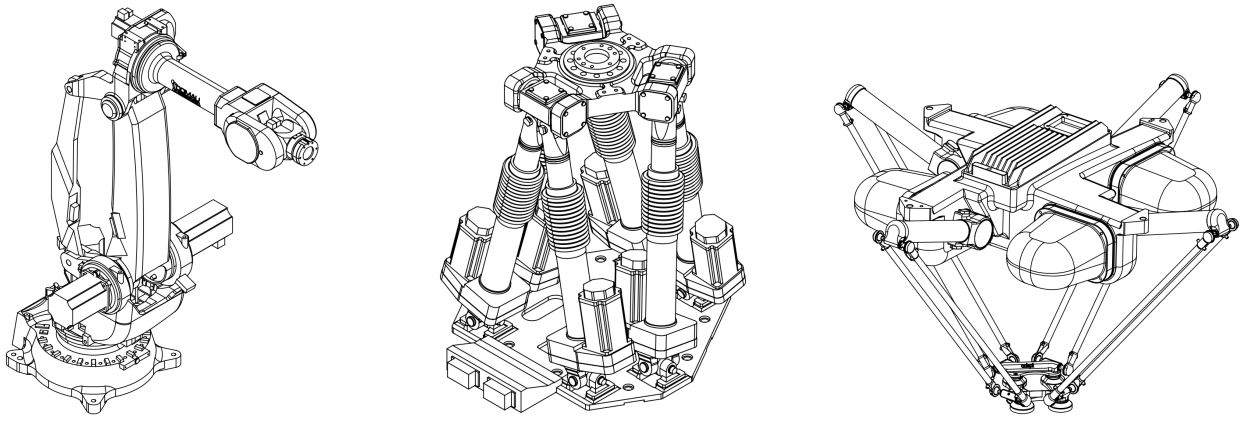

(a) *Industrial robot, the most common representative of serial mechanisms.*

(b) *Parallel mechanism in the design of a Gough-Stewart platform.*

(c) *Parallel mechanism in the design of a Delta robot.*

Figure 1.1: Graphical representation of different designs of serial mechanisms (a) and parallel mechanisms (b) and (c).

having to move comparatively lightweight cables[2] allows for high dynamics with cables wound and unwound quickly on rigidly attached winches. In addition, the yield strength of cables i.e., the maximum tension before breakage, is very high compared to their density allowing for huge workspaces (see Table 1.1 for a comparison of different material yield strengths and unit densities).

When using cable-driven mechanisms, they must not always be set up like cranes. Two distinct topological mechanism designs exist, namely 1) serial mechanisms, and 2) parallel mechanisms. A third design exists, so-called hybrid mechanisms, which combine serial mechanisms and parallel mechanisms. However, their design is not distinctively different from the already mentioned ones as it is a mere combination thereof.

Serial mechanisms are composed from consecutively attaching actuated joints to one another which provides a final structure similar to the human arm. Typical serial mechanisms are industrial robots as shown in Fig. 1.1(a). On the other hand, parallel mechanisms feature actuated joints connected to the same base and the same platform or end effector. Typical parallel mechanisms

[2] Even though cables may have densities of several thousand kilogram per cubic meter (cf. Table 1.1), comparing their weight for a given length, it is much lower than an equivalent beam structure.

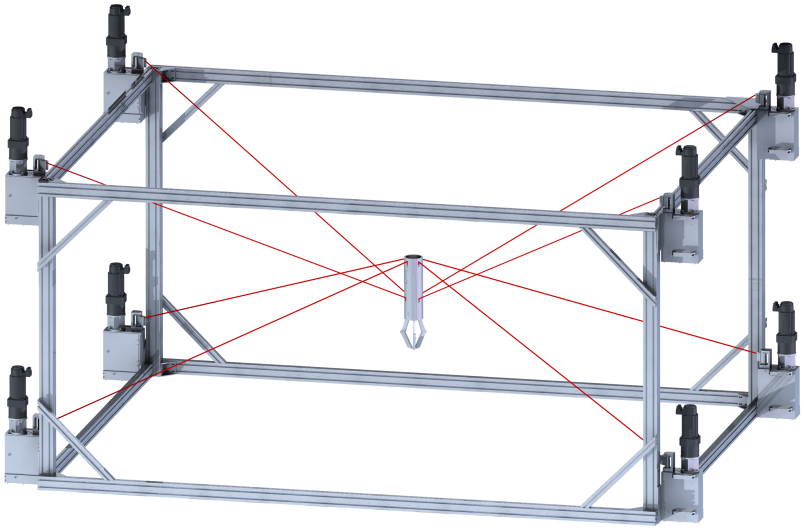

Figure 1.2: Illustration of a cable robot with its core components: a frame (surrounding), attached winches, cables (red), and the mobile platform (center).

are the Gough-Stewart platform (Stewart 1965; Gough 1962) with actuated prismatic joints (see Fig. 1.1(b)) and the Delta robot with actuated revolute joints (see Fig. 1.1(c)).

Serial mechanisms generally achieve larger workspaces and higher dynamics, whereas stiffness and accuracy of parallel mechanisms renders them superior—even though the quantitative measure of accuracy is still a topic of discern (Briot et al. 2007). In principle, however, both serial and parallel designs can be equipped with cables providing cable-driven serial and cable-driven parallel manipulators, respectively. However, since cables can only exert tensile forces, any serial chain implemented using cables requires two thereof to be a homologous replacement. This necessity can be exemplified on the human body where flexing of the lower arm is performed by an antagonistic pair of muscles namely the biceps brachii muscle and triceps brachii muscle.

1.1 Cable-Driven Parallel Robots

Cable-driven parallel robots—we will use the shorter form *cable robot* in the remainder—combine the advantages of serial mechanisms with those of parallel

mechanisms and of cable-based actuation aiming at overcoming the mechanisms' shortcomings (a schematic sketch is shown in Fig. 1.2). The concept of cable robots is as simple as it is ingenious: by replacing prismatic joints with elastic cables, the stroke of each actuating chain can be drastically increased while at the same time reducing its inertia. Since cables are almost infinitely flexible[3], it is possible to store the superfluous cable in a limited space e.g., on a winch or simply inside a container. These cable storage and retrieval units can then be stored outside of the workspace and fixed to the environment i.e., the ground, the wall, or a separate frame. This implicates a reduction in moving inertia as this now reduces to the end effector inertia, the inertia of the cables, and the inertia of the coiling mechanism i.e., drum itself. In general one assumes that, in contrast to the platform inertia, the cable inertia can be neglected as it does not primarily affect the dynamics. However, this largely depends on the scale and configuration of the cable robot, the mechanical properties of the cables in use, the designated application, as well as the maneuver performed. Experimental observations have shown that cable dynamics cannot be neglected completely, but a common approach to understanding and modeling the cables is yet to be found and is thus the main focus of this thesis.

A cable robot is generally composed of four components: 1) an end effector or mobile platform with n degrees of freedom, positioned within the workspace to perform a certain task, 2) m cables to control the pose i.e., position and orientation of the platform, 3) winches that change the length of the cables, and 4) a frame that is used to attach the winches to. One may not always see a closed frame, or even any frame, on a cable robot as simple towers can be used in their place, or the environment itself may be used as frame. The simplest form of a cable robot would be a building crane, however, to be precise, a crane is not a robot as per definition. Following the definition of the Robotics Industries Association RIA, a robot "is a reprogrammable, multifunctional manipulator

[3] To some extent this holds true as cables can be bend and twisted without providing any significant resistance. Of course, at some point, the mechanical structure of the cable or its strands will yield and the cable breaks.

designed to move material, parts, tools or specialized devices through variable programmed motions for the performance of a variety of tasks" ((RIA) 1999). In this case, building cranes are no robots as they are no reprogrammable, multifunctional manipulators.

Compared to building cranes, cable robots used in industrial or entertainment applications are more complex and make use of more than one cable, however, challenges are very much alike in both systems. At the core of all challenges of cable robots are the cables as they are the driving element of such systems. When comparing cable robots to their rigid body counterparts, with which they share very much every other benefit and demerit, the only apparent difference is the use of cables instead of rigid joints. It is remarkable that this at first sight very small structural change has major impact on positioning accuracy, control, workspace, dynamics, and more related to cable robots. Any sort of cable, be it $d = 0.5\,\mathrm{mm}$ nylon fibers, $d = 6\,\mathrm{mm}$ polyethylene fibers, or even $d = 200\,\mathrm{mm}$ steel cables, suffers from noticeably low flexural rigidity with respect to its tensile rigidity. This fact becomes apparent in cables tending to sag under their own weight due to gravity when spanned between two points, with the magnitude of sag dependent on the applied tension and mechanical properties (a mechanical derivation can be found in Section 2.3.1.3). Three side-effects emerge from cable sag being 1) the cable length being larger than the geometric distance between the cable's two ends, 2) the direction of cable force at the distal end changing from the direct-line connection to also comprise vertical drag, and 3) the inability to transmit large forces through the cable i.e., only a tensed and nearly straight cable can transmit any force wit marginal loss from one end to the other. Sagging occurs in even very lightweight cables, however, it may be neglected as the magnitude of sag is small compared to the cable length (Irvine 1974).

Going from statics to dynamics, any excitation perpendicular to the cable's neutral axis will not be hindered by restoring shear forces, as is the case for rigid bodies. Ultimately, this results in longitudinal motion or vibration of the cable which are subject to gravity and the cable's internal dynamics—neglecting

effects like air friction or contact with the environment. In any event, vibration will decline, yet magnitude and decay time vary largely depending on cable tension and magnitude of excitation. What is even worse than a freely vibrating cable, is a vibrating cable interacting with other bodies onto which the vibration may propagate. This is the case in cable robots where the vibration of a single cable propagates in both directions, toward the winch and the platform where the wave continues traveling farther. While the winch can robustly compensate for the waves due to its high inertia and being rigidly attached to the ground, the mobile platform is attached to only the cables thus it will also start vibrating and propagating its motion onto the other cables. This affects not only dynamic trajectory tracking, but also reflects itself in the overall system stiffness being degraded due to vibrating cables.

While international standards exist for structurally designing and selecting cables in engineering technologies like cable-stayed bridges, elevators, aerial tramways, or cranes, choosing mechanical cable properties is done based on empirical values and expert know-how (Jung et al. 2018; Ji et al. 2019; Collings 2016). In many cases, the dynamics of such systems are neither considered nor investigated when designing the application, but are based on finite element static analysis—and considerably high safety factors. Even so, to this date, no comprehensive and agreed upon modeling of cable robots with elastic and flexible cables of time-varying length has been made which is why understanding of cable robot dynamics remains in a state of uncertainty. For small scale cable robots, a simplified dynamics model based on pure kinematic properties suffices, however, there is discrepancy between simulation and experiment which cannot solely be lead back to non-modeled effects like friction. Particularly, cable motion as the platform sways along a trajectory can be observed in experiments, but it is unclear as to how a suitable model for a cable robot together with its cables can be found (Tang 2014). In the following section, we will give an overview of literature focusing on modeling of cable robots, as well as cables to use in cable robots to point out the improvements already made and shortcomings, as well as the direction research is headed.

1.2 Literature Overview

Despite cables being a mechanical structure that has been known to mankind for many millennia, comparatively only very little is known about these structures. It is generally accepted that cables can exert only tensile forces, and that their elastic behavior can, in a first-order approximation, be considered linear with a certain factor of stiffness. However, exact cable models, in particular for use in cable robots, are still scarce with a lot of the state of modeling being academic research findings rather than versatile formulations. This is last due to the complex nature of how cables are manufactured and the vast variety of different structures making modeling very involved. In this literature overview, we will focus on this thesis' primary direction i.e., modeling of spatial cable dynamics explicitly considering transversal cable motion. An overview of research on longitudinal cables waves i.e., stress-strain dynamics will comprise this section.

Different approaches to modeling cables in various fields of engineering can be found which can be categorized into 1) detailed modeling as a composition of multiple strands of wires, 2) approximate models of only the large signal dynamics, or 3) fake dynamics models. While each of these approaches has its merits and demerits, every single one has its right to exist. Coming from material sciences, the detailed modeling of cables and wires is done on a very small-scale level i.e., while microscopic effects may not be considered after all, the interaction between single cable strands is at the root of these models. If the intra-cable dynamics are of only little interest, we can assume the cable to be composed of one solid body exhibiting respective elastic and flexural rigidity. In this case, only the overall shape or motion of the cable and its response to excitation—either motion or force—are to be of interest. Such models will reduce the complexity and provide only for the essential data, but may lack in covering effects such as rupture or disintegration of single fiber strands. Lastly, especially in the field of animation, fake dynamics of cables or cable-like objects, are employed as one is merely interested in having an object that behaves physically plausible. However, its physically correct behavior i.e., allowing for

correct interpretation of forces and moments is not of interest thus requiring little to no physical foundation for the models.

One of the first publications on cable robots is the aforementioned Skycam by Cone in which the basic kinematic and dynamics formulations for cable robots were given incorporating nonlinear elastic cables (Cone 1985) and Newtonian mechanics of a free-floating rigid body. It was not until 1992, when Albus et al. published a more in-depth analysis of cable robots and possible fields of applications. Already then, a viscoelastic cable model composed of a parallel combination of linear spring and linear damper was considered in modeling and simulation of the NIST RoboCrane (Albus et al. 1992). Further consideration of the kinematics and dynamics of the cables were not performed until much later and cables were considered unilateral constraints—providing tensile forces when elongated and no compressive forces when shortened. This resulted in the cables being assumed massless slender rods of only viscoelastic behavior with unilateral stress-strain dynamics, which over time ultimately evolved into the so-called *standard cable robot model*. After almost one decade of no further contributions, Nahon presents the dynamics modeling of a tethered aerostat cable robot based on finite element discretization of the cables by a lumped-mass approach with absolute nodal coordinate formulation (Nahon 1999). Changes in cable length are accounted for by varying the length of the very first segment.

The lumped mass approach was later followed by further researchers (Hajžman et al. 2011; Caverly et al. 2014; Caverly et al. 2015b; Bedoustani et al. 2008; Duan et al. 2010; Duan et al. 2011) and proven not suitable to the winding and guiding dynamics of cables nor to covering well the flexural rigidity due to the type of discretization used. In cable robots, these models can be used for static, kinetostatic, and vibration analysis of the system i.e., for any static scenario. Spatially discretized cables can be successfully employed in cases where cable length does not change and where the cable must not be guided like in underwater riser applications (Du et al. 2012; Quisenberry et al. 2006). However, finding numerically efficient formulations with high accuracy is a contradictory task due to the inherent kinematic constraining of each segment to its preceding

and succeeding element. Simulation times of several hours [sic.] are not unlikely, even with just one cable freely swinging (Adamiec-Wójcik et al. 2014).

Bestowed on discretized models is the ability to allow for kinetostatic and vibration analysis of the cable robot's mobile platform at any given pose within the workspace. Further, (Nahon 1999; Duan et al. 2011) show the theoretical workspace of cable robots with lumped mass cables differs from the one obtained using the standard model. In fact, in-depth research by Bedoustani et al. points out neither cable mass nor cable elasticity can be neglected with both having non-negligible effect on terminal accuracy of the platform (Bedoustani et al. 2008; Bedoustani et al. 2011).

While cable mass was willfully neglected in early years in both statics and dynamics, Kozak et al. first consider cable mass and elasticity in the workspace analysis of cable robots by employing Irvine's infamous hefty cable model, turning cable robot both the kinematics problem and workspace calculations into a kinetostatic problem (Kozak et al. 2006). Reaching from the 1974 work by Irvine, further models for vibration and stiffness analysis of cable robots emerged, both in two dimensions (Nan et al. 2011), as well as three dimensions (Diao et al. 2009). In all these contributions, the static solution given the cable model by Irvine is superimposed by the linear wave equation allowing for additional transversal deflection of the cable. The results signify the importance of considering not only longitudinal cable elasticity, but also their transversal flexibility, already in the statics case. Unfortunately, the results are valid in only a very limited range around the taut string due to the linearization employed during derivation of the linear wave equation.

Other approaches to modeling and simulation of cable robots where proposed using either Robotran software (Collard et al. 2011) or computer-aided design (CAD)-based simulation (Michelin et al. 2015). With Robotran being a multibody simulation framework designed for robotic applications, Collard et al. built a cable robot using a segmentized cable of fixed length, where the number of segments is chosen as a trade-off between model complexity, accuracy, and simulation speed (Collard et al. 2011). Michelin et al., on the other hand,

built a complete CAD environment of a cable robot containing every component to simulate CoGiRo, a suspended cable robot. Despite simplifying the complexity of the used CAD model, simulations still run very inefficiently as high number of segments per cable cause the collision detection algorithm of XDE to have to consider many collisions. Even though there are also other software solutions to simulating cables or ropes, it is the high stiffness and kinematic redundancy that causes most cable models to be ill-suited for simulation of cable robots (García-Fernández et al. 2008).

Only recently, more sophisticated models for cable robots with consideration of cable dynamics have been proposed for both the transversal motion (Ayala Cuevas et al. 2017) and the longitudinal motion (Godbole et al. 2017). In both contributions, the cable deflection is described by means of linear combinations of shape functions; the dynamics are thoroughly derived using Lagrange's equation of the first kind. While Ayala Cuevas et al. describes only the transversal motion of an inelastic string using a low-degree polynomial, their model allows for showing interaction between cable and platform especially during jerky motion. In addition, change of cable length is incorporated into the model by considering the change of inertia during cable coiling (Ayala Cuevas et al. 2017). Godbole et al. on the other hand describe only the longitudinal motion using a set of harmonic shape functions, which highlights the high-frequency elastic deformation vibrations inside the cable. Using simple normalization of the shape functions, variable cable length is incorporated into the dynamics, and for energetic consistency incorporated into the inertia of the winding drum (Godbole et al. 2017).

Besides addressing transversal motion of cables in the context of cable robots, their longitudinal dynamics are also of interest i.e., their dynamics of stress and strain or likewise of elongation and force. Since cables are not allowed to go slack during operation of cable robots, cable force control algorithms are heavily being developed ranging from linear controllers like proportional-integral controller (PI controller) or proportional-integral-derivative controller (PID controller) (Kraus et al. 2014; Mikelsons et al. 2008; Bruckmann et al. 2006;

Kawamura et al. 1995a; Khosravi et al. 2013; Reichert et al. 2015) over optimal controllers like linear–quadratic regulator (LQR) or linear–quadratic–Gaussian controller (LQG) (Lambert et al. 2007; Korayem et al. 2011; Abdolshah et al. 2015) or sliding mode (Liu et al. 2009; Oh et al. 2004; Schenk et al. 2015; Alikhani et al. 2011; El-Ghazaly et al. 2014) to methods like H_∞ (Chellal et al. 2014; Laroche et al. 2012) or passivity based control (Zarebidoki et al. 2011b; Caverly et al. 2014). In most, if not all of these contributions, cable length or elongation is the control input whereas cable force on the platform is the output, where the tracking errors are calculated based on deviation of nominal cable forces from a calculated force distribution. While the latter topic of calculation of cable force distributions in itself is yet another involved task, in particular for cable robots with more cables than DOF, we may simply assume that cable force control will reduce error between a desired cable force and the currently prevalent force. Any control law used in this scenario must apparently provide stability of the closed-loop in order to not cause harm to or destroy the system (Lunze 2010). Stability can be proven either analytically or through simulation where in either case some knowledge of the to-be-controlled plant[4] must be available.

Since some knowledge of the underlying cable dynamics must be know, most cable force controller are based on linear elastic models—cable is assumed to behave like a spring—or linear viscoelastic model—cable is assumed to behave like a spring-damper. While it may still be difficult to obtain quantitative parameters of elasticity and particularly of viscosity for a cable, these models have a wide range of validity for both steel cables as well as polyethylene fiber-based cables like Dyneema®. However, since cables are no single elastic body but merely composed of several hundreds or thousands of strands, interstrand friction emerges during any cable tensing and relaxing. This happens for both steel cables in cable-stayed bridges (Sauter 2003) or surgical devices (Miyasaka et al. 2016) but also polyethylene cables typically used in cable robots of small size (Miermeister et al. 2015), medium size (Palli et al. 2012), and large

[4] In this case, plant simply means cable.

scale (Lalo 2013). Since polyethylene fiber cables are more promising to use in cable robots due to their small inertia-to-tensile-strength ratio, a deeper understanding of such fiber cables' stress-strain dynamics has been of interest to several research groups.

Miermeister et al. present an elastic cable model with hysteresis effect that allows for good approximation of the cable's actual stress-strain dynamics, based on linear elastic Hookean material superimposed with a polynomial function of elongation, tension, and excitation frequency for compensation. For use in a surgical robotic system, Miyasaka et al. identify cable force models based on Buoc-Wen hysteresis and also incorporate cable-pulley interaction modeling, increasing approximation quality for steel wires of diameter $d = 0.610\,\mathrm{mm}$ and $d = 1.190\,\mathrm{mm}$. Palli et al. use a general viscoelastic material model composed of serial springs and dampers combined in parallel to model the stress-strain dynamics for their use case of tension-prediction on a tendon-based hand. In the field of cable robots, Piao et al. (2018) and Tempel et al. (2018) also make use of a general viscoelastic material model to describe the dynamics and then later use experimental data to identify material parameters. Piao et al. measure cable elongation as a response of instantaneous stress increase, whereas Tempel et al. measure cable stress given strain inputs. Either contribution show an improvement in the quality of approximation of both creep phenomena and hysteretic behavior while providing a purely mechanics-based model with physically meaningful parameters.

Findings by Piao et al. and Tempel et al. can be used for improving cable force control laws by providing either a more comprehensive cable strain model for simulative analysis, or by providing a model that can be used in feed-forward control laws to anticipate the cable's stress dynamics. However, some questions remain unanswered like the linearity or nonlinearity of mechanical parameters with respect to the unstrained cable length, or the influence of pulleys.

1.3 Open Problems

While cable robots may ultimately not be replacing parallel robots in their line of duty, there are promising applications for cable robots, as the overview of applications in Section 1.6 shows. However, to further improve accuracy and control of cable robots, their key difference to conventional parallel robots needs to be better addressed and more thoroughly investigated. Since the key difference is made up by the use of cables, research focus is more and more being shifted toward modeling cables. There have been several promising research results in the past as shown in Section 1.2, however, most of the models lack key factors like either elasticity, flexibility, or variable length, or are purely kinematics based.

Significance of considering cables, especially their mass, has been proven by Bedoustani et al. in 2008, however, only few contributions thoroughly investigated modeling approaches and compared them. Ayala Cuevas et al.; Godbole et al. presented promising approaches, yet limit their applicability due to the assumptions being made—no longitudinal motion or no transversal motion, respectively. Du et al. presented a cable robot model capturing spatial cable motion well, however, with issues of numerical stability. Most literature on cable modeling for cable robots is based on purely geometric description of the cable and incorporating some kinematics to make it a physically equivalent body. A coherent modeling of cable robots viewing them as a system of multiple flexible bodies has yet to be established. In addition, little attention has been paid to the internal dynamics of the cables used in many applications, which affects both statics and dynamics, in particular in control tasks. Large scale and high dynamics applications of cable robots require profound knowledge of the overall system dynamics and do not allow for regarding the system as a free-floating rigid body.

With beam theory, more comprehensive approaches like the linear and nonlinear Euler-Bernoulli beam (Zohoor et al. 2013; Zohoor et al. 2008), or the geometrically more consistent Kirchhoff beams (Boyer et al. 2011), Reissner

beams (Ibrahimbegović 1995), and Cosserat rods (Lang et al. 2011; Lang et al. 2009) are available. No contributions have yet been made transferring classical mechanics topics like beam theory and incorporating them into a cable robot formulation last because its transferability is unknown and its model complexity is rather high. Nevertheless, this approach seems the most promising as it provides a geometrically-exact and mechanically-consistent formulation of cables for cable robots.

1.4 Problem Statement and Goal

This thesis aims at finding a model formulation suitable for forward dynamics simulation of cable robots under consideration of spatial cable dynamics as current modeling approaches describe the system only partially mechanically consistent. To advance cable robot research and applications, we want to coherently research and evaluate modeling approaches of cable robot dynamics allowing for more holistic formulations of said systems under consideration of the main components—platform and cables. Let us state the goal of this thesis in the following way:

> *We desire a low-complexity and low-dimensional cable robot model describing the overall dynamics of the mobile platform in conjunction with the cables. Particular emphasis shall be put on spatial dynamics of the cables, while we also want to address the stress-strain dynamics of cables used in cable robots of the* IPAnema *family type.*

We shall further impose the following assumptions or simplifications on the modeling under investigation in this thesis:

Fiber Cables Only Cables in cable robots are usually made from either steel or polyethylene fibers, which makes them behave very differently. Not only are steel cables heavier thus tend to sag more drastically, they also feature

higher stiffness, resulting in less strain with the same amount of tensile force, and showcase very linear stress-strain relationships. However, fiber cables are advantageous due to their reduced inertia allowing for higher dynamics and larger scale cable robots, yet come at the price of more unknown intra-cable kinematics and nonlinear stress-strain dynamics. With most cable robots being operated with fiber cables, we limit our focus to these materials only.

Deformation-free Torsion The cable does not undergo any spreading deformation during torsion. Since torsional displacement of the cable would—depending on the direction of torsion and the cable's direction of weave—stretch or relax the fibers, their length would decrease or increase, respectively. From this follows a nonlinear change in cable strain and as such a difference in force transmission behavior. In case of severe twisting of the cable, phenomena like birdcaging (Costello 1990) or twisting of the wire will occur causing damage to the cable and largely different stress-strain or spatial dynamics.

No Dependence on Environmental Changes Mechanical properties of any material characteristically change with varying environmental properties. For example, the elasticity of a beam made of steel becomes larger with increasing temperature. Such effects can also be observed for polyethylene fibers such as Dyneema® (Schmidt 2016) but may not be explicitly considered in this work.

Solid Cross-Section We assume the cable to be of solid cross-section i.e., not composed of single strands or multiple strands. While physically any cable or wire rope is made from laying or weaving single strands of wires into larger strands which then in turn are laid or woven into the resulting wire rope, we assume the cable given with solid cross-section area. This assumption goes hand in hand with the next two.

Unaltered Cross-Section While the cable's cross-section does in fact change during stress-induced elongation (Howell 1992; Schmidt 2016), we shall assume the cross-section to always be of circular shape. Not only does this provide for cleaner equations of motion and computationally less expensive numerical integration, but it is also not of major concern to determine the change of cable shape. With regards to cable collision detection, this may be of interest,

however, as shown by e.g., Schmidt (2016), the ovalization characteristics of Dyneema® cables do not change the cross-section shape too drastically. As such, the worst-case bounding box of a cable under high tension may be given by a foursquare of edge length set to the cable's diameter.

No Relative Intra-Cable Kinematics With assuming our cables being made from one strand only, this also implies that there is no relative intra-cable kinematics affecting the whole cable kinematics and dynamics. As a cable is made from many strands, these will inevitably be stressed or strained differently depending on the overall bending of the cable. Concluding, there is relative motion between single adjacent strands which implies intra-cable friction. In fact, this causes elastic strain relaxation due to low speed friction, as will be shown in a later chapter.

1.5 Structure of This Thesis

To begin, Chapter 2 presents the fundamentals of cable robots covering basic concepts, notation, and classification as well as introducing existing kinematic, static, and dynamic formulations of cable robots. The chapter will put particular emphasis on the kinematics formulations and how cable models are currently being viewed, but also how a new cable model can make use of existing methods and formulations. Further insight into solving the static and kinetostatic equilibrium of cable robots, as well as methods and algorithms for finding force distributions will be given. Cable robot dynamics will be presented for the standard free-floating rigid-body formulation particularly with regard to Chapter 4.

With the technical terms at hand, Chapter 3 is presenting the spatial cable model based on Cosserat rod theory for use on cable robots. To show the reasoning why this model is believed most suitable and where it propels over other modeling approaches, two other cable modeling approaches are summarized pinpointing on their shortcomings and challenges. Simulative assessment and validation of the cable model will be given with respect to the conventional

linear beam theory, of which the basis is laid out, too. Our Cosserat rod-based cable model is gradually established starting with the kinematics of a flexible body in space, from which the equations of motion can be derived. With the model as-is being a continuum formulation, discretization is injected based on the Rayleigh-Ritz approach, which also shows how cable length changes are incorporated. After selecting a set of bases functions, the cable model is evaluated with regards to natural frequencies under various scenarios, as well as its static comparison against the Irvine cable model. Lastly, the DOF of the Rayleigh-Ritz discretization are evaluated and a minimum requirement for suitable quality of cable approximation is given.

In Chapter 4, the Cosserat rod cable model is incorporated into a multibody cable robot simulation framework. First, the framework's general structure is presented with the kinematics of cable and platform referenced, much like defining the constraints fixing cables to the platform and frame. Before presenting results of forward dynamics simulation, statics solution of four use case cable robots are presented highlighting both the applicability of the framework to different sizes and configurations of cable robots, but also pointing out how the new multibody formulation is interlinked to existing methods of workspace analysis and cable force distribution. Subsequently, forward dynamics results of IPAnema 3 are shown to present energetic consistency through the integration scheme chosen, but also presenting limitations of the cable model formulation as such.

Next to spatial cable dynamics, Section 5.3.2 presents experimental identification of the stress-strain dynamics of Dyneema® fiber cables. First, fundamental principles of modeling viscoelastic materials are presented from which a suitable formulation is found in the generalized Maxwell material. From the ordinary differential equation (ODE) derived through first principles, parameter identification based on transfer function fitting is introduced. Identified transfer function coefficients are lastly converted into elastic and viscous parameters using conventional Newton's method. Estimated parameters are then validated by simulating cable stress response to a strain input showing validity of the

selected model and parameters estimated, in particular because stress relaxation can be recovered.

To summarize this thesis, Chapter 6 concludes all findings and presents an outlook into further research.

1.6 Applications and Demonstrators

We will present several noteworthy applications of cable robots which are partially industry-driven and partially readily commercially available applications that only in hindsight entered academia, whereas other applications went from academic into industrial use, and still others are purely academia-based or conceptual applications. The second half of this section presents demonstrators within reach of the department.

1.6.1 Applications

In this section, we will focus on applications of cable robots in different fields such as virtual reality, manipulation tasks, entertainment, and other applications. This selection of some of the most noticeable cable robots shall highlight their wide range of applicability as well as the range of scale—both geometrically as well as dynamically—in which cable robots are developed.

1.6.1.1 Virtual Reality

Virtual reality may be more generalized to manipulation and handling tasks as the cable robot performs manipulation of its end effector, which in turn is connected or controlled directly by a human operator. However, in scenarios of virtual reality, the cable robot and human must either cooperatively manipulate the end effector or the robot is designed to provide a certain feedback to the human thus actively working against the human input.

INCA6D by Chellal et al. uses thin cables since these are very unobtrusive to the human and hardly harmful (Chellal et al. 2012; Chellal et al. 2015). These two characteristics make cable robots a very useful haptic interface and force display system, which is already commercially available as product of Haption SA. INCA6D is a force feedback haptic interface developed to investigate manipulation of objects in an environment of virtual reality. It uses passive pretensioning of the cables by means of a spring-based balancing mechanism and infrared cameras for vision-based control of the end effector.

Virtual Tennis is presented by Kawamura et al. using a cable robot by means of which the reactive forces during playing tennis are generated (Kawamura et al. 1995b). The system itself is in a sideways-laid suspended configuration, as such the player's force input is used to keep all cables taut. In combination with a helmet-mounted display, the user can experience the mass of the tennis racket, the moment of inertia of the same, and reaction forces when the ball is hit.

1.6.1.2 Manipulation

Previously presented virtual reality applications differ from manipulation tasks with respect to how a human operator interacts with the system. In manipulation tasks, we assume the operator to not directly be interacting with the end effector but controlling its position by means of some control input e.g., control joysticks. Manipulation tasks may also be programmed and automated, whereas virtual reality tasks in general are immersive and dynamically changing tasks.

Wind Tunnels of various sizes can be realized with cable robots as the cables can be made with comparatively small diameter making them very unobtrusive to causing wind turbulences (Kawamura et al. 1995a). Any other suspension system would either lack structural integrity within large wind tunnels or would cause the wind flow to be disturbed. However, care needs to be taken as tensed cables are subject to wind-induced vibration which can propagate onto the supported structure.

NIST RoboCrane by Dagalakis et al. of the National Institute of Standards and Technology was one of the first projects to investigate possible applications for cable robots (Dagalakis et al. 1989; Bostelman et al. 1994). As the name suggests, the primary direction of research were automated cranes, but Bostelman et al. also presented aircraft painting and stripping with hybrid cable-driven robot arms. The NIST RoboCrane was the first cable robot system that was operated with a conventional, industry-like control system.

1.6.1.3 Entertainment

SkyCam as well as Spidercam and CableCam are computer-controlled, stabilized, cable-suspended camera system that are more and more often deployed in both film and movie studios as well as during big scale sport events like soccer, football, or Formula 1 races (Cone 1985). They provide for a bird's-eye view of an event allowing for better visually capturing the extent. While this technology may generally not be called a robot, it still employs cable robot technology to move the end-effector—its camera—in a large workspace with high dynamics. Further, cable-suspended camera systems are prime examples of the ease of reconfiguration of cable robots as there are no systems permanently installed in stadiums, but they are set up for each event.

Expo CableRobots shown in Fig. 1.3(b), are twin cable robots developed by Tempel et al. of the Institute for Control Engineering of Machine Tools and Manufacturing Units ISW and the Institute of Engineering and Computational Mechanics ITM and benefited from some research findings also available in this thesis (Tempel et al. 2015d; Tempel et al. 2015c). The Expo CableRobots again nicely show benefits of cable robots over their rigid link counterparts as the systems were operated continuously above audiences' heads over a period of 6 months on a workspace of approximately $7 \times 6 \times 14\,\mathrm{m}^3$ per robot. With the intention of making the perfect illusion of two freely floating eyes in space with 6 DOF, it was improbable to use an actuating system other than cable robots. One of the key challenges was the increased level of safety as the cable

(a) *Arecibo radio telescope, as seen from the observatory deck. Image by courtesy of David Broad released under CC BY 3.0.*

(b) *One of the two* Expo *CableRobots during their show in the German Pavillon at the universal exposition Expo 2015 in Milan, Italy. © Deutscher Pavillon Expo Milano 2015/Jacopo Bianchini.*

Figure 1.3: Cable robot applications Arecibo (a) and Expo (b).

robots must not have failed during operation i.e., cable rupture or tipping over of the suspended cable robots was to be avoided.

1.6.1.4 Other Applications

Telescopes and Aerostats are large structures that can span hundreds of meters in diameter like the 500 m-aperture telescope in China (Nan et al. 2003). Telescopes generally use a primary and secondary reflector, of which the latter one is designed to be movable when the telescopic structure as a whole cannot be moved (Tang et al. 2009). However, with telescopes becoming even larger to see farther into the universe, their secondary reflectors become larger, too, requiring new means of support and moving. One of the first telescopes using the cable robot technology is the Arecibo observatory in Puerto Rico (Fig. 1.3(a)). Its secondary reflector is supported by cables wound onto three towers over a 305 m-aperture reflector (Altschuler 2002; Altschuler 1998). Arecibo was superseded as largest telescope by the 500 m-aperture telescope FAST in 2016, which also set new standards for cable robot research such as design (Luo et al. 2001; Qian 2007), kinematic enhancements (Kozak et al. 2006; Li et al. 2011), vibration analysis (Liu et al. 2013; Tang et al. 2014), force distribution calculation and

control (Li et al. 2012), workspace analysis (Li et al. 2008), or simulation and accuracy analysis (Sun et al. 2008).

Search and Rescue Operations are usually scenarios with dangerous and subpar environment of uneven or unstable ground surface in possibly even remote locations. As such, not all robotic devices can be put to use in these environments and research for all-terrain robots, whether humanoid or not, is still an active field. To the rescue come cable robots like MARIONET by Merlet, which are by design lightweight robots and allow for easy transportation as well as quick installation as their requirements to the environment are rather few. MARIONET is intended for lifting objects of up to 2.500 t, scalable to workspaces of $100 \times 100 \times 50\,\mathrm{m}^3$, while still being very portable at just 200 kg total weight (Merlet 2014).

Contour Crafting is a layered fabrication technology for automated construction of structures where Bosscher et al. propose using a cable robot to construct such large objects (Bosscher et al. 2007). Since robotic systems based on the gantry concept will require huge elements to keep their own structural integrity, they drop out of competition. Cable robots, on the other hand, can span large workspaces and, by means of an adjusted design, still will not suffer from collision with the printed structure (Fabritius et al. 2019; Pott et al. 2019). This concept is also transferable to printing of smaller scaled objects in modern day additive manufacturing.

Exoskeletons are strictly speaking no real cable-driven parallel robots, but merely hybrid structures for they have a serial chain of links actuated by parallel pairs of cables—due to the need for antagonistic pairs of cables. However, exoskeletons using cables are a very promising technique to reducing the inertia of the device while still allowing for high supportive forces. In fact, Mao et al. present a cable-based exoskeleton used for rehabilitation treatment of upper-limb impairments with the added benefit of reducing the risk of harming the patient (Mao et al. 2015). A proper cable-driven parallel robot was developed

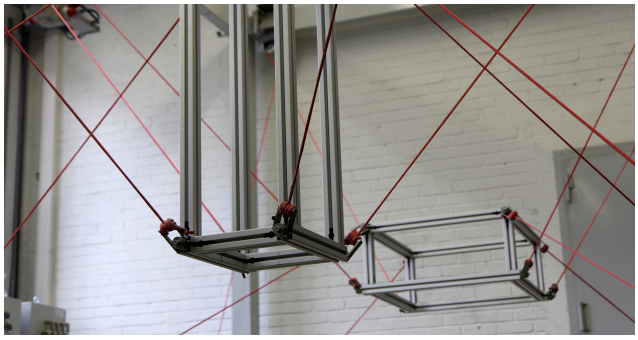

(a) COPacabana *at Institute for Control Engineering of Machine Tools and Manufacturing Units ISW of University of Stuttgart, Stuttgart, Germany.*

(b) IPAnema 3 *at Fraunhofer Institute for Manufacturing Engineering and Automation IPA, Stuttgart, Germany. Image by courtesy of Werner Kraus ibidem.*

Figure 1.4: Cable robot demonstrators COPacabana (a) and IPAnema (b).

by Rosati et al. in several publications where they focus on treatment of patients with stroke-related paralyzed or paretic upper limb (Rosati et al. 2005; Rosati et al. 2007; Rosati et al. 2008). Surdilovic et al. developed a cable robot-based full body harness that can be used for treatment of paretic lower limbs or as a training device for athletes. In all these applications, the technology of cable-driven systems makes the robots intrinsically safe and is used to its full potential.

1.6.2 Demonstrators

We classify cable robots as demonstrator when their main purpose is demonstrating cable robot technology and using it as test carrier for various applications.

1.6.2.1 COPacabana

Designed as pair of cooperating cable robots, COPacabana comprises two medium-scale cable robots (see Fig. 1.4(a)), one designated for handling i.e., loading and unloading of pieces into a CNC drilling machine, the other for inspection of the same pieces. While their workspaces are only $3 \times 4 \times 4\,\mathrm{m}^3$ each, both systems can attain maximum accelerations of $\|\boldsymbol{a}\|_\infty = 1.400\,\mathrm{m\,s^{-2}}$ linear and $\|\boldsymbol{\alpha}\|_\infty = 45\,^\circ\mathrm{s}^{-2}$ angular, respectively, with a maximum payload

of 40 kg each. Their design is based on the IPAnema winches and designed as trade-off between lower dynamics yet higher payload.

1.6.2.2 IPAnema

The IPAnema system by Pott et al. is a family of cable robots ranging from the smallest cable robot IPAnema Mini, barely larger than an elevator cab, up to the large-scale configuration IPAnema 3, with a workspace of $16 \times 12 \times 3\,\mathrm{m}^3$ (Pott et al. 2012) (see Fig. 1.4(b)). In their research, Pott et al. created the first cable robot with industrial grade servo drives and control aiming at introducing a modular concept for different cable robot applications of either high dynamics or high payloads. With these demonstrators, Pott et al. address issues such as cable force control (Kraus et al. 2015c; Kraus et al. 2015a), forward kinematics (Pott et al. 2015; Pott 2010; Schmidt et al. 2014), and system identification (Kraus et al. 2014), but also application driven research like haptic interfaces (Kraus et al. 2015b). IPAnema 3 is the world's second largest cable robot in any research facility—only outdone by the MPI CableRobot Simulator, while it is the world's largest cable robot for research on cable robot technology.

1.6.2.3 Marionet

Like IPAnema, Marionet is a family of modular cable robots developed primarily by Merlet with four different sizes application purposes. The author's designs comprise 1) Marionet Rehab (7 cables), intended for tasks in patient rehabilitation and fast pick-and-place applications, 2) Marionet Crane (6 cables), designed for search and rescue operations and as manipulator for high payloads over large workspaces, 3) Marionet Assist (6 cables), envisioned as personal assistance robot for elderly and handicapped people, 4) Marionet VR (6 cables), to be used as haptic device in virtual reality environments. With these differently purposed cable robots, Merlet wants to discover new theoretical and practical problems, in particular of suspended cable robots. Their work focuses primarily on kinematics (Berti et al. 2012; Berti et al. 2015; Berti et al.

(a) CoGiRo *used at Laboratoire d'Informatique, de Robotique et de Microélectronique de Montpellier (LIRMM), Montpellier, France. Image courtsey Philipp Tempel with special thanks to Marc Gouttefarde, Ph.D., LIRMM, Montpellier, France.*

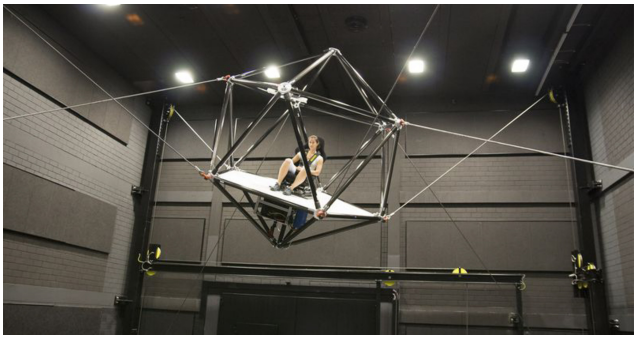

(b) MPI CableRobot Simulator *by Prof. Bülthoff's group at Max Planck Institute for Biological Cybernetics, Tübingen, Germany. Image by courtesy of Philipp Miermeister, MPI for Biological Cybernetics, Tübingen, Germany.*

Figure 1.5: Cable robot demonstrators CoGiRo (a) and MPI CableRobot Simulator (b).

2017; Merlet 2015c; Merlet 2016), workspace analysis (Blanchet et al. 2014; Carricato et al. 2010), and design methodologies (Hao et al. 2005) in order to improve accuracy, but also on trajectory generation (Ramadour et al. 2014).

1.6.2.4 CoGiRo

CoGiRo shown in Fig. 1.5(a) is a large-scale industrial, suspended cable robot designed by Gouttefarde et al. at LIRMM in Montpellier, France. The aimed-at tasks are handling of large scale structures (Izard et al. 2018) and manipulation tasks like surface painting or assembly (Izard et al. 2012). In addition, it is being used for better understanding of tension distribution of suspended cable robots (Lamaury et al. 2012), kinetostatic analysis (Gouttefarde et al. 2012), workspace optimization (Hussein et al. 2018), and reconfiguration (Izard et al. 2012). With its workspace size of $15 \times 10 \times 6\,\mathrm{m}^3$ and a payload of 400 kg, driven by steel cables, it is the only cable robot with large rotational workspaces allowing for rotations of up to $\pm 105°$ about the vertical axis (Gouttefarde et al. 2007) due to its unique cable routing.

1.6.2.5 MPI CableRobot Simulator

Designed as large-scale motion simulator, the MPI CableRobot Simulator at the Max Planck Institute for Biological Cybernetics, is the first cable robot certified for carrying passengers aboard its icosahedron shaped platform. With stunning specifications, the system is a prime example of the newly opened possibilities deploying cable robots in real-world examples. According to Miermeister et al. (2016), the acceleration limits at $\|\boldsymbol{a}\|_\infty = 14\,\mathrm{m\,s^{-2}}$ and $\|\boldsymbol{\alpha}\|_\infty = 100\,^\circ\,\mathrm{s^{-2}}$ linear and angular, respectively, at maximum velocities of $\|\boldsymbol{v}\|_\infty = 5\,\mathrm{m\,s^{-1}}$, $\|\boldsymbol{\omega}\|_\infty = 100\,^\circ\,\mathrm{s^{-1}}$ linear and angular, respectively, while allowing for safe translation in a $4 \times 5 \times 5\,\mathrm{m^3}$ sized workspace. Allowing for up to 500 kg of payload, the system can not only carry passengers, but also a physical chassis to render the motion experience even more immersive. Research on MPI CableRobot Simulator focuses on cable vibration analysis and compensation (Schenk et al. 2016), position control (Schenk et al. 2015).

Chapter 2

Fundamentals

In order to give the reader better understanding of the topics dealt with in this thesis, this chapter will introduce well-established fundamentals of cable robots such as the overall mechanical layout and the general cause of inverse kinematics and forward kinematics. First, Section 2.1 will introduce a generic mechatronic system of cable robots to introduce the different components of the robot and find a common language. Following that, Section 2.2 introduces two fundamental concepts to classify cable robots: redundancy and motion pattern. The two kinematic transformations, inverse and direct kinematics, will be introduced for the general case in Section 2.3, which serves as basis for static analysis of cable robots presented in Section 2.4, also stating the most general form of the so-called structure equation or structure matrix. Extending these results, Section 2.5 will describe the dynamics of most components of a cable robot per state of the art. Lastly, Section 2.6 will cover cable force calculation used for controlling cable robots and a convenient algorithm for determining such force values.

2.1 Mechatronic System

Since cable robots are more than just their mobile platform or end effector, it is beneficial to consider a full mechatronic system for representation (see Fig. 2.1). A cable robot usually consists of one mobile platform with n DOF and m cables, each attached to one winch. These winches are made up of a drum which coils and uncoils the cable, and a motor (most often a synchronous servo motor). Lastly, a control system is used to correctly drive all motors to synchronously control the cable coiling. Each of these parts has its own dynamics influencing the

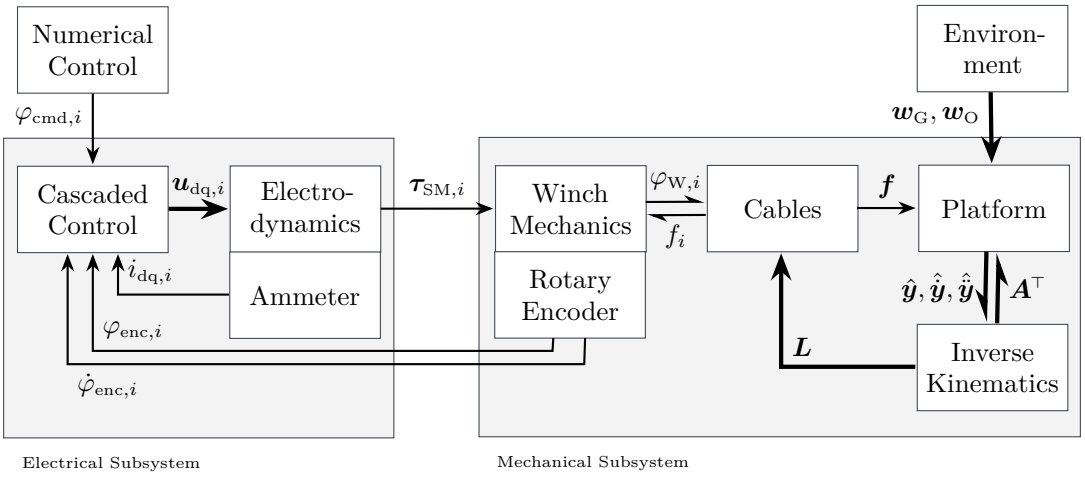

Figure 2.1: System-dynamics model of the mechatronic system of cable robots with the robot electrics in the left half and the robot mechanics in the right half.

overall system dynamics as has been previously investigated for the IPAnema cable robot family (Miermeister et al. 2010a; Kraus et al. 2015b; Tempel et al. 2015a). A short overview of these components will be given in the following list in order from platform to winch, while the mathematical models for dynamics will be further explained and quantified in Section 2.5.

Platform Without loss of generality, it can be assumed that for any cable robot class, the platform is rigid and of given dimensions and inertia. This allows the platform to be considered as rigid body for which the equations of motion can be derived using Newton-Euler equations, Lagrangian mechanics, or d'Alembert's principle. The forces causing platform motion come from

1. cables, due to their strain and their spatial motion;
2. a process i.e., forces and torques from e.g., a milling process;
3. the environment, where in most cases only forces and torques due to gravity are considered.

Cable The connecting and motion-generating elements of a cable robot. It connects to the platform on the distal end and to the winch on the proximal end. In comparison to other cable robot components, cables show lower tensile rigidity and almost negligible flexural rigidity. That is to say, cables are elastic when it comes to longitudinal deformation i.e., stretching, and almost perfectly elastic when it comes to transversal deformation i.e., bending.

This leads to more sophisticated behavior of the cables when considering it in modeling or control of cable robots. In addition, cables are less resilient to resisting transversal motion causing them to vibrate when either end is moved not in direction of the neutral axis.

Pulley In the simplest case, a pulley can be considered a roller of certain diameter and gauge. As with other bodies of mass, these systems undergo certain dynamics which in the case of a pulley reflect mostly as rotational dynamics as the cable runs on the circumference of the pulley. It has been observed during experiments, not only in cable robots, that pulleys affect both the cable tension due to their rotational inertia when the cable abruptly changes direction of travel (Kraus et al. 2015a; Miyasaka et al. 2015), as well as affecting the effective cable direction due to bearing friction of the swiveling arm of the pulley.

Drum Designed as a hollow cylinder, the drum itself has limited inertia affecting only winding dynamics and accuracy rather than platform dynamics. A larger impact on the dynamics however comes from friction in the bearings at either end of the drum and backlash in the gearbox. Especially for small torques transmitted from the motor to the drum, static friction prohibits the drum from moving right away and may cause backlash to be visible in the cable tension.

Motor Each drum is driven by a motor receiving its command value from the control system. This commanded value can be either a motor torque, angular velocity, or angular position, depending on the control system's configuration. In case of the demonstrators used in this thesis, angular position is commanded to the motors which then control angular velocity and torque.

Control System All input to the system and output from the system is controlled and processed by the control system. With the system running in a dedicated process in real-time at a given sampling rate set to 1 ms for the COPacabana and IPAnema cable robots, there are certain dynamics in the process itself. These dynamics come from how computers and especially control computers operate as they read and write the output only at certain

instances to and from a shared memory or a field bus. This implies a certain delay between setting an output value such as the set-point of a drive and the target system actually obtaining this value. This delay has been identified to be a multiple of the control cycle time (Kraus et al. 2014). If cable robots were to reach even higher dynamics and still remain controllable[5], the clock frequency of the control system also plays a vital role in process stability.

2.2 Classification

The concepts of classifying cable robots is not without reason taken from their rigid-body counterparts, as both systems are dually equivalent. Despite the use of cables as main driving elements, cable robots can be classified in terms of their level of redundancy or their DOFs. Redundancy, in general terms, relates to the number of DOFs of a robotic manipulator with respect to a given task. If the robot has more DOFs than required for a given motion, it is called kinematically redundant (Cubero 2006; Merlet 2015b).

2.2.1 Redundancy

Originally introduced by Ming et al., cable robots can be classified depending on their actuator redundancy $r = m - n$, yielding two fundamentally different classes (Ming et al. 1994). An extension derived by Verhoeven splits the second class into two sub-classes that are concept-wise the same but differ in their respective level of redundancy (Verhoeven 2004):

1. *Incompletely restrained positioning mechanism* (IRPM): Number of cables m is less than or equal to the number of DOFs n i.e., $m \leq n$. If $m = n - 1$, gravitational force stemming from a mobile platform with comparably high

[5] With maximum velocities of up to $\|\boldsymbol{a}\|_\infty = 30\,\mathrm{m\,s^{-1}}$ on some systems, a cable robot will travel 30 mm within one clock of $h = 1\,\mathrm{ms}$ of the control system. This distance can be crucially important in case of high-speed and high-accuracy application requirements.

Table 2.1: Classification scheme of cable robots depending on the number of DOF of the mobile platform where T stands for translational and R stands for rotational DOFs, respectively, after Verhoeven (2004).

motion pattern	DOFs		Implementation	
	translation	rotation	motion	spatiality
1T	1	–	linear	point
2T	2	–	planar	point
3T	3	–	spatial	point
1R2T	2	1	planar	body
2R3T	3	2	spatial	beam
3R3T	3	3	spatial	body

mass[6] acts as a virtual cable (the $(m+1)$-th cable). In any other case, one or more DOFs will remain uncontrollable—imagine a crane with $m = 1$ cables but $n = 6$ DOFs of the end-effector.

2. *Completely restrained positioning mechanism* (CRPM): With $m = n + 1$ cables, the system state is completely defined by the cable tensions and no external forces are needed.
3. *Redundantly restrained positioning mechanism* (RRPM): Such mechanisms feature more cables than DOFs i.e., $m > n + 1$, which makes them redundant in the number of constraints, not in their kinematics.

As noted by Verhoeven, the classes completely restrained positioning mechanism (CRPM) and redundantly restrained positioning mechanism (RRPM) can more generally be referred to as fully restrained positioning mechanism (FRPM) (Verhoeven 2004).

2.2.2 Degrees of Freedom

Another concept of classification of parallel robots makes use of the number of DOFs and type of DOFs of the mobile platform or end effector. Going from the simplest case of end effector DOFs with $n = 1$ up to the spatial case

[6] "Comparably" in this sense means the weight of the platform m_P is much larger than the total weight of the cables i.e., $m_P \gg 10\, m_C$.

with $n = 6$ (here $n_{\mathrm{T}} = 3$ translational and $n_{\mathrm{R}} = 3$ rotational) DOFs, respectively, a scheme as shown in Table 2.1 can be mapped out. These cases cover all possible configurations of end effector motion and were previously introduced by Verhoeven. His exhaustive attempt to investigate all fully parallel cable robots prove the list complete under the assumption of each cable being actuated independently of the others (Verhoeven 2004). He also showed that there exist no cable robots with purely rotational motion patterns i.e., 1R, 2R, and 3R are not possible, much like a 1R3T cable robot (Schoenflies motion) and 2R2T are not possible to build.

Closing Remarks

Despite being able to classify cable robots using both of the above mentioned procedures, some cable robots presented in Section 1.6 differ from others in ways that they are so-called *suspended* cable robots whereas others are *redundantly restrained*. The actual difference between these two classes lies in the routing of the cables from the platform to the winches. In case of suspended cable robots, the cables are all routed upwards from the platform, for redundantly restrained systems cables are routed likewise upwards and downwards from the platform (see Fig. 2.2 for a visualization). These two classes are fundamentally different as the former class does require gravitational force to keep all cables taut. This not only affects the kinematics and dynamics of such systems, but also algorithms for determination of valid cable tension distributions or workspaces.

The primary application and target of algorithms presented in this thesis gears toward the class of FRPM cable robots, and results are exemplified for the motion patterns 1R2T and 3R3T. Their applicability to other configurations is not always thoroughly shown, but the findings may easily be transferred to other cable robot classes.

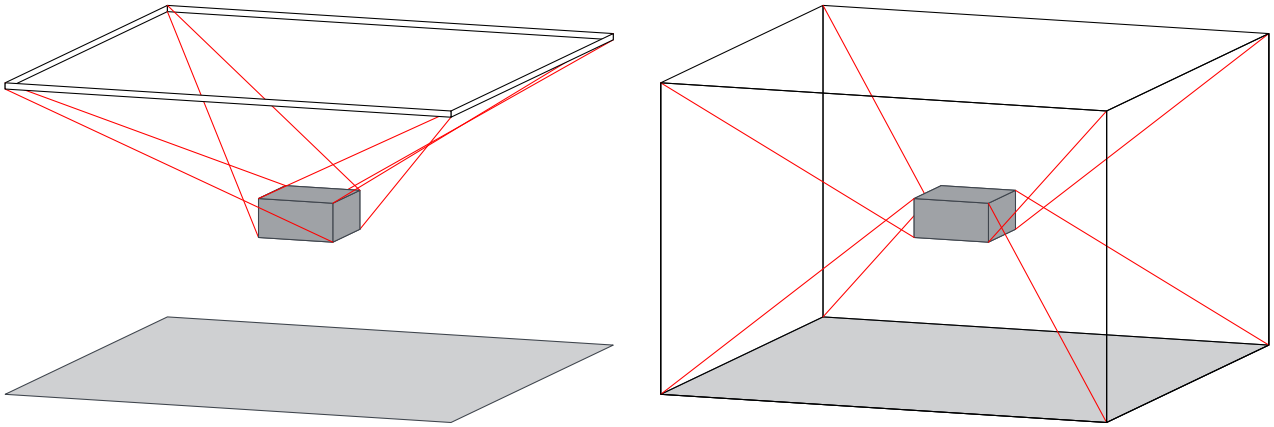

(a) *Schematic drawing of a suspended cable robot in* CoGiRo *configuration with its cables routed only upwards away from the platform.*

(b) *Schematic drawing of a restrained cable robot in* IPAnema *configuration with its cables routed upwards and likewise downwards away from the platform.*

Figure 2.2: Graphical representation of a suspended cable robot (a) and a redundantly restrained cable robot (b).

2.3 Kinematics

Despite its name being similar with the branch of classical mechanics, kinematics with respect to robotics focuses on applying geometric introspection to the motion of robotic systems (McCarthy 1990; Paul 1981). Before the two types of kinematic equations are mapped out, a brief introduction of nomenclature and variables used within this context are given.

In pursuance of solving kinematics of robotic systems, a clear notation of the robot configuration of interest must be given. We call such a state a *pose*—a set of position and orientation—given by the vector tuple $\hat{\boldsymbol{y}}$ defined as

$$\hat{\boldsymbol{y}} = \langle \boldsymbol{r}; \boldsymbol{R}_{\mathrm{P}} \rangle, \tag{2.1}$$

in which $\boldsymbol{r}$ is the position of the platform's point of reference[7] and $\boldsymbol{R}_{\mathrm{P}}$ is the orientation of the platform with respect a body-fixed frame expressed in world-frame coordinates. Parametrization for position and orientation may be chosen

[7] Usually, but not always, coinciding with its center of gravity, compare with e.g., CoGiRo's dimensions given in Table A.1.

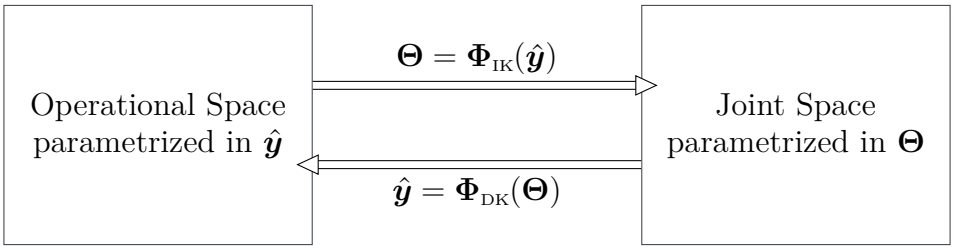

Figure 2.3: Relation between the two kinematic problems of robotic manipulators: the FKP $\boldsymbol{\Phi}_{\text{DK}}$ solves for the operational space coordinates $\hat{\boldsymbol{y}}$ while the IKP $\boldsymbol{\Phi}_{\text{IK}}$ solves for the joint space coordinates $\boldsymbol{\Theta}$.

arbitrarily as long as position and orientation can be described through the following vector and matrix, respectively

$$\boldsymbol{r} = \begin{bmatrix} r_{\text{x}} \\ r_{\text{y}} \\ r_{\text{z}} \end{bmatrix}, \qquad \boldsymbol{R}_{\text{P}} = \begin{bmatrix} R_{11} & R_{12} & R_{13} \\ R_{21} & R_{22} & R_{23} \\ R_{31} & R_{32} & R_{33} \end{bmatrix}. \tag{2.2}$$

Rotation matrix $\boldsymbol{R}_{\text{P}}$ transforms the platform local coordinate system $\mathcal{K}_{\text{P}}$ into the global coordinate system $\mathcal{K}_{\text{O}}$.

For the main, two kinematic problems exist (see Fig. 2.3) complementing each other: inverse kinematics—also called inverse kinematics problem (IKP)—calculates joint space coordinates i.e., cable lengths, from operational space coordinates—world coordinates or Cartesian coordinates. Reverse calculation—determining operational space coordinates from joint space coordinates—is called forward kinematics problem (FKP). The reader is referred to literature showing the IKP of parallel structures being easier to solve than the FKP e.g., Merlet (2000), Cubero (2006), Siciliano et al. (2008), and Merlet et al. (2008). Both problems can be solved on different levels of complexity ignoring or incorporating certain physical properties or effects. As the contribution of this thesis gears mainly toward solving the IKP and forward dynamics problem (FDP), only a brief overview of specifics to the FKP will be given.

Motion of a cable robot is achieved through changing cable lengths by means of coiling or uncoiling. To determine the correct length needed along a spatial trajectory, the IKP needs to be solved along that given trajectory. The general

formulation of the IKP is given by the equation

$$\boldsymbol{L} = \boldsymbol{\Phi}_{\text{IK}}(\hat{\boldsymbol{y}})\,, \tag{2.3}$$

in which $\boldsymbol{L} = [L_1, L_2, \dots L_m]^\top$ is the solution to the IKP as a function of pose $\hat{\boldsymbol{y}}$. No matter the parametrization of the pose, the inverse kinematics function $\boldsymbol{\Phi}_{\text{IK}}$ will always be a nonlinear function, though its complexity can be greatly reduced given some simplifications. Vice versa, the pose $\hat{\boldsymbol{y}} = \langle \boldsymbol{r}; \boldsymbol{R}_{\text{P}} \rangle$ is the solution to the FKP

$$\hat{\boldsymbol{y}} = \boldsymbol{\Phi}_{\text{DK}}(\boldsymbol{L})\,, \tag{2.4}$$

as a function of m cable lengths $\boldsymbol{L}$. It may be noted that calculated cable lengths denoted $\boldsymbol{L}$ most generally differ from the geometric distances $\boldsymbol{d}$ between the cable's proximal and distal point either due to cable strain or since cable sag is assumed. We denote $d_i = \|\boldsymbol{p}_{i,\text{D}} - \boldsymbol{p}_{i,\text{P}}\|$ the geometric distance between the i-th cable's proximal point $\boldsymbol{p}_{i,\text{P}}$ and its distal point $\boldsymbol{p}_{i,\text{D}}$, and $\boldsymbol{d} = [d_1, d_2, \dots d_m]^\top$.

Solving Eq. (2.4) is only needed when the end effector position in space is needed in a control task like Cartesian position or force control. Complexity of the FKP highly depends on the parametrization of pose $\hat{\boldsymbol{y}}$ as well as the level of redundancy of the robotic system. It is, additionally, not a priori known if solutions exist nor if they are unique (Rolland 2005; Faugère et al. 2006).

2.3.1 Inverse Kinematics

Inverse kinematics of cable robots, and of parallel robots in general, are based on different geometric or mechanical assumptions which can allow for the kinematics to be solved explicitly and in closed form, or implicitly and iteratively. Three kinematics formulations of the cable exist, which we will briefly cover on the following pages.

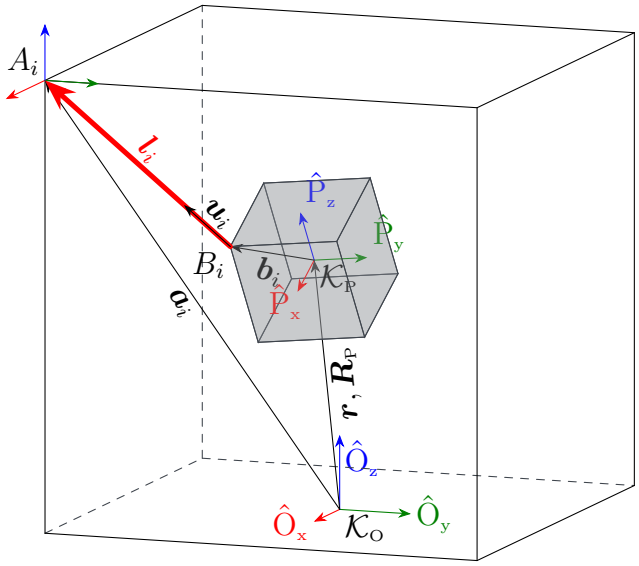

Figure 2.4: Kinematic loop of the standard inverse kinematics problem with cable entry point A_i at $\boldsymbol{a}_i$, platform pose $\hat{\boldsymbol{y}} = \langle \boldsymbol{r}; \boldsymbol{R}_\mathrm{P} \rangle$, and local platform anchor B_i at $\boldsymbol{b}_i$ given in $\mathcal{K}_\mathrm{P}$.

2.3.1.1 Standard Kinematics

Like other parallel robotic manipulators term their linear or rotational actuator quantities joint space coordinates, cable lengths are usually referred to as joint space coordinates, too. An absolute change of these joint coordinates results in a change of position or orientation of the platform, which is independent of the underlying cable coiling and guiding mechanisms.

The most simple model for the IKP with highest degree of simplification can be found when postulating the joints be massless and perfectly straight lines between two points, one on the frame and one on the platform. This model is indubitably the most widely accepted and understood model, as based on early works by Albus et al. and is most generally referred to as the *standard model* (Albus et al. 1992). Because the standard model assumes ideal cables i.e., without mass nor elongation, a very simple vector loop between both cable ends can be defined that can then be used to determine the actual cable length. Referring to Fig. 2.4, defining the position of the cable entering the workspace as $\boldsymbol{a}_i$ and the point on the platform it is attached to as $\boldsymbol{b}_i$, with a given pose $\hat{\boldsymbol{y}}$,

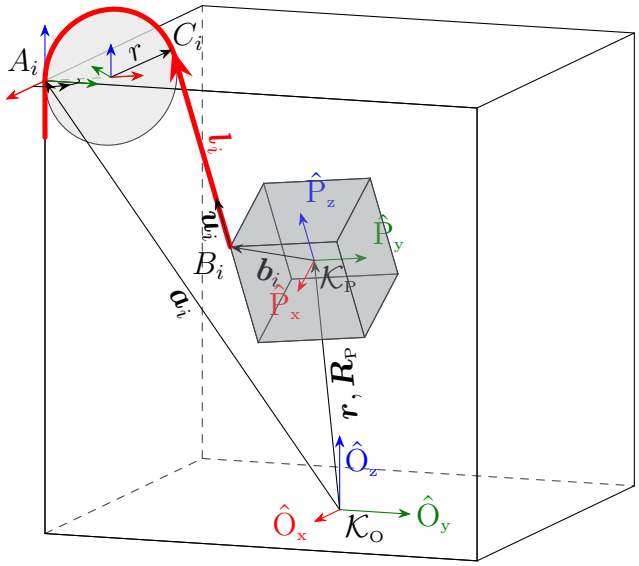

Figure 2.5: Kinematic loop of the pulley-based inverse kinematics problem with cable entry point A_i at $\boldsymbol{a}_i$, corrected cable leave point C_i, platform pose $\hat{\boldsymbol{y}} = \langle \boldsymbol{r}; \boldsymbol{R}_\mathrm{P} \rangle$, and local platform anchor B_i at $\boldsymbol{b}_i$ given in $\mathcal{K}_\mathrm{P}$.

the vector loop

$$\boldsymbol{l}_i = \boldsymbol{a}_i - (\boldsymbol{r} + \boldsymbol{R}_\mathrm{P}\, \boldsymbol{b}_i)\,, \tag{2.5}$$

can be formulated, which states the direction of the cable as a vector from the platform to the frame. To solve Eq. (2.5) for the desired cable length, the magnitude of vector $\boldsymbol{l}_i$ needs to be obtained through the ℓ_2-vector norm such that

$$L_i = \|\boldsymbol{l}_i\| = \|\boldsymbol{a}_i - (\boldsymbol{r} + \boldsymbol{R}_\mathrm{P}\, \boldsymbol{b}_i)\|\,. \tag{2.6}$$

Only in case of this standard kinematics formulation are unstrained cable lengths $\boldsymbol{L}$ equal to the geometric distances $\boldsymbol{d}$ between their proximal points $\boldsymbol{a}_i$ and their distal points $\boldsymbol{b}_i$.

2.3.1.2 Pulley-Based Kinematics

While the standard inverse kinematics model is valid in many cases, it is—from a mechanical point of view—seldomly possible to achieve a perfect punctiform

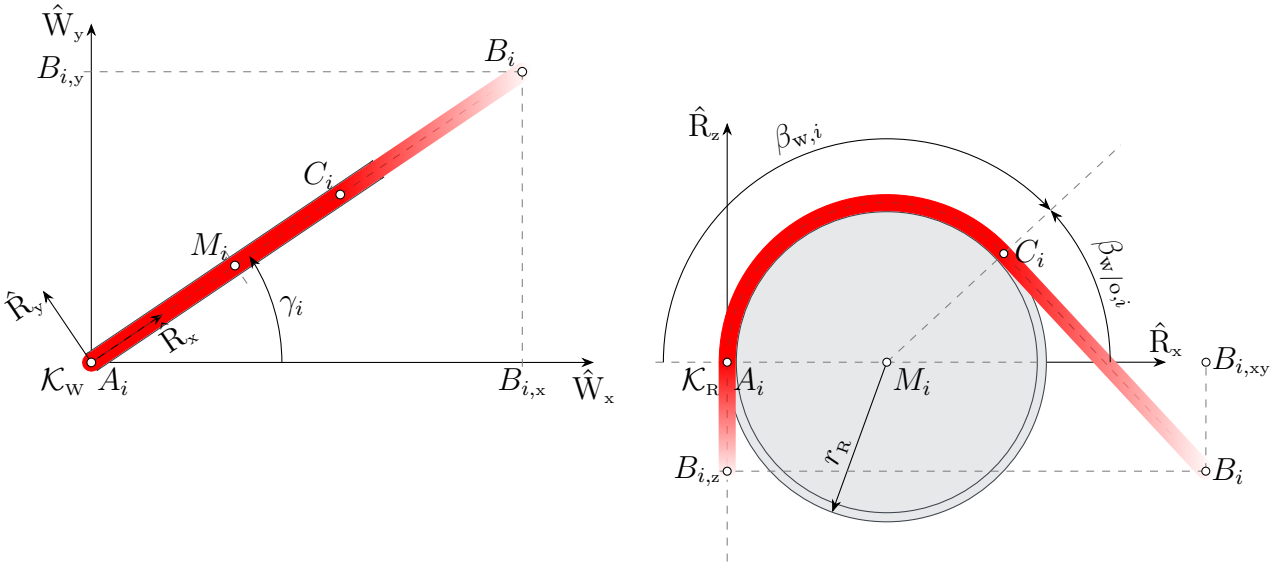

(a) *Pulley top view with winch coordinate system $\mathcal{K}_W$ and pulley coordinate system $\mathcal{K}_{Rr}$ rotated by swivel angle γ about $\hat{\mathrm{w}}_\mathrm{z}$.*

(b) *Side view of the pulley with angle of wrap $\beta_{\mathrm{w},i}$ and opposite wrap angle $\beta_{\mathrm{w/o},i}$.*

Figure 2.6: Kinematic components of the pulley-based inverse kinematics with side-view (b) in winch coordinates $\mathcal{K}_\mathrm{W}$ and top-view (a) in pulley coordinates $\mathcal{K}_\mathrm{Rr}$; cable drawn in red.

deflection unit. For one reason being manufacturing tolerances yielding nonideal punctiform points—there always is some spatial extent to them—, for another reason being the sharpness of the punctiform unit causing the cables to grind on the surface ultimately causing premature cable rupture. Pulley-based deflection units with the cable guided over a pivotally mounted pulley of circular shape reduce wear and tear on the cable increasing its lifespan drastically. However, the cable now follows a longer path as it is now directed along the pulley circumference to the platform attachment point. Extensions of the standard inverse kinematics model to include these effects were proposed by Bruckmann et al. (2008) and Pott (2012).

In short terms based on Fig. 2.5, the pulley-based inverse kinematics model yields the equation for the i-th cable as

$$L_i = r_i\,\beta_{\mathrm{w},i} + \|\boldsymbol{l}_i\|$$

with the pulley radius r_i, the angle of wrap of cable on the pulley $\beta_{\mathrm{w},i}$, and the opposite angle of wrap $\beta_{\mathrm{w/o},i}$ defined as $\beta_{\mathrm{w/o},i} = \pi - \beta_{\mathrm{w},i}$, (see Fig. 2.6). The cable direction vector $\boldsymbol{l}_i$ corrects for the geometrical displacement of the cable leave point due to pulley swiveling and cable wrapping; it follows from

$$\boldsymbol{l}_i = \boldsymbol{a}_i + {}^{\mathrm{O}}_{\mathrm{W}}\boldsymbol{R}_{\mathrm{Rr}_i}\, {}^{\mathrm{W}}_{\mathrm{C}}\boldsymbol{R}_i(\gamma_i)\,(\mathbb{1} + \boldsymbol{R}_i(\beta_{\mathrm{w},i}))\,\hat{\boldsymbol{e}}_{\mathrm{x}}\, r_i - (\boldsymbol{r} + \boldsymbol{R}_{\mathrm{P}}\,\boldsymbol{b}_i)\,, \tag{2.7}$$

where ${}^{\mathrm{O}}_{\mathrm{W}}\boldsymbol{R}_{\mathrm{Rr}_i}$ is the winch rotation w.r.t. world frame $\mathcal{K}_{\mathrm{O}}$, ${}^{\mathrm{W}}_{\mathrm{C}}\boldsymbol{R}_i(\gamma_i)$ is the rotation of the pulley w.r.t. its winch with γ_i the angle of swivel of the i-th pulley, and $\boldsymbol{R}_i(\beta_{\mathrm{w},i})$ is the rotation matrix of wrapping (see Fig. 2.6).

We can calculate γ_i by inspecting the position of $\boldsymbol{b}_i$ expressed in coordinates of frame $\mathcal{K}_{\mathrm{W}}$ obtained from

$${}^{\mathrm{W}}\boldsymbol{b}_i = {}^{\mathrm{W}}\boldsymbol{R}\,(\boldsymbol{r} + \boldsymbol{R}_{\mathrm{P}}\,\boldsymbol{b}_i - \boldsymbol{a}_i)\,.$$

Since the pulley rotates about ${}_{\mathrm{W}}\hat{\boldsymbol{e}}_{\mathrm{z}}$ only, the angle of rotation is defined through the local x and y coordinates of ${}^{\mathrm{W}}\boldsymbol{b}$ thus

$$\gamma_i = \operatorname{atan2}\left({}^{\mathrm{W}}\boldsymbol{b}_{i,\mathrm{y}}, {}^{\mathrm{W}}\boldsymbol{b}_{i,\mathrm{x}}\right).$$

Given the platform anchor ${}^{\mathrm{Rr}}\boldsymbol{b}_i$ be expressed in pulley frame $\mathcal{K}_{\mathrm{Rr}}$, we can obtain the angle of wrap from

$$\beta_{\mathrm{w}} = \operatorname{atan2}\left(\lambda\left({}^{\mathrm{Rr}}\boldsymbol{b}_{i,\mathrm{x}} - d_{\mathrm{Rr}}\right) + {}^{\mathrm{Rr}}\boldsymbol{b}_{i,\mathrm{z}}\, d_{\mathrm{Rr}}, -d_{\mathrm{Rr}}\left({}^{\mathrm{Rr}}\boldsymbol{b}_{i,\mathrm{x}} - d_{\mathrm{Rr}}\right) + \lambda\, {}^{\mathrm{Rr}}\boldsymbol{b}_{i,\mathrm{z}}\right),$$

where $\lambda = \sqrt{{}^{\mathrm{M}}\boldsymbol{b}_i^2 - d_{\mathrm{Rr}}^2}$ is the geometric cable length in the workspace and ${}^{\mathrm{M}}\boldsymbol{b}_i$ is the position of $\boldsymbol{b}_i$ with respect the pulley center such that ${}^{\mathrm{M}}\boldsymbol{b}_i = {}^{\mathrm{Rr}}\boldsymbol{b}_i - d_{\mathrm{Rr}}\,\hat{\boldsymbol{e}}_{\mathrm{x}}$.

With pulley based kinematics, the cable lengths $\boldsymbol{L}$ differ from the geometric distances between its proximal point $\boldsymbol{a}_i$ and its distal point $\boldsymbol{b}_i$ as the cable wound around the pulley has to be considered.

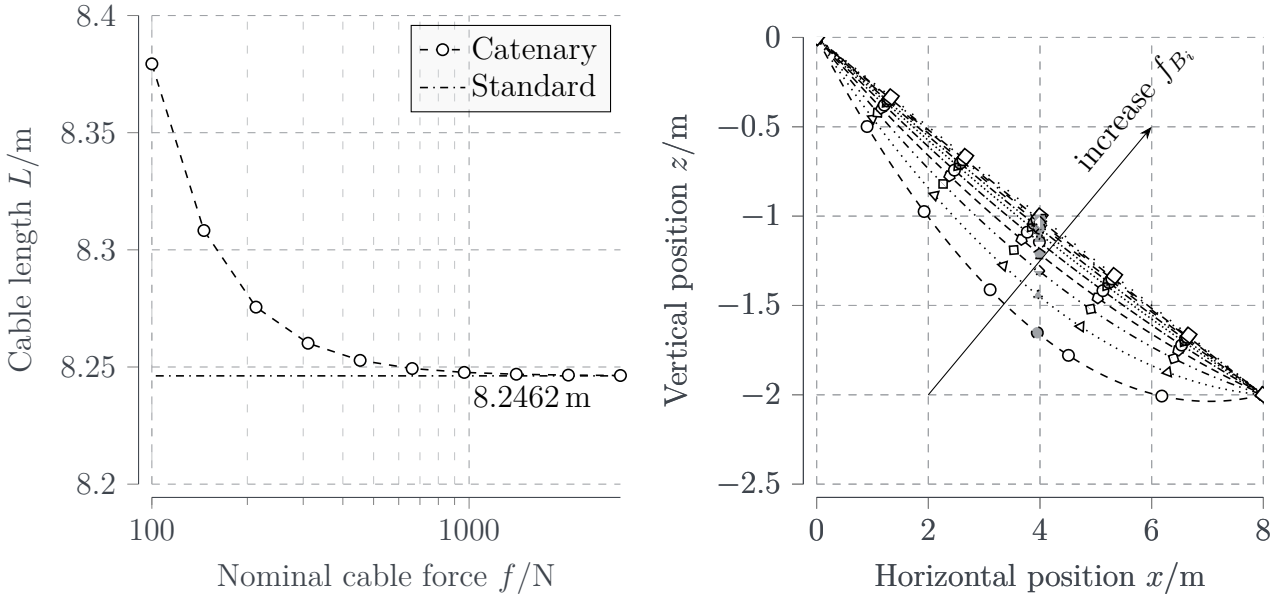

(a) *Logarithmic display of the difference of cable lengths from standard kinematics and hefty kinematics when varying distal cable forces in their allowed range.*

(b) *Comparison of cable sag (maximum sag marked with gray fill) for different cable forces reaching a maximum sag of* 0.645 m *at the minimum of allowed nominal distal cable forces.*

Figure 2.7: Effect of nominal distal cable force on the resulting cable length (a) and on the resulting cable shape (b). Cable-elasticity induced elongation of the cable above the geometric distance affects unstrained length by up to $\Delta = 0.133\,\mathrm{m}$ and induces maximum sag of up to 0.645 m.

2.3.1.3 Mechanical Kinematics

While both the geometric and pulley-based inverse kinematics provide a good approximation under a wide range of assumptions, it has limitations due to the assumption of totally massless cables. In fact, for cable robots even of the COPacabana size (robot geometry given in Tables A.4 and A.5, respectively), this assumption does not hold true. Even though cable mass is relatively low at $\varrho = 970\,\mathrm{kg\,m^{-3}}$ compared to steel cables at $\varrho = 7800\,\mathrm{kg\,m^{-3}}$, cable sag occurs last in case of low cable tension. Figure 2.7(a) shows numerically evaluated unstrained cable lengths given a range of distal cable forces of $f \in \{100, 3000\}\,\mathrm{N}$, while Fig. 2.7(b) shows the actual cable shape and apparent sagging. It is obvious that low-tension cables do no longer form a straight line between two points but sag at a maximum of 0.645 m. This effect of cable sag is an apparent

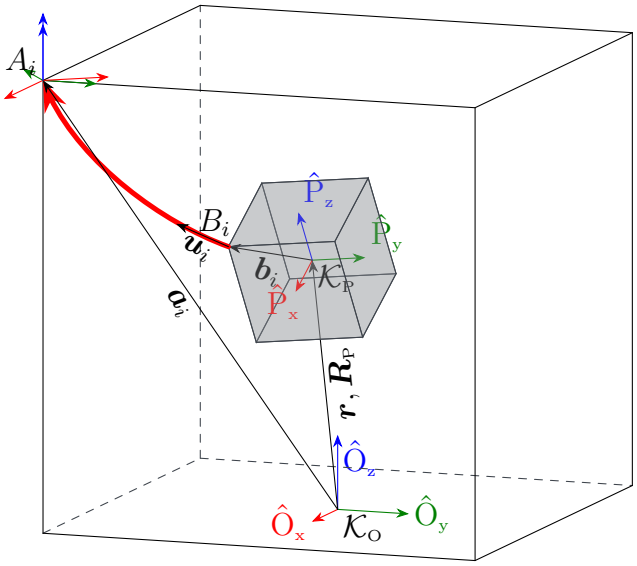

Figure 2.8: Kinematic loop of inverse kinematics problem for hefty cables with cable entry point $\boldsymbol{a}_i$, platform pose $\hat{\boldsymbol{y}} = \langle \boldsymbol{r}; \boldsymbol{R}_\mathrm{P} \rangle$, and local platform anchor $\boldsymbol{b}_i$ given in $\mathcal{K}_\mathrm{P}$. Cable drawn in red highlights (exaggeratedly) cable sagging where it does not form a straight line between $\boldsymbol{a}_i$ and $\boldsymbol{b}_i$.

characteristic of cable robots such as the Expo cable robots (Tempel et al. 2015d), as well as on the 500 m-aperture FAST cable robot (Kozak et al. 2006; Nan et al. 2011), where deflections in the pose of absolute up to 4 m and in the cable lengths of absolute up to 7 m occur due to cable sag.

Irvine was first to derive the kinetostatics of cables under the influence of gravitation in 1974 (Irvine 1974), based on which Kozak et al. derived the kinetostatic problem of cable robots with cables of non-negligible mass (Kozak et al. 2006). We briefly derive the essential equations according to (Irvine 1974; Kozak et al. 2006) and given Fig. 2.9.

Considering a linear-elastic cable with Young's Modulus E, cross-section A, and unit density ϱ, satisfying Hooke's law, its tension at some point $\mathrm{T} = \mathrm{T}(\lambda)$ along the unstrained path length reads

$$\varepsilon(\lambda) = E\,A\left(\frac{\mathrm{d}\varsigma}{\mathrm{d}\lambda} - 1\right), \tag{2.8}$$

where $\frac{\mathrm{d}\varsigma}{\mathrm{d}\lambda}$ is the cable strain at λ. At point T, with horizontal and vertical force component $f_{B_{i,\mathrm{x}}}$ and $f_{B_{i,\mathrm{z}}}$, respectively, the static equilibrium of forces must read

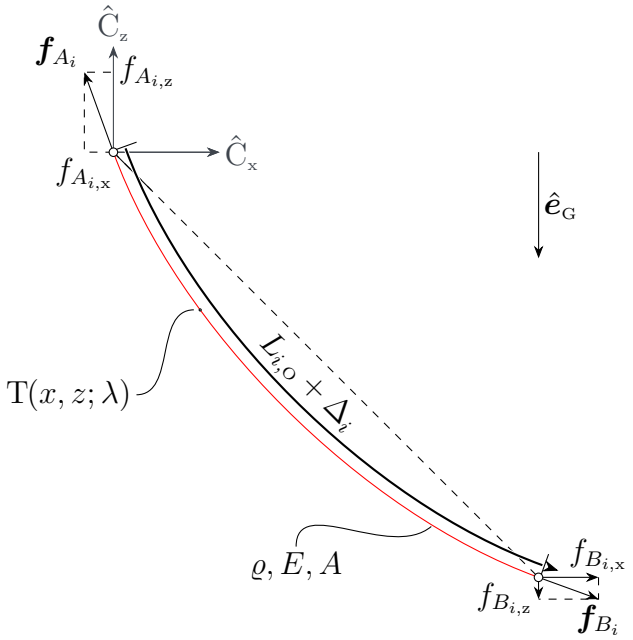

Figure 2.9: Diagram of sagging cable acting under the influence of gravity fixed at cable drawing point A_i with force $\boldsymbol{f}_{B_i}$ applied at its distal attachment point B_i.

$$\varepsilon(\lambda)\,\frac{\mathrm{d}x}{\mathrm{d}\varsigma} = f_{B_{i,\mathrm{x}}}\,,$$
$$\varepsilon(\lambda)\,\frac{\mathrm{d}z}{\mathrm{d}\varsigma} = f_{B_{i,\mathrm{z}}} + \varrho\,A\,(\lambda - L_\mathrm{O}).$$

Solving for $\mathrm{d}x/\,\mathrm{d}\varsigma$ and $\mathrm{d}z/\,\mathrm{d}\varsigma$, respectively, under assumption of the geometric constraint

$$\left(\frac{\mathrm{d}x}{\mathrm{d}\lambda}\right)^2 + \left(\frac{\mathrm{d}z}{\mathrm{d}\lambda}\right)^2 = 1\,,$$

and identities

$$\frac{\mathrm{d}(\cdot)}{\mathrm{d}\lambda} = \frac{\mathrm{d}(\cdot)}{\mathrm{d}\varsigma}\,\frac{\mathrm{d}(\cdot)}{\mathrm{d}\lambda}\,,$$

we find another expression for the tension at unstrained path coordinate λ, such that

$$\varepsilon(\lambda) = \sqrt{\left(f_{B_{i,\mathrm{x}}}\right)^2 + \left(f_{B_{i,\mathrm{z}}} + \varrho\,A\,(\lambda - L_\mathrm{O})\right)^2}\,,$$

which in turn must also satisfy Eq. (2.8). Requiring such equality and applying some mathematical simplifications, we obtain differential equations for the cable shape along x and z in λ

$$\frac{\mathrm{d}x}{\mathrm{d}\lambda} = \frac{f_{B_{i,\mathrm{x}}}}{E\,A} + \frac{f_{B_{i,\mathrm{x}}}}{\sqrt{f_{B_{i,\mathrm{x}}}^2 + \left(f_{B_{i,\mathrm{z}}} + \varrho\,g\,(\lambda - L_\mathrm{O})\right)^2}} \tag{2.10a}$$

$$\frac{\mathrm{d}z}{\mathrm{d}\lambda} = \frac{f_{B_{i,\mathrm{z}}}}{E\,A} + \frac{\varrho\,g\,(\lambda - L_\mathrm{O})}{E\,A} + \frac{f_{B_{i,\mathrm{z}}} + \varrho\,g\,(\lambda - L_\mathrm{O})}{\sqrt{f_{B_{i,\mathrm{x}}}^2 + \left(f_{B_{i,\mathrm{z}}} + \varrho\,g\,(\lambda - L_\mathrm{O})\right)^2}}\,. \tag{2.10b}$$

Integrating Eq. (2.10) for λ and applying the boundary conditions at $\lambda = 0$ taken from Fig. 2.9 i.e., $x(0) = 0$ and $z(0) = 0$, yields the equation of the cable sagging under the influence of gravity

$$\begin{aligned} x(\lambda) = \frac{f_{B_{i,\mathrm{x}}}}{E\,A}\,\lambda + \frac{|f_{B_{i,\mathrm{x}}}|}{\varrho\,g}\Bigg(&\operatorname{arcsinh}\left(\frac{f_{B_{i,\mathrm{z}}} + \varrho\,g\,(\lambda - L_\mathrm{O})}{f_{B_{i,\mathrm{x}}}}\right) + \cdots \\ &- \operatorname{arcsinh}\left(\frac{f_{B_{i,\mathrm{z}}} - \varrho\,g\,(\lambda - L_\mathrm{O})}{f_{B_{i,\mathrm{x}}}}\right)\Bigg)\,, \end{aligned} \tag{2.11a}$$

$$\begin{aligned} z(\lambda) = \frac{\lambda}{E\,A}\left(f_{B_{i,\mathrm{z}}} + \varrho\,g\left(\frac{\lambda}{2} - L_\mathrm{O}\right)\right) + \cdots \\ + \frac{1}{\varrho\,g}\Bigg(\sqrt{f_{B_{i,\mathrm{x}}}^2 + \left(f_{B_{i,\mathrm{z}}} + \varrho\,g\,(\lambda - L_\mathrm{O})\right)^2} + \cdots \\ - \sqrt{f_{B_{i,\mathrm{x}}}^2 + \left(f_{B_{i,\mathrm{z}}} - \varrho\,g\,L_\mathrm{O}\right)^2}\Bigg)\,. \end{aligned} \tag{2.11b}$$

To determine the strained length of the cable between proximal and distal point, we integrate Eq. (2.8) with respect to the λ and evaluate for $\lambda = L_\mathrm{O}$, yielding the strained length $L_\mathrm{S} = L_\mathrm{O} + \Delta$ with Δ calculated from

$$\begin{aligned} \Delta = \frac{1}{2\,\varrho\,E\,A}\Bigg(&f_{B_{i,\mathrm{z}}}\sqrt{f_{B_{i,\mathrm{x}}}^2 + f_{B_{i,\mathrm{z}}}^2} + f_{B_{i,\mathrm{x}}}^2\,\operatorname{arcsinh}\left(\frac{f_{B_{i,\mathrm{z}}}}{|f_{B_{i,\mathrm{x}}}|}\right) + \cdots \\ &- \left(f_{B_{i,\mathrm{z}}} - \varrho\,g\,L_\mathrm{O}\right)\sqrt{f_{B_{i,\mathrm{x}}}^2 + \left(f_{B_{i,\mathrm{z}}} - \varrho\,g\,L_\mathrm{O}\right)^2} + \cdots \end{aligned}$$

$$- f_{B_{i,\mathrm{x}}}^2 \operatorname{arcsinh}\left(\frac{f_{B_{i,\mathrm{z}}} - \varrho\, g\, L_{\mathrm{O}}}{f_{B_{i,\mathrm{x}}}}\right)\Bigg).$$

Since cable shape as well as cable length are now directly linked to the force at the distal cable end, solving Eq. (2.11) now requires two out of the three independent variables 1) distal point coordinates, 2) applied distal cable force, or 3) unstrained cable length. In general, the solution to Eq. (2.11) must be found iteratively for the unknown variable—usually the unstrained cable length. It may be pointed out when considering cable mass in the IKP, the problems of finding a suitable cable force distribution and solving the IKP are now no longer decoupled; the problem turns from a purely geometric formulation to a kinetostatic formulation. As such, we need to solve the kinetostatic problem from Eq. (2.15) while at the same time respecting Eq. (2.11) (see Section 2.4 for the mathematical formulation). This fact may also be visually apprehended from Fig. 2.8 showing the vector loop of the inverse kinematics under consideration of cable mass. The cable attached to the platform produces additional downwards drag in the vertical direction, which must be compensated for by opposing cables.

2.3.2 Forward Kinematics

Due to its high nonlinearity, solving the FKP provides for non-unique solutions (Rolland 2005; Faugère et al. 2006). Dietmaier; Raghavan show existence of up to 40 real solutions to the FKP of a cable robot with $n = 6$ DOF and likewise $m = 6$ cables, not all of which must be physically feasible in the first place (Dietmaier 1998) (see also (Husty 1996; Pott 2018; Rolland 2005; Faugère et al. 2006)).

With the cable robot pose being at least an n-dimensional tuple and the control input being a tuple of dimension m, and under the constraint of $m \geq n$, we see that solving the forward kinematics is overdetermined in the cable lengths. In addition, when referring back to the inverse kinematics problem, we observe the cable length being a scalar value obtained from a vector norm.

Mathematically, this involves solving for the square root of the radicand which is known to provide two solutions—the positive-signed or principal square root and the negative-signed square root. To circumvent this shortcoming, it is possible to rewrite Eq. (2.6) such that it contains no square roots and reads

$$L_i^2 = \|\boldsymbol{a}_i - (\boldsymbol{r} + \boldsymbol{R}_{\text{P}}\, \boldsymbol{b}_i)\|^2 = \boldsymbol{l}_i^\top \boldsymbol{l}_i \,. \tag{2.12}$$

While above equation may still lead to two solutions, it is numerically more stable as it avoids calculating square roots (see (Pott et al. 2015) for an algorithmic point of view of the forward kinematics). For solving the FKP, we recast Eq. (2.12) into residual form in the to-be-estimated platform pose $\hat{\boldsymbol{y}}$ as there exists closed-form solutions only in certain robot configurations

$$\mathbb{0} = \boldsymbol{L}^2 - \boldsymbol{\Phi}_{\text{IK}}(\hat{\boldsymbol{y}}) = \boldsymbol{e}_{\text{DK}}(\hat{\boldsymbol{y}}) \,.$$

Robot configurations with $n = 2$ DOFs and $m = 3$ cables provide for closed-form solutions, same as some robots with $n = m = 6$ of special geometry (Hiller et al. 2005; Husty et al. 2002; Merlet 1990; Rolland 2005)

When it comes to calculating the solutions of the FKP, there exist many different algorithms dealing with different motion patterns (see Table 2.1) and different levels of redundancy (see Section 2.2.1) for which the numerical solutions need to be obtained differently. In addition, different parametrization of the platform pose $\hat{\boldsymbol{y}}$ additionally require different handling of the FKP (Schmidt 2016). Lastly, it all comes down to solving the FKP using either an iterative method like Newton's Method, Levenberg-Marquardt, or Trust-Region-Reflective (a brief introduction into root-finding problems like these is given in Appendix E), or by employing interval analysis. While methods based on interval analysis may provide all possible solutions, iterative methods may only find one of them and their region of convergence cannot be stated a priori. Lastly, any solving method for the FKP ultimately makes use of the inverse kinematics formulation. In addition, some algorithms make use of the kinetostatic problem formulation that also takes into account cable elasticity by means of incorporating cable

tensions into the problem formulation (see e.g., Merlet et al. (2015) and Merlet (2015a)).

Remark on Kinematics Problems

All methods and methodologies to solving the kinematics problems are ultimately based on some geometric or kinematic formulation of the cable robot and may consider some a priori chosen material model for cable elasticity. Integrating cable elasticity into the kinematic problems already yields better results and leads to increased accuracy in position control and in estimating the platform pose (Kraus 2015). However, nongeometric i.e., kinetostatic methods require a cable model, be it either simply for considering cable elasticity and cable inertia causing cable sagging, or be it also considering elasticity causing the strained cable length being larger than the unstrained, calculated and commanded cable length. Only for smaller scale cable robots like the IPAnema Mini (Kraus 2015) or CaRoPrinter (Pott et al. 2019), an ideal cable model may be assumed to yield good results with respect to accuracy, yet medium to larger scale robots like the Expo robots (Tempel et al. 2015d), Marionet (Merlet 2010), or FAST (Li 2015) require explicitly considering cable mass and elasticity to improve static positioning accuracy. Cable reeling becomes a highly nonlinear problem when integrating effects like elasticity, flexibility, friction, and interaction of cable and the environment through pulleys or the reeling mechanism (see (Kozak et al. 2006)).

2.4 Statics

Since cables used in cable robots can only exert tensile forces, it is not a priori known if a pose can be statically attained. Answering this question involves solving the static equilibrium at a given pose and under the influence of external

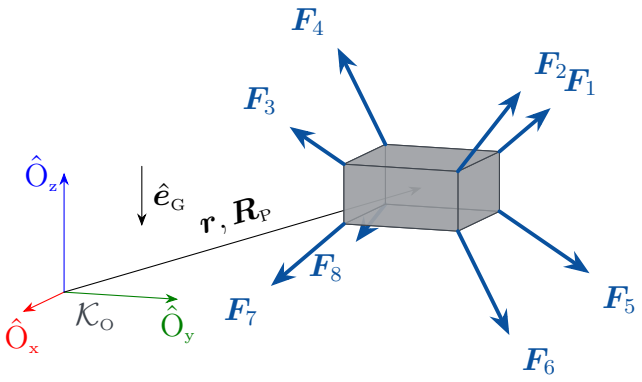

Figure 2.10: Schematic of the static equilibrium of a cable robot mobile platform at pose $\hat{\boldsymbol{y}} = \langle \boldsymbol{r}; \boldsymbol{R}_\mathrm{P} \rangle$ with cable forces $\boldsymbol{F}_i$ and external forces due to gravity $\hat{\boldsymbol{e}}_\mathrm{G}$.

forces reading

$$\begin{aligned} \mathbb{0} &= \boldsymbol{f}_\mathrm{P} + \sum_{i=1}^{m} \boldsymbol{F}_i \,, \\ \mathbb{0} &= \boldsymbol{\tau}_\mathrm{P} + \sum_{i=1}^{m} \boldsymbol{\tau}_i \,, \end{aligned}$$

where $\boldsymbol{f}_\mathrm{P}$ and $\boldsymbol{\tau}_\mathrm{P}$ are, respectively, the forces and torques applied onto the point of reference on the platform and $\boldsymbol{\tau}_i = \boldsymbol{b}_i \times \boldsymbol{F}_i$ are the torques induced by i-th cable force $\boldsymbol{F}_i$. By splitting each cable force $\boldsymbol{F}_i$ into its nominal value f_i and direction $\boldsymbol{u}_i$ for which holds $\|\boldsymbol{u}_i\| \equiv 1$ such that $\boldsymbol{F}_i = f_i \, \boldsymbol{u}_i$, we can recast the i-th cable's external wrench to read

$$\boldsymbol{w}_{\mathrm{C}_i} = \begin{bmatrix} f_i \, \boldsymbol{u}_i \\ f_i \, (\boldsymbol{b}_i \times \boldsymbol{u}_i) \end{bmatrix} = f_i \begin{bmatrix} \boldsymbol{u}_i \\ \boldsymbol{b}_i \times \boldsymbol{u}_i \end{bmatrix} , \tag{2.13}$$

given that cable force $\boldsymbol{F}_i$ generates a torque about platform point of reference P at distance $\boldsymbol{b}_i$.

To determine the full cable tension-induced wrench, we add Eq. (2.13) for all m cables and obtain the total cable wrench $\boldsymbol{w}_\mathrm{C}$ in matrix-vector form as

$$\boldsymbol{w}_\mathrm{C} = \underbrace{\begin{bmatrix} \boldsymbol{u}_1 & \boldsymbol{u}_2 & \dots & \boldsymbol{u}_m \\ \boldsymbol{b}_1 \times \boldsymbol{u}_1 & \boldsymbol{b}_2 \times \boldsymbol{u}_2 & \dots & \boldsymbol{b}_m \times \boldsymbol{u}_m \end{bmatrix}}_{\boldsymbol{A}^\top} \cdot \underbrace{\begin{bmatrix} f_1 \\ f_2 \\ \vdots \\ f_m \end{bmatrix}}_{\boldsymbol{f}} = \boldsymbol{A}^\top \boldsymbol{f}\,, \tag{2.14a}$$

with $\boldsymbol{A}^\top$ being the so-called *structure matrix* first named by Verhoeven (2004). For solving the statics of cable robots[8], we then solve the equation

$$\mathbb{0} = \boldsymbol{A}^\top \boldsymbol{f} + \boldsymbol{w}\,, \tag{2.15}$$

in which the wrench $\boldsymbol{w}$ combines all external wrenches such as gravitational forces and torques or process forces and torques. Finding one or all solutions to Eq. (2.15) is a nontrivial task since the cable forces must always be positive—cables can only exert tensile forces—and generally, the number of cables m outgrows the number of DOF n resulting in Eq. (2.15) being an underdetermined system linear of equations. What is to be kept in mind is the source of entries of structure matrix $\boldsymbol{A}^\top$ which are time-independent platform anchor positions $\boldsymbol{b}_i$ and time and pose-dependent cable directions $\boldsymbol{u}_i$. We observe the structure matrix's numerical values to be dependent on the cable model put in use since generally the platform-sided cable force direction is a function of the cable model.

Kinetostatics

The kinetostatic problem combines the static equilibrium from Eq. (2.15) with a cable model of choice, such as a massless viscoelastic cable (see Section 2.5.1.2)

[8] A brief overview of solving Eq. (2.15) for $\boldsymbol{f}$ will be given in Section 2.6.

or a hefty elastic cable (see Section 2.3.1.3). In either case, the kinetostatic equations is rewritten to read

$$\mathbb{0} = \boldsymbol{A}^\top \boldsymbol{f} + \boldsymbol{w}\,, \tag{2.16a}$$

$$\mathbb{0} = \boldsymbol{p}_{\mathrm{D},i}(\boldsymbol{L}_{i,\mathrm{O}}, \ldots) - (\boldsymbol{r} + \boldsymbol{R}_{\mathrm{P}}\, \boldsymbol{b}_i)\,, \quad i = (1, \ldots, i)\,, \tag{2.16b}$$

in which Eq. (2.16b) ensures that the i-th cable's distal point $\boldsymbol{p}_{\mathrm{D},i}(\boldsymbol{L}_{i,\mathrm{O}}, \ldots)$ as a function of at least the unstrained cable length $\boldsymbol{L}_{i,\mathrm{O}}$ equals the spatial position of the respective platform cable anchor. The kinetostatic problem is then formulated to read

$$\text{solve} \qquad \boldsymbol{L}^* = \arg\min_{\boldsymbol{L}} \|\boldsymbol{L}\| \tag{2.17a}$$

$$\text{subject to} \qquad \mathbb{0} = \boldsymbol{A}^\top \boldsymbol{f} + \boldsymbol{w}\,, \tag{2.17b}$$

$$\mathbb{0} = \boldsymbol{p}_{\mathrm{D},i}(\boldsymbol{L}_{i,\mathrm{O}}, \ldots) - (\boldsymbol{r} + \boldsymbol{R}_{\mathrm{P}}\, \boldsymbol{b}_i)\,, \tag{2.17c}$$

where our cost functional is determined by minimizing cable lengths $\boldsymbol{L}$ under the nonlinear constraints of static equilibrium (Eq. (2.17b)) and of all cable distal ends being located at the platform (Eq. (2.17c)). At the end, we obtain the unstrained cable lengths $\boldsymbol{L}^*$ satisfying static equilibrium.

2.5 Dynamics

Since kinematics consider only motion—position, velocity, acceleration—without explicitly studying the forces causing such motion, this field is only partially applicable to assessment of real-world robot designs. Dynamics extends kinematics by explicating consideration of forces and their emergence, their time evolution, as well as the forces' impact on the kinematics i.e., position, velocity, and acceleration. When it comes to dynamics, much like in the kinematics case, there exist two different directions of dynamics, namely 1) forward dynamics (Section 2.5.1), and 2) inverse dynamics (Section 2.5.2). In either of these two cases, we consider the platform a free-floating rigid body, much like the

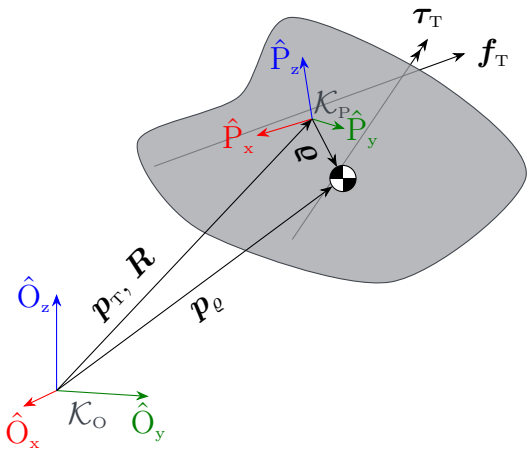

Figure 2.11: Schematics of a free-floating rigid body B under forces $\boldsymbol{f}_\mathrm{P}$ and torques $\boldsymbol{\tau}_\mathrm{P}$ w.r.t. point P. The position of interest of the body is given in world frame $\mathcal{K}_\mathrm{O}$.

one shown in Fig. 2.11, with its point of reference P, on which forces $\boldsymbol{f}_\mathrm{P}$ and torques $\boldsymbol{\tau}_\mathrm{P}$ act. Very often, point P denotes the tool center point of the mobile platform or end effector, in some cases it also refers to the geometric center or center of mass of the mobile platform. For practical use, the linear position $\boldsymbol{r}$ and the orientation of the mobile platform $\boldsymbol{R}_\mathrm{P}$ are of interest for which the dynamics are generally formulated.

2.5.1 Forward dynamics problem

The forward dynamics problem provides an ordinary differential equation (ODE) in the generalized positions $\boldsymbol{q}$, generalized velocities $\dot{\boldsymbol{q}}$, and generalized accelerations $\ddot{\boldsymbol{q}}$ such that

$$\boldsymbol{M}\,\ddot{\boldsymbol{q}} + \boldsymbol{h}(\boldsymbol{q}, \dot{\boldsymbol{q}}) = \boldsymbol{f}(\boldsymbol{q}, \dot{\boldsymbol{q}}, t)\,,$$

where the second derivative $\ddot{\boldsymbol{q}}$ of the positions $\boldsymbol{q}$ is subject to forces $\boldsymbol{f}(\boldsymbol{q}, \dot{\boldsymbol{q}}, t)$, which may be external depending on positions and velocities, but may also be subject to internal forces such as strain, bending, friction, or fictitious forces (rectilinear acceleration, centrifugal forces, Coriolis forces, and Euler forces). It may be apparent to the experienced reader that such systems do not,

in general, have an analytic solution but can only be solved for the solution tuple $\langle \boldsymbol{q}; \dot{\boldsymbol{q}} \rangle$ by means of numerical integration.

2.5.1.1 Platform

Following well-known mechanics i.a. (Featherstone 2008), for a free-floating rigid body, with its position and orientation of interest given in a world coordinate frame as shown in Fig. 2.11, we can state the combined translational and rotational dynamics for an arbitrary point P indexed $(\cdot)_{\mathrm{P}}$ on the rigid body located at $\boldsymbol{\varrho}$ from the center of mass using Newton-Euler equations as

$$\underbrace{\begin{bmatrix} m\,\mathbb{1}_3 & -m\,[\boldsymbol{\varrho}]_\times \\ m\,[\boldsymbol{\varrho}]_\times & \boldsymbol{R}_{\mathrm{P}}\,{}^{\mathrm{P}}\boldsymbol{J}_{\mathrm{P}}\,\boldsymbol{R}_{\mathrm{P}}^\top \end{bmatrix}}_{\boldsymbol{M}(\boldsymbol{q})} \underbrace{\begin{bmatrix} \boldsymbol{a}_{\mathrm{P}} \\ \boldsymbol{\alpha}_{\mathrm{P}} \end{bmatrix}}_{\ddot{\boldsymbol{q}}} + \underbrace{\begin{bmatrix} m\,[\boldsymbol{\omega}]_\times\,[\boldsymbol{\omega}]_\times\,\boldsymbol{\varrho} \\ [\boldsymbol{\omega}]_\times\,\boldsymbol{R}_{\mathrm{P}}\,{}^{\mathrm{P}}\boldsymbol{J}_{\mathrm{P}}\,\boldsymbol{R}_{\mathrm{P}}^\top\,\boldsymbol{\omega} \end{bmatrix}}_{\boldsymbol{h}(\boldsymbol{q},\dot{\boldsymbol{q}})} = \underbrace{\begin{bmatrix} \boldsymbol{f}_{\mathrm{P}} \\ \boldsymbol{\tau}_{\mathrm{P}} \end{bmatrix}}_{\boldsymbol{w}_{\mathrm{P}}}, \tag{2.18}$$

where $\boldsymbol{f}_{\mathrm{P}}$ and $\boldsymbol{\tau}_{\mathrm{P}}$ are, respectively, the forces and torques about point P; $\boldsymbol{a}_{\mathrm{P}}$ and $\boldsymbol{\alpha}_{\mathrm{P}}$ are the linear and angular acceleration, respectively, of P w.r.t. the world frame $\mathcal{K}_{\mathrm{O}}$; ${}^{\mathrm{P}}\boldsymbol{J}_{\mathrm{P}}$ is the inertia tensor w.r.t. point P given in world coordinates i.e.,

$${}^{\mathrm{P}}\boldsymbol{J}_{\mathrm{P}} = {}^{\mathrm{P}}\boldsymbol{J}_{\mathrm{com}} - m\,[\boldsymbol{\varrho}]_\times\,[\boldsymbol{\varrho}]_\times\,,$$

and $[\cdot]_\times$ denotes the skew-symmetric cross product matrix given as

$$[\boldsymbol{a}]_\times = \begin{bmatrix} 0 & -a_3 & a_2 \\ a_3 & 0 & -a_1 \\ -a_2 & a_1 & 0 \end{bmatrix}, \tag{2.19}$$

for any vector $\boldsymbol{a} = [a_1, a_2, a_3]^\top$ that holds $[\boldsymbol{a}]_\times \boldsymbol{b} = \boldsymbol{a} \times \boldsymbol{b}$ for $\boldsymbol{b} = [b_1, b_2, b_3]^\top$.

The left-hand side of Eq. (2.18) defines an algebraic equation for the external wrench as a function of the states $\boldsymbol{y} = \langle \boldsymbol{q}; \dot{\boldsymbol{q}}; \ddot{\boldsymbol{q}} \rangle$. That is, given a trajectory of the rigid body, the external wrench enforcing said motion can be calculated. However, for forward dynamics, we interpret the same equation as an ordinary differential

equation yielding the acceleration $\ddot{\boldsymbol{q}}$ given the current system state $\boldsymbol{y} = \langle \boldsymbol{q}; \dot{\boldsymbol{q}} \rangle$ and an external wrench $\boldsymbol{w}_\mathrm{P}$. This equation is fully qualified for dynamics simulation, if we can determine the external wrench for a given system state. Without loss of generality, we state the external wrench to be composed of three wrenches: 1) cable tension-induced forces and torques $\boldsymbol{w}_\mathrm{C}$, 2) process-induced forces and torques $\boldsymbol{w}_\mathrm{O}$, and lastly 3) gravity-induced forces and torques $\boldsymbol{w}_\mathrm{G}$, such that the external wrench reads

$$\boldsymbol{w}_\mathrm{P} = \boldsymbol{w}_\mathrm{C} + \boldsymbol{w}_\mathrm{O} + \boldsymbol{w}_\mathrm{G} \,. \tag{2.20}$$

Cable tension-induced wrench $\boldsymbol{w}_\mathrm{C}$ and process-induced wrench $\boldsymbol{w}_\mathrm{O}$ are subject to the cable robot and process, while gravitational wrench $\boldsymbol{w}_\mathrm{G}$ can most generally be written as concatenation of gravitational forces $\boldsymbol{f}_\mathrm{G} = m_\mathrm{P}\, \hat{\boldsymbol{e}}_\mathrm{g}$ and gravitational torques $\boldsymbol{\tau}_\mathrm{G} = \boldsymbol{R}_\mathrm{P}\, \boldsymbol{\varrho} \times \boldsymbol{f}_\mathrm{G}$. Given a generalized cable robot, the action wrench $\boldsymbol{w}_\mathrm{O}$ may be chosen arbitrarily and we impose no physical limitation on it. The cable tension-induced wrench, on the other hand, cannot be chosen arbitrarily as it depends on the current state (and possibly previous states) of the cable robot.

Plugging Eq. (2.14a) into Eq. (2.18), we obtain the fully qualified second-order ODE for the cable robot's mobile platform as

$$\begin{bmatrix} m\,\mathbb{1}_3 & -m\,[\boldsymbol{\varrho}]_\times \\ m\,[\boldsymbol{\varrho}]_\times & \boldsymbol{J}_\mathrm{P} \end{bmatrix} \begin{bmatrix} \boldsymbol{a}_\mathrm{P} \\ \boldsymbol{\alpha}_\mathrm{P} \end{bmatrix} + \begin{bmatrix} m\,[\boldsymbol{\omega}]_\times\,[\boldsymbol{\omega}]_\times\,\boldsymbol{\varrho} \\ [\boldsymbol{\omega}]_\times\,\boldsymbol{J}_\mathrm{P}\,\boldsymbol{\omega} \end{bmatrix} = \boldsymbol{A}^\top \boldsymbol{f} + \boldsymbol{w}_\mathrm{G} + \boldsymbol{w}_\mathrm{O} \,, \tag{2.21}$$

which, given in matrix-vector notation for the generalized coordinates $\boldsymbol{q}$ and its time derivatives using the notation introduced in Eq. (2.18), reads

$$\boldsymbol{M}(\boldsymbol{q})\,\ddot{\boldsymbol{q}} + \boldsymbol{h}(\boldsymbol{q}, \dot{\boldsymbol{q}}) = \boldsymbol{A}^\top \boldsymbol{f} + \boldsymbol{w}_\mathrm{G} + \boldsymbol{w}_\mathrm{O} \,. \tag{2.22}$$

2.5.1.2 Cables

To resolve the kinematic reduncany of having $m > n$ cables, the drive-commanded position values are recast into a force-based formulation. This requires finding a

model suitable for both numerical analysis and simulation as well as for closely capturing physical effects. A kinematic formulation of the cable forces $\boldsymbol{f}$ impinging on the platform is defined such that every cable force f_i provides a unilateral constraint force that acts only if the cable is strained i.e., $\Delta_i > 0$, writing the equation of cable dynamics

$$f_i = \begin{cases} f_{i_{\mathrm{mdl}}}(\Delta_i, \dot{\Delta}_i, t) & \Delta_i > 0\,, \\ 0 & \Delta_i \leq 0\,, \end{cases} \tag{2.23}$$

in which in most cases (Behzadipour et al. 2006; Bulín et al. 2017; Dallej et al. 2012; Hajžman et al. 2011; Lambert 2006; Nahon 1999; Miermeister et al. 2010b; Palli et al. 2012; Piao et al. 2017; Tempel et al. 2015b), the model for cables forces $f_{i_{\mathrm{mdl}}}(\Delta_i, \dot{\Delta}_i)$ are calculated based on Hooke's law or a linear viscoelastic material model providing for the cable force model $f_{i_{\mathrm{mdl}}}$

$$f_{i_{\mathrm{elas}}}(\Delta_i, \dot{\Delta}_i, t) = \frac{E\,A}{L_{i,\mathrm{O}}}\,\Delta_i\,, \tag{2.24a}$$

or respectively

$$f_{i_{\mathrm{visco}}}(\Delta_i, \dot{\Delta}_i, t) = \frac{E\,A}{L_{i,\mathrm{O}}}\,\Delta_i + \frac{\eta\,A}{L_{i,\mathrm{O}}}\,\dot{\Delta}_i\,. \tag{2.24b}$$

The mechanically consistent formulation of Eq. (2.24b) in material coordinates strain ε and stress σ reads

$$\sigma_i = \begin{cases} E\,A\,\varepsilon + \eta\,A\,\dot{\varepsilon}\,, & \varepsilon_i > 0\,, \\ 0\,, & \varepsilon_i \leq 0\,. \end{cases} \tag{2.25}$$

Conditions different to the one given in Eqs. (2.24a) and (2.24b) on the zero-strain case may be enforced such as positive strain and positive strain rate i.e., $(\varepsilon_i > 0 \wedge \dot{\varepsilon}_i > 0)$. Such conditions are rarely used, but may achieve better description of the modeled cable force as viscous forces may supersede elastic forces by magnitude yet opposite sign resulting in a negative cable tension.

2.5.2 Inverse dynamics problem

For the sake of completeness, though not used in the remainder of this thesis, the inverse dynamics problem (IDP) provides a system of nonlinear algebraic equations (SNAE) in the generating forces or torques $\boldsymbol{f}(\boldsymbol{q}, \dot{\boldsymbol{q}}, \ddot{\boldsymbol{q}}, t)$ such that the system follows a given trajectory tuple $\langle \boldsymbol{q}; \dot{\boldsymbol{q}}; \ddot{\boldsymbol{q}} \rangle$ subject to its dynamics reading

$$\boldsymbol{f}(\boldsymbol{q}, \dot{\boldsymbol{q}}, \ddot{\boldsymbol{q}}, t) = \boldsymbol{M}\, \ddot{\boldsymbol{q}} + \boldsymbol{h}(\boldsymbol{q}, \dot{\boldsymbol{q}})\,.$$

Such equations are not very useful to determine the system's dynamics response or motion given an input trajectory as this trajectory is the input into above equations. The IDP is useful for designing the motion generating drives given desired maximum dynamics or design of model-based and feed-forward control laws. In general however, also the IDP cannot be solved in closed-form, however, it consists only of algebraic equations in the system's generalized coordinates and its derivatives making solving it a more trivial task compared to the FDP.

Closing Remarks

Numerically solving the forward dynamics of cable robots with the dynamics equation introduced in this chapter is a comparatively straightforward task. Since cable dynamics are only considered on a kinematic force level and not on an inertial level, as would be the case for simulation of conventional parallel robots with non-negligible link mass, all simulation merely comprise a single rigid body. If we were also interested in drive torques needed to perform certain motion, a simplified or full servo drive model may be implemented that allows for simulating dynamics of the drive trains (Miermeister et al. 2010a; Khosravi et al. 2014; Tempel et al. 2015b). In either case, from change of position and change of velocity of wound cable results a strain on the cable which ultimately leads to a corresponding stress moving the platform.

With the cable robot dynamics model defined in this thesis, a cable robot simulation framework is given that is applicable to a wide range of cable robots,

as will be shown in Chapter 4. While the model derived in this chapter comprises only very basic kinematic and dynamic formulations of cable robots—in the kinetostatic realm, cable mass can be considered through Irvine's cable model, in the dynamic realm no common form of consideration of cable dynamics has been established—the model is accepted as being generally valid. However, integration of these models into a more detailed dynamics simulation is not possible due to two shortcomings in the model derivation: 1) the nonlinear model is mathematically underconstrained, and 2) it is based on purely kinematic i.e., force considerations. The latter model shortcoming renders it not applicable to simulation of compound dynamics simulation where spatial cable motion i.e., vibration is of interest, as this is not covered by the model equations. The former shortcoming becomes apparent when observing the equations for the cable shape of Irvine's cable model from Eq. (2.11): given an unstrained cable length L_o and the horizontal and vertical distal point forces f_x and f_z, respectively, we can directly solve for the horizontal and vertical displacement of the cable distal point. However, when given the distal cable point displacement and either the unstrained cable length or the distal point forces, the nonlinear equations become implicit in either of these values. In addition, while previously having uncoupled equations for the distal cable point displacement, the equations for distal cable force or unstrained cable length are now coupled and thus cannot be solved for independently. We can, however, rewrite the equations in residual form and solve the resulting root-finding problem using algorithm's like Newton's method or Levenberg-Marquardt (see Appendix E).

2.6 Cable Force Distribution

Even though cable robots are generally very similar to their rigid link counterparts, not all theory transfers directly. The most dominant difference are the cables, which can only transmit tensile forces, making it ineluctable to ensure positive tension in the cables at all times. At first, this problem may sound like a trivial task, but depending on the cable robot's level of redundancy (see Sec-

tion 2.2.1), it is in fact a nontrivial task. Only in case of CRPM, with number of cables m equaling the number of DOF n, i.e., $m = n$, it is possible to uniquely solve the kinetostatic[9] equation Eq. (2.15) for the cable forces $\boldsymbol{f}$ given an external wrench $\boldsymbol{w}$. The straightforward calculation of the solution follows directly from mathematics as the structure matrix $\boldsymbol{A}^\top \in \mathbb{R}^{m\times m}$ and the external wrench $\boldsymbol{w} \in \mathbb{R}^m$ form a system of linear equations of equal dimension. Thus, the cable force distribution solution follows directly to read $\boldsymbol{f}_\sim = (\boldsymbol{A}^\top)^{-1}\,\boldsymbol{w}$ as the structure matrix's invers exists. Of course, the solution still needs to satisfy $\boldsymbol{f} > \mathbb{0}$ in order to be able to employ cables since positive cable forces represent tensile cable forces. If this requirement is not satisfied i.e., $\boldsymbol{f} \not> \mathbb{0}$, then there is no valid force distribution.

For cable robots of type RRPM, the problem of finding valid force distributions becomes more involved, since Eq. (2.15) no longer is well-posed but underconstrained for there are less equations than unknowns to solve for. We can then solve the static equilibrium for the cable forces by calculating the nonnegative least squares solution such that

$$\begin{aligned} & & \boldsymbol{f} &= \arg\min_{\boldsymbol{f}} \|\boldsymbol{A}^\top \boldsymbol{f} + \boldsymbol{w}\| \\ &\text{subject to} & \boldsymbol{f} &\geq \mathbb{0}\,, \end{aligned}$$

which can be rewritten as a quadratic programming problem

$$\begin{aligned} & & \boldsymbol{f}_\sim &= \arg\min_{\boldsymbol{f}\geq 0}\left(\frac{1}{2}\,\boldsymbol{f}^\top \boldsymbol{Q}\,\boldsymbol{f} + \boldsymbol{c}^\top \boldsymbol{f}\right), \\ &\text{subject to} & \boldsymbol{Q} &= \boldsymbol{A}\,\boldsymbol{A}^\top, \\ & & \boldsymbol{c} &= -\boldsymbol{A}\,\boldsymbol{w}\,. \end{aligned}$$

Inspecting Eq. (2.15) with at least $m > n$, we see now $\boldsymbol{A}^\top \in \mathbb{R}^{n\times m}$ and $\boldsymbol{w} \in \mathbb{R}^n$. As such, we may still obtain the solution by simply pre-multiplying the equation

[9] Without loss of generality, we introduce calculation of valid cable force distributions only on the kinetostatic level. It can be easily shown that the same methods also apply for the dynamic case where a cable force distribution valid to balancing the dynamic forces is sought by simply replacing the static wrench $\boldsymbol{w}$ with the dynamic wrench from the left-hand side of Eq. (2.22).

with the inverse structure matrix yielding $\boldsymbol{f}_{\sim} = (\boldsymbol{A}^{\top})^{-1}\boldsymbol{w}$, however, the inverse of $\boldsymbol{A}^{\top}$ is not unique since the matrix is rectangular i.e., it has more columns than rows.

Literature overview states many different approaches the solution of calculating valid force distributions for overconstrained systems with different characteristics on the resulting force distribution. Several researchers have developed algorithms to determine a minimal or maximal force distribution with respect to some norm, yielding either systems with low stored energy or high stiffness (Gouttefarde et al. 2015; Caverly et al. 2015a). While many algorithms are iterative by nature, there also exist several closed-form solutions that also satisfy minimum norm and other characteristics such as continuity along a trajectory. The algorithm called *closed-form cable force distribution* by Pott and briefly derived here, is valid for cable robots of arbitrary redundancy $r = m - n > 0$ (Pott 2013). It makes use of a limit on the minimum and maximum cable forces $\boldsymbol{f}_{-}$ and $\boldsymbol{f}_{+}$, respectively. Such limits arise on the lower end since a minimum tension to keep is desirable in order to avoid slack cables, and on the upper end since the driving motors, without loss of generality, cannot produce an infinitely large torque/force on the cable but are physically limited to providing a maximum torque. If the drives were to create infinitely large torques, one may choose the yield strength of the cable as maximum force limit.

We begin by splitting the sought-for cable force distribution $\boldsymbol{f}_{\sim}$ into a mean value $\bar{\boldsymbol{f}} = (\boldsymbol{f}_{+} + \boldsymbol{f}_{-})/2$ and an arbitrarily scaled force vector $\boldsymbol{f}_{\text{arb}}$ such that $\boldsymbol{f}_{\sim} = \bar{\boldsymbol{f}} + \boldsymbol{f}_{\text{arb}}$. After some mathematical manipulation of Eq. (2.15), this gives us the solution

$$\boldsymbol{f}_{\sim} = \bar{\boldsymbol{f}} - \left(\boldsymbol{A}^{\top}\right)^{+}\left(\boldsymbol{w} + \boldsymbol{A}^{\top}\,\bar{\boldsymbol{f}}\right),$$

where $(\boldsymbol{A}^{\top})^{+}$ is the Moore-Penrose inverse of $\boldsymbol{A}^{\top}$ computed as

$$\boldsymbol{A}^{\top+} = \left(\boldsymbol{A}^{\top\mathsf{H}}\,\boldsymbol{A}^{\top}\right)^{-1}\boldsymbol{A}^{\top\mathsf{H}},$$

with $\boldsymbol{A}^{\top\mathsf{H}} = \overline{(\boldsymbol{A}^{\top})^{\top}}$ the Hermitian transpose (conjugate transpose) matrix. The obtained result then needs to be checked for consistency i.e., $\boldsymbol{f}_{\sim} > \mathbb{0}$ as negative cable forces may still result. It is favorable to increase numerical stability by not calculating the Moore-Penrose inverse explicitly, but by solving the system of linear equations for $\boldsymbol{f}_{\mathrm{arb}}$

$$\boldsymbol{A}\,\boldsymbol{A}^{\top}\,\boldsymbol{f}_{\mathrm{arb}} = -\boldsymbol{A}\left(\boldsymbol{w} + \boldsymbol{A}^{\top}\,\bar{\boldsymbol{f}}\right),$$

for which efficient algorithms like Gaussian elimination exist (Pott 2018).

Equation (2.15) is fundamental to all force distribution algorithms, with the only variable capturing the geometric structure and model of the cable robot being the structure matrix $\boldsymbol{A}^{\top}$. Since the cable forces $\boldsymbol{f}$ and wrench $\boldsymbol{w}$ are independent of the cable model in use, they are invariant under substitution of cable models. One can also read the structure matrix as a linear mapping from a higher-dimensional space (cable forces) into a lower-dimensional space (platform wrench). Clearly, this transformation depends on the coordinate system used in the higher dimensional case, which can be thought of as being spanned by the directional vectors of cable forces.

Chapter 3

Spatial Cable Dynamics

One part of this thesis is concerned with suitable modeling of the spatial kinematics and dynamics of cables in the context of cable robots. Describing spatial cable motion is an involved task that requires a comprehensive description of the continuum we deem cable. Two commonly used approaches to modeling motion of strings and beams are first presented, as well as having their demerits highlighted. Following these, a continuum formulation of a cable based on Cosserat rod theory is presented that allows for geometrically exact cable kinematics and dynamics. These results are an extension to the planar case in previously published by Tempel et al. (2019). By means of the Rayleigh-Ritz approach, we discretize the solution space of cable motion into a set of shape functions composed of Splines, which reduce model complexity from a continuum to a spatially discretized model. The resulting model is then numerically analyzed and compared against a simply-supported beam, as well as the Irvine cable model. At the end, we conclude on the number and degree of Splines required for a suitable cable model.

We want to describe the spatial dynamics of cable robots[10] by providing a more detailed model for the dynamics of the force and motion transmitting elements. Physically correct and meaningful, these cables ought be considered a continuum of certain unit density, length, cross-section, and possibly other mechanical properties like elasticity of viscosity. On an even higher level of detail, modeling the cables can be split down to modeling every single fiber the

[10] Spatial dynamics are not limited to cable robots with more than one DOF, they are also applicable to 1T cable robots. An intuitive example of such cable robots, though technically not fully coherent, is an elevator which experiences lateral cable vibration due to uneven guiding and uneven weight-distribution of the elevator car.

cable is composed of, while each fiber may again be considered a continuum with former properties. However, such models become highly complex as there is no readily applicable literature to describe the governing dynamics. We limit the model to some key dynamics by wanting a cable that

1. describes the large signal response[11] of the cable to a given distal point motion, as such it
2. neglects internal kinematics and dynamics reaching from interaction of all fibers[12].

One key challenge in modeling cables of cable robots is their varying unstrained length between pulley leave point and platform anchor point, resulting in more involved equations. Assuming the cable to be of constant unstrained length makes for simple dynamics as there is no mass flow resulting from cable coiling or uncoiling. Such models, however, do not enable the cable robot to be positioned in space as the cable length cannot be changed. The only resulting change in spatial position of the mobile platform results from elastic strain of the cables and the response to external forces. Their applicability to dynamics simulation is thus limited if not equivalent none, yet they may be used for kinetostatic analysis of the cable robot under design. Ultimately, we may also consider the cable of constant unstrained length between its very proximal point where it is physically attached to the winch and its very distal point where it is attached to the platform. While this approach may seem less challenging to derive, it introduces more complicated phenomena such as unilateral interaction forces of the cables and its guiding structures, but also friction of the cable on the guiding pulleys and the winch.

Formulating these interactions requires finding values for mechanical parameters that are difficult to physically obtain like the coefficient of static and kinetic friction. Without rigorous analysis of the material properties of the cables and all their contacting objects' materials, a thorough modeling of the contact me-

[11] We may also use the term "macroscale signal response" for better understanding.
[12] As stated in the assumptions in Section 1.4, we consider the cable of full circular cross-section.

chanics and contact dynamics becomes a mathematically trivial task compared to finding the nominal parameter values. Kraus et al.; Choi et al. have previously investigated pulley-cable friction (Kraus et al. 2015a) and pulley-bearing friction (Choi et al. 2017), respectively, showing that Dahl friction more precisely captures the friction emerging in their respective demonstrators. Additionally considering the cable's tendency to strain, the exact points of contact of the cable and its surrounding are subject to the kinematics and dynamics of the stress-strain model and as such more arduous to derive.

In this chapter, Section 3.1 presents two different approaches for describing spatial cable dynamics as often found in literature. Each of these models is based on different assumptions and results in differently complex formulations. These key differences and model equations are pointed out, analyzed, and evaluated with regards to applicability to cable robot simulation. For further analysis of the cable model, Section 3.2 will lay the analytical foundation of analyzing the later derived model's goodness of fit. Following these sections will be the proposed cable model for cable robot simulation for which we first state the kinematics in Section 3.3, then present one way to obtain the equations of motion in Section 3.4, followed by the discretization approach of Rayleigh-Ritz in Section 3.5, needed to obtain a finite set of equations. As we make use of Rayleigh-Ritz, we present the selection of bases functions in Section 3.6, allowing us to provide a purely geometric description of the cable shape. Subsequent Sections 3.7 and 3.8 present, respectively, numerical comparison of the model with its analytical counterpart, as well as the statics solution in comparison to the Irvine cable model from Section 2.3.1.3. Section 3.9 gives some insight into the numerical complexity of the proposed model, while Section 3.10 concludes the chapter with closing remarks.

3.1 Modeling Approaches

To extend the kinematic formulation of cable robots, kinematics and dynamics of the cables must explicitly be considered. The most simple approach, as also

followed by Bedoustani et al., assumes each cable a rigid body of certain physical and mechanical properties—length, unit density, linear and angular inertia—for which the dynamics are formulated. Since cable length varies, the dynamics formulations become more involved and require either an approach based on the conservation of linear and angular momentum such that $\frac{\mathrm{d}}{\mathrm{d}t}(m\,\boldsymbol{v}) \equiv \text{const.}$ and $\frac{\mathrm{d}}{\mathrm{d}t}(\boldsymbol{J}\,\boldsymbol{\omega}) \equiv \text{const.}$, respectively, or a formulation based on Lagrangian variable mass Bedoustani et al. In either case, time-infinitesimal impulses due to impelling and expelling mass at the cable proximal end affect the dynamics of the overall system. To obtain a comprehensive formulation of cable robots with considering cable mass, the kinematics of each cable can be expressed in terms of the minimal coordinates—platform position $\boldsymbol{r}$ and orientation η_{P}, or a constrained multibody system can be constructed. Bedoustani et al. show that consideration of cable dynamics leads to changes in the system dynamics which produce results lying more closely to the physical system. However, they only consider the cable as a linear elastic cylinder, much like the dynamics formulation of conventional parallel robots i.e., Gough-Stewart platforms already imply. What their model neglects is the bending flexibility of cables which affects both statics and dynamics.

3.1.1 Segmentized Cable

An extension to the approach presented by Bedoustani et al. introduces more than one linear elastic cylinder in the cable model yielding a spatially discretized cable model as shown in Fig. 3.1. While Tempel et al. have shown this model applicable to simulation of cable robots in the static or quasi-static case, they also highlight two of the major drawbacks of said model (Tempel et al. 2017). Consequentially, the cable model only forms a discrete approximation of the actual cable, resulting in the final cable shape matching the physical cable in only discrete points. In addition, choosing elongation and orientation of each segment as minimal coordinates, a highly coupled system of nonlinear equations is derived causing expensive evaluation of the dynamics. Further challenges arise from incorporating varying cable length into the discretized cable model

as this is a task that is more challenging than it seems at first. In particular, we may choose to have each segment length vary with time, however, this implies impelling or expelling mass along the cable which is physically incorrect. We may also choose to change the length of only the very first segment, however, this becomes involved when its length reaches zero.

In case of the first segment being of near-zero length, re-discretization of the model with one fewer segment may be performed, however, this comes at both computational expense as well as imperfect transition between two physically related but not equivalent models. Applicability of the approach is further limited by the fact that guiding of the discretized cable over circular shapes like a pulley or winch inevitable causes induction of artificial vibration. Since a chain of discrete rigid links cannot perfectly wrap around a circular shape[13] there is a discrete number of points of contact between cable and pulley. Any longitudinal motion of the cable results in motion tangential to the circumference ultimately inducing vibration where there physically is none (Szczotka 2010). Similar findings were presented by Lambert (2006), Quisenberry et al. (2006), Spak et al. (2014), and Michelin et al. (2015), as well.

To briefly summarize the challenges of a segmentized cable model, let us introduce its kinematics and the overall structure of the resulting differential-algebraic equation (DAE). For means of simplicity, the cable model under investigation will be a planar cable in the $\hat{\boldsymbol{e}}_{\mathrm{x}}\hat{\boldsymbol{e}}_{\mathrm{z}}$-plane in which both linear and rotational deformation i.e., strain and bending, are considered.

Figure 3.1 shows a global sketch of the cable divided into n_{s} segments. We assume the cable to be of total unstrained length L_{O}, of circular diameter d thus of cross-section area $A = \pi\, d^2/4$, and of unit density ϱ, from which follows directly the length and mass of the j-th segment[14]. Using this segmentation approach, we obtain a system of free-floating rigid bodies that need additional

[13] This holds true unless the segment length is negligibly small, in which case the discrete model may already be considered an infinitesimal description of a continuous cable.

[14] In this section, lower-case Latin letters e.g., j, k, l, are $\{j, k, l\} \in \{1, \ldots, n_{\mathrm{s}}\}$ denoting the segment, whereas lowercase Greek letters e.g., α are $\alpha \in \{1, 2\}$ denoting the body part of the respective segment. If no superscript is given, then the quantity is assumed to refer to the respective segment.

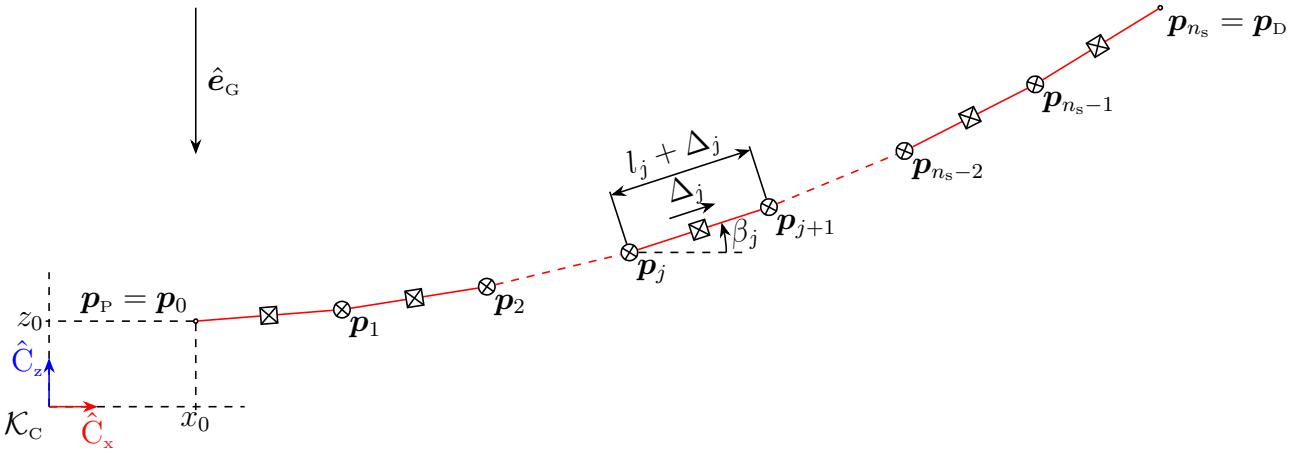

Figure 3.1: Spatially discretized cable into n_s segments interconnected by angular spring-damper elements at nodes $\boldsymbol{p}_j$, each segment composed of two rigid bodies linked by a linear spring-damper element with extension Δ_j and orientation β_j w.r.t. the horizontal axis.

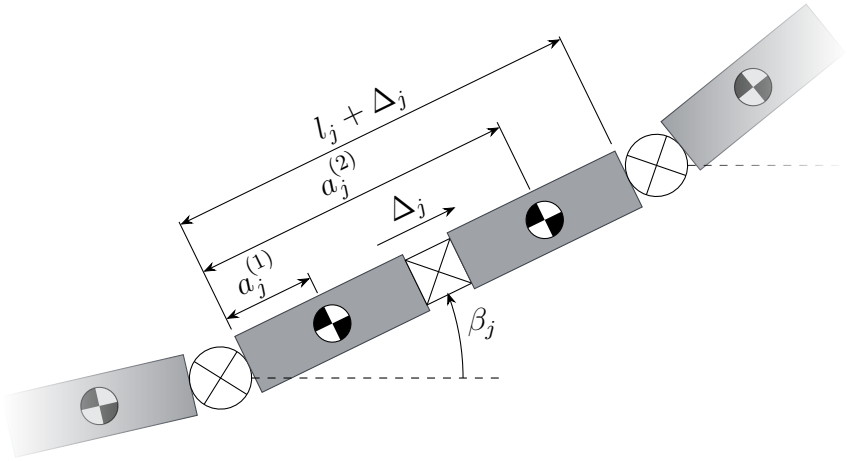

Figure 3.2: Single segment j of the rigid finite element cable composed of a linear SDE linking rigid bodies $(\cdot)^{(1)}$ to $(\cdot)^{(2)}$, and an angular SDE linking segments $(\cdot)_j$ to previous segment $(\cdot)_{j-1}$ and subsequent segment $(\cdot)_{j+1}$.

kinematics to allow for capturing elasticity and flexibility. Assuming the cable material time- and space-independent i.e., with constant Young's modulus E, constant cross-section A, thus constant second moment of area, we introduce linear spring-damper elements (SDEs) in of each segment, and rotational SDEs between adjacent segments j and $j+1$. This enables capturing of both cable strain and cable bending. Figure 3.2 shows a close-up of the j-th segment, which clearly depicts it as being split into two rigid bodies indexed $(\cdot)^{(1)}$ and $(\cdot)^{(2)}$.

Both rigid bodies share the same mechanical properties i.e., lengths $l_j^{(\alpha)}$, linear inertias $m_j^{(\alpha)}$, and rotational inertias $J_j^{(\alpha)}$, which may be calculated from the global cable properties. Both rigid bodies are connected through a linear SDE which obeys Hooke's law for its restoring stress thus reading

$$\sigma_j = E_j \, A \left(\frac{\Delta_j}{l_j} - 1 \right) .$$

All but the first and last segments' proximal and distal ends are connected with rotational SDE to the precedent $j-1$-th and subsequent $j+1$-th segment, respectively, with their restoring moment

$$\begin{aligned} \tau_{j-1,j} &= E_j \, I \, (\beta_j - \beta_{j-1}) \\ \tau_{j,j+1} &= E_j \, I \, (\beta_{j+1} - \beta_j) \end{aligned}$$

yielding the resulting moment on the j-th segment as

$$\tau_j = E_j \, I \, (2\,\beta_j - \beta_{j-1} - \beta_{j+1}) .$$

Segment specific elasticities E_j can be calculated from elasticity E of the cable under the assumption of a series of n_s linear springs of same elasticity with equivalent spring stiffness

$$\frac{1}{E} = \sum_{j=1}^{n_\mathrm{s}} \frac{1}{E_j} = \frac{n_\mathrm{s}}{E_j} ,$$

and thus $E_j = E \, n_\mathrm{s}$.

Let the point of reference of the j-th segment be defined through the position of the j-th node located at the proximal end of the segment. Then follows for the j-th node positions $\boldsymbol{p}_j$ recursively with $j = (1, \ldots, n_\mathrm{s})$

$$\boldsymbol{p}_0 = \boldsymbol{p}_\mathrm{P} ,$$

$$\boldsymbol{p}_j = \boldsymbol{p}_{j-1} + (l_l + \Delta_l) \begin{bmatrix} \cos\beta_{j-1} \\ \sin\beta_{j-1} \end{bmatrix},$$

where $\boldsymbol{p} = [x_0, z_0]^\top$ is a possibly time-dependent arbitrary point in $\mathbb{R}^2$. We obtain $n_\mathrm{n} = n_\mathrm{s} + 1$ nodes, including the distal end of the last segment $j = n_\mathrm{s}$. Alternatively, we can deduce an explicit form of $\boldsymbol{p}_j$

$$\boldsymbol{p}_j = \boldsymbol{p} + \sum_{l=0}^{j-1} (l_l + \Delta_l) \begin{bmatrix} \cos\beta_l \\ \sin\beta_l \end{bmatrix}. \tag{3.2}$$

We define the position vectors of the j-th segment's two rigid bodies' center of mass $\boldsymbol{p}_j^{(1)}$ and $\boldsymbol{p}_j^{(2)}$ to yield

$$\boldsymbol{p}_j^{(1)} = \boldsymbol{p}_j + a_j^{(1)} \begin{bmatrix} \cos\beta_j \\ \sin\beta_j \end{bmatrix}, \tag{3.3a}$$

$$\boldsymbol{p}_j^{(2)} = \boldsymbol{p}_j + \left(a_j^{(2)} + \Delta_j\right) \begin{bmatrix} \cos\beta_j \\ \sin\beta_j \end{bmatrix}. \tag{3.3b}$$

Defining constraints on the cable distal point $\boldsymbol{p}_{n_\mathrm{s}}(\boldsymbol{q})$ requiring it to be located at a desired distal point $\boldsymbol{p}_\mathrm{D}(t)$ imposes a kinematic constraint of form

$$\boldsymbol{g}(\boldsymbol{q}, t) = \boldsymbol{p}_{n_\mathrm{s}}(\boldsymbol{q}) - \boldsymbol{p}_\mathrm{D}(t)\,,$$

which, after extensive mathematical manipulation (exact derivation can be found in Adamiec-Wójcik et al. (2015) and Fritzkowski et al. (2013)) yields a DAE-formulation of the system reading

$$\begin{aligned} \boldsymbol{M}(\boldsymbol{q})\,\ddot{\boldsymbol{q}} &= -\boldsymbol{h}(\boldsymbol{q}) + \boldsymbol{f}_\mathrm{int}(\boldsymbol{q}) - \boldsymbol{f}_\mathrm{ext}(\boldsymbol{q}) \\ \mathbb{0} = \boldsymbol{g}(\boldsymbol{q}, t) &= \boldsymbol{p}_{n_\mathrm{s}+1}(\boldsymbol{q}) - \boldsymbol{p}_\mathrm{D}(t)\,. \end{aligned}$$

We exemplify the system's complexity by showing the structure of the state-dependent mass-matrix $\boldsymbol{M}(\boldsymbol{q})$ reading

$$\boldsymbol{M}(\boldsymbol{q}) = \begin{bmatrix} \boldsymbol{M}_{\boldsymbol{pp}} & \boldsymbol{M}_{\boldsymbol{p}1} & \dots & \boldsymbol{M}_{\boldsymbol{p}k} & \dots & \boldsymbol{M}_{\boldsymbol{p}n_\mathrm{s}} \\ \boldsymbol{M}_{1\boldsymbol{p}} & \boldsymbol{M}_{11} & \dots & \boldsymbol{M}_{1k} & \dots & \boldsymbol{M}_{1n_\mathrm{s}} \\ \vdots & \vdots & & & & \vdots \\ \boldsymbol{M}_{k\boldsymbol{p}} & \boldsymbol{M}_{k1} & \dots & \boldsymbol{M}_{kk} & \dots & \boldsymbol{M}_{kn_\mathrm{s}} \\ \boldsymbol{M}_{n_\mathrm{s}\boldsymbol{p}} & \boldsymbol{M}_{n_\mathrm{s}1} & \dots & \boldsymbol{M}_{n_\mathrm{s}k} & \dots & \boldsymbol{M}_{n_\mathrm{s}n_\mathrm{s}} \end{bmatrix}, \tag{3.4a}$$

with the sub-mass matrices

$$\boldsymbol{M}_{\boldsymbol{pp}} = \begin{bmatrix} m_\mathrm{C} & 0 \\ 0 & m_\mathrm{C} \end{bmatrix}, \tag{3.4b}$$

$$\boldsymbol{M}_{\boldsymbol{p}l} = \boldsymbol{M}_{l\boldsymbol{p}}^\top = \begin{bmatrix} A_l \cos\beta_l & -B_l \sin\beta_l \\ A_l \sin\beta_l & B_l \cos\beta_l \end{bmatrix}, \tag{3.4c}$$

$$\boldsymbol{M}_{kl} = \begin{bmatrix} a_{kl}^{\boldsymbol{\varepsilon}} \cos(\beta_k - \beta_l) & b_{kl}^{\boldsymbol{\varepsilon}} \sin(\beta_k - \beta_l) \\ -a_{kl}^{\boldsymbol{\kappa}} \sin(\beta_k - \beta_l) & b_{kl}^{\boldsymbol{\kappa}} \cos(\beta_k - \beta_l) \end{bmatrix}. \tag{3.4d}$$

and the shorthand substitutions

$$m_{jl} \coloneqq \begin{cases} m_j\,, & l < j\,, \\ m_j^{(2)}\,, & l \equiv j\,, \end{cases} \qquad n_{jl} \coloneqq \begin{cases} m_j\,(l_l + \Delta_l)\,, & l < j\,, \\ \alpha_l + m_l^{(2)}\,\Delta_l\,, & l \equiv j\,. \end{cases}$$

$$l_{jl} \coloneqq \begin{cases} l_l + \Delta_l\,, & l < j\,, \\ a_j^{(2)}\,, & l \equiv j\,, \end{cases} \qquad \alpha_{jl} \coloneqq \begin{cases} \alpha_j + m_j\,\Delta_j\,, & l < j\,, \\ m_j^2\left(a_j^{(2)} + \Delta_j\right), & l \equiv j\,, \end{cases}$$

$$m_\mathrm{C} = \sum_{j=1}^{n_\mathrm{s}} m_{js}\,, \qquad \beta_{jl} \coloneqq \begin{cases} \left(\alpha_j + m_j^{(2)}\,\Delta_j\right)(l_l + \Delta_l)\,, & l < j\,, \\ m_j^{(2)}\left(a_l^{(2)} + \Delta_j\right)^2 + J_j\,, & l \equiv j\,. \end{cases}$$

$$m_{jkl} \coloneqq \begin{cases} m_{jl}\,, & k < j\,, \\ m_j^{(2)}\,, & k \equiv j\,, \end{cases} \qquad n_{jkl} \coloneqq \begin{cases} n_{jl}\,, & k < j\,, \\ m_j^{(2)}(l_{jl} + \Delta_j)\,, & k = j\,, \end{cases},$$

$$\alpha_{jkl} := \begin{cases} (l_k + \Delta_{jl})\, m_{jl}\,, & k < j\,, \\ \alpha_{jl}\,, & k \equiv j\,, \end{cases} \qquad \beta_{jkl} := \begin{cases} (l_k + \Delta_{jl})\, n_{jl}\,, & k < j\,, \\ \beta_{jl}\,, & k \equiv j\,. \end{cases}$$

$$a_{kl}^{\boldsymbol{\varepsilon}} = \sum_{j=\max(k,l)}^{n_\mathrm{s}} m_{jkl}\,, \qquad b_{kl}^{\boldsymbol{\varepsilon}} = \sum_{j=\max(k,l)}^{n_\mathrm{s}} n_{jkl}\,,$$

$$a_{kl}^{\boldsymbol{\kappa}} = \sum_{j=\max(k,l)}^{n_\mathrm{s}} \alpha_{jkl}\,, \qquad b_{kl}^{\boldsymbol{\kappa}} = \sum_{j=\max(k,l)}^{n_\mathrm{s}} \beta_{jkl}\,.$$

$$A_l = \sum_{j=l}^{n_\mathrm{s}} m_{jl}\,, \qquad B_l = \sum_{j=l}^{n_\mathrm{s}} n_{jl}\,.$$

We see a strict state-dependence of the dense mass matrix $\boldsymbol{M}(\boldsymbol{q})$ which renders its evaluation computationally expensive, already for small numbers of segments i.e., $n_\mathrm{s} \geq 6$ (Tempel et al. 2017; Adamiec-Wójcik et al. 2013). In addition, due to its state-dependence, it must be evaluated at every time step of integration and cannot be pre-calculated prior to simulation. It is in fact the integration of linear elasticity i.e., strain that makes deriving the equations of motion involved, and introduces numerical issues and challenges; more details on which can be found in Tempel et al. (2017). We may circumvent dense mass matrices in the model formulation by designing the rigid cable as a constrained multibody system where the segments are joined through kinematic constraints, then given in maximal coordinates of each body's center of mass position and orientation. While this does reduce the dense mass matrix to block-diagonal form rendering it sparse, this design entails adding two kinematic constraints per segment[15] turning the conventional ODE into a DAE system. Both formulations are equivalent as the kinematic constraint can just be introduced into the states by transforming it from maximal coordinates to minimal coordinates. In fact, (Adamiec-Wójcik et al. 2013) show the latter, constrained formulation provides faster simulation results since evaluating the dynamics is less expensive and evaluation of the additional kinematic constraints does not increase computational cost. However, this does not remedy another problem inherent to the modeling approach.

[15] In the planar case we obtain two constraints in the horizontal and vertical coordinate, in the spatial case we obtain three constraints in the two horizontal and one vertical coordinate.

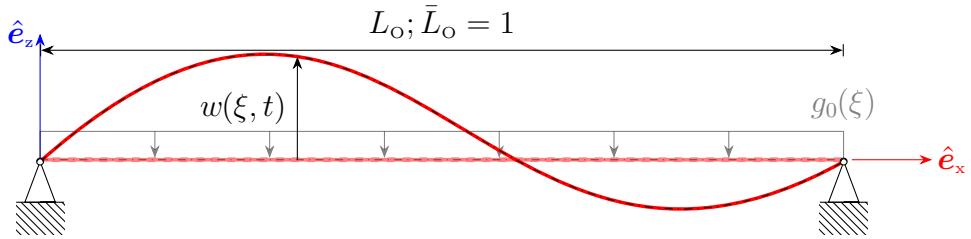

Figure 3.3: Simplified depiction of the kinematics model of the linear wave equation describing wave perturbation function $w(\xi, t)$ of a string of length L_o normalized to $\bar{L}_\mathrm{o} = 1$, with uniform load $g_0(\xi)$ along the cord resulting from at least gravitational forces.

The model introduced here portrays fixed-length cables, which shows the complexity of the model when introducing time-varying length through dynamic rescaling of the unstrained length of each segment. Lastly, we may use the model as-is with fixed-length, then requiring to introduce winding and guiding mechanisms by means of kinematic inequalities, which renders the problem complex on the numerical scale while not remedying the burden of evaluating a state-dependent mass matrix. Atop, with a fixed-length and guided cable, the segment size must be chosen so small as to not introduce numerically artificial vibration resulting from guiding a chain-like cable over round surfaces. As (Adamiec-Wójcik et al. 2015; Dreyer et al. 1984; Huston et al. 1982) point out, segment length l_j must satisfy $l_j \leq r^2$ if r be the radius of the smallest circular surface the cable is guided over. In practical use cases of cable robots, the smallest pulley features a diameter of $d = 5\,\mathrm{cm}$ (Pott et al. 2012) which implies segment lengths of $l_j \leq 0.001\,\mathrm{m}$ resulting in $n_\mathrm{s} = 32\,000$ segments for a $L_\mathrm{o} = 20\,\mathrm{m}$ long cable.

To circumvent the challenges and issues arising from a spatially discretized cable model, we shift our interest toward infinitesimal formulations of the cable resulting in a continuum formulation of the dynamics. The most common representatives of this formulation are the nonlinear wave equation and its linearized form.

3.1.2 Linear Wave Equation

In this formulation, the cable of unstrained length L_o is subject to drastic simplifications like perfect flexibility, constant tension, constancy of length, yet may be subject to external loads (see Fig. 3.3). The most limiting simplification is requiring small displacements and slopes allowing for simplification of trigonometric functions i.e., $\sin x \approx x$, $\cos x \approx 1 - x^2/2 \approx 1$. To derive the equations of motion of the cable, we introduce the perturbation functions $w(\xi, t)$ with $\xi \in \Xi = [0, 1]$, which can be obtained from the perturbation formulation $\hat{w}(\lambda, t)$ with $\lambda \in \Lambda = [0, L_\mathrm{o}]$ by means of a coordinate transformation $\xi = \lambda / L_\mathrm{o}$. The resulting perturbation function can then conveniently be described by the linear wave equation reading in short form

$$\frac{\partial^2 w(\xi,t)}{\partial t^2} + 2\,k\,\frac{\partial w(\xi,t)}{\partial t} = c^2\,\frac{\partial^2 w(\xi,t)}{\partial \xi^2} + e(\xi,t)\,, \tag{3.5a}$$

with boundary constraints

$$w(0,t) = 0\,, \tag{3.5b}$$

$$w(1,t) = 0\,, \tag{3.5c}$$

with initial conditions

$$w(\xi,0) = h_0(\xi)\,, \tag{3.5d}$$

$$\frac{\mathrm{d}}{\mathrm{d}t}\,w(\xi,0) = h_1(\xi)\,, \tag{3.5e}$$

with residual

$$e(\xi,t) = f(\xi,t) - \frac{\partial^2 r(\xi,t)}{\partial t^2} + 2\,k\,\frac{\partial r(\xi,t)}{\partial t}\,, \tag{3.5f}$$

where external forces consider gravitational load

$$f(\xi,t) = g_0(\xi)\,, \tag{3.5g}$$

and the global motion function of proximal point $g_\mathrm{P}(t)$ and distal point $g_\mathrm{D}(t)$

$$r(\xi,t) = g_\mathrm{P}(t) + (1-\xi)\,g_\mathrm{D}(t)\,, \tag{3.5h}$$

This formulation covers the most widely applicable form of the linear wave equation allowing for both the proximal and distal end to move in space over time as described by functions $g_{\mathrm{P}}(t)$ and $g_{\mathrm{D}}(t)$, respectively. In simplified ways, it has been applied to several cases of vibration analysis of large scale cable robots like the FAST telescope (Diao et al. 2009), but also in the simulation and visualization of harbor cranes (García-Fernández et al. 2011). Parameter $c = \sqrt{\tau/(\varrho\, A)}$ describes the speed of a wave traveling through the string which is proportional to the tension applied to the string.

In general, the speed of wave c is assumed constant with respect to its arguments[16], however, with time-dependent tension, the speed of wave also becomes time-dependent. This can be circumvented in twofold ways: 1) assuming small changes in tension during small increments of time, linearly approximating the tension yields constancy of speed of waves, or 2) under the assumption of discrete-time simulation or control, at a given moment in time, the applied tension is assumed constant thus time-dependence vanishes (this is also employed by e.g., García-Fernández et al. (2007) and García-Fernández et al. (2008) in their application of the linear wave equation to the simulation of harbor cranes).

Equation (3.5) describes a partial differential equation (PDE) of the wave perturbation function in both path abscissae ξ and time t, which can only in some cases be solved for analytically. The most commonly used approach is discretization of the path abscissae ξ into intervals of fixed length yielding coupled ODEs, which can be integrated over time.

Mostly due to the requirement of constant tension and no elongation, the linear wave equation does not render itself applicable to the simulation of cable robots. Liu et al. have applied this technique in their research on longitudinal vibration characteristics of the FAST cable robot showing that linear wave equations may be used in the static case for such investigations (Liu et al. 2013). By means of superimposing the linear wave equation to the catenary solution of a statically sagging cable, Liu et al. showed that transversal flexibility

[16] Which holds true if at least density and cross-sectional area do not change with time

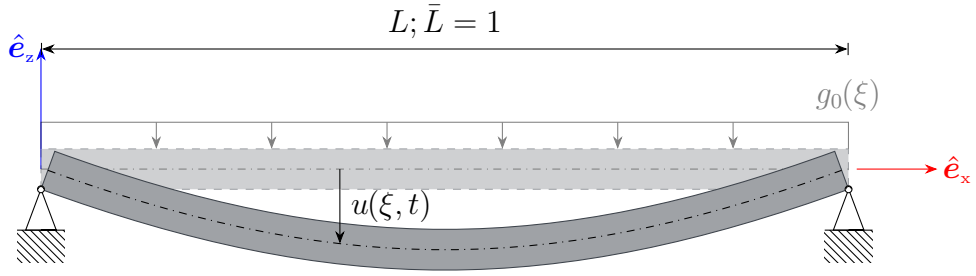

Figure 3.4: Simply-supported beam of length L normalized to $\bar{L} = 1$ with uniform load $g_0(\xi)$ along the due to to e.g., gravitational forces resulting in deflection $u(\xi, t)$ of the neutral axis.

considerations of the cable show a decrease in the natural frequencies yielding a less stiff cable robot.

3.2 Mechanical Model of Comparison

Validating accuracy of the cable model presented in this section and incorporated into a forward dynamics simulation of cable robots in the following chapter will be performed twofold. On the one hand, an analytical expression for a hefty cable with axial elasticity is given by Irvine's cable model, introduced in Section 2.3.1.3. Comparison against this model can be performed straightforward and aims at identifying the amount of congruency of this thesis' cable model. On the other hand, with the model presented in the following section approximating a taut string or an axially pre-tensioned beam, evaluating the model's quality of approximation of the natural frequencies of said beam implies itself. The reference for comparison will thus be the analytical solution to the natural frequencies of a simply-supported beam, both in the tension-free and a pre-tensioned configuration.

We assume a perfect beam of length L, with cross-sectional area A, Young's modulus of elasticity E, and second moment of area I as depicted in Fig. 3.4. Following Labuschagne et al. (2009), the equations of motion for the beam deflection function $u(\xi, t)$ follows the partial differential equation in path coordi-

Table 3.1: Mechanical cable properties used throughout this chapter for numerical analysis, evaluation and comparison of cable model and its parametrization.

Property	Variable	Value	Unit
Diameter	d	6	mm
Cross-Section	A	28.274	mm^2
Moment of Area	I	3.976	mm^4
Unit Density	ϱ	7850	$\mathrm{kg\,m}^{-3}$
Young's Modulus	E	0.005	GPa
Poisson's Ratio	ν	0.410	–
Shear Modulus	G	0.002	GPa

nate $\xi \in [0,1] =: \Xi$ and time t

$$\frac{\partial^4 u(\xi,t)}{\partial \xi^4} + \frac{\varrho\, A}{E\, I} \frac{\partial^2 u(\xi,t)}{\partial t^2} = 0\,.$$

After employing Rayleigh-Ritz with shape function $u(\xi,t)$ split into a path-dependent term $w(\xi)$ and time-dependent term $q(t)$ such that

$$u(\xi,t) = w(\xi)\, q(t)\,,$$

we obtain the recast equation of motion

$$-\frac{1}{w(\xi)} \frac{E\, I}{\varrho\, A} \frac{\partial^4 w(\xi)}{\partial \xi^4} = \frac{1}{q(t)} \frac{\partial^2 q(t)}{\partial t^2} = -\omega_k^2 \equiv \mathrm{const}\,.$$

Using this formula, we can determine the k-th natural frequency for the twofold simply-supported beam reading

$$\omega_k = \left(\frac{k\,\pi}{L}\right)^2 \sqrt{\frac{E\, I}{\varrho\, A}}\,. \tag{3.6}$$

In addition, since cables are under axial tension when under operation, we want to assess model quality also by evaluating natural frequencies against the beam under axial tensile load. Given this load as axial tensile force σ_{ax}, we can determine the k-th natural frequency for the same mechanical beam

following Bokaian (1990) and Hamed et al. (2006) as

$$\omega_k = \left(\frac{k\,\pi}{L}\right)^2 \sqrt{\frac{E\,I}{\varrho\,A}} \sqrt{1 + \frac{\sigma_{\text{ax}}\,L^2}{E\,I\,(k\,\pi)^2}}\,. \tag{3.7}$$

Comparing our cable model also against a beam with an axially preloaded tensile force provides deeper insight into the range of validity of the model. Since the tensile range of cables in cable robots can range anywhere from a few millinewton up to several hundred kilonewton, the model should ideally be applicable to simulation of all these cable robots. Based on requirements of the IPAnema 3 cable robot, we assess validity over an axial tensile force range taken such that $\sigma_{\text{ax}} \in \{0, 100, 1500, 3000\}\,\text{N}$, yet we use for the sake of more significant results a cable with mechanical parameters as given in Table 3.1[17].

3.3 Kinematics

In general, a cable may be assumed a very slender rod, consequently making it mechanically equivalent to a beam of given mechanical properties. As such, we manage with formulation of beam kinematics given as geometrically-exact beams presented by Zhang et al. (2016), Lang et al. (2011), Boyer et al. (2011), Soler et al. (2018), Vu-Quoc et al. (1995), and Antman (2005), and of differential geometry as found in Cao et al. (2008) and Bensoam (2013).

Let $\mathcal{C} \subset \mathbb{E}^3$ be the cable in Euclidean space $\mathbb{E}^3$ at current point in time called the *current configuration* or *deformed configuration*, while $\mathcal{C}_0 \subset \mathbb{E}^3$ be the undeformed cable called the *reference configuration* or *undeformed configuration*. We shall denote the function mapping a point along the unstrained path coordinate $\lambda \in [0, L] = \Lambda$—equivalently its arc length—into the reference configuration by $\boldsymbol{\Gamma}$. This configuration be defined such that $\boldsymbol{\Gamma} : \Lambda = [0, L] \to \boldsymbol{\Gamma}(\lambda) \in \mathcal{C}_0 \subset \mathbb{E}^3$.

[17] This is a mere choice to highlight the wide range of applicability of the cable model to cable robots with elastic and flexible cables. It further allows for visibly more distinguishable results since cable sag and elongation are much more prominent with an elastic modulus and density as chosen here.

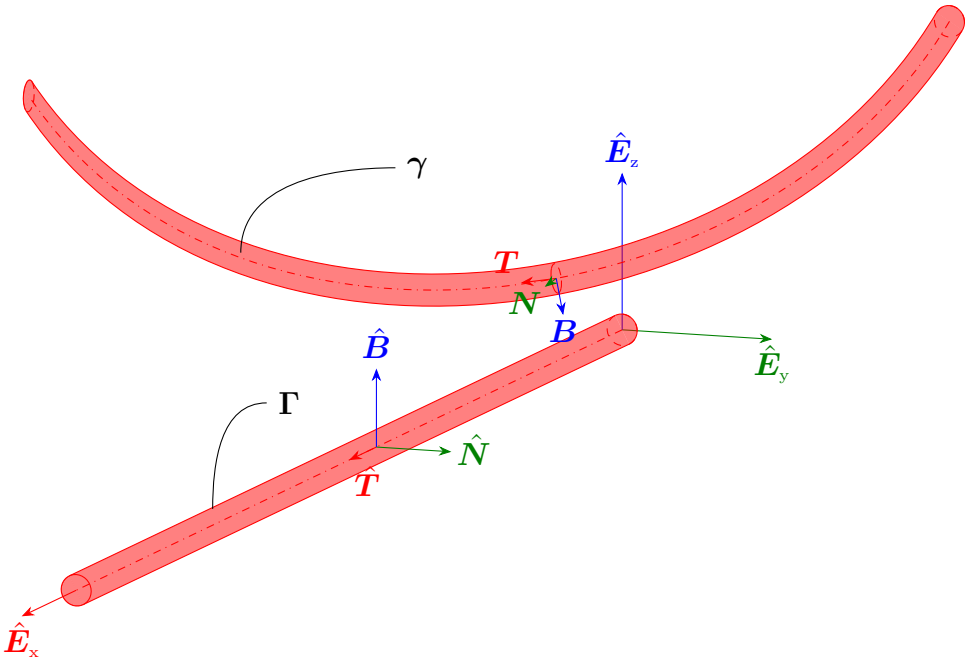

Figure 3.5: Spatial depiction of cable based on Cosserat rod theory with undeformed configuration $\boldsymbol{\Gamma}(\lambda) \in \mathcal{C}_0$ and deformed cable $\boldsymbol{\gamma}(\lambda, t) \in \mathcal{C}$. Local material frame at unstrained path coordinate λ is defined through the frame spanned by its orthonormal director triad $\langle \boldsymbol{T}; \boldsymbol{N}; \boldsymbol{B} \rangle$.

Further, the function mapping a point along the unstrained path coordinate λ and time $t \in [0, \infty[$[18] into the current configuration shall be given through

$$\boldsymbol{\gamma} : \Lambda \times \mathbb{R}_{\geq 0} = [0, L] \times [0, \infty[\to \boldsymbol{\gamma}(\lambda, t) \in \mathcal{C} \subset \mathbb{E}^3 \,.$$

Without loss of generality, the undeformed cable configuration $\mathcal{C}_0$ is assumed collinear with the world $\hat{\boldsymbol{E}}_{\mathrm{x}}$-axis such that $\boldsymbol{\Gamma} \in \mathbb{E}^3$ reads

$$\boldsymbol{\Gamma}(\lambda) = \begin{bmatrix} \lambda \\ 0 \\ 0 \end{bmatrix} = \lambda \, \hat{\boldsymbol{E}}_{\mathrm{x}} \,,$$

[18] Without loss of generality we can assume the open interval of positive real numbers for time $t \in \mathbb{R}_{\geq 0} = [0, \infty[$. This mostly depends on assuming that material properties like elasticity or viscosity are time-invariant as such do not change over time. In fact, this property may be further investigated down the line, but for the initial modeling of cables, it is assumed to hold true.

whereas the current cable configuration $\mathcal{C}$ is not imposed similar restrictions and as such $\boldsymbol{\gamma} \in \mathbb{E}^3$ most generally reads

$$\boldsymbol{\gamma}(\lambda, t) = \begin{bmatrix} x(\lambda, t) \\ y(\lambda, t) \\ z(\lambda, t) \end{bmatrix} = x(\lambda, t)\, \hat{\boldsymbol{E}}_{\mathrm{x}} + y(\lambda, t)\, \hat{\boldsymbol{E}}_{\mathrm{y}} + z(\lambda, t)\, \hat{\boldsymbol{E}}_{\mathrm{z}}\,.$$

To derive forces and moments resulting from arbitrary deformation of the cable in Section 3.4, a local frame or material frame must be introduced that allows for measuring such deformations. A convenient definition of such a material frame can be found in the Frenet-Serret frame or *TNB*-frame which is a geometric invariant of every curve. As such, its expression is independent of the explicit parametrization of any curve $\boldsymbol{\gamma}$ given there exists a parametrization in terms of a single parameter such that $\boldsymbol{\gamma} = \boldsymbol{\gamma}(\lambda, t)$ where $\lambda \in [a, b]$ with $a < b$. To further ease application of the *TNB*-frame, we may parametrize the curve in terms of its arc length such that $\lambda \in [0, L]$ where now L is the arc length of curve $\boldsymbol{\gamma}(\lambda, t)$.

The *TNB*-frame is defined such that there exists a orthonormal triad of three vectors $\boldsymbol{T}, \boldsymbol{N}, \boldsymbol{B}$ that uniquely define a right-hand coordinate system at $\boldsymbol{\gamma}(\lambda, t)$ with only very few assumptions on the curve. In the notation of Frenet and Serret, these vectors are tangent vector $\boldsymbol{T}$, normal vector $\boldsymbol{N}$, and binormal vector $\boldsymbol{B}$. Their mathematical formulation is given completely through curve $\boldsymbol{\gamma}(\lambda, t)$ and its derivatives denoted by $(\cdot)' = \frac{\partial(\cdot)}{\partial \lambda}$ such that

$$\boldsymbol{T} = \frac{\boldsymbol{\gamma}'}{\|\boldsymbol{\gamma}'\|}\,, \tag{3.8a}$$

$$\boldsymbol{N} = \frac{\boldsymbol{T}'}{\|\boldsymbol{T}'\|} = \frac{\boldsymbol{\gamma}' \times (\boldsymbol{\gamma}'' \times \boldsymbol{\gamma}')}{\|\boldsymbol{\gamma}' \times (\boldsymbol{\gamma}'' \times \boldsymbol{\gamma}')\|}\,, \tag{3.8b}$$

$$\boldsymbol{B} = \boldsymbol{T} \times \boldsymbol{N} = \frac{\boldsymbol{\gamma}' \times \boldsymbol{\gamma}''}{\|\boldsymbol{\gamma}' \times \boldsymbol{\gamma}''\|}\,. \tag{3.8c}$$

Equation (3.8) define a relatively parallel adapted frame (Bishop 1975) moving along the curve and allowing for tracking of its change of frame while always

being relatively parallel to the frame of $\mathbb{E}^3$ under only rigid body translation. As such, the *TNB*-frame defines the material deformation at every point $\lambda \in \Lambda$ allowing for measuring material deformation in global coordinates. To track the changes of the orthonormal triad vectors $\boldsymbol{T}$, $\boldsymbol{N}$, and $\boldsymbol{B}$ as we move along the curve, we require the evolution of the former vectors with respect to λ i.e., $\frac{\partial(\cdot)}{\partial\lambda}$ for every triad vector. Following the Frenet-Serret formula, we find

$$\frac{\partial \boldsymbol{T}}{\partial \lambda} = \kappa\, \boldsymbol{N}\,, \tag{3.9a}$$

$$\frac{\partial \boldsymbol{N}}{\partial \lambda} = -\kappa\, \boldsymbol{T} + \tau\, \boldsymbol{B}\,, \tag{3.9b}$$

$$\frac{\partial \boldsymbol{B}}{\partial \lambda} = -\tau\, \boldsymbol{N}\,, \tag{3.9c}$$

in which the curvature κ measures how much the curve fails to form a straight line, and the torsion τ measures the failure of the curve to be planar. Intuitively, this can be exemplified on a helix which has constant curvature and torsion as we move along the curve. Here, constant curvature results in a left-handed circular motion around its center and constant torsion resulting in mathematically positive elevation along the path.

Curvature κ and torsion τ are invariant under a parametrization of the curve and can always be expressed as

$$\kappa = \frac{\|\boldsymbol{\gamma}' \times \boldsymbol{\gamma}''\|}{\|\boldsymbol{\gamma}'\|^3}\,, \tag{3.10a}$$

$$\tau = \frac{[\boldsymbol{\gamma}', \boldsymbol{\gamma}'', \boldsymbol{\gamma}''']}{\|\boldsymbol{\gamma}' \times \boldsymbol{\gamma}''\|^2}\,, \tag{3.10b}$$

where $[\boldsymbol{\gamma}', \boldsymbol{\gamma}'', \boldsymbol{\gamma}''']$ is the scalar triple product defined as

$$[\boldsymbol{\gamma}', \boldsymbol{\gamma}'', \boldsymbol{\gamma}'''] = \det(\boldsymbol{\gamma}', \boldsymbol{\gamma}'', \boldsymbol{\gamma}''') = \boldsymbol{\gamma}' \bullet (\boldsymbol{\gamma}'' \times \boldsymbol{\gamma}''')\,,$$

providing a signed measure for the volume of the parallelepiped spanned by the three vectors.

We can equivalently write Eq. (3.9) in matrix form

$$\begin{bmatrix} — & \boldsymbol{T}' & — \\ — & \boldsymbol{N}' & — \\ — & \boldsymbol{B}' & — \end{bmatrix} = \underbrace{\begin{bmatrix} 0 & \kappa & 0 \\ -\kappa & 0 & \tau \\ 0 & -\tau & 0 \end{bmatrix}}_{[\boldsymbol{\omega}]_\times^\top} \begin{bmatrix} — & \boldsymbol{T} & — \\ — & \boldsymbol{N} & — \\ — & \boldsymbol{B} & — \end{bmatrix}$$

yielding the relations

$$\boldsymbol{T}' = \boldsymbol{\omega} \times \boldsymbol{T}\,, \tag{3.11a}$$

$$\boldsymbol{N}' = \boldsymbol{\omega} \times \boldsymbol{N}\,, \tag{3.11b}$$

$$\boldsymbol{B}' = \boldsymbol{\omega} \times \boldsymbol{B}\,, \tag{3.11c}$$

from which we can see that $[\boldsymbol{\omega}]_\times$ is the skew-symmetric matrix to the vector $\boldsymbol{\omega}$. To the experienced reader, this relationship seems rather familiar if we substitute the derivative w.r.t. path coordinate λ by the derivative w.r.t. time t yielding the relationship of angular velocity given the time rate of a rotation matrix $\dot{\boldsymbol{R}}$ and the rotation matrix $\boldsymbol{R}$ itself such that $[\boldsymbol{\omega}]_\times = \dot{\boldsymbol{R}}\,\boldsymbol{R}^\top$ (Mladenova 1999; Eade 2017; Gorbatsevich et al. 1993). The angular velocity $\boldsymbol{\omega} = [\tau, 0, \kappa]^\top$ used in Eq. (3.11) is given in terms of the local *TNB*-frame showing the rotation happens only about the $\boldsymbol{T}$ and $\boldsymbol{B}$ vectors with rates of torsion τ and curvature κ, respectively. In terms of a local material-fixed coordinate frame, the rate of change of the *TNB*-frame reads $\boldsymbol{\omega} = \boldsymbol{R}_{\text{TNB}}\,\boldsymbol{\omega}'$ which can also be inferred from the Darboux vector (Edelsbrunner et al. 2008; Oprea 2007) given as

$$\boldsymbol{\omega} = \tau\,\boldsymbol{T} + \kappa\,\boldsymbol{B}\,. \tag{3.12}$$

For consistency with later derived virtual work of the cable and the resulting equations of motion, we represent the transformation $\boldsymbol{R}_{\text{TNB}}$ from the *TNB*-frame into $\mathbb{E}^3$ by the exponential rotation mapping that affects the cross product with rotation axis $\boldsymbol{\theta}$: $\boldsymbol{R}(\boldsymbol{v}) = \boldsymbol{\theta} \times \boldsymbol{v}$. The axis-angle representation $\boldsymbol{\theta} = \theta\boldsymbol{\mu}$ of $\boldsymbol{R}_{\text{TNB}}$

can be calculated with the angle of rotation $\boldsymbol{\theta}$ from

$$\theta = \arccos\left(\frac{\operatorname{tr}\left(\boldsymbol{R}_{\mathrm{TNB}}\right) - 1}{2}\right)$$

and the normalized axis of rotation $\boldsymbol{\mu}$ from

$$\boldsymbol{\mu} = \frac{1}{2\,\sin\theta}\begin{bmatrix}\boldsymbol{N}_3 - \boldsymbol{B}_2\\ \boldsymbol{B}_1 - \boldsymbol{T}_3\\ \boldsymbol{T}_2 - \boldsymbol{N}_1\end{bmatrix}, \tag{3.13}$$

where the vector subscript index $(\cdot)_k$ corresponds to the k-th entry of the respective vector. The change of orientation angles along the curve $\frac{\partial\boldsymbol{\theta}}{\partial\lambda}$ can be inferred directly from the Darboux vector (see Eq. (3.12)) such that

$$\frac{\partial\boldsymbol{\theta}}{\partial\lambda} = \boldsymbol{\theta}' = \boldsymbol{\omega} = \tau\,\boldsymbol{T} + \kappa\,\boldsymbol{B}\,. \tag{3.14}$$

With the kinematics formulation at hand, we can now derive the equations of motion using d'Alembert's Principle.

3.4 Equations of Motion

Due to its nature, deriving the equations of motion using D'Alembert's Principle is more convenient for continua and generally applicable without considering specialties as making the transition from Lagrangian mechanics to continuum mechanics. We follow the principle of virtual work to obtain the equations of motion of the cable model.

Within Newtonian mechanics, two types of forces can be identified: those that can do work, and those that cannot. A force that can do work is destined to perform infinitesimal work $\delta W_{\mathrm{w}} = \boldsymbol{f}_{\mathrm{w}}^{\top}\,\delta\boldsymbol{x}$ along an infinitesimal displacement $\delta\boldsymbol{x}$. These forces include conservative forces e.g., gravity, or non-conservative forces e.g., friction. Forces that cannot do work (passive forces if one wants to call

them such) are generally constraint forces such as normal or tension forces. It may be clear that such a constraint force $\boldsymbol{f}_\mathrm{p}$ will not perform work $\delta W_\mathrm{p} = \boldsymbol{f}_\mathrm{p}^\top \delta \boldsymbol{x}$ as the infinitesimal displacement $\delta \boldsymbol{x}$ would violate the constraints.

D'Alembert's Principle may find its origin in the works on static equilibrium of levers by Aristotle. The formulation used in modern days is based on Jean Bernoulli and is given for a system composed of N particles in static equilibrium with vanishing virtual works such that

$$\delta W = \sum_{i=1}^{N} \boldsymbol{f}_i^\top \delta \boldsymbol{x}_i = 0\,, \tag{3.15}$$

for all of the physical constraints satisfying virtual displacements $(\delta \boldsymbol{x}_1, \ldots, \delta \boldsymbol{x}_N)$. Later, Jean-Baptiste le Rond d'Alembert extended the above principle by Bernoulli to include inertial forces $m_i\, \ddot{\boldsymbol{x}}_i$ in the principle of virtual work rendering it

$$\sum_{i=1}^{N} \left(\boldsymbol{f}_i - m_i \frac{\mathrm{d}^2 \boldsymbol{x}_i}{\mathrm{d}t^2} \right)^\top \delta \boldsymbol{x}_i = 0\,. \tag{3.16}$$

We can read d'Alembert's Principle from Eq. (3.16) such that work done by all active forces acting on a system of N particles is algebraically equal to the work done by all the acceleration forces. To further extend d'Alembert's principle to the use case in this thesis, we split the total amount of virtual work δW into three distinct virtual1) internal work δW_int (see Section 3.4.2) 2) external work δW_ext (see Section 3.4.1), and 3) dynamic work δW_dyn (see Section 3.4.3) such that they compose as

$$\delta W = \delta W_\mathrm{int} - \delta W_\mathrm{ext} + \delta W_\mathrm{dyn}\,. \tag{3.17}$$

By appropriate substitution of Eq. (3.16) in Eq. (3.17) we obtain the equations of motion form of d'Alembert's principle reading

$$\mathbb{0} = \left(\boldsymbol{f}_\mathrm{int} - \boldsymbol{f}_\mathrm{ext} + \boldsymbol{f}_\mathrm{dyn} \right)^\top \delta \boldsymbol{x}\,.$$

Assuming that we find a formulation of all forces given a set of generalized coordinates $\boldsymbol{q}$ and their respective time-derivatives, we can rewrite the equations of motion to a more commonly known form

$$\mathbb{0} = \left(\boldsymbol{f}_{\text{int}}(\boldsymbol{q}) - \boldsymbol{f}_{\text{ext}}(\boldsymbol{q}) + \boldsymbol{f}_{\text{dyn}}(\boldsymbol{q}, \ddot{\boldsymbol{q}})\right)^{\top} \delta\boldsymbol{q}\,,$$

which must hold true, according to Bernoulli and d'Alembert, for every displacement and for all times i.e., $\forall\, \delta\boldsymbol{q}, t$. This is only valid if the sum of forces vanishes from which we obtain the standard formulation of the equations of motion

$$\mathbb{0} = \boldsymbol{M}(\boldsymbol{q})\, \ddot{\boldsymbol{q}}(t) - \boldsymbol{f}_{\text{ext}}(\boldsymbol{q}(t), \dot{\boldsymbol{q}}(t)) + \boldsymbol{f}_{\text{int}}(\boldsymbol{q}(t))\,. \tag{3.18}$$

Equation (3.18) no longer contains terms of $\boldsymbol{f}_{\text{dyn}}(\boldsymbol{q}, \ddot{\boldsymbol{q}})$ since we used linearity of the dynamic forces in generalized accelerations $\ddot{\boldsymbol{q}}$ such that

$$\boldsymbol{f}_{\text{dyn}}(\boldsymbol{q}, \ddot{\boldsymbol{q}}) = \boldsymbol{M}(\boldsymbol{q})\, \ddot{\boldsymbol{q}}\,.$$

3.4.1 External Forces

It is possible to consider a magnitude of external forces acting on a mechanical structure, such as point forces, line forces, area forces, or even volume forces. In general, external forces can be accounted for by

$$\delta W_{\text{ext}} = \sum_k \boldsymbol{f}_k^{\top}\, \delta\boldsymbol{x}_k + \sum_l \boldsymbol{\tau}_l^{\top}\, \delta\boldsymbol{e}_l + \int_{\mathcal{C}} \bar{\boldsymbol{n}}^{\top}\, \delta\boldsymbol{\gamma}\,,$$

where $\boldsymbol{f}_k$ are point forces acting at $\boldsymbol{x}_k$, $\boldsymbol{\tau}_l$ are torques acting about axis of rotations $\hat{\boldsymbol{e}}_{\text{l}}$, and $\bar{\boldsymbol{n}}$ is the vector of acting line forces. We limit ourselves to considering only one line force resulting from gravity which then reads

$$\delta W_{\text{ext}} = \int_{\mathcal{C}} \hat{\boldsymbol{e}}_{\text{G}}^{\top}\, \delta\boldsymbol{\gamma}\,, \tag{3.19}$$

with the vector of acting force $\bar{\boldsymbol{n}} = \hat{\boldsymbol{e}}_{\text{G}} = [0, 0, -g]^{\top}$.

3.4.2 Internal Forces

Forces doing internal virtual work result from deformation stresses inside a body, stemming from extension, shear, torsion, or bending of the material. For a Cosserat Rod, the internal virtual work is composed of strain and shear resultants $\boldsymbol{\sigma}$ and bending and torsion resultants $\boldsymbol{\tau}$ such that it reads

$$\delta W_{\text{int}} = \int_{\mathcal{C}} \boldsymbol{\sigma}^{\top} \delta\boldsymbol{\gamma}' + \boldsymbol{\sigma}^{\top} (\boldsymbol{\gamma}' \times \delta\boldsymbol{\theta}) + \boldsymbol{\tau}^{\top} \delta\boldsymbol{\theta}' . \tag{3.20}$$

Deformation measures of the physical cable are given in terms of strain measures $\boldsymbol{\varepsilon}$ and bending measures $\boldsymbol{\beta}$ as

$$\boldsymbol{\varepsilon} = \frac{\partial \boldsymbol{\gamma}}{\partial \lambda} - \boldsymbol{\theta} \times \boldsymbol{T} = \begin{bmatrix} \varepsilon_{\text{T}} \\ \varepsilon_{\text{N}} \\ \varepsilon_{\text{B}} \end{bmatrix} , \tag{3.21a}$$

$$\boldsymbol{\beta} = \frac{\partial \boldsymbol{\theta}}{\partial \lambda} = \begin{bmatrix} \beta_{\text{T}} \\ \beta_{\text{N}} \\ \beta_{\text{B}} \end{bmatrix} . \tag{3.21b}$$

If the tangent is not of unit length $\|\frac{\partial \boldsymbol{\gamma}}{\partial \lambda}\| \neq 1$ i.e., the length changes compared to the undeformed configuration, the cable is subject to stretch—or compression, for that matter. If the normal to the cross-section surface is noncollinear to the tangent $\boldsymbol{\theta} \times \boldsymbol{T} \neq \mathbb{0}$, the cable is subject to shear deformation.

The constitutive relations between deformation measures and resulting forces and moments in the local material frame read

$$\boldsymbol{N} = \begin{bmatrix} E\,A_{\text{T}} & 0 & 0 \\ 0 & G\,A_{\text{N}} & 0 \\ 0 & 0 & G\,A_{\text{B}} \end{bmatrix} \begin{bmatrix} \varepsilon_{\text{T}} \\ \varepsilon_{\text{N}} \\ \varepsilon_{\text{B}} \end{bmatrix} = \boldsymbol{C}^{\varepsilon}\,\boldsymbol{\varepsilon} , \tag{3.22a}$$

$$\boldsymbol{M} = \begin{bmatrix} G\,I_{\mathrm{T}} & 0 & 0 \\ 0 & E\,I_{\mathrm{N}} & 0 \\ 0 & 0 & E\,I_{\mathrm{B}} \end{bmatrix} \begin{bmatrix} \beta_{\mathrm{T}} \\ \beta_{\mathrm{N}} \\ \beta_{\mathrm{B}} \end{bmatrix} = \boldsymbol{C}^{\beta}\,\boldsymbol{\beta}\,, \tag{3.22b}$$

where E is Youngs Modulus, G is shear modulus with $G = E/(2+2\nu)$ with ν being Poisson's ratio, A_k are the effective cross-sectional area about the k-th axis, and I_k is the second moment of area about the k-th axis. We assume circular cross-section thus

$$\begin{aligned} A_{\mathrm{T}} = A_{\mathrm{N}} = A_{\mathrm{B}} &= \pi\,r^2\,, \\ I_{\mathrm{T}} &= \frac{\pi\,r^4}{2}\,, \\ I_{\mathrm{B}} = I_{\mathrm{N}} &= \frac{\pi\,r^4}{4}\,. \end{aligned}$$

In global coordinates of $\mathbb{E}^3$, the strain measures simply need rotation about the relatively parallel adapted frame thus

$$\boldsymbol{\sigma} = \boldsymbol{R}_{\mathrm{TNB}}\,\boldsymbol{N}\,, \tag{3.23a}$$

$$\boldsymbol{\tau} = \boldsymbol{R}_{\mathrm{TNB}}\,\boldsymbol{M}\,. \tag{3.23b}$$

3.4.3 Dynamic Forces

Equation (3.16) can be understood such that a virtual work of dynamics exists that maps inertial forces to virtual displacements. As such, we can formulate the dynamic virtual work to readily read

$$\delta W_{\mathrm{dyn}} = \int_{\mathcal{C}} m\,\ddot{\boldsymbol{\gamma}}^{\top}\,\delta\boldsymbol{\gamma}\,. \tag{3.24}$$

3.4.4 Energies

For later numerical analysis of statics and dynamics of our cable and cable robot model, we also require having the potential energies of the cable available.

Potential energies are composed of energies in the potential field of gravity U_{G} given a point of reference inside the world frame, of energies of strain deformation U_ε, and of energies of bending deformation U_κ. The total potential energy can then be written to read

$$U = U_{\mathrm{G}} + U_\varepsilon + U_\kappa \,, \tag{3.25a}$$

with

$$U_{\mathrm{G}} = \int_{\mathcal{C}} m\, \boldsymbol{g}\, \hat{\boldsymbol{e}}_{\mathrm{z}}^{\top}\, \boldsymbol{\gamma}(\lambda, t) \,, \tag{3.25b}$$

$$U_\varepsilon = \frac{1}{2} \int_{\mathcal{C}} \boldsymbol{\sigma}^{\top}\, \boldsymbol{C}^{\boldsymbol{\varepsilon}}\, \boldsymbol{\sigma} \,, \tag{3.25c}$$

$$U_\kappa = \frac{1}{2} \int_{\mathcal{C}} \boldsymbol{\tau}^{\top}\, \boldsymbol{C}^{\boldsymbol{\beta}}\, \boldsymbol{\tau} \,, \tag{3.25d}$$

and $\boldsymbol{\sigma}, \boldsymbol{\tau}$ as given in Eq. (3.23), $\boldsymbol{C}^{\boldsymbol{\varepsilon}}, \boldsymbol{C}^{\boldsymbol{\beta}}$ given in Eq. (3.22).

3.4.5 Constraints

As is the case with most mechanical systems that are to be investigated in interaction with other bodies, constraints need to be put in place in order to allow for joining bodies. We require the proximal and distal ends of the cable to be constrained to holonomic position vectors reading

$$\boldsymbol{g}_{\mathrm{P}}(\boldsymbol{q}, t) = \boldsymbol{\gamma}(\lambda = 0, t) - \boldsymbol{p}_{\mathrm{P}}(t) \,, \tag{3.26a}$$

$$\boldsymbol{g}_{\mathrm{D}}(\boldsymbol{q}, t) = \boldsymbol{\gamma}(\lambda = L, t) - \boldsymbol{p}_{\mathrm{D}}(t) \,, \tag{3.26b}$$

where we allow the proximal position $\boldsymbol{p}_{\mathrm{P}}(t)$ to be time-varying much like the distal position $\boldsymbol{p}_{\mathrm{D}}(t)$. It may not be necessary to describe a time-dependent motion of the cable proximal point as this is generally assumed to be the winch position, while the distal cable point is going to be attached to the platform. As such, during dynamics simulation, this constraint is time-dependent.

The equations of motion derived in this section provide a DAE in unstrained path coordinate λ and time t that allows for forward-in-time projection of the

dynamics of a Cosserat rod—or in our case of a cable. What is lacking is a tractable formulation of the still integral formulation of the dynamics. To remedy the up to now infinite dimensional problem, we introduce the Rayleigh-Ritz approach in order to discretize the solution space of our cable into a lower-dimensional subspace of possible shapes. In the end, we want to obtain a discrete DAE-system in a set of generalized coordinates and their time-derivatives of which we can perform forward-in-time integration.

3.5 Discretization

To solve the infinite dimensional problem obtained from Section 3.3, we assume the kinematics can be discretized by means of a discrete displacement function satisfying geometric constraints at the proximal and distal cable end such that we can write the spatial curve $\boldsymbol{\gamma}(\lambda, t)$ as

$$\boldsymbol{\gamma}(\lambda, t) = \boldsymbol{r}(\lambda, \boldsymbol{q}(t)) \,, \tag{3.27}$$

for which we introduce time-dependent generalized coordinates $\boldsymbol{q}(t)$. Introducing a discrete displacement function implies constraints on the kinematic properties of the curve between the discrete points. In the simplest case, we may impose a linear blending function between two discrete points $\boldsymbol{q}_1$ and $\boldsymbol{q}_2$ such that the resulting curve shape reads

$$\boldsymbol{\gamma}(\lambda, t) = (1 - \lambda)\, \boldsymbol{q}_1(t) + \lambda\, \boldsymbol{q}_2(t) \,.$$

We can directly see from above equation that the discrete displacement function can be written as linear combination of some later-to-defined blending functions $\boldsymbol{\Pi}(\lambda)$ and the generalized coordinates $\boldsymbol{q}(t)$. In above example, we would have $\boldsymbol{\Pi} = [1 - \lambda, \lambda]$ and $\boldsymbol{q}(t) = [q_1(t), q_2(t)]^\top$. More generally, this approach yields the discrete displacement field given through

$$\boldsymbol{\gamma}(\lambda, t) = \boldsymbol{r}(\lambda, \boldsymbol{q}(t)) = \boldsymbol{\Pi}(\lambda)\, \boldsymbol{q}(t) \,. \tag{3.28}$$

Let us assume from here on $\boldsymbol{\Pi}(\lambda) \in \mathbb{R}^{3\times 3\,n_\Pi}$ and thus $\boldsymbol{q}(t) \in \mathbb{R}^{3\,n_\Pi\times 1}$, such that we obtain a three-dimensional curve with three, not necessarily equal, sets of generalized coordinates. Alternatively, we may write our curve in components as

$$\boldsymbol{\gamma}(\lambda,t) = \begin{bmatrix} x(\lambda,t) \\ y(\lambda,t) \\ z(\lambda,t) \end{bmatrix} = \begin{bmatrix} \boldsymbol{\Pi}_x(\lambda)\,\boldsymbol{q}_x(t) \\ \boldsymbol{\Pi}_y(\lambda)\,\boldsymbol{q}_y(t) \\ \boldsymbol{\Pi}_z(\lambda)\,\boldsymbol{q}_z(t) \end{bmatrix} = \underbrace{\begin{bmatrix} \boldsymbol{\Pi}_x(\lambda) & \mathbb{0} & \mathbb{0} \\ \mathbb{0} & \boldsymbol{\Pi}_y(\lambda) & \mathbb{0} \\ \mathbb{0} & \mathbb{0} & \boldsymbol{\Pi}_z(\lambda) \end{bmatrix}}_{\boldsymbol{\Pi}(\lambda)} \underbrace{\begin{bmatrix} \boldsymbol{q}_x(t) \\ \boldsymbol{q}_y(t) \\ \boldsymbol{q}_z(t) \end{bmatrix}}_{\boldsymbol{q}(t)} .$$

Following the kinematics in Section 3.3, we require not only the discrete curve but also its first three derivatives w.r.t. path coordinate λ and time t due to the measurement of torsion Eq. (3.10b), such that we obtain

$$\boldsymbol{\gamma}' = \frac{\partial \boldsymbol{r}(\lambda,\boldsymbol{q})}{\partial \lambda} = \boldsymbol{\Pi}'(\lambda)\,\boldsymbol{q}(t)\,, \tag{3.29a}$$

$$\boldsymbol{\gamma}'' = \frac{\partial^2 \boldsymbol{r}(\lambda,\boldsymbol{q})}{\partial \lambda^2} = \boldsymbol{\Pi}''(\lambda)\,\boldsymbol{q}(t)\,, \tag{3.29b}$$

$$\boldsymbol{\gamma}''' = \frac{\partial^3 \boldsymbol{r}(\lambda,\boldsymbol{q})}{\partial \lambda^3} = \boldsymbol{\Pi}'''(\lambda)\,\boldsymbol{q}(t)\,, \tag{3.29c}$$

$$\dot{\boldsymbol{\gamma}} = \frac{\mathrm{d}\boldsymbol{r}(\lambda,\boldsymbol{q})}{\mathrm{d}t} = \boldsymbol{\Pi}(\lambda)\,\dot{\boldsymbol{q}}(t)\,, \tag{3.29d}$$

$$\ddot{\boldsymbol{\gamma}} = \frac{\mathrm{d}^2 \boldsymbol{r}(\lambda,\boldsymbol{q})}{\mathrm{d}t^2} = \boldsymbol{\Pi}(\lambda)\,\ddot{\boldsymbol{q}}(t)\,. \tag{3.29e}$$

Consequently, our virtual displacements require accounting for the discrete constraints resulting in

$$\delta\boldsymbol{\gamma} = \frac{\partial \boldsymbol{\gamma}}{\partial \boldsymbol{q}}\,\delta\boldsymbol{q}\,, \tag{3.30a}$$

$$\delta\boldsymbol{\gamma}' = \frac{\partial \boldsymbol{\gamma}'}{\partial \boldsymbol{q}}\,\delta\boldsymbol{q}\,, \tag{3.30b}$$

$$\delta\boldsymbol{\theta} = \frac{\partial \boldsymbol{\theta}}{\partial \boldsymbol{q}}\,\delta\boldsymbol{q}\,, \tag{3.30c}$$

$$\delta\boldsymbol{\theta}' = \frac{\partial \boldsymbol{\theta}'}{\partial \boldsymbol{q}}\,\delta\boldsymbol{q}\,, \tag{3.30d}$$

with the rotation vector $\boldsymbol{\theta}$ igiven in Eq. (3.13) and its derivative $\boldsymbol{\theta}'$ given in Eq. (3.14).

Lastly, we require resolving the integral forms over the cable body currently given as Riemann integral over body $\mathcal{C}$. Assuming a cable of constant cross-section A under all external and internal forces and of constant unit density ϱ, we obtain for the Rieman integral

$$\int_{\mathcal{C}} = \int_{M} \mathrm{d}m = \int_{0}^{L} \varrho\, A\, \mathrm{d}\lambda\,.$$

By substituting respective derivatives of the discrete displacement function from Eq. (3.29) and the virtual displacements Eq. (3.30) into the virtual works from Eqs. (3.19), (3.20) and (3.24) and respecting the explicit boundaries of integration, we obtain the virtual works as function of our sought-for forces reading

$$\delta W_{\mathrm{dyn}} = \int_{0}^{L} \varrho\, A\, (\boldsymbol{\Pi}\, \ddot{\boldsymbol{q}})^{\top}\, \boldsymbol{\Pi}\, \mathrm{d}\lambda\, \delta\boldsymbol{q} \qquad = \boldsymbol{f}_{\mathrm{dyn}}^{\top}\, \delta\boldsymbol{q}\,, \quad \text{(3.31a)}$$

$$\delta W_{\mathrm{ext}} = \int_{0}^{L} \varrho\, A\, \hat{\boldsymbol{e}}_{\mathrm{G}}^{\top}\, \boldsymbol{\Pi}\, \mathrm{d}\lambda\, \delta\boldsymbol{q} \qquad = \boldsymbol{f}_{\mathrm{ext}}^{\top}\, \delta\boldsymbol{q}\,, \quad \text{(3.31b)}$$

$$\delta W_{\mathrm{int}} = \int_{0}^{L} \left(\boldsymbol{\sigma}^{\top}\, \boldsymbol{\Pi} + \boldsymbol{\sigma}^{\top} \left((\boldsymbol{\Pi}'\, \boldsymbol{q}) \times \frac{\partial \boldsymbol{\theta}}{\partial \boldsymbol{q}} \right) + \boldsymbol{\tau}^{\top}\, \frac{\partial \boldsymbol{\theta}'}{\partial \boldsymbol{q}} \right) \mathrm{d}\lambda\, \delta\boldsymbol{q} \quad = \boldsymbol{f}_{\mathrm{int}}^{\top}\, \delta\boldsymbol{q}\,. \quad \text{(3.31c)}$$

3.5.1 Consideration of Time-Varying Length

Remembering the upper integral boundary of the virtual works being the unstrained cable length L (cf. Eq. (3.31)), which we require to be time-varying i.e., non-fixed, we obtain integral formalations of varying upper bound. To accommodate for this, we introduce a coordinate transformation of path abscissae $\lambda \in \Lambda$ such that its domain $\Lambda \coloneqq [0, L]$ becomes $\Xi \coloneqq [0, 1]$. Let us introduce $\xi \in \Xi$ for which holds

$$\xi = \frac{1}{L}\, \lambda\,,$$

and equivalently

$$\lambda = L\,\xi\,.$$

Further follows for the total differential $\mathrm{d}\xi$ with respect the original variable's total differential $\mathrm{d}\lambda$

$$\mathrm{d}\lambda = L\ \mathrm{d}\xi\,.$$

Substituting our new path coordinate into the discrete displacement function Eq. (3.27) and consequently into Eq. (3.28) yields equivalence of both curve functions

$$\boldsymbol{\Pi}(\lambda)\,\boldsymbol{q}(t) = \boldsymbol{\gamma}(\lambda,t) = \hat{\boldsymbol{\gamma}}(\xi,t) = \hat{\boldsymbol{\Pi}}(\xi)\,\boldsymbol{q}(t)\,.$$

Partial derivatives of $\hat{\boldsymbol{\gamma}}(\xi,t)$ w.r.t. λ introduce a scaling factor due to the chain rule such that

$$\begin{aligned}
\boldsymbol{\gamma}'(\lambda,t) &= \frac{1}{L}\,\hat{\boldsymbol{\gamma}}'(\xi,t)\,,\\
\boldsymbol{\gamma}''(\lambda,t) &= \frac{1}{L^2}\,\hat{\boldsymbol{\gamma}}''(\xi,t)\,,\\
\boldsymbol{\gamma}'''(\lambda,t) &= \frac{1}{L^3}\,\hat{\boldsymbol{\gamma}}'''(\xi,t)\,,
\end{aligned}$$

while the total time-derivatives of our new curve $\boldsymbol{\gamma}(\xi,t)$ read

$$\begin{aligned}
\frac{\mathrm{d}\boldsymbol{\gamma}(\lambda,t)}{\mathrm{d}t} &= -\frac{\dot{L}}{L}\,\xi\,\frac{\partial\hat{\boldsymbol{\gamma}}(\xi,t)}{\partial\xi} + \frac{\partial\hat{\boldsymbol{\gamma}}(\xi,t)}{\partial t}\,,\\
\frac{\mathrm{d}^2\boldsymbol{\gamma}(\lambda,t)}{\mathrm{d}t^2} &= \frac{\partial^2\hat{\boldsymbol{\gamma}}(\xi,t)}{\partial t^2} - \frac{\ddot{L}\,L - 2\,\dot{L}^2}{L^2}\,\xi\,\frac{\partial\hat{\boldsymbol{\gamma}}(\xi,t)}{\partial\xi} + \cdots\\
&\qquad - 2\,\frac{\dot{L}}{L}\,\xi\,\frac{\partial^2\hat{\boldsymbol{\gamma}}(\xi,t)}{\partial\xi\partial t} + \left(\frac{\dot{L}}{L}\,\xi\right)^2\frac{\partial^2\hat{\boldsymbol{\gamma}}(\xi,t)}{\partial\xi^2}\,.
\end{aligned}$$

The latter equation shows the impact of a time-varying cable length on the overall dynamics. Not only are the equations more involved, it also shows necessity of

cable velocities $\dot{L}$ and accelerations $\ddot{L}$. Partial time-derivatives $\frac{\partial \boldsymbol{\gamma}(\xi,t)}{\partial t}$ and $\frac{\partial^2 \boldsymbol{\gamma}(\xi,t)}{\partial t^2}$, respectively, simplify to read

$$\begin{aligned}\frac{\partial \hat{\boldsymbol{\gamma}}(\xi,t)}{\partial t} &= \hat{\boldsymbol{\Pi}}(\xi)\,\dot{\boldsymbol{q}}(t)\,,\\ \frac{\partial^2 \hat{\boldsymbol{\gamma}}(\xi,t)}{\partial t^2} &= \hat{\boldsymbol{\Pi}}(\xi)\,\ddot{\boldsymbol{q}}(t)\,.\end{aligned}$$

We can then obtain the new, fixed-domain integral formulation for our energies considering the rule of substitution by integration given interval $I \subseteq \mathbb{R}$ for a differentiable function $\varphi\colon [a,b] \to I$ with integrable derivative, and a continuous function $f\colon I \to \mathbb{R}$

$$\int_{\varphi(a)}^{\varphi(b)} f(u)\,\mathrm{d}u = \int_a^b f(\varphi(x))\,\varphi'(x)\,\mathrm{d}x$$

with $u = \varphi(x)$ and $\varphi'(x)\,\mathrm{d}x = \mathrm{d}u$. Omitting $\hat{(\cdot)}$ for better readability, it follows with the substitution for integration $\mathrm{d}\lambda = L\,\mathrm{d}\xi$ for the internal, external, and dynamic forces of the system

$$\begin{aligned}\boldsymbol{f}_{\text{ext}} &= \int_0^1 \varrho\, A\, \boldsymbol{\Pi}(\xi)^\top \hat{\boldsymbol{e}}_{\text{G}}\, L\,\mathrm{d}\xi\,,\\ \boldsymbol{f}_{\text{int}} &= \int_0^1 \left(\boldsymbol{\Pi}(\xi)^\top \boldsymbol{\sigma}(\xi) + \frac{1}{L}\left(\boldsymbol{\Pi}'(\xi)\,\boldsymbol{q} \times \frac{\partial \boldsymbol{\theta}(\xi)}{\partial \boldsymbol{q}}\right)^\top \boldsymbol{\sigma}(\xi)\right) L\,\mathrm{d}\xi + \dots\\ &\quad + \int_0^1 \frac{1}{L}\frac{\partial \boldsymbol{\theta}'(\xi)}{\partial \boldsymbol{q}}^\top \boldsymbol{\tau}(\xi)\, L\,\mathrm{d}\xi\,, \qquad (3.32a)\\ \boldsymbol{f}_{\text{dyn}} &= \int_0^1 \varrho\, A \left(\boldsymbol{\Pi}(\xi)\,\ddot{\boldsymbol{q}} - \frac{\ddot{L}\,L - 2\,\dot{L}^2}{L}\,\xi\,\boldsymbol{\Pi}'\,\boldsymbol{q}\right)^\top \boldsymbol{\Pi}(\xi)\, L\,\mathrm{d}\xi + \cdots\\ &\quad + \int_0^1 \varrho\, A \left(-2\,\frac{\dot{L}}{L}\,\xi\,\boldsymbol{\Pi}'\,\dot{\boldsymbol{q}} + \left(\xi\,\frac{\dot{L}}{L}\right)^2 \boldsymbol{\Pi}''\right)^\top \boldsymbol{\Pi}(\xi)\, L\,\mathrm{d}\xi\,,\end{aligned}$$

Similarly, the energies expressed in terms of the discrete displacement function given the fixed-boundary integral read

$$U_{\mathrm{G}} = \int_0^1 \varrho\, A\, \boldsymbol{g}\, \hat{\boldsymbol{e}}_{\mathrm{z}}^{\top}\, \boldsymbol{\Pi}(\xi)\, \boldsymbol{q}\, L\, \mathrm{d}\xi\,, \tag{3.33a}$$

$$U_{\varepsilon} = \frac{1}{2} \int_0^1 \boldsymbol{\sigma}^{\top}\, \boldsymbol{C}^{\boldsymbol{\varepsilon}}\, \boldsymbol{\sigma}\, L\, \mathrm{d}\xi\,, \tag{3.33b}$$

$$U_{\kappa} = \frac{1}{2} \int_0^1 \boldsymbol{\tau}^{\top}\, \boldsymbol{C}^{\boldsymbol{\beta}}\, \boldsymbol{\tau}\, L\, \mathrm{d}\xi\,. \tag{3.33c}$$

It may be pointed out that deformation measures of curvature κ and torsion τ given in Eq. (3.10) are geometric properties of the curve itself, as such these are invariant under a change of parametrization thus

$$\kappa(\lambda) = \hat{\kappa}(\xi)\,, \qquad\qquad \tau(\lambda) = \hat{\tau}(\xi)\,.$$

Combining Eq. (3.32) and omitting the explicit time-dependency of the generalized coordinates as well as their time-derivatives, we obtain the general dynamics equation for the constrained cable as

$$\boldsymbol{M}(\boldsymbol{q})\, \ddot{\boldsymbol{q}} = \boldsymbol{f}_{\mathrm{ext}}(\boldsymbol{q}, \dot{\boldsymbol{q}}) - \boldsymbol{f}_{\mathrm{int}}(\boldsymbol{q})\,, \tag{3.34a}$$

$$\mathbb{0} = \boldsymbol{g}(\boldsymbol{q}, t)\,, \tag{3.34b}$$

with

$$\boldsymbol{g}(\boldsymbol{q}, t) = \begin{bmatrix} \boldsymbol{g}_{\mathrm{P}}(\boldsymbol{q}, t) \\ \boldsymbol{g}_{\mathrm{D}}(\boldsymbol{q}, t) \end{bmatrix}. \tag{3.34c}$$

3.5.2 Gaussian Quadrature

Analytical solutions to the energy and force integrals can not generally be obtained due to the unknown nature of displacement functions $\boldsymbol{r}(\xi, \boldsymbol{q}(t))$, or simply due to the complexity of the integrands. In addition, while the integrals may be determined during numerical integration of the system, this is a

computationally very expensive task and one needs to find good step sizes for the spatial integration. However, when imposing only few assumptions on the selection of displacement functions, we can evaluate the integrals a priori i.e., once before simulation starts which noticeably reduces computational cost and increases simulation speed. To numerically solve definite integrals, we employ quadrature rules, given as weighted sums of the integrand evaluated at specific points within the domain of integration.

Assuming function $f(x)$, we can recast the integral over domain $[a, b]$ into a weighted sum of n_{qp} function values

$$\int_a^b f(x)\,\mathrm{d}x = \frac{b-a}{2} \sum_k^{n_{\mathrm{qp}}} w_k\, f\!\left(\frac{b-a}{2}\, x_k + \frac{a+b}{2}\right), \tag{3.35}$$

with weights w_k and function $f(x)$ evaluated at discrete points inside the interval. By using the left-hand side of Eq. (3.35) for the forces from Eq. (3.32) and the energies from Eq. (3.33), we can evaluate the integrals independent of the state of the cable a priori to simulation.

A short introduction into numerical integration using quadrature rules, an overview of available quadrature techniques, and how to calculate the weights w_k is given in Appendix D.

3.6 Selection of Bases Functions

The equation of motion from Eq. (3.32) derived in Section 3.4 and discretized in Section 3.5 are widely applicable to the simulation of Cosserat rods and cables. We have not made any assumptions as to what the kinematic constraints of the system are in terms of shape-describing functions $\mathbf{\Pi}(\xi)$. In other words, the kinematics of the cable are defined allowing us to determine forces based on cable displacement and deformation. A geometric representation of the cable is yet to be found that, together with the kinematics of the cable, allow for the

spatial description of the cable undergoing displacement and deformation[19]. In this section, we present and evaluate the set of bases functions that produce a low-dimensional yet accurate approximation of the most vital characteristics of the cable: natural frequencies and static response.

A straightforward formulation of the shape functions can be found in a polynomial basis such that $\mathbf{\Pi}_k = \xi^k$ for $k \in [0, n_\Pi]$. Ayala Cuevas et al. employed the same technique in their flexible yet inelastic cable model, however, truncated the series at $n_\Pi \equiv 2$ (Ayala Cuevas et al. 2017). As will be shown later, second-order polynomials yield no good approximation of the resulting cable shape, which may also be inferred from Irvine's cable model (see Eq. (2.11)). A similar approach, though for simulation of stress waves inside the cable was followed by Godbole et al. who used harmonics as their bases functions (Godbole et al. 2017). To describe the longitudinal vibration characteristics, Godbole et al. designed their harmonic bases functions scaled to unit length such that

$$\mathbf{\Pi}_k = \sin\left(\frac{(k+1)\,\pi}{2}\right).$$

With appropriate scaling to the current cable length, high-frequency cable stress oscillation can be simulated affecting the position of the mass attached to the cable distal end. Zhang et al. presented promising results on the statics analysis of a beam subject to external loads, deformation forces, and support along its chord (Zhang et al. 2016). Their discretization is based on non-uniform rational B-spline (NURBS) for both the linear displacement field of a beam as well as the rotational displacement field. Similarly, the kinematics are derived using Cosserat's rod theory, however, no dynamic forces nor forward dynamics simulation is performed.

[19] In other words, previous sections presented a cable formulation on the level of forces. This section presents a purely geometric description of the cable without considering any mechanics or kinematics. It is only due to injecting the discretization of Section 3.5 that we can link a geometric formulation of the cable shape with its kinematic formulation. Down the road, we cannot independently observe the geometric description of the cable without respecting its kinematics. It may be clear to the experienced reader that a geometric curve cannot be aware of its elasticity whereas an elastic deformation is unaware of its underlying geometric reasoning.

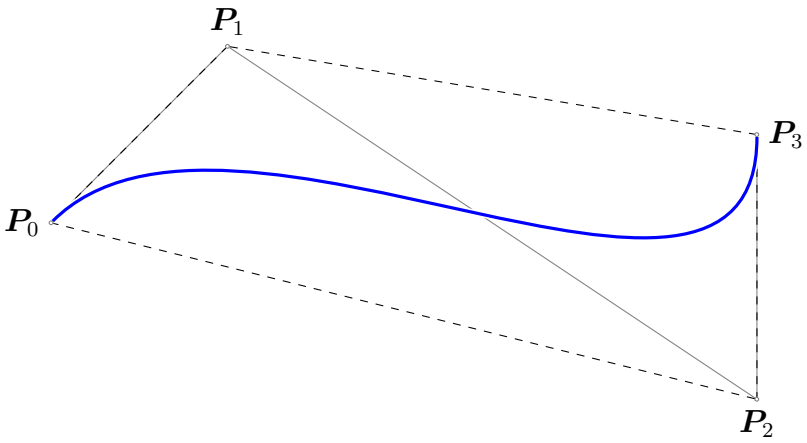

Figure 3.6: A cubic Bézier curve (blue) with four control points $\boldsymbol{P}_0$ through $\boldsymbol{P}_3$ and their convex hull (dashed).

It suggests itself to use an orthogonal basis composed of univariate polynomials as shape functions e.g., $\{\, 1, x, (3\,x^2 - 1)/2, \ldots \}$, as this is common procedure in interpolation and approximation of data sets[20] using e.g., Lagrange interpolation, Hermite interpolation, or Newton's series (Funaro 1992; Farouki et al. 2003; Davis 1975; Greenstein 1965; Phillips 2003). When it comes to solving differential equations, the homogeneous solution can be obtained by an exponential description, which in itself is simply an infinite sum of (scaled) monomials. As such, from a mathematical point of view, we may directly inject polynomial bases into the solution of differential equations, as performed by Bhatti et al. who used Bernstein basis polynomials for solutions of differential equations (Bhatti et al. 2007).

A set of bases functions often found in the analysis of mechanical structures is composed of Bernstein polynomials, which in the context of spatial curves can be found in computer graphics, where they are called Bézier curves. Used in computer graphics, a Bézier curve (see Fig. 3.6) is simply a parametric polynomial curve in space—either 2D or 3D—with Bernstein polynomials of certain degree as its basis. For any polynomial of degree p, a Bézier curve is

[20] In interpolation, points of the basis figure are located on the created figure whereas in approximation, points on the basis figure need not be on the created figure but in some proximity.

defined as

$$\boldsymbol{C}_{k,p}(\xi) = \sum_{k=0}^{p} \binom{p}{k} \xi^k \, (1-\xi)^{p-k} \, \boldsymbol{P}_k \,, \qquad 0 \leq \xi \leq 1 \,, \tag{3.36}$$

where $\binom{p}{k} = \frac{p!}{k!(p-k)!}$ are the binomial coefficients and $\boldsymbol{P}_k$ are the so-called control points of the Bézier curve. It must be noted that the control points do not in general lie on the Bézier curve but are merely defining the convex hull of the Bézier curve (see also Fig. 3.6). In Eq. (3.36), the summands are the k-th Bernstein polynomials of degree p i.e.,

$$b_{k,p}(\xi) = \binom{p}{k} \xi^k \, (1-\xi)^{p-k} \,. \tag{3.37}$$

Figure 3.7 shows $p+1$ Bernstein basis polynomials for several polynomial degrees $p \in \{1, 2, 3\}$ over their interval of validity $\xi \in \Xi = [0, 1]$. Bernstein basis polynomials satisfy positiveness $b_{k,p}(\xi) \geq 0$, symmetry $b_{k,p}(\xi) = b_{p-k,p}(\xi)$, and form a partition of unity $\sum b_{k,p}(\xi) = 1$ on interval $[0, 1]$. Further useful properties are also satisfied, yet not discussed in detail here as these are of less significance to the applied use case. The interested reader is referred to Farouki (2012), Dadkhah (2015), and Bellucci (2014).

While we may add arbitrarily many control points $\boldsymbol{P}_k$ to the Bézier curve to increase its goodness of interpolation, it entails introducing further kinematic constraints into the system as well as numerical instabilities. In addition, high polynomial degrees are not necessarily required from the kinematic definition of our cable—we merely require the curve to be $\boldsymbol{\gamma} \in C^3$ in order to have at least continuous torsion. As such, we may employ composite Bézier curves where we adjoin several Bézier curves at their respective end and beginning.

Assuming at least C^0 continuity of two Bézier curves $\boldsymbol{C}^{(0)}$ and $\boldsymbol{C}^{(1)}$ (both of same degree p, each with control points $\boldsymbol{P}_k^{(1)}$, $\boldsymbol{P}_k^{(2)}$, respectively) requires

$$\boldsymbol{C}^{(0)}(\xi^{(0)} = 1) = \boldsymbol{C}^{(1)}(\xi^{(1)} = 0)$$

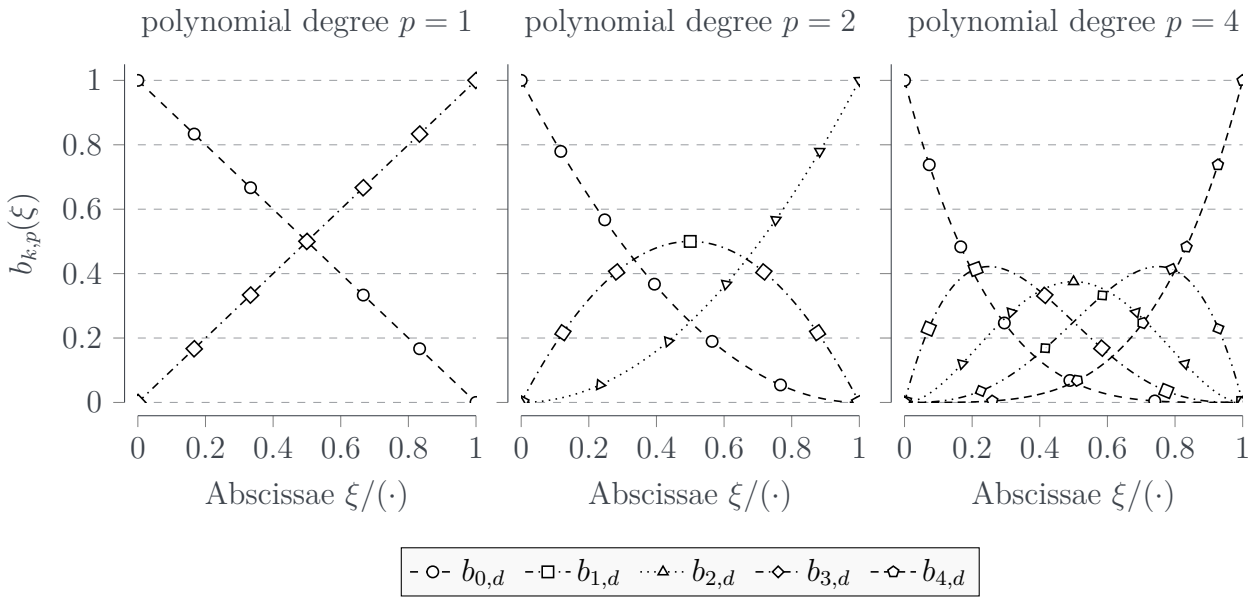

Figure 3.7: Bernstein polynomials of degrees $p \in \{1, 2, 4\}$ interpolated over path coordinate $\xi \in [0, 1]$.

or equivalently

$$\boldsymbol{P}_{p+1}^{(0)} = \boldsymbol{P}_{0}^{(1)} ,$$

to be satisfied, that is the last control point of the first Bézier curve must coincide with the first point of the second Bézier curve —which is to be expected intuitively. Requiring C^1 continuity leads to necessity of having the vertices

$$\boldsymbol{P}_{p}^{(0)} , \boldsymbol{P}_{p+1}^{(0)} = \boldsymbol{P}_{0}^{(1)} , \boldsymbol{P}_{1}^{(1)}$$

collinear. Similarly, C^2 continuity requires the vertices

$$\boldsymbol{P}_{p-1}^{(0)} , \boldsymbol{P}_{p}^{(0)} , \boldsymbol{P}_{p+1}^{(0)} = \boldsymbol{P}_{0}^{(1)} , \boldsymbol{P}_{1}^{(1)} , \boldsymbol{P}_{2}^{(1)}$$

to be collinear. Consequently, for C^j continuity, the vertices

$$\boldsymbol{P}_{p-j+1}^{(0)} , \boldsymbol{P}_{p-j}^{(0)} , \ldots , \boldsymbol{P}_{p+1}^{(0)} = \boldsymbol{P}_{0}^{(1)} , \boldsymbol{P}_{1}^{(1)} , \ldots , \boldsymbol{P}_{j}^{(1)}$$

must be collinear. To gain C^2 continuity, the Bézier curve loses local control as the continuity requirement makes control points next to the adjoining point be

dependent resulting in the whole spline being affected if a single control point moves.

Following this recursive definition, it is apparent that higher levels of continuity require a higher polynomial degree of the connecting Bézier curves, as the polynomial degree is directly linked to the number of control points with $p = n_{\text{ctrl}} - 1$. In addition, while the constraints resulting from continuity may be integrated into the dynamics model by either further holonomic constraints, they may also be incorporated into the equations for the coefficients themselves rendering some generalized coordinates redundant. Since every Bézier control point has global support—in our case the Bézier control points translate to be the generalized coordinates i.e., the system's mechanical DOFs—, requiring higher continuity of the curves causes a kinematically tightly constrained system.

Remedy for this drawback of Bézier curves comes from using functions of a given degree with only minimal support that provide smoothness and domain partition. In the field of numerical analysis, such functions are referred to as basis splines, or B-splines, as coined by Isaac Jacob Schoenberg (Boor 1978). B-splines can have continuity in e.g., C^2 with only local control, but they loose piecewise Bézier's interpolation property. The points where piecewise B-splines meet are called knots and allow for simple incorporation of certain continuity requirements. Each spline control point is associated with a basis function such that a curve $\boldsymbol{C} \in \mathbb{R}^2$ or $\boldsymbol{C} \in \mathbb{R}^3$ reads

$$\boldsymbol{C}(\xi) = \sum_{k=0}^{n_{\text{ctrl}}} \Pi_{k,p}(\xi)\, \boldsymbol{P}_k \,, \tag{3.38}$$

in which $\Pi_{k,p}(\xi)$ is the k-th basis function of polynomials of degree p and $\boldsymbol{P}_k$ is the associated control point (with planar $\boldsymbol{P}_k \in \mathbb{R}^2$ and spatial $\boldsymbol{P}_k \in \mathbb{R}^3$). With B-splines, the degree p of the bases functions is not dependent of the number of control points n_{ctrl}—which is the case for Bézier curves where $p = n_{\text{ctrl}} - 1$. Equation (3.38) defines a general polynomial spline which can be chosen with an arbitrary degree per basis function. Each basis function is a recursive formulation of linear combinations of lower-dimensional bases functions on the local interval

of validity. In general, spline functions can be of any sort as long as they satisfy the requirements of spline functions, the most common spline functions however are linear interpolation functions, but also hyperbolic ones (Lü et al. 2002) or logarithmic ones (Schröppel et al. 2016) exist. The recursive formulation for the k-th spline bases functions $\Pi_{k,p}(\xi)$ is given as

$$\Pi_{k,0}(\xi) = \begin{cases} 1\,, & \xi \in [\xi_k, \xi_{k+1}[\,, \\ 0\,, & \xi \notin [\xi_k, \xi_{k+1}[\end{cases}, \tag{3.39a}$$

$$\Pi_{k,p}(\xi) = \frac{\xi - \xi_k}{\xi_{k+p} - \xi_k}\,\Pi_{k,p-1}(\xi) + \frac{\xi_{k+p+1} - \xi}{\xi_{k+p+1} - \xi_{k+1}}\,\Pi_{k+1,p-1}(\xi)\,, \tag{3.39b}$$

which is the Cox-de Boor recursion formula (Piegl et al. 1997). Any B-spline of degree p is composed of piecewise polynomial functions in ξ of degree $p-1$. These piecewise functions are defined over only $p+1$ points ξ_j, called knots, which are collected in the nondecreasing knot vector $\boldsymbol{\xi}$. This also implies that, contrary to Bézier curves, each B-spline contributes only locally in the range between its first and last knot. A B-spline's j-th derivative can be found by induction and is given purely for consistency and completeness to

$$\frac{\mathrm{d}^j}{\mathrm{d}\xi^j} = \frac{p}{\xi_{k+p} - \xi_k}\,\frac{\mathrm{d}^{j-1}}{\mathrm{d}\xi^{j-1}}\,\Pi_{k,p-1}(\xi) - \frac{p}{\xi_{k+p+1} - \xi_{k+1}}\,\frac{\mathrm{d}^{j-1}}{\mathrm{d}\xi^{j-1}}\,\Pi_{k+1,p-1}(\xi)\,,$$

which holds for all $j > 0$, otherwise Eq. (3.39) holds.

By choosing B-splines as basis of shape functions $\boldsymbol{\Pi}(\xi)$, we achieve in a first step discretization of the continuum into a set of polynomial bases. That is, the resulting cable shape can be composed of superimposing these polynomial bases. Further, with B-splines per-definition being composed of piecewise local functions, we introduce an additional spatial discretization of the cable into local shape functions that are in addition only locally valid. This removes dependence of control points—which in our case are going to be the generalized coordinates—and thus removes kinematically constraining generalized coordinates simply due to our choice of bases functions. Lastly, due to the spatial discretization into splines we can achieve better approximation of more

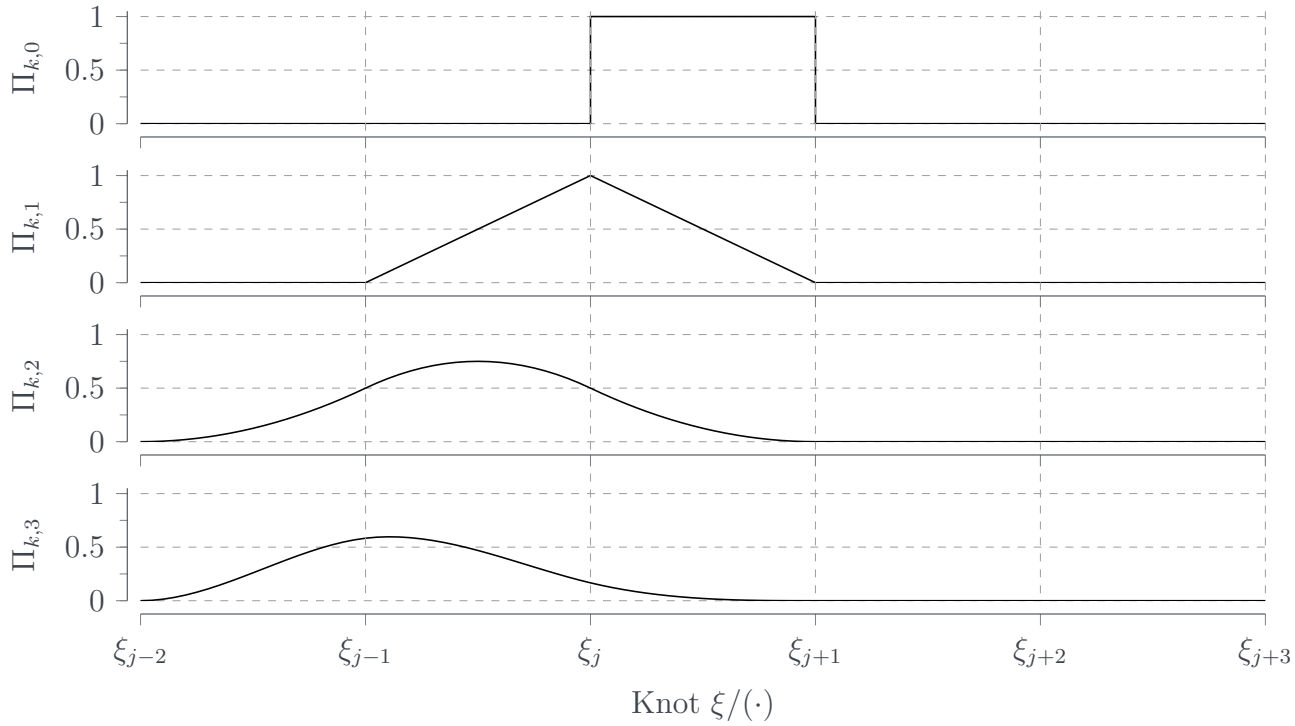

Figure 3.8: Blending functions $\Pi_{k,p}$, $k = (0, \ldots, p)$ of a B-spline with $n_\mathrm{s} = 5$ segments and local polynomial degree $p = 3$. The k-th blending function $\Pi_{k,p}$ is obtained through convolution of blending function $\Pi_{k,p-1}$ with the latter.

complex shapes of the cable[21] while using lower polynomial degree. As shown by Dokken et al. (1990), a circle may only be approximated using a single Bézier curve with $p = 3$ (neglecting possibility of employing composite Bézier curves), whereas an $n_\mathrm{s} = 4$ B-spline of local polynomial degree $p = 2$ suffices to perfectly describe the circle.

3.7 Natural Frequencies

One reason for considering B-splines is their ability to approximate continuous spatial curves $\boldsymbol{\gamma}(\xi) \in C^2$ with only two parameters. Since B-splines are piecewise polynomial curves, we can change both the number of pieces composing our B-spline as well as we can change the local polynomial degree. In addition,

[21] Whether this be necessary is out of the scope of this section.

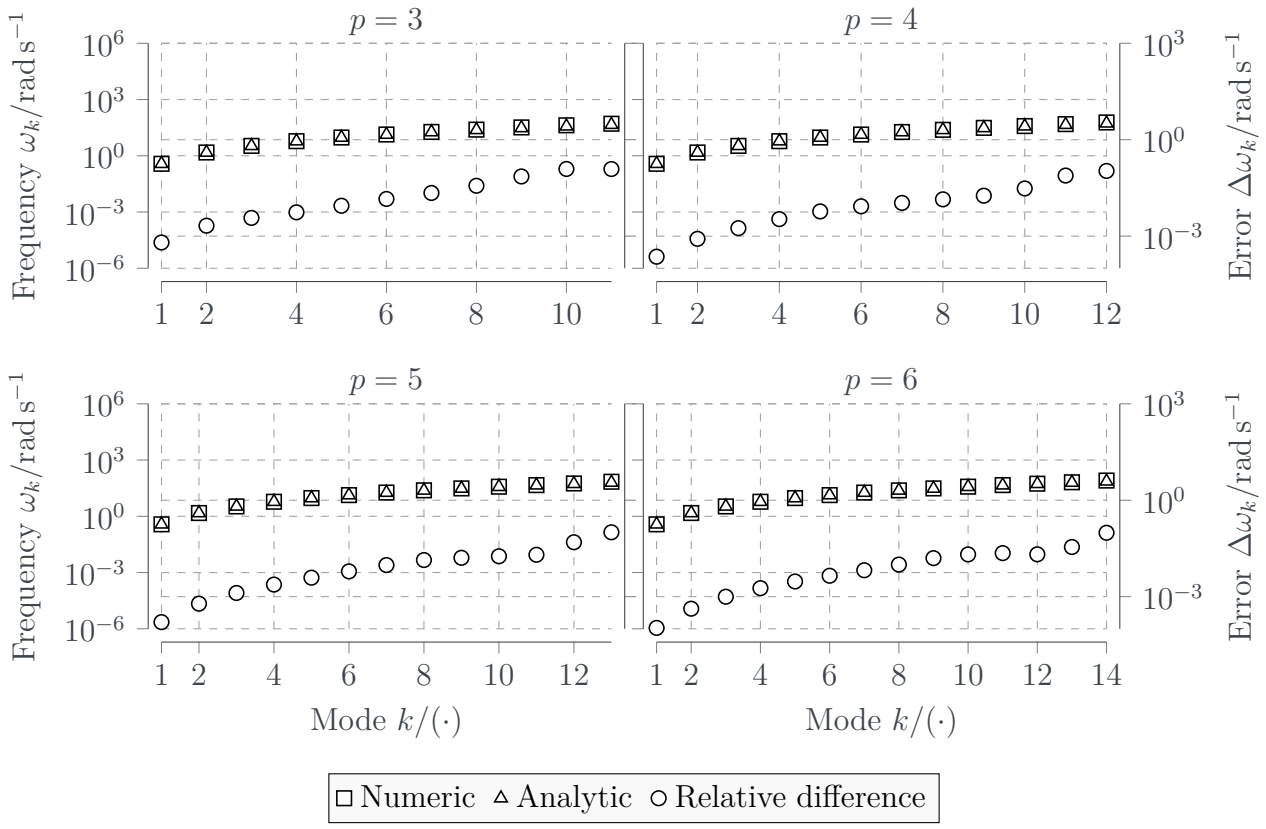

Figure 3.9: Natural frequencies of B-spline cable with number of segments $n_\mathrm{s} = 10$ and local polynomial degree $p \in \{3, 4, 5, 6\}$ compared to natural frequencies of the tension-free beam. Data are tabularized in Appendix B.

as given in Section 3.6 presenting the investigated basis functions, the control points of a curve defined by B-splines only have local support i.e., changes in one control point—in our case the control points are generalized coordinates—affects the curve shape only locally. In other terms, the generalized coordinates are only locally coupled to a limited number of their preceding and succeeding control points which depends only on the local polynomial degree. Theoretically, this B-spline property leads to making the system numerically less stiff thus better predicting the natural frequencies (see the example on composite Bézier curves in Section 3.6).

In a first evaluation, we split our cable into $n_\mathrm{s} = 10$ segments each defined through local B-splines of varying polynomial degree. Figure 3.9 shows decreasing relative differences in the prediction of natural frequencies of the simply-supported beam as the local polynomial degree is increased. Further, the approx-

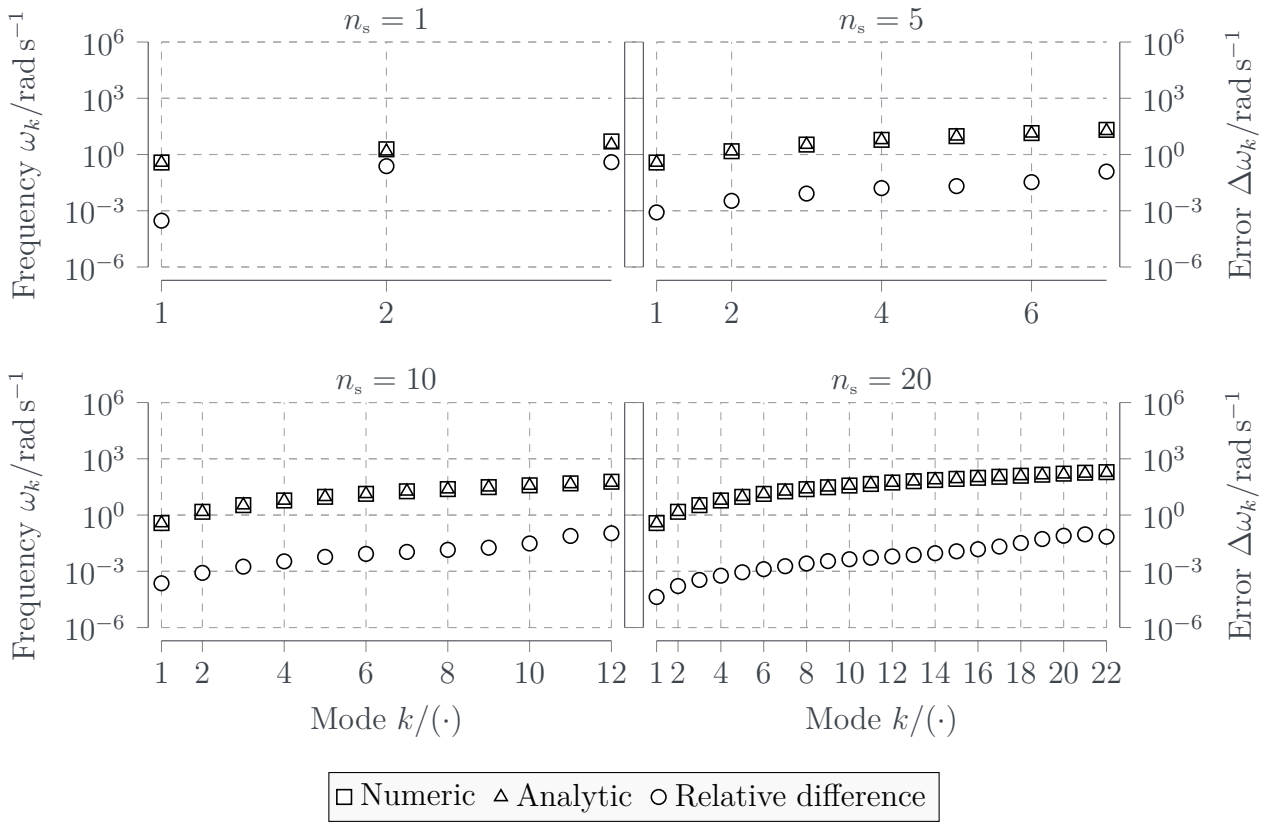

Figure 3.10: Natural frequencies of B-spline cable with local polynomial degree $p = 4$ and number of segments $n_s \in \{1, 5, 10, 20\}$ compared to natural frequencies of the tension-free beam. Data are tabularized in Appendix B.

imation error between numerical and analytical solution always stays below the threshold of $\Delta\omega_k < 1$ for all natural frequencies, the first 7 natural frequencies are bounded by a relative difference of $\Delta^{\text{rel}}\omega_k \leq 1 \times 10^{-2}$, $k \in \{1, \ldots, 7\}$, yielding an absolute error of $\Delta^{\text{abs}}\omega_k \leq 0.180\,\text{rad}\,\text{s}^{-1}$, equivalently $\Delta^{\text{abs}}\omega_k \approxeq 0.029\,\text{Hz}$.

In a second evaluation, we set the local polynomial degree to fixed $p = 4$ and vary the number of segments (see Fig. 3.10). We assume the impact of increasing number of segments more significant than raising local polynomial degree since increased segmentation allows to form more complex curves. With number of segments $n_s \leq 5$, worsening of approximation of natural frequencies is entailed with maximum underestimations of $|\Delta\omega_k| \approxeq 0.980\,\text{rad}\,\text{s}^{-1}$ or equivalently of $|\Delta\omega_k| \approxeq 0.156\,\text{Hz}$; still comparatively low. Once the number of segments outgrows $n_s \geq 2\,p - 1$, approximation of lower-order natural frequencies converges toward differences of $\Delta\omega_k \lessapprox 1 \times 10^{-6}\,\text{rad}\,\text{s}^{-1} \approxeq 1.592 \times 10^{-7}\,\text{Hz}$.

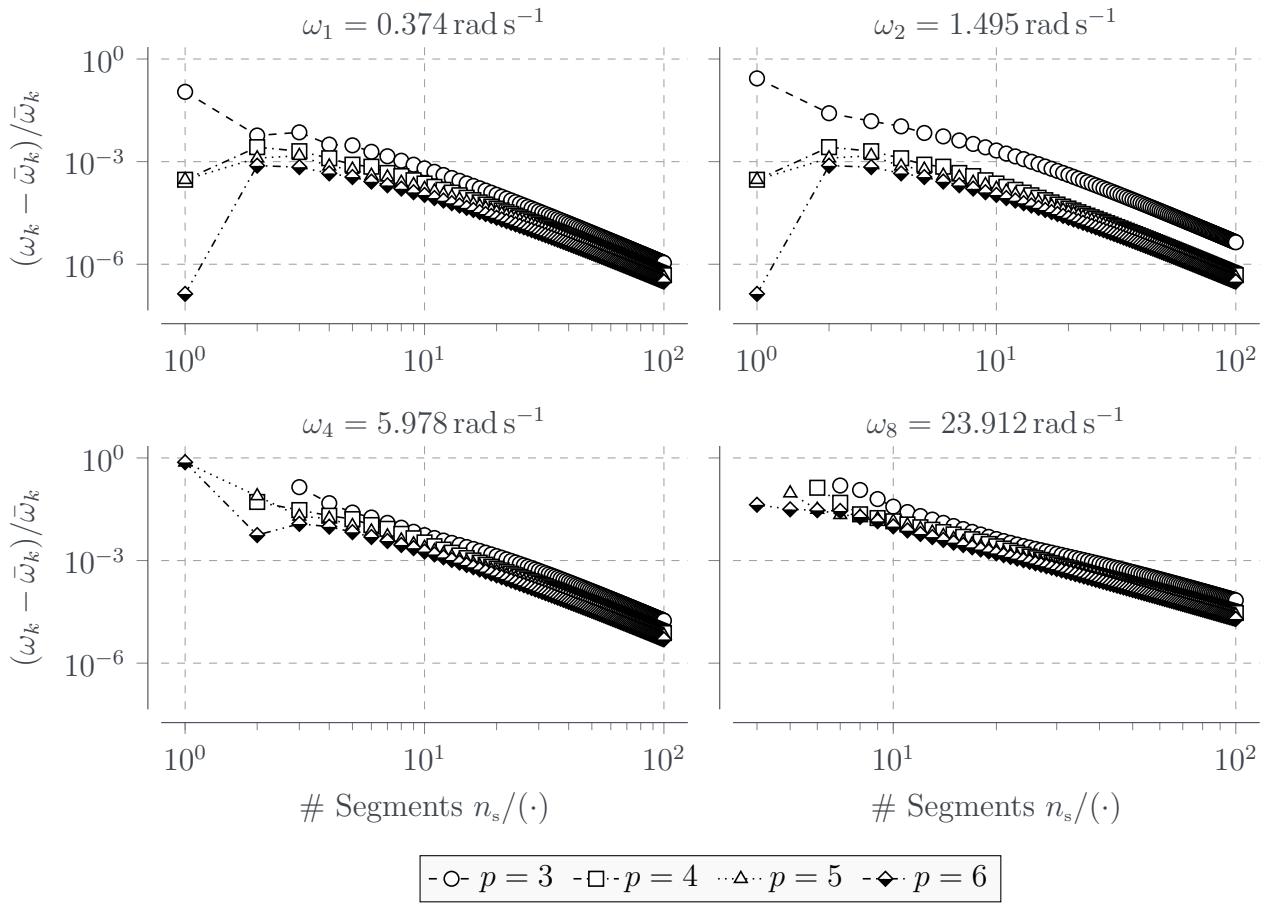

Figure 3.11: Convergence rate of natural frequencies ω_k, ($k \in \{1, 2, 4, 8\}$) for local polynomial degree $p \in \{3, 4, 5, 6\}$ confirming our expectation of lower error for higher local polynomial degree p and quicker approximation with increasing number of segments n_s.

Varying of local polynomial degree p affects approximation of natural frequencies likewise as variation of number of segments does. However, noticeable improvement can only be achieved by high-order local polynomial degree, which does not provide the same convenience as increased number of segments. It is thus beneficial to vary the number of segments, not only because it allows for representing more complex geometric curves but also because it provides for quick convergence of the lower-order natural frequencies with only few segments (see Fig. 3.11). As such, we fix the local polynomial degree for the remainder of this thesis to $p \equiv 4$ as a good trade-off between approximation quality, numerical stability, but also continuity of the cable (we require at least $\boldsymbol{\gamma}(\xi, t) \in C^3$ to have continuous torsion i.e., $p \geq 4$).

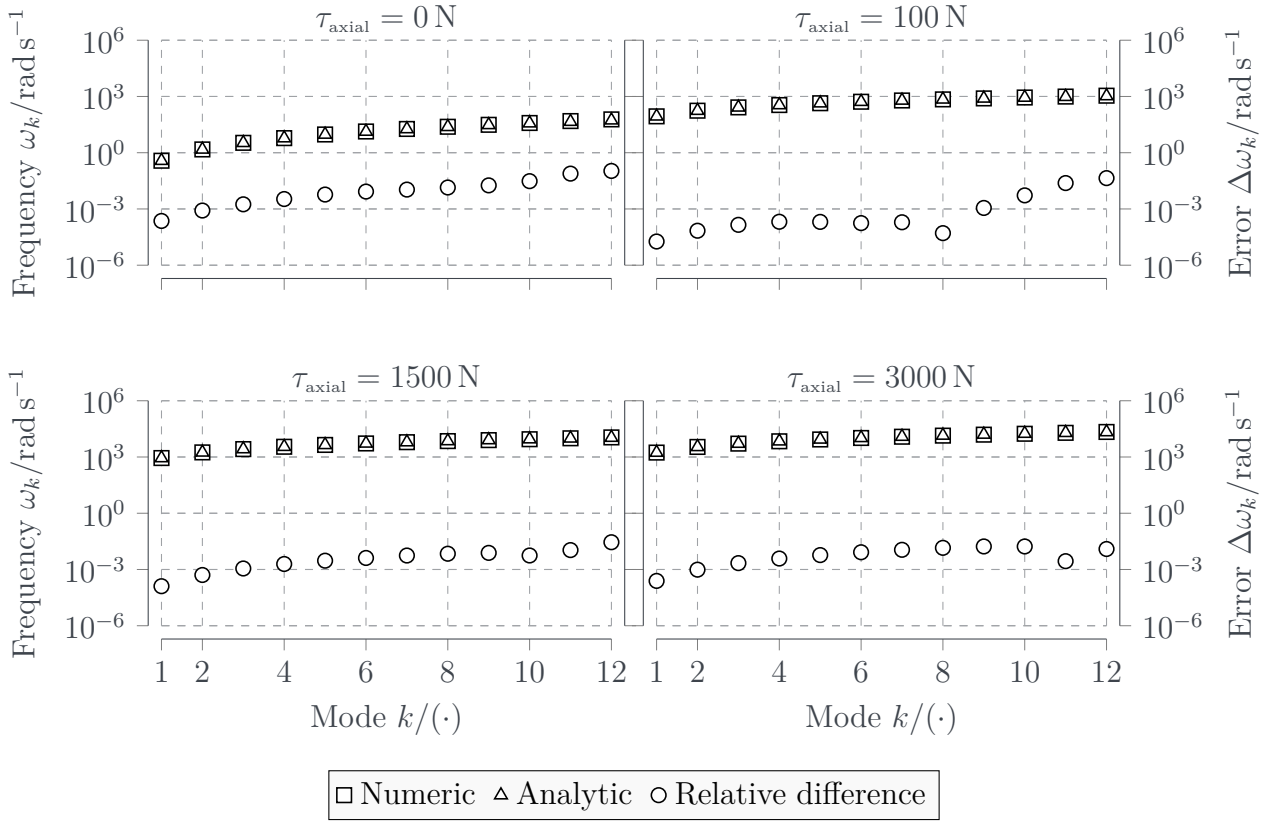

Figure 3.12: Natural frequencies of B-spline cable with number of segments $n_\text{s} = 10$ and local polynomial degree $p = 4$ compared to natural frequencies of the axially loaded beam with tension varying in $\sigma_\text{axial} \in \{0, 100, 1500, 3000\}\,\text{N}$.

Increasing axial beam stress within the range of interest $f \in [100, 3000]\,\text{N}$ has negligible effect on the approximation of natural frequencies. For higher order natural frequencies, we do see a decrease in the error as axial tension increases with the maximum error being lower than $\Delta^\text{abs}\omega_k < 4\,\%$, a decrease of approximately 63 %. At the same time, lower order natural frequencies are approximated equally well as in the axially tension-free case.

3.8 Statics

Besides analyzing the goodness of approximation of natural frequencies, we focus our attention in this section toward the accuracy of predicting the static cable shape. The reference implementation we use is Irvine's cable model we briefly presented in Section 2.3.1.3. While this model is also a simplification of

a string spanned between two points due to its neglecting bending stiffness, it provides an analytic solution that can be used in comparison. Since the cable model presented in this chapter aims at extending the framework of cable robot analysis, its main purpose is to provide a coherent description of the cable shape in space between the cable drawing point and the platform anchor. This is of particular interest in the design process of cable robots in order to allow for evaluating the robot design for possible interference with the environment, but also for the analysis of the static workspace.

Since the static cable shape is evaluated, we can without loss of generality confine the motion of the cable to the vertical plane spanned by the $\hat{\boldsymbol{e}}_{\mathrm{x}}\hat{\boldsymbol{e}}_{\mathrm{z}}$-pair of vectors. This holds true as we may find a constant transformation matrix that maps the global Cartesian space $\mathbb{E}^3$ into a subspace $\mathbb{E}^2$ by simply applying a rotation about the $\hat{\boldsymbol{e}}_{\mathrm{z}}$-axis. Let us assume the cable be fixed at its proximal point with $\boldsymbol{g}_{\mathrm{P}}(t) = \mathbb{0} \in \mathbb{R}^2$ where we choose the origin $\mathbb{0}$ for mere convenience. Further, we set the mechanical properties of the cable according to the *Rubber-like steel cable* from Table 3.1 which allow for more severe cable sag. The distal cable point is assumed to be defined through the geometric constraint given as

$$\boldsymbol{g}_{\mathrm{D},k}(t) = \boldsymbol{g}_{\mathrm{D},k_1,k_2} \coloneqq L_{k_1} \begin{bmatrix} \cos\beta_{k_2} \\ \sin\beta_{k_2} \end{bmatrix},$$

with

$$\begin{aligned} L_{k_1} &= k_1\, L_{\mathrm{O}}\,, & k_1 &\in \{0.6, 0.8, 1.0\}\,, \\ \beta_{k_2} &= \frac{2\,k_2}{5}\,\pi\,, & k_2 &\in \{0\,, \ldots, 4\}\,, \end{aligned}$$

yielding uniformly spaced points on a unit circle around the origin.

We will consider two quantitative measure of goodness of approximation of our B-spline cable model with respect to the Irvine cable model. First, let us assume the B-spline cable to be given by curve $\boldsymbol{\gamma}_{\text{b-spline}}$ and Irvine cable to be given by curve $\boldsymbol{\gamma}_{\text{irvine}}$. Since both curves are parametrized by unstrained path coordinate ξ, we obtain parametric curves $\boldsymbol{\gamma}_{\text{b-spline}}(\xi), \boldsymbol{\gamma}_{\text{irvine}}(\xi) \colon [0,1] \to \mathbb{R}^2$. As such calculating the deviation is less straightforward than simply subtracting

the curves. To remedy this, we introduce the *residual curve* $\boldsymbol{\gamma_e}$ defined as

$$\boldsymbol{\gamma_e}(\xi) = \boldsymbol{\gamma}_{\text{irvine}}(\xi) - \boldsymbol{\gamma}_{\text{b-spline}}(\xi)\,,$$

which can be understood as a vector field resulting from mapping the error between B-spline curve and Irvine into $\mathbb{R}^2$. That is, at coordinate ξ^* along the path, $\boldsymbol{\gamma_e}(\xi^*)$ points from the B-spline cable curve toward the Irvine cable. We then define two measures of interest for quantifying the residual such that we obtain a formulation of nominal deviation along unstrained path coordinate ξ, and a total area of deviation. Let our *residual vector norm* deviation be defined by

$$\boldsymbol{e}_{\boldsymbol{\gamma}}(\xi) = \|\boldsymbol{\gamma}_{\text{irvine}}(\xi) - \boldsymbol{\gamma}_{\text{b-spline}}(\xi)\|\,, \tag{3.40}$$

along the curve i.e., for $\xi \in \Xi = [0, 1]$. This gives us the residual mapping $\boldsymbol{e}_{\boldsymbol{\gamma}} \colon [0, 1] \ni \xi \mapsto \boldsymbol{e}_{\boldsymbol{\gamma}}(\xi) \in \mathbb{R}_{\geq 0}$, where each point along the curve is associated with a scalar residual. Further, let us take the vectorial residual $\boldsymbol{e}_{\boldsymbol{\gamma}}$ and associate it with a scalar value called *residual area norm* such that

$$e_{\boldsymbol{\gamma}} = \int_0^1 \boldsymbol{e}_{\boldsymbol{\gamma}}(\xi)\ \mathrm{d}\xi\,, \tag{3.41}$$

which simply denotes the area underneath residual curve Eq. (3.40). With this definition, we can quantify the error between the Irvine cable and the B-spline cable where a value close to zero represents perfect approximation of the cable shape; and larger values correspond to worse approximation.

Spanning the cable horizontally i.e., inducing the most evenly distributed sag, better approximation of the catenary shape can be more easily achieved by increasing the number of segments and leaving the local polynomial degree low at $p = 4$. Throughout all scenarios assessing the influence of the number of segments on the resulting cable shape, a cable with small number of segments e.g., in our case $n_{\text{s}} \leq 3$, does show smaller mean residual error, however, it is incapable of capturing well the point of maximum sag at $\xi = 0.5$ (see Fig. 3.13). A cable

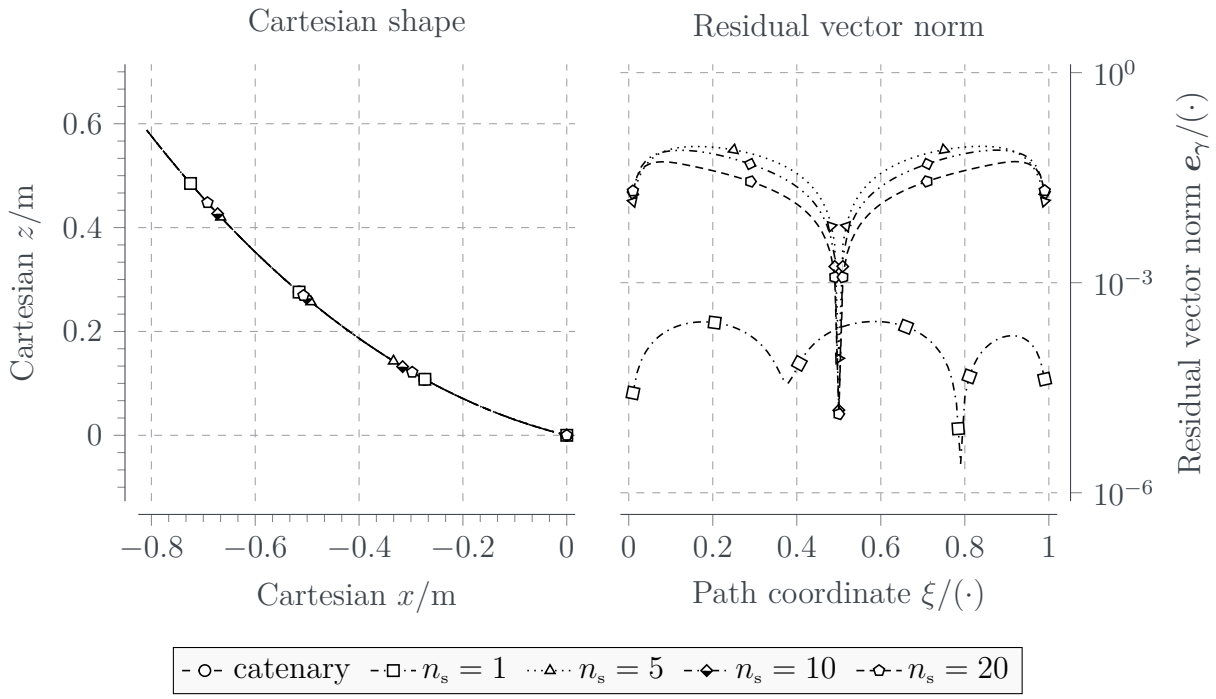

Figure 3.13: Static cable shape approximation of catenary solution (left) for cable spanned at $\beta_{k_2} = 144°$ with varying number of segments in $n_s \in \{1, 5, 10, 20\}$; local polynomial degree fixed to $p = 4$. Residual vector norm $\boldsymbol{e}_\gamma$ (right) between catenary and B-spline cable shows increase of residual error as number of segments increase; when $n_s \geq 10$ the residual error norm decreases and converges.

with only $n_s = 1$ segment is less flexible than its physical counterpart and behaves much more like a highly flexible beam. This evinces in the resulting sagging cable shape being rather parabolic than hyperbolic. We may equivalently infer this observation from approximation of natural frequencies since only the first two natural frequencies can be approximated by a one-segment cable (see Fig. 3.10).

With increasing number of segments, the residual error norm first increases, up until it reaches a maximum at $n_s = 10$ (in case of $p = 4$) and then converges toward an error of $e_\gamma \leq 0.020$ (see Fig. 3.16). Even with cables in cable robots being most often taut diagonally, since a horizontally tauten cable is both impracticable and technically difficult to achieve, a higher number of segments does show both more symmetric residual error over unstrained path coordinate, as well as better approximation of the maximum sag at $\xi = 0.5$. An increase in the number of segments from 1 to 20 drastically decreases the deviation between the catenary cable and the B-spline cable. With $n_s = 20$ segments, equivalent

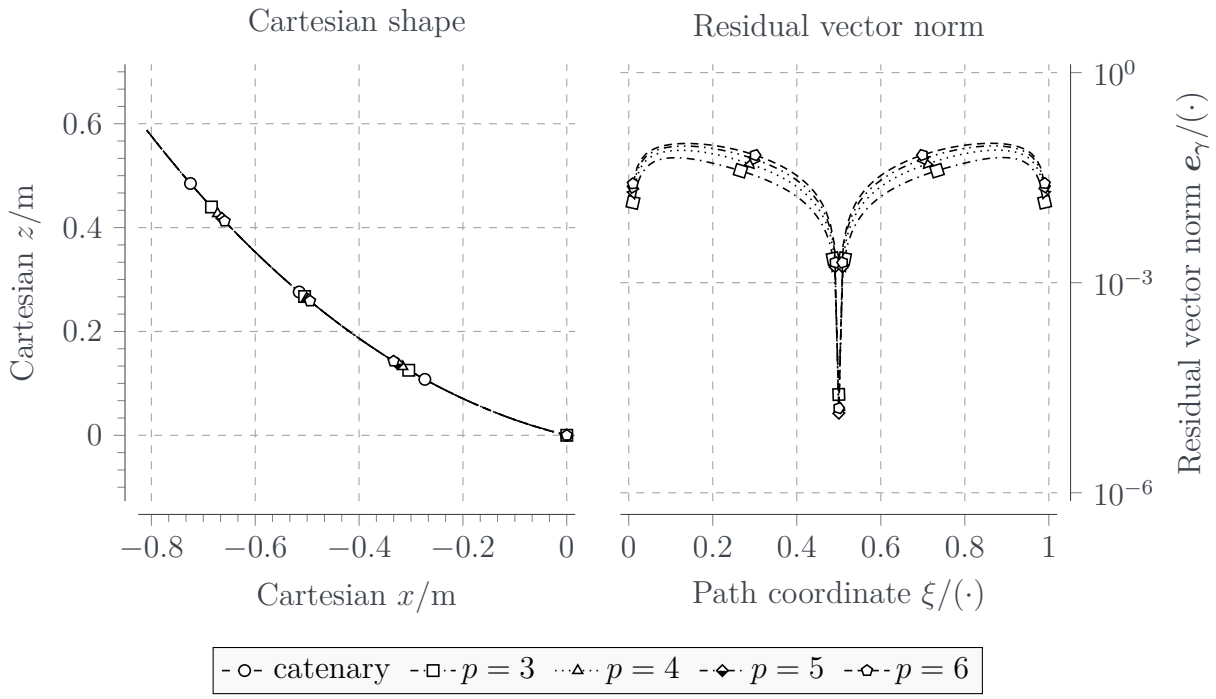

Figure 3.14: Static cable shape approximation of catenary solution (left) for cable spanned at $\beta_{k_2} = 144°$ with varying polynomial degree fixed $p \in \{3, 4, 5, 6\}$; number of segments in $n_\mathrm{s} = 10$; Residual vector norm $\boldsymbol{e}_\gamma$ (right) between catenary and B-spline cable shows nearly no difference between different local polynomial degree.

to a discretization of the cable into segments of length 5 cm, the approximation is lowest independent of the general cable direction.

Influence of local polynomial degree, however, is far less significant to the overall goodness of approximation. Figure 3.14 show the vectorial residual norm $\boldsymbol{e}_\gamma$ for a nearly diagonally spanned cable with number of segments fixed to $n_\mathrm{s} = 10$ and local polynomial degree varying in $p \in \{3, 4, 5, 6\}$. Each polynomial degree is capable of capturing well the maximum sag at $\xi = 0.5$ with the residual vector norm $\boldsymbol{e}_\gamma(\xi = 0.5) \in [239.015 \times 10^{-6}, 357.639 \times 10^{-6}]$. Result of the cable shape differs in particular for largely sagging cables i.e., with the unstrained cable length longer than the direct distance between proximal and distal point and a non-diagonally hanging cable, see e.g., Fig. 3.15 where the distal point is on the circumference of a circle with radius $0.800\, L_\mathrm{O}$. With few segments, a higher local polynomial degree p is necessary to approximate the sagging cable shape well, whereas cables with lower local polynomial degree p

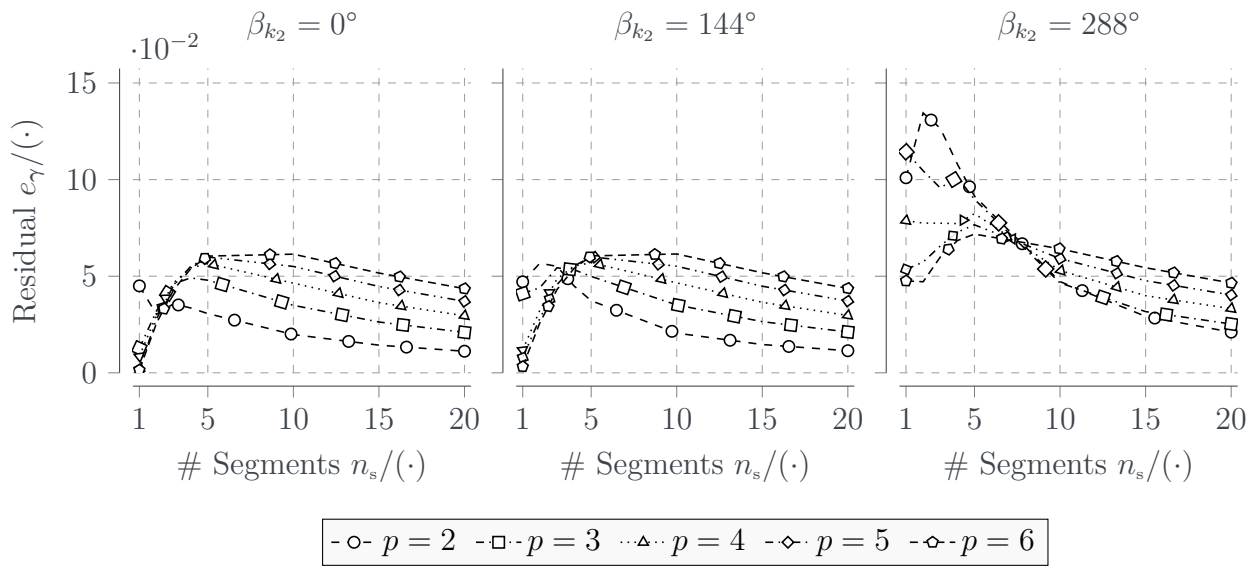

Figure 3.15: Evolution of the residual area norm $e_\gamma(n_s)$ as function of the number of segments for cable spanned at angles $\beta_{k_2} \in \{0, 144, 288\}°$ and radius $L_{k_1} = 0.800\, L_o$.

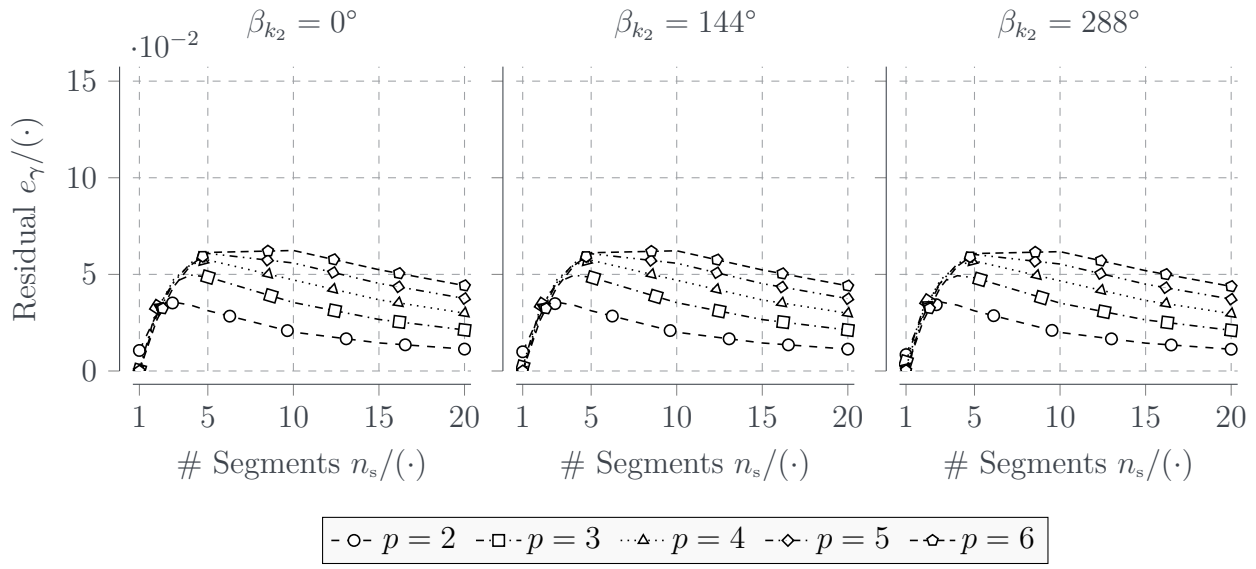

Figure 3.16: Evolution of residual area norm $e_\gamma(n_s)$ as function of the number of segments for cable spanned at angles $\beta_{k_2} \in \{0, 144, 288\}°$ and cable radius $L_{k_1} = 1\, L_o$.

show quicker convergence of the residual area norm as the number of segments increases.

Concluding, local polynomial degree p shows minor impact on the quality of approximating Irvine's cable model in various scenarios of different spanning angles as well as for various unstrained cable lengths as long as the number of segments is chosen to be $n_s \geq 10$. While a cable of local polynomial degree $p =$

2 shows the largest error, it is also not suitable for simulation of a spatial cable robots since its third derivative then contains discontinuities, which is in contradiction to the requirements posed in context with Eqs. (3.8) and (3.10)[22]. Focusing on the number of segments, a far more significant impact of the selected number on the quality of approximation is apparent—which is what was to be expected.

Much like in Section 3.1.1, the more segments we use for discretization, the better approximation of both natural frequencies as well as static shape is. However, in the former case, it comes at the cost of much higher computational expenses due to large dense mass matrices, while in the latter case there is no major numerical impact noticeable due to B-splines only local support of its segments. It may be favorable to set the number of segments to at least $n_\mathrm{s} = 10$, while $n_\mathrm{s} \geq 15$ shows even smaller residual vector norm and residual area norm in comparison to the Irvine cable model. Care needs to be taken in ultimate comparison of the two models (B-spline vs. Irvine) since the former includes bending stiffness, whereas the latter neglects this mechanical property. As such, it must not be possible to obtain a B-spline model that matches perfectly with the Irvine model.

3.9 Numerical Complexity

With the ultimate goal of finding a computationally efficient formulation for the dynamics of cable robots under consideration of the cable, numerical complexity of the derived cable model is of interest. Since in a combined cable robot simulation the mobile platform will be considered a rigid body with a maximum of six DOF, its complexity and cost is low and the major contribution to the overall complexity stems from the cable model. The focus for evaluating the

[22] It may be worth noting that planar cable robots do not require a parametric curve with continuous third-derivative since in the planar case, the cable does not exhibit torsion as per the Frenet-Serret formulation. In the spatial case, however, a $p = 2$ model is not suitable for lack of continuity of derivatives.

model's complexity will be on both the selected bases functions, as well as the entailed Gaussian quadrature used in computing the integral forces.

3.9.1 B-Splines

B-splines share the same weakness as Bézier curves in terms of numerical complexity when it comes to evaluating higher order polynomials. However, much to the disadvantage of Bézier curves, to approximate a complex shape, the number of control points and thus the number of bases functions does not have to increase. Due to the locality of the B-splines, we may subdivide the B-spline curve into more segments providing better control and approximation while keeping the numerical complexity of a single B-spline. The locality property of B-splines is advantageous for two reasons: 1) the recursion depth of the curve evaluation algorithm is very low thus evaluation is much quicker, and 2) numerical issues of too high polynomial degree causing double floating point precision issues are less likely to evolve. Further, when observing the full equations of motion of the spatial cable, B-spline ultimately require less DOFs than Bézier curves resulting in lower dimensional mass matrices that need to be evaluated or inverted, depending on whether explicit or implicit numerical integration schemes are used.

3.9.2 Gaussian Quadrature

One problem independent of the underlying selection of basis functions stems from numerically solving the integral forces and energies (see Eqs. (3.32) and (3.33), respectively) by means of quadrature. While Gaussian quadrature is defined such that it yields an exact result for polynomials of degree $p = 2\,n_{\mathrm{qp}} - 1$, this does not apply straightforward to the integrals needing solving. Closely inspecting the integrands of said integrals shows second powers and square roots, especially for the internal energies and forces. This does affect the cumulative polynomial degree, in particular the second powers lift the polynomial degree by

factor 2 which would then require $2\,p = 4\,n_{\mathrm{qp}} - 2$ quadrature points for evaluation. It can be shown when evaluating natural frequencies that higher order frequencies are more strongly overestimated when choosing fewer quadrature points. On the downside of choosing a higher number of quadrature points definitely lies the extra cost of evaluating the basis functions at these points. Ultimately, the degree of accuracy is in trade-off between the approximation quality, evaluation cost for numerical integration, and the tendency of over-estimating higher-order natural frequencies.

3.10 Conclusions

The cable model presented in this chapter based on the Cosserat-rod theory and discretized using B-splines renders itself a suitable formulation for cables as those used in cable robots. In the beginning of this chapter, we proclaimed wanting to find a cable model that captures the large signal response and neglects internal kinematics from fiber interaction. These two goals have been reached since the B-spline cable considers the cable a consistent i.e., full cross-section body and thus neglects intra-fiber dynamics. Further, it describes only the overall dynamics of cable motion in space while describing only strain and bending deformation on the material level due to mere necessity for mechanical consistency. While the fundamental elastica theory underlying the cable model has been known for more than a century and has been applied to the modeling and simulation of rods, fibers, and hair, its application to cable robots is new. Cosserat rod-based cables provide a more holistic formulation of the internal and external forces of the cable collected in a continuum model. Possible side effects of inaccuracy or artificial vibration as found in the finite element method are inherently avoided by means of this model.

B-spline cables have two independent parameters that affect their quality of approximation, one being the local polynomial degree p, the other being the number of segments n_{s}. As expected, local polynomial degree p has smaller impact on both the natural frequencies as well as the static cable shape than

does the number of segments n_s. It is insufficient to choose a cable with only one or two segments since the static catenary cable shape cannot be well approximated. Likewise, choosing an arbitrarily large number of segments yields a real continuum formulation for one thing, yet for another it does not provide better approximation of the static catenary shape. Concluding, while it is, to some extent, still a question of the specific use case, a cable model of local polynomial degree $p = 4$ suffices with a sufficiently large number of segments $n_s \geq 10$. The number of segments and local polynomial degree must not be determined by the number of natural frequencies to-be-approximated, but by the final use case with respect to how much cable sag is anticipated. Lastly, a B-spline cable of local polynomial degree $p = 4$ and $n_s = 3$ segments can suffice for cable robots like IPAnema Mini, whereas they are insufficient for large scale robots like Expo or CoGiRo (cf. Section 4.2).

The next steps toward further improving the spatial cable model given in this thesis would include physical damping and explicitly considering guiding and winding of the cable. While this may seem a simple and straightforward task, it requires not only integrating inequality constraints but also finding suitable numerical integration schemes for this task. Inequality constraints result from the cable being in one-sided contact with its surrounding such as e.g., on guiding pulleys or on the winch. With the cable wrapped around an object, it cannot penetrate through the surface, however, it may without loss of generality deflect from the surface and then be unconstrained again. Such problems are particularly involved to handle numerically, since the point in time of surface contact needs to be captured precisely in order to switch from unconstrained to constrained simulation i.e., from not-in-contact to an in-contact model description.

Chapter 4

Cable Robot Dynamics

The previously introduced and assessed cable model based on Cosserat rod theory will be incorporated into a cable robot simulation model. On the use case of two different cable robot configurations, we will present applicability of the cable models to simulation of the behavior of interest—transversal cable vibration. First, Section 4.1 introduces the multibody simulation framework for kinetostatics and dynamics analysis of cable robots as well as the numerical procedure of obtaining results. Following, Section 4.2 assesses numerical properties of the kinematic and kinetostatic solving of four different cable robots using the proposed simulation framework. Lastly, simulation results of the dynamics simulation of a spatial cable robot will be shown in Section 4.3 highlighting the oscillation of cables and platforms during a simple upward motion.

4.1 Multibody Cable Robot Formulation

Simulations carried out in this section require numerically solving equations of statics or numerically integrating equations of motion to obtain results. In order to accomplish this task, we propose a multibody simulation framework for solving of the statics and dynamics of cable robots. The challenging task in multibody simulation, in particular when dealing with kinematically redundant systems like cable robots with more cables than DOF of the mobile platform i.e., $m > n$, cf. Section 2.2.1, the kinematics and dynamics may not be simplified in terms of a small set of independent coordinates. While splitting coordinates

describing a multibody system into independent and dependent coordinates is a common task, it is not applicable to the cable robot framework presented in this thesis.

Let us assume a cable robot with a single platform of n DOF ($n \equiv 3$ in the planar case, $n \equiv 6$ in the spatial case) with its dynamics described in residual form[23]

$$\mathbb{0} = \boldsymbol{M}_{\mathrm{P}}(\boldsymbol{q}_{\mathrm{P}})\,\ddot{\boldsymbol{q}}_{\mathrm{P}} - \boldsymbol{f}_{\mathrm{ext,P}} + \boldsymbol{f}_{\mathrm{int,P}} + \mathrm{D}\,\boldsymbol{g}_{\mathrm{P}}^{\top}(\boldsymbol{q}_{\mathrm{P}}, t)\,\boldsymbol{\lambda}_{\mathrm{P}}\,, \tag{4.1a}$$

$$\mathbb{0} = \boldsymbol{g}_{\mathrm{P}}(\boldsymbol{q}_{\mathrm{P}}, t)\,, \tag{4.1b}$$

much like presented in Section 2.5 except free of any off-center point of reference i.e., the mass is concentrated at the platform's point of reference. In addition, the platform is subject to geometric constraints $\boldsymbol{g}_{\mathrm{P}}(\boldsymbol{q}_{\mathrm{P}}, t)$ following from it being linked to the cables at each of its l anchors such that

$$\boldsymbol{g}_{\mathrm{P}} = \left[\boldsymbol{g}_{\mathrm{P},1}^{\top},\ \ \boldsymbol{g}_{\mathrm{P},2}^{\top},\ \ \ldots\ \ \boldsymbol{g}_{\mathrm{P},l}^{\top},\right]^{\top}\,, \tag{4.2a}$$

$$\boldsymbol{g}_{\mathrm{P},i} = \boldsymbol{r}(\boldsymbol{q}_{\mathrm{P}}) + \boldsymbol{R}_{\mathrm{P}}(\boldsymbol{q}_{\mathrm{P}})\,\boldsymbol{b}_i - \boldsymbol{p}_i(t)\,. \tag{4.2b}$$

Each position constraint is of dimension $\boldsymbol{g}_{\mathrm{P},i} \in \mathbb{R}^{n_{\mathrm{dim}}}$ with $n_{\mathrm{dim}} \equiv 2$ in the planar, and $n_{\mathrm{dim}} \equiv 3$ in the spatial case. The total amount of nonlinear geometric constraints sums to $n_g = n_{\mathrm{dim}}\,m$. It can generally be assumed that the number of platform anchors matches the number of cables i.e., no two cables are attached to one point. While this is a mere assumption out of convenience, it does not limit applicability of the simulation framework presented.

Each of the m cables can similarly be described through its equations of motion following Eq. (3.32) reading

$$\mathbb{0} = \boldsymbol{M}_{\mathrm{C}_i}(\boldsymbol{q}_{\mathrm{C}_i})\,\ddot{\boldsymbol{q}}_{\mathrm{C}_i} - \boldsymbol{f}_{\mathrm{ext,C}_i} + \boldsymbol{f}_{\mathrm{int,C}_i} + \mathrm{D}\,\boldsymbol{g}_{\mathrm{C}_i}^{\top}(\boldsymbol{q}_{\mathrm{C}_i}, t)\,\boldsymbol{\lambda}_{\mathrm{C}_i}\,,$$

$$\mathbb{0} = \boldsymbol{g}_{\mathrm{C}_i}(\boldsymbol{q}_{\mathrm{C}_i}, t)\,.$$

[23] Explicit derivation of the equations of motion and the set of generalized coordinates follows in Section 4.1.2.1.

Cable constraints $\boldsymbol{g}_{\mathrm{C}_i}(\boldsymbol{q}_{\mathrm{C}_i}, t)$ result from requiring the proximal cable point be located at the frame anchor and the distal cable point be located at the platform anchor yielding

$$\begin{aligned}
\boldsymbol{g}_{\mathrm{C}_i} &= \left[\boldsymbol{g}_{\mathrm{C}_i,\mathrm{P}}^{\top},\ \ \boldsymbol{g}_{\mathrm{C}_i,\mathrm{D}}^{\top}\right]^{\top}, \\
\boldsymbol{g}_{\mathrm{C}_i,\mathrm{P}} &= \boldsymbol{\Pi}_{\mathrm{C}_i}(0)\,\boldsymbol{q}_{\mathrm{C}_i} - \boldsymbol{p}_{\mathrm{C}_i,\mathrm{P}}(t)\,, \\
\boldsymbol{g}_{\mathrm{C}_i,\mathrm{D}} &= \boldsymbol{\Pi}_{\mathrm{C}_i}(1)\,\boldsymbol{q}_{\mathrm{C}_i} - \boldsymbol{p}_{\mathrm{C}_i,\mathrm{D}}(t)\,.
\end{aligned}$$

The number of positions constraints for each cable sums up to $n_g = 2\,n_{\mathrm{dim}}$. In order to respect linking cables to winch and platform, we introduce the geometric constraints $\boldsymbol{g}_{\boldsymbol{a}_i}$ and $\boldsymbol{g}_{\boldsymbol{b}_i}$ given through

$$\boldsymbol{g}_{\boldsymbol{a}_i} = \boldsymbol{\Pi}_{\mathrm{C}_i}(0)\,\boldsymbol{q}_{\mathrm{C}_i} - \boldsymbol{a}_i\,, \tag{4.4a}$$

$$\boldsymbol{g}_{\boldsymbol{b}_i} = \boldsymbol{\Pi}_{\mathrm{C}_i}(1)\,\boldsymbol{q}_{\mathrm{C}_i} - (\boldsymbol{r} + \boldsymbol{R}_{\mathrm{P}}\,\boldsymbol{b}_i)\,. \tag{4.4b}$$

Positions constraints Eq. (4.4) define spatial constraints i.e., constraints on the $\hat{\boldsymbol{e}}_{\mathrm{x}}$, $\hat{\boldsymbol{e}}_{\mathrm{y}}$, and $\hat{\boldsymbol{e}}_{\mathrm{z}}$ component of the cable's proximal and distal point. While this may at first seem counterintuitive since cables physically constraint only in one direction—along the direction of its axis—this formulation does not change the physicality of the constraint as such. It merely provides separate constraint forces per spatial axis of $\mathbb{E}^3$ rather than one constraint force of the cable. Since constraints are incorporated into the multibody formulation by means of their Jacobian, both expressions are equivalent as the Jacobian—and thus directions of constraint forces—are equivalent.

Let the cable robot state vector $\boldsymbol{q}$ be obtained from concatenation of the platform state vector $\boldsymbol{q}_{\mathrm{P}}$ and all m cable state vectors $\boldsymbol{q}_{\mathrm{C}_i}$ holding[24]

$$\boldsymbol{q} = \left[\boldsymbol{q}_{\mathrm{P}}^{\top},\ \ \boldsymbol{q}_{\mathrm{C}_1}^{\top},\ \ \boldsymbol{q}_{\mathrm{C}_2}^{\top},\ \ \ldots\ \ \boldsymbol{q}_{\mathrm{C}_m}^{\top}\right]^{\top} = \left[\boldsymbol{q}_{\mathrm{P}}^{\top},\ \ \boldsymbol{q}_{\mathrm{C}}^{\top}\right]^{\top}.$$

[24] We shall omit any subscript index to our variables. If the reference is unambiguous, then we refer to the cable robot, otherwise $(\cdot)_{\mathrm{C}}$ refers to cable/cables and $(\cdot)_{\mathrm{P}}$ refers to the platform.

Noting that the constraints between platform and cable appear in pairs yielding the same constraint forces only in opposite directions, the Lagrange multipliers for these constraints must be the same. As such, we introduce the vector of Lagrange multipliers $\boldsymbol{\lambda}$ reading

$$\boldsymbol{\lambda} = \begin{bmatrix} \lambda_{\boldsymbol{a}_1}, & \lambda_{\boldsymbol{a}_2}, & \dots, & \lambda_{\boldsymbol{a}_m}, & \lambda_{\boldsymbol{b}_1}, & \lambda_{\boldsymbol{b}_2}, & \dots, & \lambda_{\boldsymbol{b}_m}, \end{bmatrix}^\top = \begin{bmatrix} \boldsymbol{\lambda}_{\boldsymbol{a}}^\top, & \boldsymbol{\lambda}_{\boldsymbol{b}}^\top \end{bmatrix}^\top ,$$

where $\lambda_{\boldsymbol{a}_i}$, $(i \in \{1, \dots, m\, n_{\mathrm{dim}}\})$, are constraint forces enforcing constraints at the cable proximal end, $\lambda_{\boldsymbol{b}_i}$, $(i \in \{1, \dots, m\, n_{\mathrm{dim}}\})$, are constraint forces enforcing constraints at the cable distal end i.e., link it to the platform. We can write the full cable robot system to read similarly

$$\begin{aligned} \mathbb{0} &= \boldsymbol{M}(\boldsymbol{q})\, \ddot{\boldsymbol{q}} - \boldsymbol{f}_{\mathrm{ext}}(\boldsymbol{q}, \dot{\boldsymbol{q}}) + \boldsymbol{f}_{\mathrm{int}}(\boldsymbol{q}, \dot{\boldsymbol{q}}) + \mathrm{D}\, \boldsymbol{g}^\top(\boldsymbol{q}, t)\, \boldsymbol{\lambda} \,, \\ \mathbb{0} &= \boldsymbol{g}(\boldsymbol{q}, t) \,, \end{aligned} \tag{4.5a}$$

where

$$\boldsymbol{M}(\boldsymbol{q}) = \mathrm{blockdiag}(\boldsymbol{M}_{\mathrm{P}}, \boldsymbol{M}_{\mathrm{C}_1}, \boldsymbol{M}_{\mathrm{C}_2}, \dots, \boldsymbol{M}_{\mathrm{C}_m}) \,, \tag{4.5b}$$

$$\boldsymbol{f}_{\mathrm{ext}}(\boldsymbol{q}) = \begin{bmatrix} \boldsymbol{f}_{\mathrm{ext,P}}^\top, \boldsymbol{f}_{\mathrm{ext,C}_1}^\top, \boldsymbol{f}_{\mathrm{ext,C}_2}^\top, \dots, \boldsymbol{f}_{\mathrm{ext,C}_m}^\top \end{bmatrix}^\top , \tag{4.5c}$$

$$\boldsymbol{f}_{\mathrm{int}}(\boldsymbol{q}) = \begin{bmatrix} \mathbb{0}, \boldsymbol{f}_{\mathrm{int,C}_1}^\top, \boldsymbol{f}_{\mathrm{int,C}_2}^\top, \dots, \boldsymbol{f}_{\mathrm{int,C}_m}^\top \end{bmatrix}^\top , \tag{4.5d}$$

$$\boldsymbol{g}(\boldsymbol{q}, t) = \begin{bmatrix} \boldsymbol{g}_{\boldsymbol{a}_i}^\top, \boldsymbol{g}_{\boldsymbol{b}_i}^\top \end{bmatrix}^\top , \tag{4.5e}$$

$$\boldsymbol{g}_{\boldsymbol{a}_i}(\boldsymbol{q}, t) = \begin{bmatrix} \boldsymbol{g}_{\mathrm{C}_1,\mathrm{P}}^\top, \boldsymbol{g}_{\mathrm{C}_2,\mathrm{P}}^\top, \dots, \boldsymbol{g}_{\mathrm{C}_m,\mathrm{P}}^\top \end{bmatrix}^\top , \tag{4.5f}$$

$$\boldsymbol{g}_{\boldsymbol{b}_i}(\boldsymbol{q}, t) = \begin{bmatrix} \boldsymbol{g}_{\boldsymbol{b}_1}^\top, \boldsymbol{g}_{\boldsymbol{b}_2}^\top, \dots, \boldsymbol{g}_{\boldsymbol{b}_m}^\top \end{bmatrix}^\top , \tag{4.5g}$$

$$\mathrm{D}\, \boldsymbol{g} = \begin{bmatrix} \mathbb{0} & \frac{\partial \boldsymbol{g}_{\boldsymbol{a}_i}}{\partial \boldsymbol{q}_{\mathrm{C}}} \\ \frac{\partial \boldsymbol{g}_{\boldsymbol{b}_i}}{\partial \boldsymbol{q}_{\mathrm{P}}} & \frac{\partial \boldsymbol{g}_{\boldsymbol{b}_i}}{\partial \boldsymbol{q}_{\mathrm{C}}} \end{bmatrix} , \tag{4.5h}$$

$$\frac{\partial \boldsymbol{g}_{\boldsymbol{a}_i}}{\partial \boldsymbol{q}_{\mathrm{C}_i}} = \begin{cases} \mathrm{D}\, \boldsymbol{g}_{\mathrm{C}_k} & i = k \,, \\ 0 & i \neq k \,, \end{cases} \tag{4.5i}$$

$$\frac{\partial \boldsymbol{g}_{\boldsymbol{b}_i}}{\partial \boldsymbol{q}_{\mathrm{P}}} = \mathrm{D}\, \boldsymbol{g}_{\mathrm{P}} \,, \tag{4.5j}$$

$$\frac{\partial \boldsymbol{g}_{\boldsymbol{b}_i}}{\partial \boldsymbol{q}_{\mathrm{C}_i}} = \begin{cases} -\mathrm{D}\, \boldsymbol{g}_{\mathrm{C}_k} & i = k \,, \\ 0 & i \neq k \,. \end{cases} \tag{4.5k}$$

Closely inspecting Eqs. (4.1) and (4.2) and comparing with Eq. (2.21), we observe the well-known structure matrix $\boldsymbol{A}^\top$ is expressed through the transposed constraint Jacobian $\mathrm{D}\boldsymbol{g}_\mathrm{P}^\top(\boldsymbol{q},t)$, whereas the cable forces are now expressed in terms of the constraint forces $\boldsymbol{\lambda_b}$. In particular, we can express the i-th cable force direction $\boldsymbol{u}_i$ in terms of the i-th cable shape $\boldsymbol{\gamma}_i(\xi,t)$, respectively its tangent, such that it reads

$$\boldsymbol{u}_i = -\frac{\boldsymbol{\gamma}'_i(\xi=1,t)}{\|\boldsymbol{\gamma}'_i(\xi=1,t)\|} = -\boldsymbol{\Pi}'_i(\xi=1)\,\boldsymbol{q}_{\mathrm{C},i}(t)\,,$$

yielding the structure matrix expressed through the Cosserat rod cable model

$$\boldsymbol{A}^\top = \begin{bmatrix} -\boldsymbol{\Pi}'_1\,\boldsymbol{q}_{\mathrm{C},1} & \dots & -\boldsymbol{\Pi}'_m\,\boldsymbol{q}_{\mathrm{C},m} \\ -\boldsymbol{b}_1 \times (\boldsymbol{\Pi}'_1\,\boldsymbol{q}_{\mathrm{C},1}) & \dots & -\boldsymbol{b}_m \times (\boldsymbol{\Pi}'_m\,\boldsymbol{q}_{\mathrm{C},m}) \end{bmatrix},$$

allowing us to analyze the platform motion in the static case.

4.1.1 Solving the Statics

Determining the solution to the static case of Eq. (4.5) at some time value t_0 implies solving the static[25] equilibrium state of the cable robot i.e., velocities $\dot{\boldsymbol{q}}$ and accelerations $\ddot{\boldsymbol{q}}$ are equal zero, thus all dynamic forces vanish and we obtain the simplified set of nonlinear equations

$$\mathbb{0} = -\boldsymbol{f}_\mathrm{ext}(\boldsymbol{q},t_0) + \boldsymbol{f}_\mathrm{int}(\boldsymbol{q},t_0) + \mathrm{D}\boldsymbol{g}^\top(\boldsymbol{q},t_0)\,\boldsymbol{\lambda}\,, \tag{4.6a}$$

$$\mathbb{0} = \boldsymbol{g}(\boldsymbol{q},t_0)\,, \tag{4.6b}$$

[25] We may alternatively also find the dynamic equilibrium solution in case the velocities and accelerations are unequal zero. The methods to solving the static equilibrium apply similarly to solving the dynamic equilibrium. However, the static equilibrium is of more interest to the analysis of cable robots.

or equivalently in full residual form

$$\mathbb{0} = \boldsymbol{e}(\boldsymbol{q}, \boldsymbol{\lambda}) = \begin{bmatrix} -\boldsymbol{f}_{\text{ext}}(\boldsymbol{q}, t_0) + \boldsymbol{f}_{\text{int}}(\boldsymbol{q}, t_0) + \mathrm{D}\,\boldsymbol{g}^{\top}(\boldsymbol{q}, t_0)\,\boldsymbol{\lambda} \\ \boldsymbol{g}(\boldsymbol{q}, t_0) \end{bmatrix}, \tag{4.6c}$$

to be solved concurrently for the unknown state $\boldsymbol{q}$ and unknown constraint forces $\boldsymbol{\lambda}$. Denoting the vector of sought-for variables $\boldsymbol{x} \coloneqq [\boldsymbol{q}^{\top}, \boldsymbol{\lambda}^{\top}]^{\top}$, we are looking for the solution $\boldsymbol{x}^* = \left[\boldsymbol{q}^{*\top}, \boldsymbol{\lambda}^{*\top}\right]^{\top}$ to the root-finding problem of Eq. (4.6) satisfying $\boldsymbol{e}(\boldsymbol{x}^*) \equiv \mathbb{0}$.

Literature provides a wide variety of different methods for solving root-finding problems of underdetermined, overdetermined, or constrained systems (see Appendix E for an overview of root-finding algorithms), with the most common and simple method being *Newton's method*, or its extension *Damped Newton's method*, sometimes referred to as *Softened Newton's method*. Since Newton's method is an iterative solution finding algorithm, it requires calculating the k-th iteration step $\Delta\boldsymbol{x}_k$ such that $\boldsymbol{x}_{k+1}$ is closer to the analytical residual $\boldsymbol{x}^*$ than $\boldsymbol{x}_k$ is. In Newton's method, the k-th iteration step $\Delta\boldsymbol{x}_k$ is calculated from

$$\Delta\boldsymbol{x}_k = -(\mathrm{D}_{\boldsymbol{x}}\,\boldsymbol{e})^{-1}(\boldsymbol{x}_k)\,\boldsymbol{e}(\boldsymbol{x}_k)\,,$$

where

$$\mathrm{D}_{\boldsymbol{x}}\,\boldsymbol{e}(\boldsymbol{x}_k) = \left.\frac{\partial \boldsymbol{e}(\boldsymbol{x})}{\partial \boldsymbol{x}}\right|_{\boldsymbol{x}=\boldsymbol{x}_k}$$

such that the iteration rule reads

$$\boldsymbol{x}_{k+1} = \boldsymbol{x}_k + \Delta\boldsymbol{x}_k\,.$$

In particular, the iteration matrix $\mathrm{D}_{\boldsymbol{x}}\,\boldsymbol{e}(\boldsymbol{x}_k)$ reads

$$\mathrm{D}_{\boldsymbol{x}}\,\boldsymbol{e}(\boldsymbol{x}_k) = \begin{bmatrix} -\frac{\partial \boldsymbol{f}_{\text{ext}}}{\partial \boldsymbol{q}} + \frac{\partial \boldsymbol{f}_{\text{int}}}{\partial \boldsymbol{q}} + \sum\limits_{k=1}^{n_g} \boldsymbol{\lambda}_k \frac{\partial^2 \boldsymbol{g}_k}{\partial \boldsymbol{q}^2} & \mathrm{D}\,\boldsymbol{g}^{\top} \\ \mathrm{D}\,\boldsymbol{g} & \mathbb{0} \end{bmatrix}.$$

Table 4.1: Solver parameters for solving kinematic and kinetostatic equilibria.

Property	Parameter	Value	Unit
Maximum iterations	$k_{\max}$	500	—
Residual threshold	ϵ_e	5×10^{-9}	—
Stepsize threshold	$\epsilon_{\Delta x}$	1×10^{-12}	—
Machine constant	$\varepsilon_{\text{mach}}$	2.22×10^{-16}	—

Due to numerical rounding precision, the value of the analytical residual value $\boldsymbol{x}^*$ of Eq. (4.6c) cannot be calculated, thus a measure of "being close to $\boldsymbol{x}^*$" must be introduced. According to Newton's method, being close to the residual occurs if either 1) the residual $\boldsymbol{e}(\boldsymbol{x}_k)$ is sufficiently small, or 2) the step size $\Delta\boldsymbol{x}_k$ is sufficiently small. Sufficiently small translates to the residual or step size norm being smaller than a user-defined threshold such that the termination conditions of Newton's method read

$$\begin{aligned} \|\boldsymbol{e}(\boldsymbol{x}_k)\| &\leq \epsilon_e \,, \\ \|\Delta\boldsymbol{x}_k\| &\leq \epsilon_{\Delta\boldsymbol{x}} \,. \end{aligned}$$

The value of residual and step-size threshold ϵ_e and $\epsilon_{\Delta\boldsymbol{x}}$, respectively, must be determined manually and should also account for any numerical round off issues (values we chose can be found in Table 4.1).

4.1.2 Solving the Dynamics

The dynamic solution to Eq. (4.5) may be obtained similarly to the static solution taking into account to solve for the unknown accelerations $\ddot{\boldsymbol{q}}$ and constraint forces $\boldsymbol{\lambda}$. However, since the formulation of the dynamics equation reads

$$\mathbb{0} = \boldsymbol{M}(\boldsymbol{q})\,\ddot{\boldsymbol{q}} - \boldsymbol{f}_{\text{ext}}(\boldsymbol{q},\dot{\boldsymbol{q}}) + \boldsymbol{f}_{\text{int}}(\boldsymbol{q},\dot{\boldsymbol{q}}) + \mathrm{D}\,\boldsymbol{g}^{\top}(\boldsymbol{q},t)\,\boldsymbol{\lambda}\,, \tag{4.7a}$$

$$\mathbb{0} = \boldsymbol{g}(\boldsymbol{q},t)\,, \tag{4.7b}$$

we have to deal with a system of differential-algebraic equations (DAEs) that are ordinary differential equations (ODEs) in the state of generalized coordinates $\langle \boldsymbol{q}; \dot{\boldsymbol{q}}; \ddot{\boldsymbol{q}} \rangle$ and algebraic equations in the generalized positions $\boldsymbol{q}$.

Obtaining the solution to Eq. (4.7) is an involved task, since simple forward-in-time integration is inapplicable as the transient state may violate constraints. Especially in the case of multibody simulations with rigid and flexible bodies, this is a challenge as the coupled nature of dynamics results in differential equations with a high ratio of stiffness[26] requiring explicit ODE-solvers to proceed with small integration time steps (Arnold 2004). This is apparent in explicit forward-in-time integration schemes such as Euler's method or higher-order extensions such as Runge-Kutta or Adams-Bashforth-Moulton. Commercially available solvers for ODEs out of the box integrate a first-order differential equation of nonlinear form $\dot{\boldsymbol{y}} = f(\boldsymbol{y}, t)$ or linear form $\dot{\boldsymbol{y}} = \boldsymbol{A}\,\boldsymbol{y} + \boldsymbol{B}\,\boldsymbol{u}$ by means of a Taylor series of the transient state at the next time step (Stoer et al. 2002). Since this Taylor series is based on the integration step size, a rapid transient state leads to large errors in the ODE's Taylor approximation, thus requiring the solver to reduce the step size, which results in either slow time integration or in failure of meeting integration tolerances.

Besides this numerical burden, commercially available ODE solvers are unaware of the underlying structure of nature of the system-to-integrate. While any higher order system can be easily transformed into a system of first-order ODEs, it removes the physical meaning of states and their inherent connection. Looking at a dynamic system from Hamiltonian mechanics, a system's velocities are the cotangents to its positions, as such they are inherently linked through their conjugate momentums (Ardema 2005). When using a first-order ODE solver on such systems, which treats the transient changes of positions and velocities independent of each other thus ignoring their physical meaning and

[26] The stiffness ratio is defined as the ratio between the real parts of the largest and smallest eigenvalue of a linear constant coefficient inhomogeneous system. In other words, it describes the ratio between the fastest transient and the slowest transient. The ratio is mathematically expressed as $|\mathrm{Re}(\overline{\lambda})|/|\mathrm{Re}(\underline{\lambda})|$ (Lambert 1991).

connection, the transient states are merely integrated over time, and constraint violation is unavoidable[27].

To the rescue in finding numerical solutions to the FDP of the presented cable robot multibody simulation comes a different type of integration schemes. The integration schemes of interest are mechanical-based integrators or Hamiltonian-based integrators (see Appendix F). In particular, we implement Betsch energy-consistent mechanical integrator for mechanical systems with mixed holonomic and and nonholonomic constraints (Betsch 2005; Betsch 2006). We briefly present the iterative integration scheme for better understanding of the implied simplicity of the multibody formulation, its derivation and properties can be found in Appendix F.2.2.

Let us assume our mechanical system to be subject to holonomic and non-holonomic constraints given by the DAE

$$\boldsymbol{M}(\boldsymbol{q})\,\ddot{\boldsymbol{q}} + \mathrm{D}\,U(\boldsymbol{q})^{\top} = \mathrm{D}\,\boldsymbol{g}^{\top}(\boldsymbol{q})\,\boldsymbol{\lambda}\,, \tag{4.8a}$$

$$\mathbb{0} = \boldsymbol{g}(\boldsymbol{q})\,, \tag{4.8b}$$

where $\mathrm{D}\,U = \frac{\partial U}{\partial \boldsymbol{q}}$ are forces derived from their potential energy formulation. For the equation of motion given in Eq. (4.7) follows

$$\mathrm{D}\,U = \boldsymbol{f}_{\mathrm{int}} - \boldsymbol{f}_{\mathrm{ext}}\,.$$

The conserving scheme over a time interval $T_k = [t_k, t_{k+1}]$ at time t_k with states $\langle \boldsymbol{q}_k; \boldsymbol{v}_k \rangle$ given and unknowns $\langle \boldsymbol{q}_{k+1}; \boldsymbol{v}_{k+1} \rangle$ reads

$$\boldsymbol{q}_{k+1} - \boldsymbol{q}_k = \frac{h}{2}\,(\boldsymbol{v}_k + \boldsymbol{v}_{k+1}) \tag{4.9a}$$

$$\boldsymbol{M}\,(\boldsymbol{v}_{k+1} - \boldsymbol{v}_k) = -h\,\overline{\nabla} U(\boldsymbol{q}_k, \boldsymbol{q}_{k+1}) + h\,\overline{\nabla}\boldsymbol{g}(\boldsymbol{q}_k, \boldsymbol{q}_{k+1})^{\top}\,\bar{\boldsymbol{\lambda}}\,, \tag{4.9b}$$

$$\boldsymbol{g}(\boldsymbol{q}_{k+1}) = \mathbb{0}\,, \tag{4.9c}$$

[27] This is but one reason for the introduction of constraint violation handling methods such as commonly used Baumgarte stabilization (Baumgarte 1972).

Table 4.2: Solver parameters for solving forward dynamics equilibria.

Property	Parameter	Value	Unit
Maximum iterations	$k_{\max}$	100	–
Residual threshold	ϵ_e	5×10^{-9}	–
Stepsize threshold	$\epsilon_{\Delta x}$	1×10^{-12}	–
Time step size	h	1×10^{-3}	s
Machine constant	$\varepsilon_{\text{mach}}$	2.22×10^{-16}	—

for which the generally time-dependent constraint forces $\boldsymbol{\lambda}(t)$, $\boldsymbol{\mu}(t)$ are substituted by constant approximations $\bar{\boldsymbol{\lambda}}$ and $\bar{\boldsymbol{\mu}}$, respectively. Equation (4.9) can be rewritten in vectorial form yielding the set of nonlinear equations in $\boldsymbol{q}_{k+1}$ and $\boldsymbol{\lambda}_{k+1}$ which can again be solved using a root-finding algorithm like Newton's method with appropriate termination thresholds on the residual and step size (values found suitable for the cable robot simulation framework presented in this thesis can be found in Table 4.2).

Despite Eq. (4.9) being a nonlinear, implicit equation in $\langle \boldsymbol{q}_{k+1}; \boldsymbol{\lambda}_{k+1} \rangle$, its beauty lies in it being a single equation that can be iteratively solved for the solution of the dynamics in the next time step by also ensuring satisfying the constraints. The iterative scheme does not suffer from numerical instabilities as explicit Newton-Euler methods do, and additionally satisfies energy conservation i.e., neither the discrete equations of motion nor the iteration scheme add or remove energy from the system.

4.1.2.1 Platform Kinematics

Let the mobile platform be mechanically parametrized by linear inertia matrix $\boldsymbol{M}_{\text{P}} = m_{\text{P}}\, \mathbb{1}_3$ and rotational inertia matrix $\boldsymbol{J}_{\text{P}} = \text{diag}(J_{xx}, J_{yy}, J_{zz})$[28]. The platform's state is defined by the generalized coordinates $\boldsymbol{q}_{\text{P}} = [x, y, z, \phi, \theta, \psi]^\top$

[28] Explicit parameters for the test case cable robots are given in Appendix A.

following the equations of motion

$$\begin{bmatrix} \boldsymbol{M}_{\mathrm{P}} & \mathbb{0} \\ \mathbb{0} & \boldsymbol{R}_{\mathrm{P}}\,\boldsymbol{J}_{\mathrm{P}}\,\boldsymbol{R}_{\mathrm{P}}^{\top} \end{bmatrix} \ddot{\boldsymbol{q}}_{\mathrm{P}} = \boldsymbol{f}_{\mathrm{P,G}} + \mathrm{D}\,\boldsymbol{g}_{\mathrm{P}}^{\top}(\boldsymbol{q},t)\,,$$
$$\mathbb{0} = \boldsymbol{g}_{\mathrm{P}}(\boldsymbol{q},t)\,,$$

with gravitational force vector $\boldsymbol{f}_{\mathrm{P,G}}$, the constraints $\boldsymbol{g}_{\mathrm{P}}(\boldsymbol{q},t)$ as given in Eq. (4.2), and the rotation matrix $\boldsymbol{R}_{\mathrm{P}}$ given through Tait-Bryan angles $\langle\phi;\theta;\psi\rangle$. We choose $m = 8$ cables.

4.1.2.2 Cable Kinematics

In Section 3.5.1, we derived the equation of motion for a single cable under the consideration of time-varying length. By applying the integral transformation from time-varying interval $[0, L]$ to $[0, 1]$, we obtain the first and second derivative of cable length L with respect to time t. For numerical evaluation of the dynamic response of the cable robot, we thus require calculating not only desired cable lengths along a spatial trajectory, but also their derivatives. To simplify calculations but also to highlight the effect of using standard inverse kinematics for control with elastic and flexible cables of time-varying length, we use the solution to the standard IKP. The i-th cable's length is calculated from

$$L_i = \|\boldsymbol{l}_i\| = \sqrt{\boldsymbol{l}_i \bullet \boldsymbol{l}_i}\,,$$

resulting in

$$\dot{L}_i = \frac{\mathrm{d}L_i}{\mathrm{d}t} = \frac{1}{\sqrt{\boldsymbol{l}_i \bullet \boldsymbol{l}_i}}\left(\boldsymbol{l}_i \bullet \dot{\boldsymbol{l}}_i\right),$$
$$\ddot{L}_i = \frac{\mathrm{d}^2L_i}{\mathrm{d}t^2} = \frac{\boldsymbol{l}_i \bullet \boldsymbol{l}_i}{\sqrt{\boldsymbol{l}_i \bullet \boldsymbol{l}_i}^3}\left(\boldsymbol{l}_i \bullet \dot{\boldsymbol{l}}_i\right) + \frac{1}{\sqrt{\boldsymbol{l}_i \bullet \boldsymbol{l}_i}}\left(\dot{\boldsymbol{l}}_i \bullet \dot{\boldsymbol{l}}_i + \boldsymbol{l}_i \bullet \ddot{\boldsymbol{l}}_i\right),$$

where

$$\boldsymbol{l}_i = \boldsymbol{a}_i - (\boldsymbol{r} + \boldsymbol{R}_{\mathrm{P}}\,\boldsymbol{b}_i)\,,$$
$$\dot{\boldsymbol{l}}_i = -\left(\dot{\boldsymbol{r}} + \dot{\boldsymbol{R}}_{\mathrm{P}}\,\boldsymbol{b}_i\right),$$

$$\ddot{\boldsymbol{l}}_i = -\left(\ddot{\boldsymbol{r}} + \ddot{\boldsymbol{R}}_{\mathrm{P}}\, \boldsymbol{b}_i\right)$$

and

$$\dot{\boldsymbol{R}}_{\mathrm{P}} = [\boldsymbol{\omega}]_\times\, \boldsymbol{R}_{\mathrm{P}}\,,$$
$$\ddot{\boldsymbol{R}}_{\mathrm{P}} = [\boldsymbol{\alpha}]_\times\, \boldsymbol{R}_{\mathrm{P}} + [\boldsymbol{\omega}]_\times\, [\boldsymbol{\omega}]_\times\, \boldsymbol{R}_{\mathrm{P}}\,.$$

4.2 Statics

Before presenting results of forward dynamics simulation, we shift our interest to the solution of statics and kinetostatics. The main difference between statics and kinetostatics lies in the latter not neglecting the force equilibrium of the platform and the cables, but also respecting the strain induced cable elongation. In case of the static solution, we determine the unstrained cable lengths $\boldsymbol{L}_{\mathrm{O}}$ given the cable robot home pose $\hat{\boldsymbol{y}}^* = \langle \boldsymbol{r}^*; \boldsymbol{R}_{\mathrm{P}}^* \rangle$ defined through

$$\boldsymbol{r}^* = \begin{bmatrix} 0 \\ 0 \\ 0 \end{bmatrix}, \qquad \boldsymbol{R}_{\mathrm{P}}^* = \begin{bmatrix} 1 & 0 & 0 \\ 0 & 1 & 0 \\ 0 & 0 & 1 \end{bmatrix},$$

using standard inverse kinematics formulation from Section 2.3.1.1. This procedure will inevitably lead to platform deflection due to cable elongation and bending, which is what we want to provoke with this analysis.

For the kinetostatic analysis, we determine the unstrained cable length for the same cable robot home pose, yet in ways that the platform may not deflect from its home pose. Internally, we solve the kinetostatic problem from Section 2.4 with the goal of minimizing unstrained cable lengths L_{O}, while respecting lower cable force limits $\boldsymbol{f}_-$ and upper cable force limits $\boldsymbol{f}_+$, in order to yield values comparable to other methods of determining cable force distributions. We define our kinetostatic problem over the optimization vector of cable lengths $\boldsymbol{x} \coloneqq \boldsymbol{L}$ as

$$\min_{\boldsymbol{x}} \|\boldsymbol{x}\| \tag{4.10a}$$

$$\text{subject to} \qquad \mathbb{0} = -\boldsymbol{f}_{\text{ext}}(\boldsymbol{q}(\boldsymbol{x}), t_0) + \boldsymbol{f}_{\text{int}}(\boldsymbol{q}(\boldsymbol{x}), t_0) + \cdots \tag{4.10b}$$

$$+ \mathrm{D}\boldsymbol{g}^{\top}(\boldsymbol{q}(\boldsymbol{x}), t_0)\,\boldsymbol{\lambda}\,, \tag{4.10c}$$

$$\mathbb{0} = \boldsymbol{g}(\boldsymbol{q}(\boldsymbol{x}), t_0)\,, \tag{4.10d}$$

$$\mathbb{0} = \boldsymbol{r}^* - \boldsymbol{r}(\boldsymbol{x})\,, \tag{4.10e}$$

$$\mathbb{0} = \boldsymbol{R}_{\text{P}}^* - \boldsymbol{R}_{\text{P}}(\boldsymbol{x})\,, \tag{4.10f}$$

$$\boldsymbol{f}_- \leq \boldsymbol{f}(\boldsymbol{x})\,, \tag{4.10g}$$

$$\boldsymbol{f}(\boldsymbol{x}) \leq \boldsymbol{f}_+\,, \tag{4.10h}$$

where $\boldsymbol{q}(\boldsymbol{x})$ are the generalized coordinates of the cable robot confining with the static equilibrium for the given cable lengths and $\boldsymbol{f}(\boldsymbol{x})$ are the cable forces obtained from the respective constraint forces of the static equilibrium. In the end, we obtain unstrained cable lengths that satisfy a kinetostatic equilibrium for the desired home pose under the given cable force limits. We may introduce additional constraints in or different constraints on the minimization problem like minimizing the L^p norm of total cable tension or relative cable tensions (Gosselin et al. 2011; Borgstrom et al. 2009).

Examples of kinematic and kinetostatic solving will comprise cable robots a) CoGiRo in Section 4.2.1, b) Expo in Section 4.2.2, c) IPAnema Mini in Section 4.2.3, and d) IPAnema 3 in Section 4.2.4. Results of each cable robot will be presented in the respective section, while a summary of applicability of the framework will be drawn at the very end of this section.

4.2.1 CoGiRo

Robot configuration for CoGiRo can be found in Tables A.1 to A.3. Cable force limits are defined to be $\boldsymbol{f} \in [0, 5000]\,\text{N}$.

Kinematic Case

In the kinematic case, CoGiRo's mobile platform deflects from its desired home pose by $\Delta x = 7.860\,\text{mm}$, $\Delta y = 8.390\,\text{mm}$, and $\Delta z = 272.080\,\text{mm}$ which

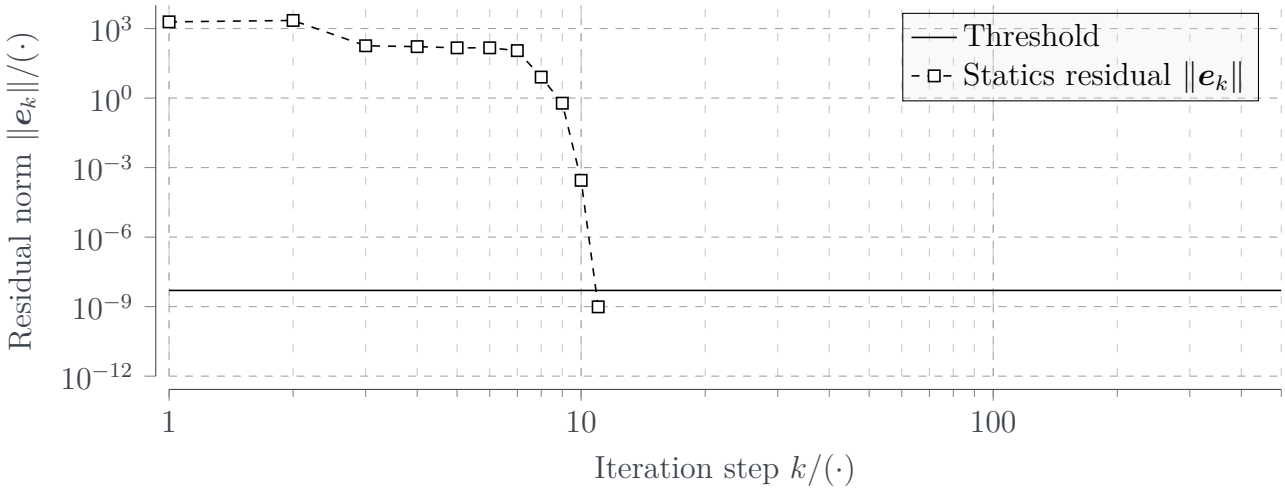

Figure 4.1: Progression of residual norm $\|\boldsymbol{e}_k\|$ over iteration solving the kinematic equilibrium case for CoGiRo.

is a noticeable deviation from the zero-pose. This deviation is to be expected due to steel cables being employed on CoGiRo with high stiffness. Further, despite steel cables being comparatively heavy, no further vertical deflection of the mobile platform is implied as there are no cables dragging down on the platform as CoGiRo is in a suspended configuration. As such, the mobile platform's weight is the only mass producing a downward drag. Lastly, fairly no cable sag can be concluded from the numerical results, which confines partially with observations made on CoGiRo. As pointed out by Gagliardini et al., visible cable sag emerges on the robot which cannot be compensated for by tightening the cables due to the suspended nature of CoGiRo (Collard et al. 2011; Sandretto et al. 2013; Gagliardini et al. 2014).

From a numerical perspective, with a well pre-conditioned simulation, the solution is obtained within $k = 11$ steps (see Fig. 4.1) with initially slow rate of convergence—resulting from the constraint forces being initialized with zero and only slowly converging toward the final value—yet later, once constraint forces are obtained, termination occurs after four more steps. Even with a numerically ill-conditioned system such as CoGiRo due to its wide range of numerical stiffnesses stemming from the high mass of cables and their high modulus of elasticity versus the low platform mass, the cable robot framework

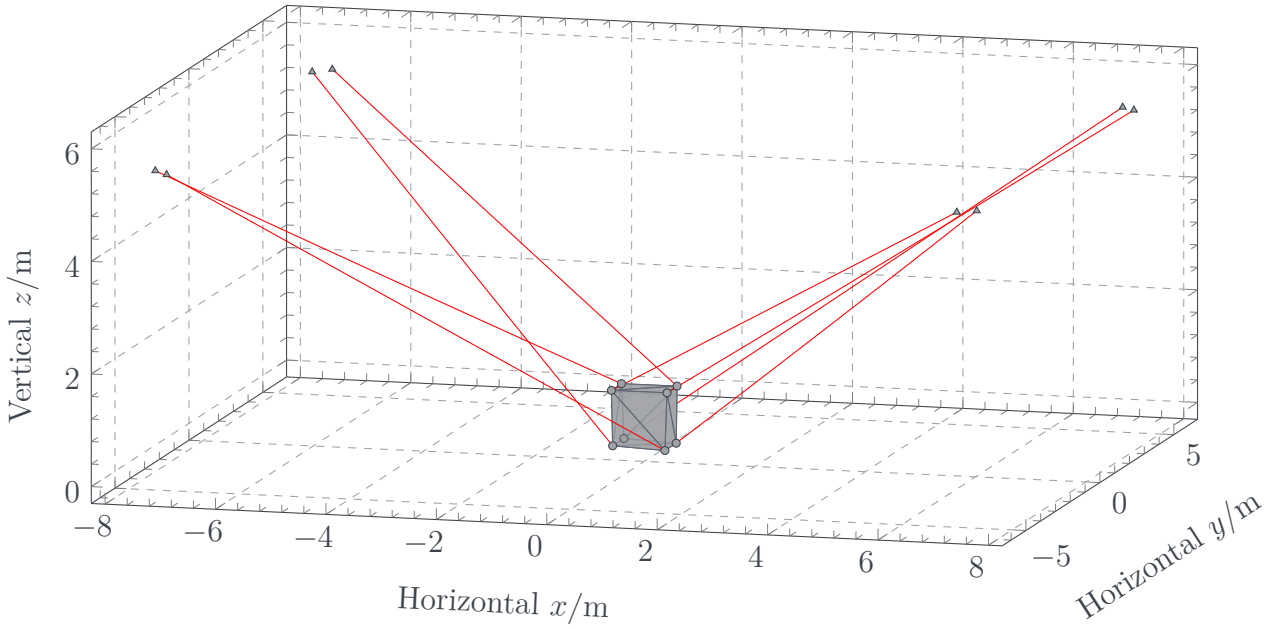

Figure 4.2: Static solution to the kinetostatically solved cable robot CoGiRo. Cable sag is negligible for the robot is suspended and thus all cables are strained no matter the platform pose.

is well capable of handling even suspended cable robots inherently, without requiring specific treatment of their special configuration.

Kinetostatic Case

Kinetostatically solving CoGiRo, the mobile platform deflects from its desired home pose by only $\Delta x = -0.032\,\text{mm}$, $\Delta y = 0.019\,\text{mm}$, and $\Delta z = -1.425\,\text{mm}$, which is a smaller deviation than a purely kinematically solved CoGiRo (see also Fig. 4.2). Horizontal deviations Δx and Δy result from marginally asymmetric frame design (see Table A.1). Since CoGiRo is a suspended cable robot, there exists only one valid force distribution for a given pose since the cable forces must balance the external wrench at the pose. Any increase or decrease of the inner level of pre-tension—or likewise an increase or decrease in stiffness—is not possible without deflecting from the desired position. For CoGiRo, we can however observe the effect of hefty cables not only by the amount of sagging of each cable, but also by the induced deflection from the desired position and the actual position when determining cable lengths purely based on the standard

Table 4.3: Comparison of cable lengths (a) and cable forces (b) of kinematic $(\cdot)_{\mathrm{km}}$ and kinetostatic $(\cdot)_{\mathrm{ks}}$ solution for CoGiRo's home pose.

Cable	$L_{i,\mathrm{km}}$/m	$L_{i,\mathrm{ks}}$/m	Δ_i/m
1	10.18	10.17	−0.01
2	9.90	9.90	−0.00
3	10.24	10.23	−0.01
4	9.91	9.91	−0.00
5	10.33	10.33	−0.00
6	10.62	10.61	−0.01
7	10.38	10.38	−0.00
8	10.62	10.62	−0.01

(a) *Cable lengths $L_{i,(\cdot)}$ and differences $\Delta_i = L_{i,ks} - L_{i,km}$.*

Cable	$f_{i,\mathrm{km}}$/N	$f_{i,\mathrm{ks}}$/N	Δf_i/N	$f_{i,\sim}$/N
1	430.9	227.3	−203.6	373.6
2	68.4	241.0	172.6	392.1
3	427.4	222.1	−205.2	358.8
4	63.5	236.5	172.9	386.8
5	67.8	240.5	172.7	82.0
6	381.7	224.6	−157.1	82.3
7	65.8	239.6	173.8	90.2
8	382.1	224.6	−157.5	83.7

(b) *Cable forces $f_{i,(\cdot)}$ and differences $\Delta f_i = f_{i,ks} - f_{i,km}$*

kinematics model (see Section 2.3.1.1). Large discrepancy of force distribution from Pott's advanced closed form and the results given in Table 4.3(b) are due to the fact that the former algorithm is suitable for only kinematically solving the force distribution but not kinetostatically. Cable robot configurations like CoGiRo, however, can only be balanced kinetostatically.

Table 4.3 shows comparison of cable lengths obtained for the kinematic and kinetostatic problem of CoGiRo (Table 4.3(a)) and of cable forces at home pose (Table 4.3(b)). As we expect, negative cable length changes of all cables result from the kinetostatic problem, in order to attain the desired pose and reduce position deviation to a minimum. However, cable length change is not equal over all cables due to the asymmetric design of CoGiRo. Cable forces on the other hand change in both positive and negative direction, despite all cables being extended. Most notably is the tendency of all cable forces being close to their mean value as the platform design in itself is nearly symmetric (see Table A.1). Previous large differences in cable forces apparently result in the observed kinematic platform deviation. We can further see the cable forces determined through the kinetostatic problem solving lie within reason with cable forces determined through the advanced closed form force distribution algorithm introduced in Section 2.6. Obvious discrepancy results

from the force distribution algorithm calculating only cable forces rather than also minimizing unstrained cable length as the case study does (see Eq. (4.10)).

4.2.2 Expo

Robot configuration for Expo can be found in Tables A.9 to A.11. Cable force limits are defined to be $\boldsymbol{f} \in [200, 2400]\,\mathrm{N}$.

Kinematic Case

Expo cable robots are very similar to CoGiRo in that they both are suspended cable robots, however, CoGiRo has a particular layout of connecting cables to the platform[29]. Still, the deflection of the kinematically solved problem for Expo cable robot is noticeable with $\Delta x = 0.364\,\mathrm{mm}$, $\Delta y = -18.890\,\mathrm{mm}$, and $\Delta z = -12.785\,\mathrm{mm}$, and no cable sag emerges. Since Expo cable robots also use steel cables (with a copper core to transmit electrical power to the platform), drag of the cables on the platform is inevitable. This cable drag results in the positive displacement of the platform in the kinematic case—Expo's frame design is asymmetric about the $\hat{\boldsymbol{e}}_{\mathrm{y}}$-axis, yet is symmetrical and trapezoidal about the $\hat{\boldsymbol{e}}_{\mathrm{x}}$-axis (see Table A.9).

Numerically solving the kinematics problem of Expo cable robots is similarly quick as for CoGiRo since both robots share similar frame and platform dimensions, much like inertia parameters of the platform and mechanical cable properties (see Fig. 4.3 and Tables A.10 and A.11). Further speed improvements may only be achieved by initializing the constraint forces on the platform and cable proximal and distal ends by means of compensating for the gravitational forces acting on the platform.

[29] Surprisingly, this so-called CoGiRo-design makes it the only cable robot with a range of rotation about the vertical axis of approximately $\psi \in [-50, 50]\,^\circ$ (Gouttefarde et al. 2007).

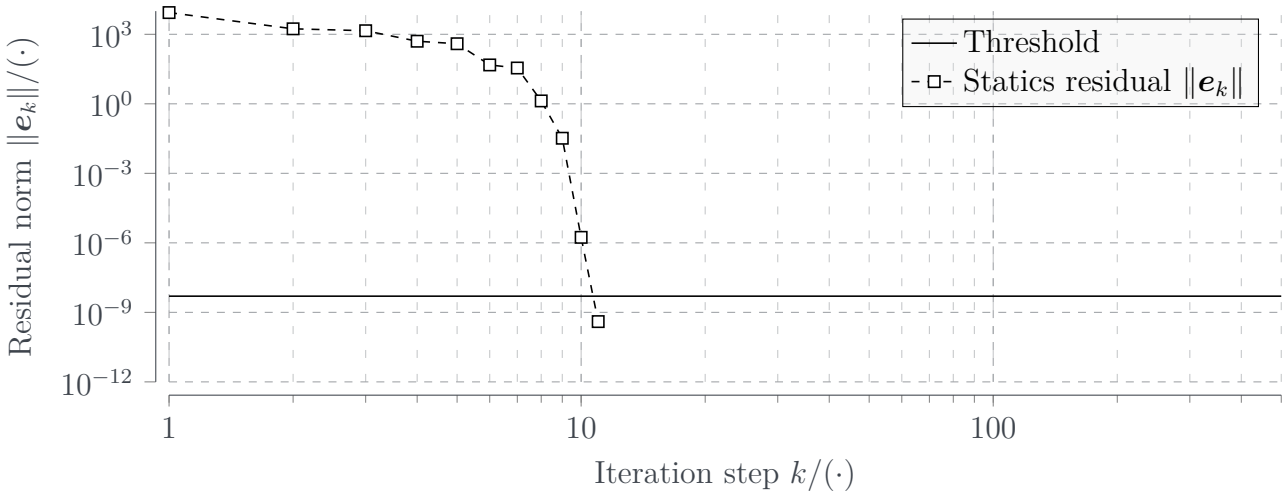

Figure 4.3: Decay of residual norm $\|e_k\|$ during iteration solving the kinematic equilibrium case for EXPO.

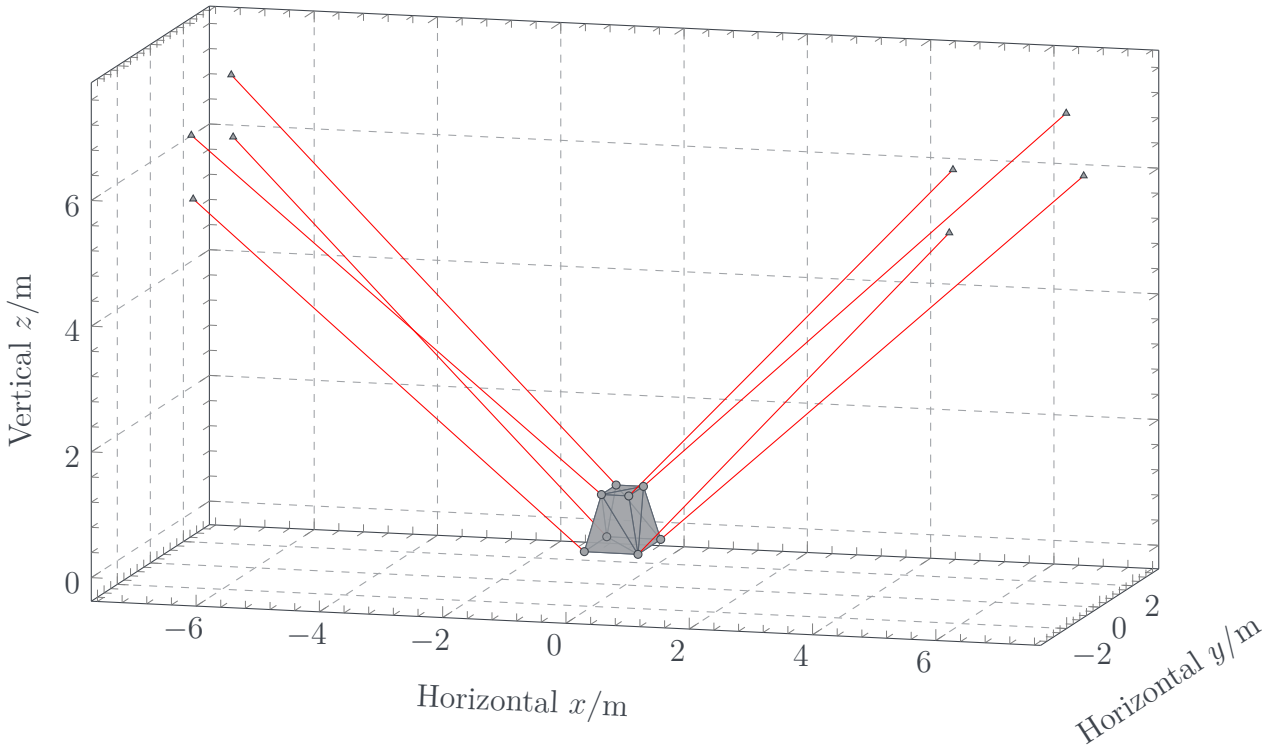

Figure 4.4: Static solution to the kinetostatically solved cable robot EXPO. Cable sag is negligible for the robot is suspended and thus all cables are strained no matter the platform pose.

Kinetostatic Case

Kinetostatically solving the EXPO cable robot yields ultimate platform position deflections of $\Delta x = -0.002\,\text{mm}$, $\Delta y = -9.200 \times 10^{-5}\,\text{mm}$, and $\Delta z = 0.003\,\text{mm}$,

Table 4.4: Comparison of cable lengths (a) and cable forces (b) of kinematic $(\cdot)_{\mathrm{km}}$ and kineto-static $(\cdot)_{\mathrm{ks}}$ solution for Expo's home pose.

Cable	$L_{i,\mathrm{km}}$/m	$L_{i,\mathrm{ks}}$/m	Δ_i/m
1	8.78	8.68	−0.10
2	8.85	8.86	0.01
3	9.10	9.13	0.03
4	8.83	8.75	−0.08
5	8.47	8.37	−0.10
6	8.78	8.79	0.01
7	8.82	8.85	0.03
8	8.51	8.44	−0.08

(a) *Cable lengths $L_{i,(\cdot)}$ and differences $\Delta_i = L_{i,ks} - L_{i,km}$.*

Cable	$f_{i,\mathrm{km}}$/N	$f_{i,\mathrm{ks}}$/N	Δf_i/N	$f_{i,\sim}$/N
1	81.4	200.5	119.1	200
2	446.3	452.7	6.4	451.7
3	420.0	427.0	7.0	426.1
4	85.9	200.5	114.6	200
5	330.5	261.8	−68.7	260.8
6	253.1	201.1	−51.9	200.2
7	253.6	200.5	−53.1	199.6
8	339.8	272.8	−67.0	271.8

(b) *Cable forces $f_{i,(\cdot)}$ and differences $\Delta f_i = f_{i,ks} - f_{i,km}$*

which renders the platform at precisely the desired position (Fig. 4.4). Compensating for the kinematic deviation results in cables $1, 4, 5, 8$ being shortened and cables $2, 3, 6, 7$ being lengthened (see Table 4.4(a)), which results in the previously horizontal deflection in direction of $+\hat{\boldsymbol{e}}_{\mathrm{y}}$ to be reduced. In addition, the initially, vertically deeper placed platform is lifted upwards and positioned closer to the desired position. Due to the asymmetric design of Expo's frame and platform design, cables $2, 3$ require the largest cable tension in order to compensate for platform roll (rotation about $\hat{\boldsymbol{e}}_{\mathrm{x}}$) (see Table 4.4(b)). Kinematically, the same two cables' forces were the lowest contributing most to the platform's deflection. Cable forces of cables 1 and 4 to 8 are all within the range of 200 N with cables 5 and 8 being under higher tension due to the downward drag of the platform. Similar observations during commissioning were reported, too (Tempel et al. 2015d).

4.2.3 IPAnema Mini

Robot configuration for IPAnema Mini can be found in Tables A.12 to A.14. Cable force limits are defined to be $\boldsymbol{f} \in [0, 40]$ N.

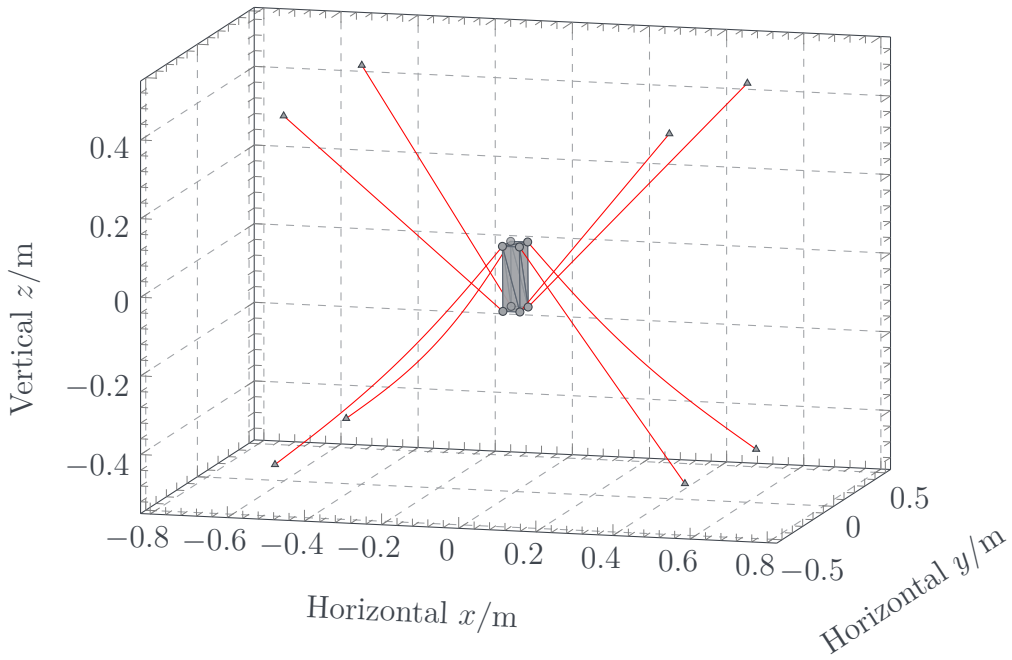

Figure 4.5: Static solution to the purely kinematically solved cable robot IPAnema Mini. Despite low platform inertia, lower four cables begin to sage and deviate from the straight line between both ends.

Kinematic Case

The smallest case study of cable robots is given by IPAnema Mini, with a workspace of close to $1 \times 1 \times 1\,\mathrm{m}^3$ (see Table A.12). Despite small magnitude of its geometrical and mechanical parameters, and thus relatively short unstrained cable lengths, kinematic solution to the static equilibrium of IPAnema Mini show likewise sagging cables and a linear platform deflections of $\Delta x = -1.086\,\mathrm{mm}$, $\Delta y = 1.587\,\mathrm{mm}$, and $\Delta z = -3.930\,\mathrm{mm}$ (see Fig. 4.5). In fact, asymmetric deflection along $\hat{\boldsymbol{e}}_\mathrm{x}$ and $\hat{\boldsymbol{e}}_\mathrm{y}$ result from minor frame asymmetry. Comparing kinematic perturbation of IPAnema Mini with e.g., IPAnema 3 or Expo yields comprehensible understanding of the dimensionality of effects on cable robots.

Much like IPAnema 3 (see Section 4.2.4), IPAnema Mini also features large iteration numbers for the purely kinematic static equilibrium with $k \leq 47$, due to the small step size of Newton's method over a wide range of iterations (see Fig. 4.6). This numerical limitation can only be partially overcome by e.g., initializing the constraint forces by means of some force distribution algorithm (see Section 2.6), however, care needs to be taken as the resulting force

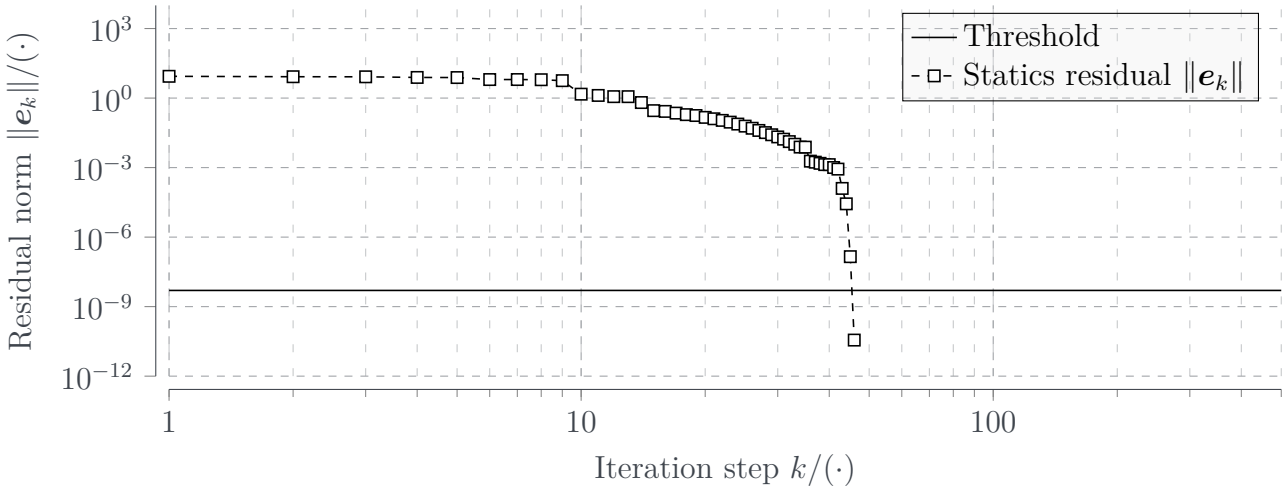

Figure 4.6: Decay of residual norm $\|\boldsymbol{e}_k\|$ during iteration solving the kinematic equilibrium case for IPAnema Mini. Small iteration step sizes initially slow down the iteration process due to large Jacobian.

values and directions may differ largely from the such obtained values[30]. Another way to overcome this limitation were by increasing cable stiffness, yet this is mostly impracticable since the physical cable's stiffness ought be approximated.

Kinetostatic Case

Kinetostatically solving the equilibrium at IPAnema Mini's home pose yields, again, zero deflection of the platform, stemming from the twofold level of redundancy allowing for increasing cable robot pre-tension without deflecting the platform (see Fig. 4.7). However, we observe that for cable robots of dimensions similar to IPAnema Mini, the resulting cable tension lies very close to the upper force limits, when defining the cost functional as minimizing cable length (see Table 4.5(b)). This is, though, a mere numerical effect as the residual stays well above the residual threshold for low cable tensions, thus the iterative solver yields minimal cable lengths with nearly maximum cable tensions. Nevertheless, initially slack cables 5 to 8 are tensed through the kinetostatic procedure with the resulting cable tensions being nearly equal amongst all

[30] Not for IPAnema Mini, as its geometry is rather confined, however, for e.g., IPAnema 3 this may well emerge.

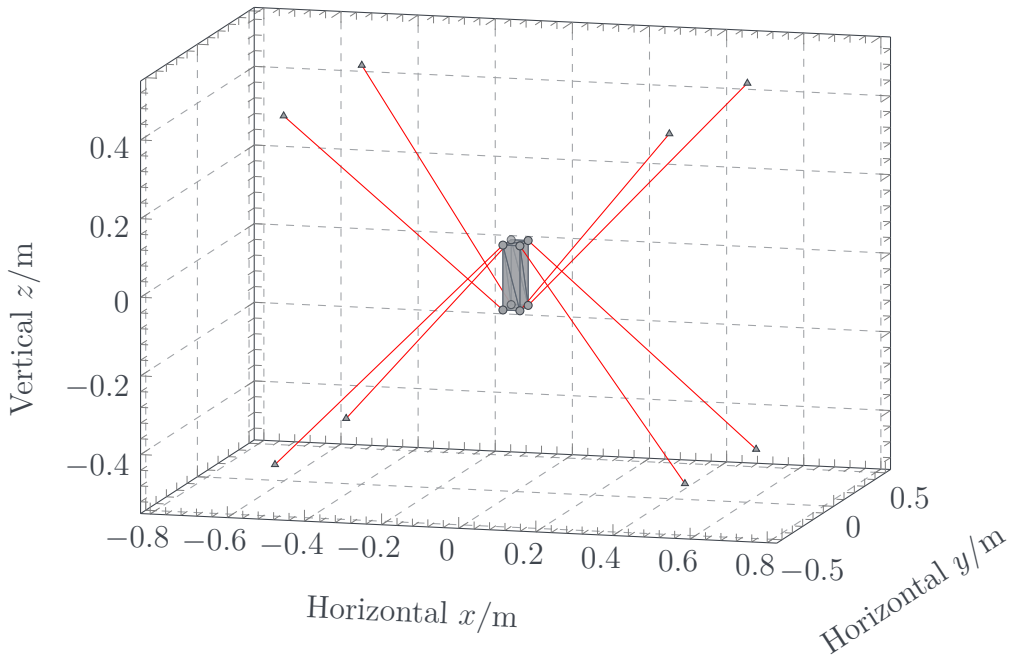

Figure 4.7: Static solution to the kinetostatically solved cable robot IPAnema Mini.

Table 4.5: Comparison of cable lengths (a) and cable forces (b) of kinematic $(\cdot)_{\mathrm{km}}$ and kinetostatic $(\cdot)_{\mathrm{ks}}$ solution for IPAnema Mini's home pose.

Cable	$L_{i,\mathrm{km}}$/m	$L_{i,\mathrm{ks}}$/m	Δ_i/m
1	0.79	0.76	−0.03
2	0.79	0.76	−0.03
3	0.79	0.76	−0.03
4	0.79	0.76	−0.03
5	0.80	0.77	−0.03
6	0.82	0.79	−0.03
7	0.80	0.77	−0.03
8	0.80	0.77	−0.03

(a) *Cable lengths $L_{i,(\cdot)}$ and differences $\Delta_i = L_{i,\mathrm{ks}} - L_{i,km}$.*

Cable	$f_{i,\mathrm{km}}$/N	$f_{i,\mathrm{ks}}$/N	Δf_i/N	$f_{i,\sim}$/N
1	3.3	40.0	36.7	21.9
2	3.3	40.0	36.7	21.9
3	3.2	39.9	36.7	22.2
4	3.3	39.7	36.4	22.4
5	0.0	36.3	36.3	18.0
6	0.0	37.2	37.2	18.4
7	0.0	36.4	36.4	17.6
8	0.0	36.6	36.6	17.4

(b) *Cable forces $f_{i,(\cdot)}$ and differences $\Delta f_i = f_{i,\mathrm{ks}} - f_{i,km}$*

cables (cf. Table 4.5(a)). Minor deviations result from marginally asymmetric frame and platform dimensions.

4.2.4 IPAnema 3

Robot configuration for IPAnema 3 can be found in Tables A.15 to A.17. Cable force limits are defined to be $\boldsymbol{f} \in [100, 3000]$ N.

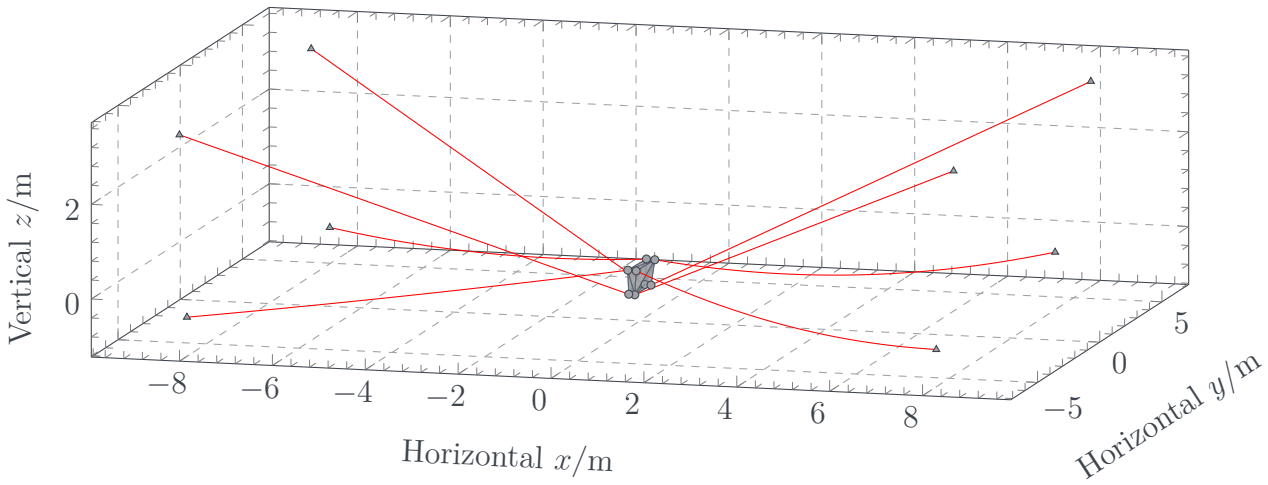

Figure 4.8: Static solution to the purely kinematically solved cable robot IPAnema 3. Visible cable sag emerges for lower for cables as their geometric distance becomes shorter than their kinematic length.

Kinematic Case

IPAnema 3 uses cables with lower elastic modulus than the previously presented cable robots, as such cable elongation is a more prevailing effect, as well as cable vibration. Solving IPAnema 3 kinematically, we obtain linear deflections of the platform pose as large as $\Delta x = 10.386\,\text{mm}$, $\Delta y = 9.363\,\text{mm}$, and $\Delta z = -307.754\,\text{mm}$, highlighting the effect of reduced cable stiffness. We can further observe apparent cable sag on cables 5 to 7 ultimately causing platform deflection (see Fig. 4.8). In particular, the platform's vertical deflection is largely due to the fact of cable elasticity, with the upper four cables straining so much, that the lower four cables are no longer supporting the platform. Asymmetric platform drift, again, results from asymmetric frame dimensions (see Table A.15).

Solving the kinematic equilibrium of IPAnema 3 yields, despite the simulation framework being initialization initialized equally as in the previous two cases, lower iterations emerge with $k \leq 43$. Since cable elasticity is larger for the IPAnema 3 cables, the initially decoupled multibody simulation requires fewer iterations for solving since the iteration steps are of larger magnitude. In addition, with reduced system stiffness, the inverse Jacobian used in Newton's iteration results in smaller step sizes thus causing longer iterations till the static

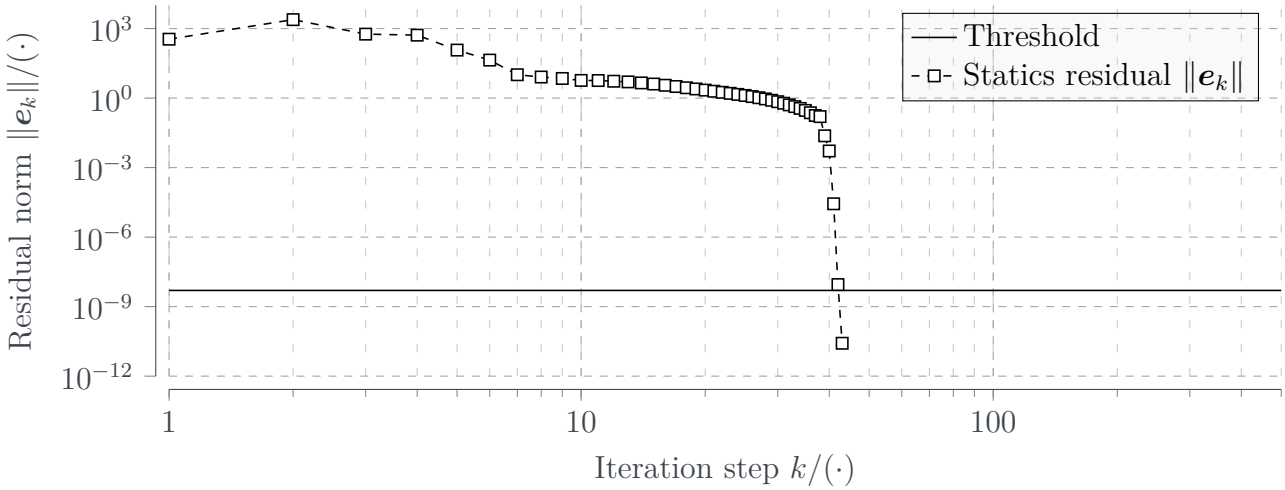

Figure 4.9: Decay of residual norm $\|\boldsymbol{e}_k\|$ during iteration solving the kinematic equilibrium case for IPAnema 3. Due to small steps of the iterative Newton's method, convergence is initially slow until $k \geq 40$.

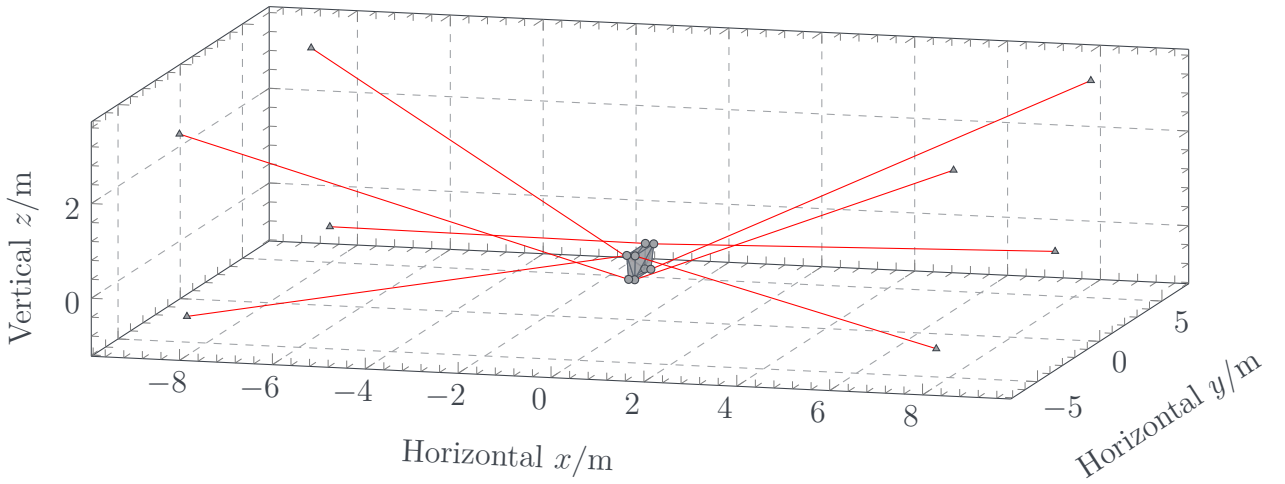

Figure 4.10: Static solution to the kinetostatically solved cable robot IPAnema 3. Cable sag of the lower four cables has mostly vanished to a nearly negligible value due to the strain on the cables.

residual norm is breached. Even in this case of a large-scale cable robot with slow iterations, the iteration count is rather deterministic and does not breach through the maximum iteration count.

Kinetostatic Case

Since IPAnema 3 is an RRPM, we can make use of the cable robot's twofold redundancy allowing for introducing an internal stiffness or level or pre-tension into

Table 4.6: Comparison of cable lengths (a) and cable forces (b) of kinematic $(\cdot)_{\mathrm{km}}$ and kinetostatic $(\cdot)_{\mathrm{ks}}$ solution for IPAnema 3's home pose.

Cable	$L_{i,\mathrm{km}}$/m	$L_{i,\mathrm{ks}}$/m	Δ_i/m
1	10.34	9.96	−0.38
2	10.18	9.80	−0.38
3	10.12	9.72	−0.40
4	10.24	9.85	−0.39
5	9.51	8.67	−0.84
6	9.16	8.27	−0.89
7	9.18	8.24	−0.93
8	9.53	8.56	−0.97

(a) *Cable lengths* $L_{i,(\cdot)}$ *and differences* $\Delta_i = L_{i,ks} - L_{i,km}$.

Cable	$f_{i,\mathrm{km}}$/N	$f_{i,\mathrm{ks}}$/N	Δf_i/N	$f_{i,\sim}$/N
1	163.2	599.6	436.4	306.9
2	168.2	606.7	438.5	340.1
3	171.7	638.9	467.2	453.3
4	165.9	613.9	448.0	441.7
5	0.5	1515.5	1515.0	1564.8
6	0.3	1686.9	1686.6	1702.6
7	0.3	1777.1	1776.7	1716.2
8	2.8	1777.1	1774.3	1705.8

(b) *Cable forces* $f_{i,(\cdot)}$ *and differences* $\Delta f_i = f_{i,ks} - f_{i,km}$

it. As such, in the kinetostatic case, the platform deflection can be completely eliminated[31] while keeping the cable tensions within their limits (see Fig. 4.10 and Table 4.6(b).). We can, however, observe non-negligible elongation of all cables of up to $\|\Delta_i\|_\infty = 0.970\,\mathrm{m}$ in order to attain both the platform position as well as to minimize cable length and satisfying cable force constraints (see Table 4.6(a)). Similarly, winding cables of IPAnema 3 results in noticeable increase of cable tension of the lower four cables 5 to 8, which were initially near slack. Since the home pose of IPAnema 3 is near the lower workspace boundary (see Table A.15 and (Pott et al. 2012; Kraus 2015)), the same four cables require larger tension to attain the low platform position.

4.2.5 Conclusions

The multibody simulation framework formulated for cable robots and their kinematic and kinetostatic equilibrium problem renders itself capable of being applicable to a wide range of cable robots i.e., of different sizes from large-scale to small-scale, and of different classes from fully restrained to suspended. Conventionally, especially for the latter property, different approaches to obtaining

[31] Up to double precision of floating point numbers.

solutions of the workspace or cable force distributions had to be employed. With the framework presented in this chapter, we can now find a common formulation of cable robots of different classes while explicitly considering cables in the formulation. This comes in handy when the asymmetry of cable robot designs, which is a common trait to most design as it avoids architectural singularities, may cause the platform to drift away from its equilibrium due to cable drag. Cable force distributions can be calculated straightforward by minimizing a user-chosen cost functional dependent the cable length, cable forces, or other values, while the system's kinematics are inherently satisfied at all times during solving.

From a numerical perspective, the framework and its Newton's method for solving the static equilibrium is capable of handling cable robots with varying stiffness like steel cables and Dyneema® cables. While there is undoubtedly room for improvement in increasing iteration speed for low-stiffness cable robots, the only cases when iterations fail is when constraints on cable forces cannot be satisfied i.e., when the system is outside of its workspace. In particular, Newton's method becomes rather slow with low-stiffness cable robots as the residual Jacobian contains large values resulting in very small step sizes per iteration. Adaptive iteration algorithms like Levenberg-Marquardt or trust region methods may yield better iteration behavior with such cable robots, especially during the first iteration steps when the residual decreased only slowly.

One major difference between determining cable force distributions or workspaces with the framework presented in this thesis and conventional methods is the inability to provide for closed-form solutions. While this may be seen advantageous since the cable forces and cable robot state are not observed independent of each other, it may also be seen disadvantageous since it is now an iterative scheme for which a priori estimates of maximum iteration step or time and further algorithmic quantities cannot be given.

4.3 Dynamics

With the results presented in Section 4.2 showing straightforward transfer of the cable model and framework to simulation statics of cable robots, we primarily want to perform forward dynamics simulation of cable robots including platform-cable interaction. As such, we shall assess forward dynamics simulation of IPAnema 3 within the multibody simulation framework presented in Section 4.1.2 with robot configuration given in Appendix A.5. With IPAnema 3's frame being of rectangular shape with height small compared to width and length, we move the platform within the vertical direction upwards i.e., along the axis of least stiffness.

We initialize the system according to the kinetostatic result presented in Section 4.2.4 i.e., with a given cable pre-tension such that slack cables can be best avoided but not ruled out a priori. Cable set lengths are calculated using the standard inverse kinematics algorithm from Section 2.3.1.1 and adjusted for the additional strain to obtain the initial cable tension. As cable stiffness is one of the most challenging parameters to obtain from both literature and data sheets or from experimental tests, choosing $E = 12.200\,\mathrm{GPa}$ is simply for the sake of convenience and making perceivable examples, yet not baseless (cf. Section 5.3.1.2).

Let the input to our simulation be a vertical upwards motion from home pose $\boldsymbol{r}_0 = \boldsymbol{r}^*$ toward final pose $\boldsymbol{r}_T$ with $\boldsymbol{r}_{0,\mathrm{z}} = 0\,\mathrm{m}$ and $\boldsymbol{r}_{T,\mathrm{z}} = 1.330\,\mathrm{m}$ and $\boldsymbol{r}_{0,\mathrm{x}} = \boldsymbol{r}_{0,\mathrm{y}} = \boldsymbol{r}_{T,\mathrm{x}} = \boldsymbol{r}_{T,\mathrm{y}} = 0$. Transition time T is set to be $T = 1\,\mathrm{s}$ yielding an average vertical velocity of $\boldsymbol{v}_{\mathrm{z}} = 1.330\,\mathrm{m\,s^{-1}}$. To prevent jerky platform motion during start and end of the transition, we make use of the non-analytic smooth function $g : [0,1] \ni x \mapsto g(x)$ reading

$$g(x) = \frac{f(x)}{f(x) + f(1-x)}\,,$$

with

$$f(x) = \begin{cases} \exp\left(-\frac{1}{x}\right) & x > 0\,, \\ 0 & x \leq 0\,, \end{cases}$$

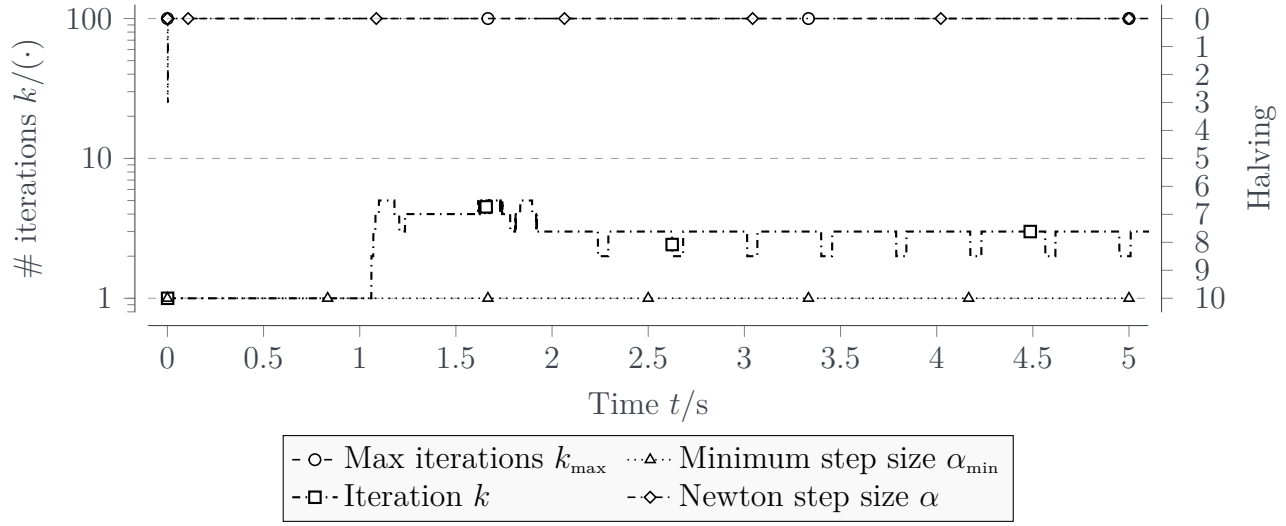

Figure 4.11: Progression of residual norm and Newton's step size solving forward dynamics given a vertical upwards motion of IPAnema 3. Maximum iteration limit was set to $k_{\max} = 100$, while maximum halving of Newton's steps was set to 10 bisections i.e., $\alpha_{\min} = 1/2^{10} = 1/1024$.

or equivalently, with transition on interval $[a, b]$, by $x \mapsto g(\frac{x-a}{b-a})$, yielding vertical transition

$$\boldsymbol{r}_{\mathrm{z}}(t) = \boldsymbol{r}_{0,\mathrm{z}} + (\boldsymbol{r}_{T,\mathrm{z}} - \boldsymbol{r}_{0,\mathrm{z}})\, g\left(\frac{t-a}{b-a}\right),$$

with chosen $a = 1, b = 2$ Further configuration parameters of the framework and integrator can be found in Table 4.2.

Observing convergence of the energy and momentum preserving integrator during solving the forward dynamics problem (see Fig. 4.11) shows efficient convergence below the threshold of $\epsilon_e = 5 \times 10^{-9}$ (cf. Table 4.2). As we expect, during the simulation's steady state i.e., for $t < 1\,\mathrm{s}$, Newton's method converges within one step, though the damped Newton's method requires reduction of the step size by up to four halving during the first $k = 6$ steps. Once motion starts, solving the residual equation converges below the residual threshold with a maximum of $k_{\max} = 5$ iterations, despite the low residual threshold. In all cases, Newton's method terminated due to too low residual error ϵ_e rather than too small step size $\epsilon_{\Delta \boldsymbol{x}}$. The system integrator shows good performance for solving the discrete nonlinear root-finding problem in the system's next

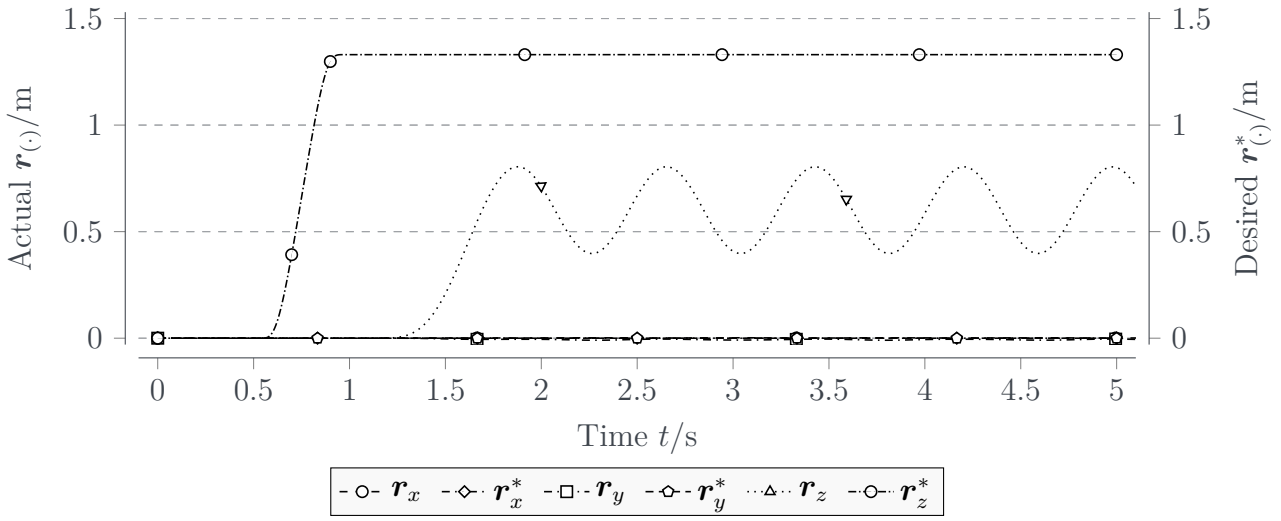

Figure 4.12: Vertical position of platform center during forward dynamics showing oscillating motion as the transition ends. Since the system is neither physics-based nor numerically damped, vertical oscillation of the platform results around mean of 0.599 m. Deviation from the desired position of 1.330 m results from incorrect selection of cable elasticity, one of the biggest issues.

state (cf. Eq. (4.9)) as it keeps well below the maximum number of iterations and provides convergence within a low count of iterations.

Time evolution of the platform's point of reference over time results in an oscillating response of the platform (cf. Fig. 4.12) which is to be expected due to lack of physics-based or numerical damping. Positional error and tracking error are not negligible as it averages at $\Delta z = 0.731\,\mathrm{m}$, however, improper selection of cable elasticities is to blame for that. While the cable model itself is capable of representing linear cable elasticity[32] under the assumption of linearity for different cable lengths, it may simply be too elastic for the given cable robot use case. Despite difficulty of selecting cable elasticity, the effect of interaction between cables and platform can be seen from the oscillating response of the platform's point of reference, much like also the cables' midpoints show oscillation (see Fig. 4.13).

[32] Whether linear elasticity is the correct model for describing Dyneema® cables is disregarded for this chapter. Refer to Chapter 5 for more insight into this topic.

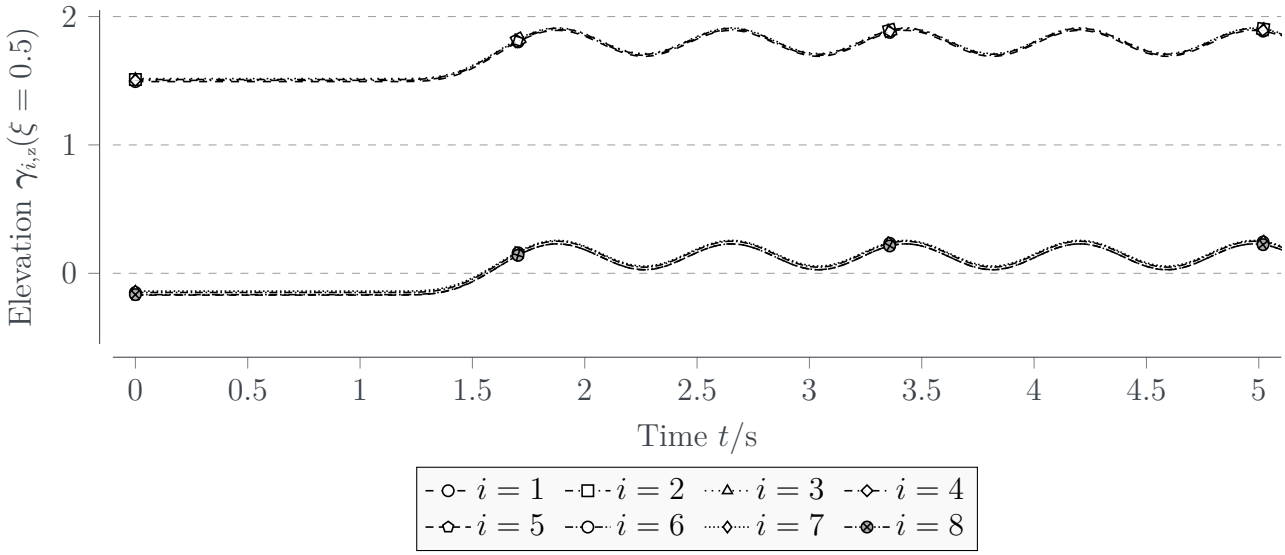

Figure 4.13: Elevation of cables' mid-points $\boldsymbol{\gamma}_i(\xi = 0.5)$ during forward dynamics showing likewise oscillating motion after transition stops. Magnitude of vibration is largest at the cable's mid-point, despite cable length changes.

Lastly, despite the iterative integration schemed derived by Betsch being energy conservative, we also investigate the conservation of energy of the simulation itself. Sum of potential and kinetic energies remains zero when the cable robot is steady before motion starts (see Fig. 4.14). Once motion starts, we can see potential energies of the lower cables $i = (5, \ldots, 8)$ reducing resulting from decrease in tension as the cables must elongate in order to allow for the platform to move upwards. Likewise, potential energies of the upper four cables $i = (1, \ldots, 4)$ increases as their length must reduce to lift the platform upwards resulting in increased tension. After motion input ends at $t = 2\,\mathrm{s}$, the system is left to oscillate freely under only external, gravitational forces which is when constant transfer from potential energies to kinetic energies and back is triggered. Interestingly, kinetic energies oscillate two times faster than potential energies, which can be led back to the motion reversal points of the platform at highest and lowest peak of oscillation.

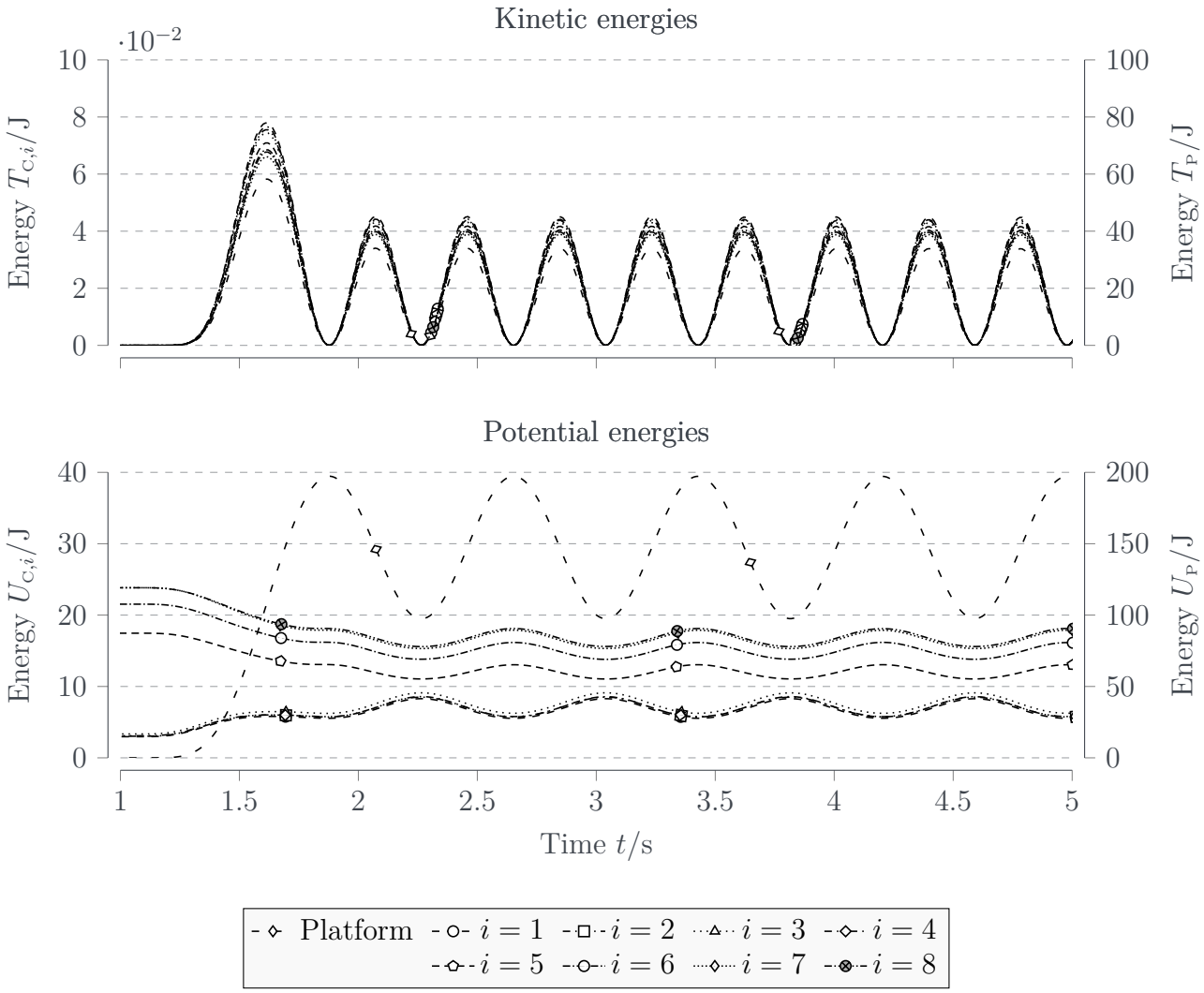

Figure 4.14: Kinetic and potential energies of cables and platform during forward dynamics simulation of IPAnema 3. Potential energy comprises cable strain and bending energies, as well as gravitational energies of cables and platform. Kinetic energies minimize at maximum and minimum potential energy i.e., whenever the platform is at its upper or lower point or motion reversal.

4.4 Conclusions

The cable robot simulation framework presented in this section provides a mechanically formulated, energy and momentum-preserving formulation for cable robots of different types. Solving the kinematics or dynamics of multibody systems, in particular those with flexible and rigid bodies, requires special care when it comes to handling the constraints between bodies. Conventionally, this is achieved by introducing constraint violation handling methods such

as Baumgarte stabilization method (BSM) or using a different formulation of the DAE such as Gear-Gupta-Leimkuhler (GGL). However, this affects the system dynamics as the constraints now feature their own dynamics, which, depending on the parametrization of its constraint violation handling, can make the forward dynamics simulation yield different results than anticipated. With the formulation given in this section, there is no recasting of the system dynamics into a different form and constraint violation is handled implicitly through the iterative scheme. Furthermore, Betsch's iterative scheme can be solved purely on the positional level and implies the energy and momentum preserving velocities—satisfying them at intermediate points—remedying the need for solving for the accelerations and then subsequent twofold integration with respect to time.

Besides the numerical advantages of the integration scheme presented in this section, the multibody formulation of cable robots within the framework given allows for arbitrary configurations of cable robots, in fact we may even add more than one platform to the framework, which we may connect through cables or by means of other bodies. We may also think of adding a serial manipulator onto the platform allowing for simulation of cable robots in different tasks than before. In the end, all that is required are the appropriate dynamics of each body and the constraints that bind it to another body; with the framework presented, the possibilities for analysis and simulation of cable robots are endless. Lastly, the framework enables its user to fully understand how the equations of motion are implemented and how exactly the forward-in-time integration scheme is laid out—in contrast to commercially available simulation tools based on e.g., FEM, the algorithmic implementation is not corporate secret but can be easily traced and understood.

Looking at the applied use case lying in cable robot analysis, both statically/kinetostatically and dynamically, the framework is based on aforementioned facts, and shows itself capable of handling many different kinds and dimensions of cable robots. Since not all algorithms existing in literature are applicable to every kind or dimension of cable robots —for example, the closed-

form force distribution presented in Section 2.6 does not yield valid results for suspended cable robots and is not even applicable to cable robots other than those of RRPM type—the use range of the framework is rather wide. We have shown applicability to obtaining both kinematic and kinetostatic solutions to cable robots of different type—CoGiRo/Expo and IPAnema—as well as of different sizes—CoGiRo and IPAnema Mini—while keeping the algorithm's speed of convergence within reasonable bounds. With further improvements, such as using an existing cable force distribution algorithm on the initial guess of the kinematic and kinetostatic problem, the number of iterations may further be reduced.

In all fair-mindedness, one implementation limitation of the proposed multibody simulation framework has to be mentioned which is its general speed of execution. While the static equilibrium solutions (Section 4.2) can be obtained in less than approximately 0.900 s in total[33], even in case of high iteration counts of IPAnema 3 and IPAnema Mini, it is still relatively slow when it comes to solving the dynamics solution. With a time step size of $h = 1\,\text{ms} = 0.001\,\text{s}$, a simulation over $T = 10\,\text{s}$ takes at least[34] $t_{\text{sim}} = 9000\,\text{s} = 150\,\text{min}$. However, the algorithmic implementation of the multibody framework can be well improved by pre-simulation code generation resolving loops over all bodies and constraints, much like the calculation of the constraint forces can be streamlined. Lastly, the iterative Newton's scheme can be improved by better conditioning of the Jacobian using a less-sparse formulation improving inversion of the high-dimensional matrix (Baraff 1996).

[33] Counting only the execution time of the iterative Newton's method; not including any simulation setup times or data pre-processing or post-processing.

[34] We say "*at least*" as the dynamic case will increase the iteration count per time step during large motion and as such, $t_{\text{step}} \approxeq 0.900\,\text{s}$ can no longer be sustained. Worst case scenarios have revealed integration step times of up to $t_{\text{step}} \approxeq 5\,\text{s}$ with iteration count reaching the self-defined limit of $\max(k) = 100$.

Chapter 5

Stress-Strain Dynamics

Strain induced stress on fiber cables like those used in prominent cable robot like the IPAnema 3 *or* COPacabana *shows largely different behavior compared to their steel-wire counterparts. While the latter, as used on* CoGiRo *and* Marionet*, are validly assumed to be linear elastic, the former show not only nonlinear behavior but also exhibit hysteretic behavior. In this chapter, we will focus on purely axial stress-strain dynamics of such fiber cables used in the* IPAnema *cable robot family. As such, no direct connection between preceding results and this chapter is made, however, sketched in the thesis' summary chapter. We will dive into viscoelastic modeling of fiber cables, providing insight into how the stress-strain dynamics are described using purely kinematic mechanics. Consequently, a mechanics-based model rather than an interpolation model based on experimental data is obtained which we then fit against experimental data to obtain quantitative values of the parameters. Lastly, the proposed model is investigated for its quality of predicting the real cable's stress given a strain input trajectory, results of which have previously been presented in Tempel et al. (2018).*

Conventional parallel kinematics use rigid joints composed of prismatic or rotational actuators for which the governing equations of force/torque transmission can be obtained straightforward under the assumption of neither static nor dynamic friction or backlash. Incorporating effects such as static and dynamic friction can be done by choice of an appropriate friction model such as Dahl (1968) or Stribeck (1903). These factors similarly affect cable robots since their main actuating system is usually composed of a rotational actuator that is in one way (gearbox e.g., IPAnema system family (Pott et al. 2012)) or another (timing belt; e.g., CoGiRo (Riehl et al. 2010)) attached to the winch. However, cable

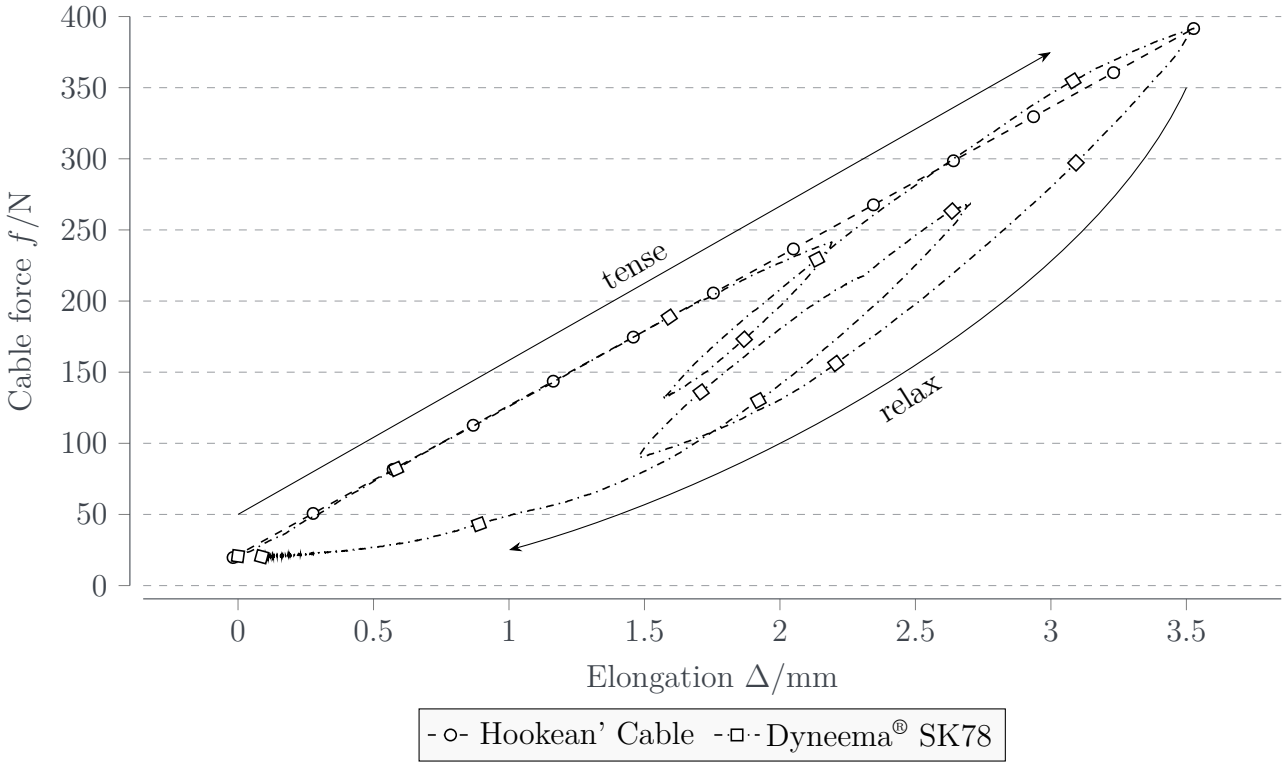

Figure 5.1: Experimentally obtained hysteretic stress-strain dynamics of Dyneema® SK78 for an arbitrary tensing-relaxing trajectory visualizing the material's hysteretic behavior. Stress during tensing is largely linear though with varying slopes depending on the previous resting stress. Stress during relaxation decays exponentially with varying slopes.

robots differ from rigid link robots in that sense that their links are flexible and elastic components, with their own dynamics. As shown in Chapter 3, flexibility of the cables introduces spatial motion, as such deviation from the rigid link's straight-line connection. However, it is the links' higher elasticity when compared to rigid links that entails more involved stress-strain dynamics of the material. Figure 5.1 shows two key response factors of polyethylene fibers in comparison to a Hookean cable. The first factor is the material's nonlinearity in the stress response given a strain input apparent by various force plateaus during relaxing or tensing. The other key factor is the material's hysteretic behavior during tensing and relaxing clearly visible through a nearly linear tensing slope yet a exponential decay during relaxing. A third property of viscoelastic polyethylene fibers is the so-called stress-relaxation i.e., a change in stress while strain remains unchanged (shown in Fig. 5.2).

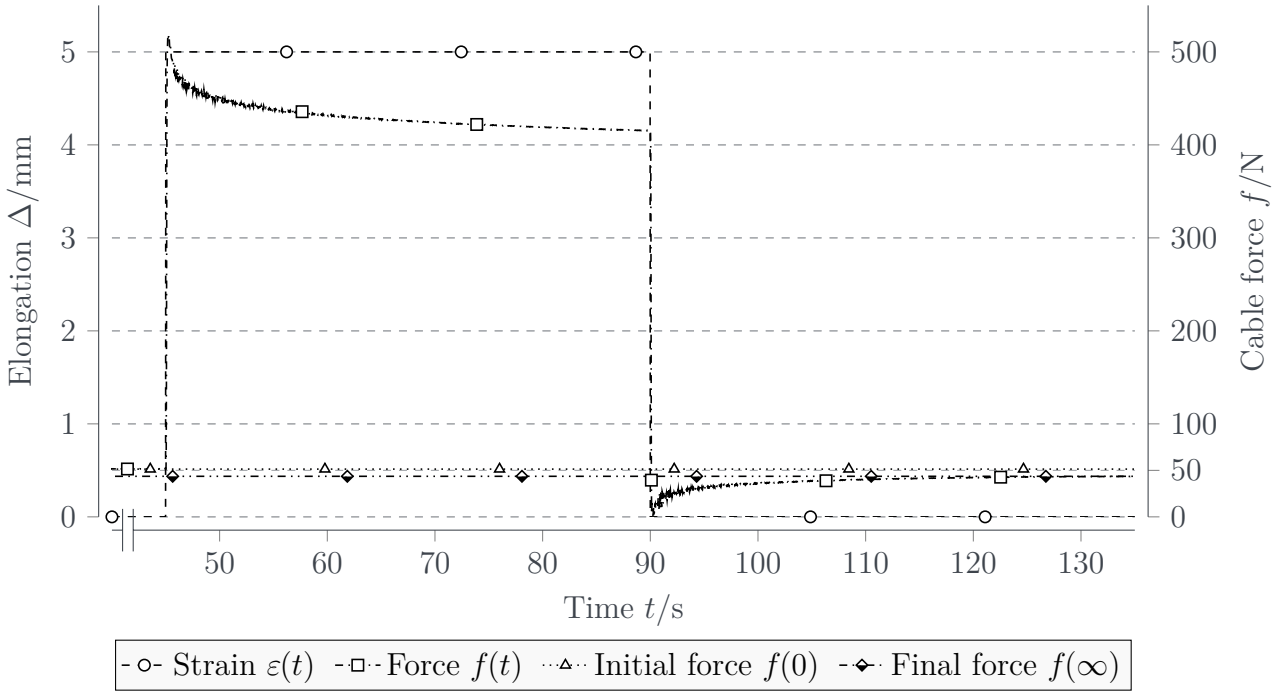

Figure 5.2: Stress relaxation of Dyneema® SK78 cable showing a decrease in the cable stress σ while its strain ε is kept constant. In addition, initial force $f(0)$ is larger by $\Delta f = 5\,\mathrm{N}$ than final force $f(\infty)$ after $t_{\mathrm{relax}} = 45\,\mathrm{s}$ of relaxation.

Keeping these three factors in mind, consequently, the distally measured tension may not be the same as the proximally applied tension—for the sake of simplicity, we shall not consider loss of tension on pulleys or other guiding elements as has been investigated by Kraus et al. (2015a). The material's dynamics to stress and strain need special consideration when it comes to better understanding cable robots, in particular during non-quasistatic motion.

Further implications of non-negligible stress-strain dynamics of fiber cables, resulting from their composition of several strains of hundreds of thin fibers (a schematic depiction of a Dyneema® cable is given in Fig. 5.3) affect cable force control much like force control in operational space. Moreover, fiber cables show inherently different behavior to tensing and relaxing as a result of their mechanical property. While linear actuators are generally built from elements with dense cross-section, fiber cables are woven or laid from hundreds of strains. Thus, in the sense of a prismatic joint, a fiber cable consists of a myriad of small-diameter linear prismatic joints—that may only pull—which are axially loaded, are in radial contact with its neighbors, and are additionally torsionally

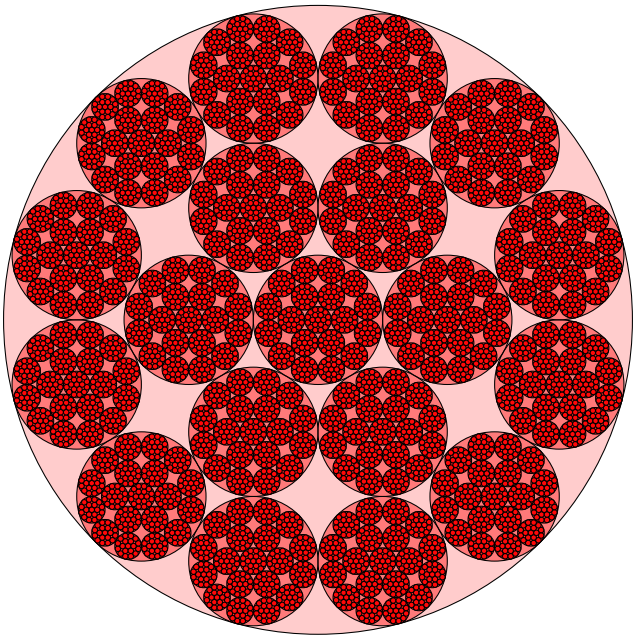

Figure 5.3: Schematic cross-section of Dyneema® fiber cable composed of multiple strands, in turn composed of assembled yarns, in turn composed of single yarns, comprising many fibers. The total area of contact is small compared to the overall surface area due to the strands having only punctiform contact to its neighboring yarns.

pre-stressed. While a single cable fiber may be assumed assimilable to a linear prismatic joint, the sum of strains of fibers results in a complex nonlinear stress-strain behavior of the cable. This makes modeling fiber cables through tribology i.e., on a microscopic level, rather challenging, last because material properties such as elastic, viscous, or friction coefficients must be obtained for a single strand. Consequently, a homologous model of the material dynamics is favored over a tribologically correct one, last because we are only interested in the overall stress-strain dynamics and not the inner workings of every single fiber.

Commonly, cables in cable robots are assumed linear elastic and modeled by a linear spring element or are assumed linear viscoelastic modeled by a serial combination of a linear spring and a linear damper. In either case, elastic or viscoelastic parameters, respectively, are assumed time-independent and vary only with respect to the nominal cable length. Most, if not all of the algorithms for design and analysis of cable robots, make use of these simplified models as they drastically reduce computational cost and approximate the static behavior

of fiber cables well. However, applicability of these models to dynamics and even quasi-static simulation of cable robots is debatably limited due to lack of four key characteristics of fiber cables: 1) comparing tensing and relaxing, fiber cables show distinctive hysteretic behavior; 2) when under constant stress, strain relaxation emerges i.e., cable elongation increases; or likewise 3) when under constant strain, stress relaxation occurs i.e., cable tension decreases; and 4) material properties change over time due to internal mechanical stress but also due to environmental influence. Knowing fiber cables show nonlinear mechanical characteristics but also short-term and long-term dynamical responses to applied stress, it becomes apparent that more sophisticated models need to be derived. These models may later be used in any step from design over analysis to control of cable robots, however, in fields such as design and static workspace analysis, it still suffices to use a purely elastic cable model composed of only a Hookean material.

The remainder of the chapter is structured as follows: Section 5.1 introduces the basic techniques for modeling of viscoelastic materials as well as two general material models. Three particular implementations of these general material models are evaluated with regards to their applicability resulting in a selection of the material model to use for the following experimental estimation In Section 5.2, the procedure of experimental model and model parameter estimation is given introducing the experimental setup as well as the techniques used during numerical analysis. Following that, Section 5.3 shows results from estimation as well as stability of the estimation and goodness of fit. Lastly, Section 5.4 concludes the chapter with a recommended selection of a material model, also commenting on challenges faced during the estimation step.

5.1 Modeling of Fiber Cables

While at its microscopic core consisting of hundreds of fibers laid next to each other and woven into strands, their precise interaction is unknown and largely unavailable. The overall large signal response of cables of such material can be

described through combination of the two most simple mechanic components 1) linear spring (a restorative force) and 2) linear damper (a damping force). A suitable yet minimal choice of serial or parallel combination of these two elasticity and viscosity representing components can provide for dynamics models describing the stress-strain dynamics sufficiently well. In literature, several well-established material models can readily be found which will be introduced after definition of the most important mechanical concepts of stress and strain.

Stress is a material quantity that expresses the internal forces of neighboring particles[35] of a continuous material exerting on each other, while strain is the measure of the (stress–resulting) deformation of the material. Assuming the material's mechanical elasticity to obey Hooke's law of a perfect solid, we obtain the relation of applied stress σ_E and resulting strain ε_E

$$\sigma_E = E\,\varepsilon_E\,,$$

where E is elasticity, usually Young's modulus of elasticity. Similarly, the material's mechanical viscosity can be described through the variation of the applied stress σ_η with the rate of change of strain $\dot{\varepsilon}_\eta$ assuming Newton's law of a perfect liquid, reading

$$\sigma_\eta = \eta\,\dot{\varepsilon}_\eta\,,$$

where η is viscosity and $\dot{\varepsilon}_\eta = \frac{\mathrm{d}\varepsilon_\eta}{\mathrm{d}t}$ is rate of change of strain.

Following Roylance (2001), to obtain material models representing physical materials, serial or parallel combinations of a total of n_{mat} elastic and viscous components are created for which the resulting material dynamics formulation can be solved under consideration of realization of the physical relations for

$$\text{serial components:} \qquad \sigma_\Sigma = \sigma_k\,, \qquad \varepsilon_\Sigma = \sum_k^{n_{\mathrm{mat}}} \varepsilon_k\,, \tag{5.1a}$$

[35] As such, these measures are along all of the material's principal axes. However, we will limit the use case to only one-dimensional stress along the material's longest axis.

$$\text{parallel components:} \qquad \sigma_\Sigma = \sum_k^{n_\text{mat}} \sigma_k \,, \qquad \varepsilon_\Sigma = \varepsilon_k \,, \tag{5.1b}$$

where ε_Σ and σ_Σ are the strain and stress of the total system, respectively, and ε_k and σ_k are the k-th component's strain and stress, respectively. It can be seen, which the novice reader may also infer from experience, that the stress on each component is the same in a serial combination while the strain of each component is the same in a parallel combination. Conversely, this means that the strain of a serial combination and the stress in a parallel combination behaves opposite to the former behavior. Using these material and mathematical relationships and their time-derivatives, the resulting material system can be described mathematically, resulting in an ODE of stress σ_Σ and strain ε_Σ for the uniaxial isotropic linear viscoelastic material in the constitutive equation reading

$$a_0\,\sigma_\Sigma + a_1\,\dot{\sigma}_\Sigma + \cdots + a_{n_a}\,\frac{\mathrm{d}^{n_a}\sigma_\Sigma}{\mathrm{d}t^{n_a}} = b_0\,\varepsilon_\Sigma + b_1\,\dot{\varepsilon}_\Sigma + \cdots + b_{n_b}\,\frac{\mathrm{d}^{n_b}\varepsilon_\Sigma}{\mathrm{d}t^{n_b}}\,, \tag{5.2}$$

where a_k and b_k can be resorted from material constants, and in general $n_a \neq n_b$. In the later presented procedure to the investigation of stress-strain dynamics, we will perform analysis not using the time-domain and its associated ODE, but we will perform analysis in the frequency-domain using the Laplace transform of the ODE from Eq. (5.2) which generally reads

$$G(s) = \frac{Y(s)}{U(s)} = \frac{b_{n_b}\,s^{n_b} + b_{n_b-1}\,s^{n_b-1} + \cdots + b_1\,s + b_0}{a_{n_a}\,s^{n_a} + a_{n_a-1}\,s^{n_a-1} + \cdots + a_1\,s + a_0}\,,$$

where $s = \sigma + \mathrm{i}\,\omega$ is a complex number frequency parameter with real numbers σ and ω, $Y(s) = \mathcal{L}\{y\}(s)$ and $U(s) = \mathcal{L}\{u\}(s)$ are the Laplace transform of the output and input, respectively. We normalize the transfer function with respect a_{n_a} such that we eliminate one free variable yielding the normalized transfer function

$$G(s) = \frac{\frac{b_{n_b}}{a_{n_a}}\,s^{n_b} + \frac{b_{n_b-1}}{a_{n_a}}\,s^{n_b-1} + \cdots + \frac{b_1}{a_{n_a}}\,s + \frac{b_0}{a_{n_a}}}{s^{n_a} + \frac{a_{n_a-1}}{a_{n_a}}\,s^{n_a-1} + \cdots + \frac{a_1}{a_{n_a}}\,s + \frac{a_0}{a_{n_a}}} = \frac{N(s)}{D(s)}\,, \tag{5.3}$$

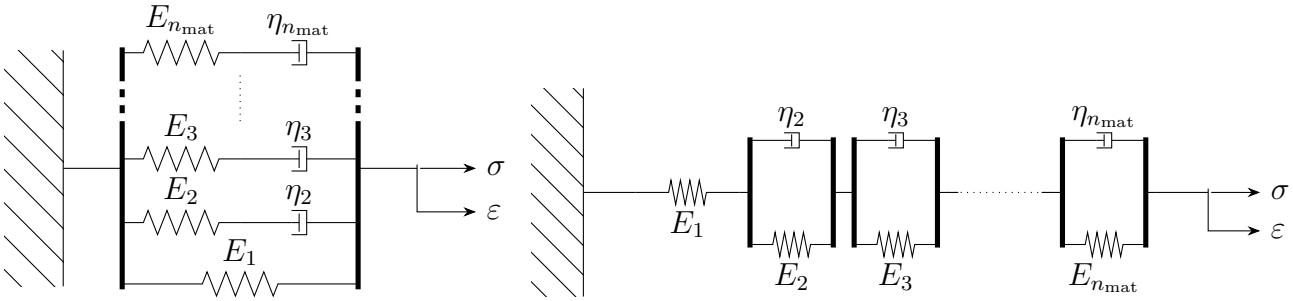

(a) *Generalized Maxwell chain material model with a single elastic component of elasticity E_1, parallel to n_{mat} parallel Maxwell material of elasticity E_l and viscosity η_l, $l \in \{1, \ldots, n_{mat}\}$.*

(b) *Generalized Kelvin chain material model with a single elastic component of elasticity E_1, in series with n_{mat} parallel Kelvin–Voigt material of elasticity E_l and viscosity η_l, $l \in \{1, \ldots, n_{mat}\}$.*

Figure 5.4: Generalized Maxwell chain (a) and generalized Kelvin chain (b) material models.

with numerator polynomial $N(s)$ and denominator polynomial $D(s)$.

Polynomial coefficients a_l of the numerator and b_l of the denominator can be inferred from the material law put in place, however, only lower-dimensional models can provide for an analytical solution to the mapping. Higher-order materials composed of three or more parallel Maxwell, respectively serial Kelvin components, yield nonlinear equations in the elastic and viscous parameters. For such models, we approximate the elastic and viscous parameters by means of solving the root-finding problem defined through the ODE in Eq. (5.2) and the numerator/denominator values from Eq. (5.3).

In general, two viscoelastic material model types of similar structure exist, one being the generalized Maxwell material (GMW material) chain, the other being the generalized Kelvin material (GKV material) chain. Due to their mechanical structure, Maxwell material (MW material) is more commonly used when we prescribe the strain history and are interested in the stress response, whereas GKV material is used in the opposite direction, prescribing stress history and outputting strain response. Either model consists of a purely elastic component, either in parallel with MW material components (see Fig. 5.4(a)), or in series with Kelvin–Voigt material (KV material) components (see Fig. 5.4(b)). Making use of equality of stress distribution on the parallel components and strain

distribution on the serial components, respectively, such that

$$\sigma_{\mathrm{MW}} = \left(E_1 + \sum_{l}^{n_{\mathrm{mat}}} \frac{\mathrm{d}}{\frac{\mathrm{d}}{E_l} + \frac{1}{\eta_l}} \right) \varepsilon_{\mathrm{MW}}, \tag{5.4a}$$

$$\varepsilon_{\mathrm{KV}} = \left(\frac{1}{E_1} + \sum_{l}^{n_{\mathrm{mat}}} \frac{1}{E_l + \eta_l \, \mathrm{d}} \right) \sigma_{\mathrm{KV}} \,, \tag{5.4b}$$

where $\mathrm{d}(\cdot) = \frac{\mathrm{d}(\cdot)}{\mathrm{d}t}$ is the differential operator with respect to time, and E_l, η_l are the elastic and viscous modulus of the l-th elastic and viscous component, respectively (Findley et al. 1976). Mathematical manipulation of either Eq. (5.4a) or Eq. (5.4b) for the respective material yields the desired transfer function, in general terms given through Eq. (5.2).

Depending on the point of view and interest, different system characteristics may be extracted from the stress-strain ODE Eq. (5.2) e.g., the strain response to a stress-step or vice versa. Given the stress step response, this equation can be readily used to assess characteristic material properties such as instantaneous elasticity or long-term creep response. For the application in cable robots, we are mostly interested in the transfer function of strain to stress i.e., we desire a description that yields

$$\sigma \coloneqq \sigma(\varepsilon, \dot{\varepsilon}, \ddot{\varepsilon}, \ldots) \,.$$

It may lastly be noted for the matter of completeness that the choice of spring or damper as well as the choice of serial or parallel combination of these components must be based on the material's dynamic response obtained through experimental data or through knowledge of the material as well as the direction of transfer i.e., stress to strain or strain to stress. Without any prior knowledge, finding a suitable material model is an involved task and will not always lead to acceptable results (Findley et al. 1976; Brinson et al. 2008; Babaei et al. 2016; Marques et al. 2012; Romanyk et al. 2013). We may, of course, simply assume an arbitrary transfer function e.g., PT_1 or PT_2 and fit this with the experimentally obtained data, however, this completely removes any physical or

mechanical meaning from the obtained dynamics and does not allow inferring elastic or viscous parameters.

As already mentioned, finding a suitable material model must thus be based on knowledge of the dynamical stress-strain behavior of the material. Luckily, literature is full of material models for different kind of visco-, plasto-, and even viscoplastoelastic materials. Most commonly used material models comprise the very simple MW material and KV material, the more advanced Zener material (ZR material) (also called standard linear solid material (SLS material)), and the Burgers material (BG material). The former three will be introduced more closely in the following subsections, where we also point out their limitations from a purely analytical perspective without explicit comparison against experimental data. Afterwards, we will zero in on a general structure of the underlying material model and its form of the equations of stress-strain dynamics to allow for successful experimental studies and estimation of Dyneema® UHMWPE fibers.

5.1.1 Maxwell Material

Maxwell material (MW material) can be represented as linear combination of a purely elastic spring and a purely viscious damper (see Fig. 5.5). Applying Eq. (5.4), we obtain the constitutive material equation

$$\dot{\varepsilon} = \frac{1}{E_1}\,\dot{\sigma} + \frac{1}{\eta_2}\,\sigma\,,$$

for which the responses to strain step and stress step are

$$\varepsilon(t) = \varepsilon_0 + \frac{\sigma_0}{E_1}\,t\,, \tag{5.5a}$$

$$\sigma(t) = \sigma_0\,\exp\left(-\frac{E_1}{\eta_1}\,t\right), \tag{5.5b}$$

with stress step of σ_0 and strain step ε_0. Materials described by MW material show a continuous linear increase of strain over time (see Eq. (5.5a)

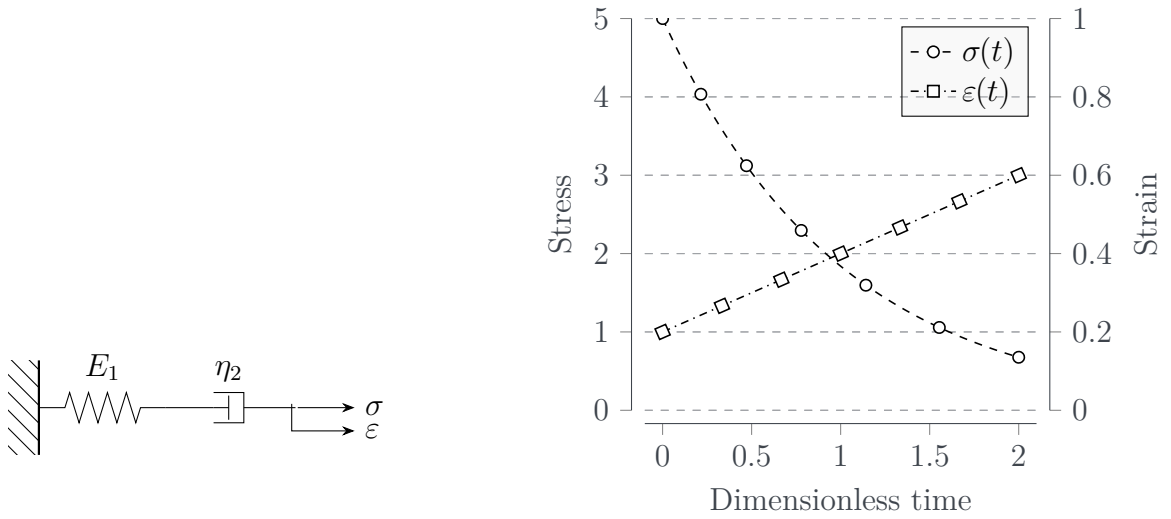

(a) *Maxwell material model composed of linear spring and linear damper in series.*

(b) *Stress and strain step response of the Maxwell material model with* $E_1 = 5\,\mathrm{Pa}, \eta_1 = 5\,\mathrm{Pa\,s}$.

Figure 5.5: Mechanical model schematic of Maxwell material model (a) and stress and strain step response of the material (b).

and Fig. 5.5(b)) which may not be observed in the physical material of Dyneema® cables.

5.1.2 Kelvin–Voigt Material

Kelvin–Voigt material (KV material) is a parallel combination of the same components as MW material (see Fig. 5.6). This material model is most often used for dynamics simulation of cable robots as it covers instantaneous and short-term dynamics of the cables well (see Miermeister (2010), Tempel et al. (2015b), Korayem et al. (2017), Zarebidoki et al. (2011a), and Mousavi et al. (2018)). Using Eq. (5.4), we obtain the constitutive material equation

$$\dot{\varepsilon} + \frac{E_1}{\eta_1}\,\varepsilon = \frac{1}{\eta_1}\,\sigma\,,$$

for which we may state the responses to strain step and stress step as

$$\varepsilon(t) = \frac{\sigma_0}{E_1} + \left(\varepsilon_0 - \frac{\sigma_0}{E_1}\right) \exp\left(-\frac{E_1}{\eta_1}\,t\right), \tag{5.6a}$$

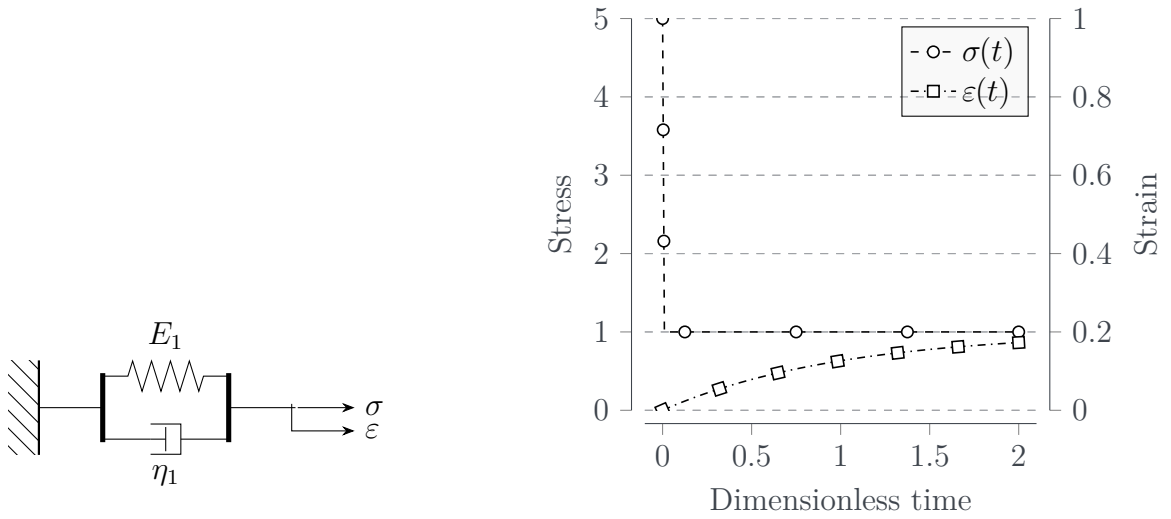

(a) *Kelvin–Voigt material model composed of linear spring and linear damper in parallel.* **(b)** *Step response of the Kelvin–Voigt material model with* $E_1 = 5\,\mathrm{Pa}$, $\eta_1 = 5\,\mathrm{Pa\,s}$.

Figure 5.6: Mechanical model schematic of Kelvin–Voigt material model (a) and stress and strain step response of the material (b).

$$\sigma(t) = \varepsilon_0\, E_1 + \varepsilon_0\, \eta_1\, \delta(t), \tag{5.6b}$$

with stress step of σ_0 and strain step ε_0.

We may directly see a (numerical) limitation of the model being a dominant effect in cable robot simulation. Conventionally, we want to infer the resulting stress induced on the platform due to cable strain, which, following Eq. (5.6b) appears to be directly linked to the strain step ε_0. However, care needs to be taken as the underlying ODE consists of a feedthrough thus is improper (noncausal) i.e., the material gives instantaneous stress relaxation due to the presence of the dashpot. Any small change in strain is immediately visible in the stress which numerically causes, during simulation, very small step sizes, in particular when paired with the discontinuity around zero strain (see Eq. (2.23)).

Limitations of the KV material are covering certain aspects of the cable material under investigation as it does not allow for an instantaneous strain response due to the damper employed in parallel (see Fig. 5.6(b)). In addition, the material model describes noncausal behavior for the strain-to-stress transfer function i.e., any change in strain ε is directly visible in the stress due to

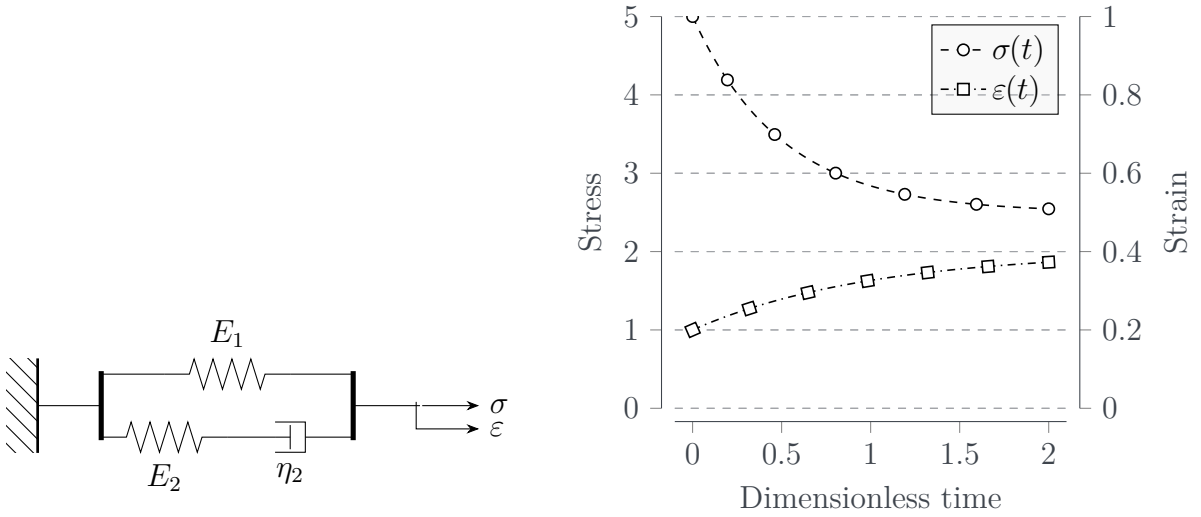

(a) *Zener material model composed of linear spring parallel to a Maxwell material in series; Maxwell representation.*

(b) *Step response of the Zener material model with* $E_1 = E_2 = 5\,\mathrm{Pa}$, $\eta_2 = 5\,\mathrm{Pa\,s}$.

Figure 5.7: Mechanical model schematic of Zener material model (a) and stress and strain step response of the material (b).

occurrence of derivatives of higher-order on the strain side than on the stress side.

5.1.3 Zener Material

Zener material (ZR material) overcomes limitations of MW material and KV material by combining a purely linear spring $\langle E_1 \rangle$ with a KV material $\langle E_2; \eta_2 \rangle$, thus allowing for both an instantaneous strain response as well as a settling strain behavior. By means of Eq. (5.4), we obtain the constitutive material equation

$$\dot{\varepsilon} + \frac{E_1\,E_2}{\eta_2\,(E_1 + E_2)}\,\varepsilon = \frac{1}{E_1 + E_2}\,\dot{\sigma} + \frac{E_2}{\eta_2\,(E_1 + E_2)}\,\sigma\,,$$

for which the responses to strain step and stress step are

$$\varepsilon(t) = \sigma_0 \left(\frac{E_1 + E_2}{E_1\,E_2} + \left(\frac{1}{E_1} - \frac{E_1 + E_2}{E_1\,E_2} \right) \exp\left(-\frac{E_2}{\eta_2}\,t \right) \right), \tag{5.7a}$$

$$\sigma(t) = \frac{E_1\,E_2}{E_1 + E_2}\,\varepsilon_0 + \left(\sigma_0 - \frac{E_1\,E_2}{E_1 + E_2}\,\varepsilon_0\right) \exp\left(-\frac{E_1 + E_2}{\eta_2}\,t\right), \tag{5.7b}$$

with initial stress σ_0 and initial strain ε_0, respectively, stepping to final stress σ_1 and final strain ε_1, respectively.

With ZR material, a decreasing creep function i.e., an asymptotic strain function at constant stress input can be achieved, which settles in at $\lim_{t\to\infty} \sigma(t) = \sigma_1(E_1\,E_2)/(E_1 + E_2)$ (see Fig. 5.6(b)).

Summary

The material models presented in Sections 5.1.1 to 5.1.3 can be used to approximate viscoelastic material behavior of not only polymers (see Haghighipanah et al. (2015), Palli et al. (2012), Piao et al. (2017), Romanyk et al. (2013), and Miyasaka et al. (2016)), however, they render unfit for further investigation due to their inability to closely reproduce stress-strain dynamics of UHMWPE Dyneema® cables with their stress relaxing over multiple relaxation times i.e., creep behavior. Experimental data (see Fig. 5.2 for a short-term overview of the stress-strain dynamics) shows stress relaxations in different time ranges of several seconds to several minutes[36]. Such multi-scale stress relaxation cannot be captured by a single MW material or KV material as we can see multiple stress relaxation responses given a single strain-step input; these must each be represented by one single MW material or KV material element. Furthermore, a one-component KV material element may be simply parametrized, yet it features two major drawbacks 1) it does not capture instantaneous stress response as the physical cable does, nor is it 2) suitable for numerical simulations due to its improper response to strain-step inputs. The reasoning for introducing a viscoelastic element into the overall cable robot model to overcome kinematic redundancy and overdeterminedness from having more cables than platform

[36] Long term observations i.e., with $T \geq 20\,\text{min}$ have not been concluded in this investigation, however, practical experience during using a cable robot with Dyneema® cables shows that stress relaxation times of several hours and days are not unlikely.

DOF is impaired by the improperness of the selected cable stress-strain dynamics model[37].

Keeping in mind the inability of the existing viscoelastic cable model to well capture the physical cable's stress dynamics, we will start off of the generalized Maxwell material (GMW material) and investigate its applicability for better capturing experimental data. We do so by sequentially increasing the number of parallel MW materials until simulation matches closely with experimental data. Our ultimate goal is not only a mathematically well-conditioned model of the stress-strain dynamics of UHMWPE Dyneema® fiber cables, but also to provide a model that is based on mechanical principles rater than providing an purely data-driven interpolation or compensation formulation.

5.2 Identification Procedure

In order to make a blanket statement about the material model suitable for predicting the stress-strain dynamics of Dyneema® cables, we must experimentally obtain data to use for later fitting of transfer functions with a suitable number of zeros and poles. After having obtained such transfer functions, we may retrieve one set of mechanical parameters that corresponds with the estimated transfer function. The estimation procedure is as follows:

1. Experimentally obtain stress-response given a stress input (Section 5.2.1)
2. Numerically fit transfer function with given number of poles and zeros to data (Section 5.2.2)
3. Estimate elastic and viscous parameters from coefficients of transfer function (Section 5.2.3)

[37] At least in the case of strain or elongation as input to the cable model and stress as output. When using force or torque based control methods such as computed torque, there is no need for avoiding the system's overdeterminedness by means of such a bracket.

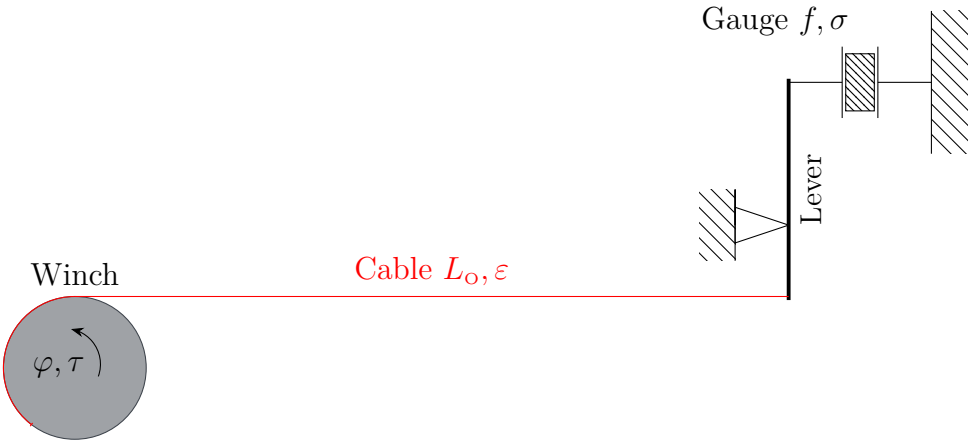

Figure 5.8: Sketch of the stress-strain dynamics identification test bench.

5.2.1 Experimental Setup and Rig

In order to approximate the strain-step response of the Dyneema® cable exemplified in Fig. 5.2, we require measurement of the stress given rapid strain changes. By means of rapidly pulling on the cable at the proximal end and measuring the stress response on the distal end, we obtain a time-dependent stress response of the material to a time-dependent strain input. This can be accomplished by either letting the cable vertically hang imposing it with various external loads, or by fixing the cable between points of which one is mechanically actuated. The former method, as implemented by Schmidt (2016) and Piao et al. (2017) and others, requires external measurement of the distal cable point to obtain elongation and allows for changing tension in only discrete steps. The latter method allows for more precise reading of the time-dependent cable stress as well as controlling using cable strain as commanded input. Since we aim for finding a model suitable of predicting the cable's stress response to a strain input, we choose the latter method allowing us to precisely describe a strain input trajectory.

We develop a cable test bench as sketched in Fig. 5.9 with a servo motor attached through a gear of ratio $i_g = 5$ to a drum of diameter $d_D = 20\,\text{cm}$ on the cable proximal end (left-hand side, cf. Fig. 5.9(a)), and a cylindrical mounting on the distal end (right-hand side, cf. Fig. 5.9(b)). Further mechanical parameters are tabularized in Table 5.1. This cylindrical mounting in turn is supported on

Table 5.1: Mechanical parameters of the cable identification test rig.

Property	Value	Unit
Winch		
Drum diameter	200	mm
Gear ratio	5	–
Drive Stall torque	12	N m
Maximum cable force	600	N
Force sensor		
Force sensor range	0—5000	N
Cable		
Unstrained cable length	2.783	m
Diameter	6	mm

a cantilever arm at the end of which a pressure sensor is attached. Measured signals obtained during experiments comprise the drive's angular position and the pressure sensor's voltage. Knowing the pressure sensor composed of a Wheatstone bridge and its data sheet, we can calculate the actual cable tension from the bridge voltage. The drive's angular position is converted using the gear ratio and drum diameter into a linear position representing the cable elongation, which, given the total unstrained cable length, can be expressed as strain. Strain rates and accelerations, much like cable force rates are not explicitly measured as these are not required for later parameter estimation. The experimental procedure implies appropriate creation and application of the input signal as well as measurement of the resulting strain in a time-synchronized manner at rates similar to those of the real cable robots control system. For satisfying these self-imposed requirements, we use the same control system as employed on the COPacabana cable robots, as well as the same servo motor (see left side of Fig. 5.9(b)).

Rapid excitation of the viscoelastic material under investigation is favorable for it allows initially only exciting the elastic component; keeping strain constant allows for the apparent effect of stress relaxation as the parallel chains of MW material components tend to relax with their specific relaxation time $\tau_l = \eta_l / E_l$. In theory, the system ought be excited with a strain-impulse $\varepsilon(t) = \delta(t)$ with its Laplace transform $\mathcal{L}\{\delta\}(s) = 1$ such that the system response in Laplace

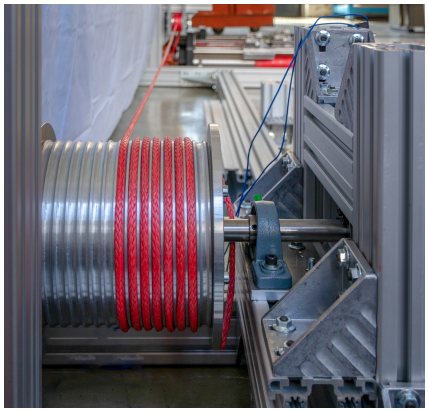

(a) *Close up view of the drum attached to the Bosch servo motor with several windings of cable wrapped around.*

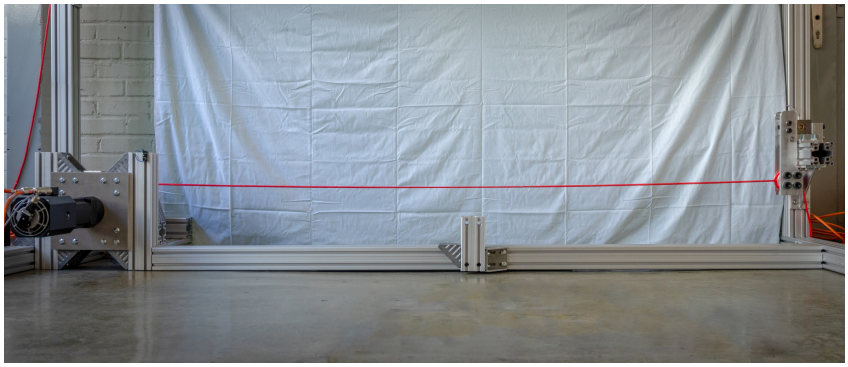

(b) *Side-view of the cable test bench with the actuating Bosch servo motor on the left-hand side and the force sensor on the right-hand side; cable in red.*

Figure 5.9: Cable test bench used for identification of stress-strain dynamics.

domain equals $Y(s) = G(s)\mathcal{L}\{\delta\}(s) = G(s)\,1$, of which the inverse Laplace transform $\mathcal{L}^{-1}\{Y\}(t) = y(t)/u(t)$ then returns the system's dynamics. However, impinging physical systems with a Dirac impulse, an infinitely large input over an infinitely small time span, is physically hardly possible due to limits arising from the system's inability to accelerate indefinitely last its inertia and discrete control system. Likewise, system identification may be performed given a step input of strain ε_0 defining the input signal as

$$\varepsilon(t) = \varepsilon_0\, H(t) = \begin{cases} \varepsilon_0\,, & t \geq 0 \\ 0\,, & t < 0 \end{cases},$$

where $H(t)$ is the Heaviside step function, its Laplace transform $\mathcal{L}\{H\}(s) = 1/s$. Due to physics in nature, it is impossible for the drive system to instantaneously transition between an initial strain ε_0 and target strain ε_1, which is why we

define the system input strain trajectory mathematically through

$$\varepsilon(t) = \begin{cases} \left(1 - \left(1 + \frac{t-T}{t_{\text{flank}}}\right)\right)\varepsilon_1 + \left(1 + \frac{t-T}{t_{\text{flank}}}\right)\varepsilon_0\,, & T - t_{\text{flank}} \leq t \wedge t < T\,, \\ \varepsilon_1\,, & \frac{T}{2} \leq t \wedge t < T - t_{\text{flank}}\,, \\ \left(1 - \left(1 + \frac{t-\frac{T}{2}}{t_{\text{flank}}}\right)\right)\varepsilon_0 + \left(1 + \frac{t-\frac{T}{2}}{t_{\text{flank}}}\right)\varepsilon_1\,, & \frac{T}{2} - t_{\text{flank}} \leq t \wedge t < \frac{T}{2}\,, \\ \varepsilon_0\,, & 0 \leq t \wedge t < \frac{T}{2} - t_{\text{flank}}\,, \end{cases}$$

with total signal period T, flank time of transition t_{flank}, and initial and final strain ε_0 and ε_1, respectively.

Despite real world applications of cable robots allowing for rapid cable velocities of up to $30\,\mathrm{m\,s^{-1}}$ (Pott et al. 2012), cable strain does not vary similarly drastically. We can size up strain and strain rate from the cable force limits and an ideal cable force controller achieving control error reduction within one control cycle[38]. Letting the cable forces be bound in $f \in [f_-, f_+] = [100, 3000]\,\mathrm{N}$ (values taken from IPAnema, cf. Pott (2018)), the control cycle be $h = 1\,\mathrm{ms}$, and the cable force error be $\Delta f = f_+ - f_- = 2900\,\mathrm{N}$. Then, under the assumption of a purely linear elastic cable with stress proportional to strain by $\sigma = \varepsilon E$ and stress proportional to applied tensile force by $\sigma = f/A$, we obtain the change of stress $\Delta\varepsilon = \Delta f / E A$. Which, for a cable of diameter $d = 6\,\mathrm{mm}$ and Young's modulus $E = 15\,\mathrm{GPa}$, gives us $\Delta\varepsilon = 0.007$, and likewise as strain rate $\dot{\varepsilon} = \Delta\varepsilon / h = 6.838\,\mathrm{s^{-1}}$. Since it is very unlikely for the cable force controller to be parametrized with such a quick control loop time, last because it may then be inherently unstable, the actual strain rate will be noticeably lower. For example, the cable force controller on the IPAnema 3 is parametrized with a control cycle time of $h = 17\,\mathrm{ms}$ (Kraus et al. 2015c) implemented as a PT_1 controller, thus it must achieve strain rates of less than $\max(\dot{\varepsilon}) = 0.101\,\mathrm{s^{-1}}$.

[38] Which, physically speaking, is very unlikely to be sustainable, yet assumed for the sake of supporting the example.

5.2.2 Fitting of Transfer Function

We assume the system dynamics be continuous in time, however, our control system operates only discrete in time, consequently we have measurements of strain input trajectory $u(t) = \varepsilon(t_l)$ and stress output $y(t) = \sigma(t_l)$ at discrete time values t_l for time values sampled at Δt. To estimate the transfer function, we require the experimental measurements be given in Laplace domain, which due to their discrete nature, are calculated by the discrete[39] Laplace transform

$$\mathcal{L}_{\Delta t}\{f\}(s) = \Delta t \sum_{l=0}^{\infty} f(l\,\Delta t)\, \exp\left(-s\, l\, \Delta t\right),$$

of a discrete function $f(t_l)$ and step size Δt. Setting $\Delta t = 1$ and $z = \exp(-s)$, we obtain the z-transform of $f(t)$ at nonnegative integers.

Using the continuous Laplace transform of our transfer function, its parameters can then be estimated by a nonlinear least-squares problem such that

$$\min_{D,N} \sum_{j}^{n_f} \left| \frac{W(s_j)}{D(s_j)} \Big(D(s_j)\, \mathcal{L}\{y\}(s_j) - N(s_j)\, \mathcal{L}\{u\}(s_j) \Big) \right|^2, \tag{5.8}$$

is the loss function to be minimized with numerator $N(s)$ and denominator $D(s)$, weight polynomial $W(s)$, and number of frequenices n_f defined by the Nyquist–Shannon sampling theorem. By choosing a non-unitary polynomial for $W(s)$ i.e., $W(s) \neq 1$, we can introduce frequency-dependent weights on the data e.g., desiring better approximation of lower or higher frequencies. For means of this thesis, we choose $W(s) \equiv 1$, putting equal trust in all frequency data. If estimation is to be performed over a set of n_{trial} trials yet for the same transfer function, then Eq. (5.8) reads

$$\min_{D,N} \sum_{j}^{n_f} \left| \frac{W(s_j)}{D(s_j)} \Big(\sum_{k}^{n_{\text{trial}}} D(s_j)\, \mathcal{L}\{y_k\}(s_j) - N(s_j)\, \mathcal{L}\{u_k\}(s_j) \Big) \right|^2. \tag{5.9}$$

[39] To be precise, the discrete Laplace transform is not discrete in ways the discrete Fourier transform is. The former evaluates a function at an infinite number of points and returns a continuous function, whereas the latter operates on a finite sequence and returns a finite sequence.

The least-squares problem is solved using S-K iteration (Sanathanan et al. 1963), a technique developed for vector fitting of frequency-domain system identification from sampled data (Drmač et al. 2015; Garnier et al. 2003; Voorhoeve et al. 2014), which iteratively solves

$$\min_{D_l,N_l} \sum_{j}^{n_f} \left| \frac{W(s_j)}{D_{l-1}(s_j)} \Big(D_l(s_j)\, \mathcal{L}\{y\}(s_j) - N_l(s_j)\, \mathcal{L}\{u\}(s_j) \Big) \right|^2$$

where $D_{l-1}(s)$ is the denominator identified in the previous iteration step, initialized with $D_0(s) = 1$. In the first iteration step, polynomials $D_1(s)$ and $N_1(s)$ are expressed in monomial basis, while all further iterations express them in terms of orthogonal rational bases functions on the unit disk. The j-th basis function reads

$$B_{j,l}(s) = \frac{\sqrt{1 - |\lambda_{j,l-1}|^2}}{q - \lambda_{j,l-1}} \prod_{r=0}^{j-1} \frac{1 - \overline{\lambda}_{j,l-1}\, q}{q - \lambda_{r,l-1}}$$

where $q = q(s)$ is the frequency-domain variable on the unit disk, $\lambda_{j,l}$ the j-th pole identified at step l, and $\overline{\lambda}_{j,l}$ its complex conjugate pole.

We may further enforce stability of the estimated transfer function which may lead to a decrease in goodness of fit, however, allows to estimate physically coherent, in particular stable, models[40]. For a linear time-invariant transfer function such as Eq. (5.3), it is sufficient to have all poles[41] in the left semi-plane of the complex variable $s \in \mathbb{C}$. In summary, the nonlinear least-squares problem is to minimize the (weighted) prediction error norm over all data samples.

[40] Additionally requiring stability may come as limitation, however, it will ensure that the estimated transfer function is physically more meaningful since the physical cable's stress-strain dynamics are inherently stable.

[41] Poles are the roots of the denominator polynomial $D(s)$.

Quantitative measure of estimation quality will be expressed as goodness of fit g given in percent such that

$$g = 100\,\% \left(1 - \frac{\|y_{\text{exp}} - y_{\text{mdl}}\|}{\|y_{\text{mdl}}\|}\right),$$

where y_{exp} are the experimental data, y_{mdl} the simulated model data and $\|\cdot\|$ indicates the 2-norm of the time-series vectors y_{exp} and y_{mdl}. Goodness of fit can vary between $g = -\infty$ (bad fit) and $g = 100$ (perfect fit), with a value of 0 indicating no better fit than a straight line equal the data mean.

5.2.3 Estimation of Mechanical Parameters

With the transfer function in form of Eq. (5.3) identified, we are able to obtain the mechanical parameters making up the numerator and denominator coefficients. Combining the symbolically obtained form of the ODE through Eq. (5.4a), we can extract the coefficients of left and right hand side which must, per definition, equal the transfer function numerator and denominator coefficients. Lastly, a nonlinear root-finding problem can be stated reading

$$\boldsymbol{e}(\boldsymbol{x}) = \begin{bmatrix} \bar{\boldsymbol{a}}(\boldsymbol{x}) - \boldsymbol{a} \\ \bar{\boldsymbol{b}}(\boldsymbol{x}) - \boldsymbol{b} \end{bmatrix}, \tag{5.10}$$

where $\boldsymbol{a}, \boldsymbol{b}$ are numerator and denominator coefficients obtained from the transfer function, $\bar{\boldsymbol{a}}, \bar{\boldsymbol{b}}$ are coefficients of the left and right-hand side of the stress-strain ODE, and $\boldsymbol{x} = [\boldsymbol{E}^\top, \boldsymbol{\eta}^\top]^\top$ are the vectors of to-be-estimated elasticities $\boldsymbol{E} = [E_1, E_2, \ldots, E_{n_{\text{mat}}}]^\top$ and viscosities $\boldsymbol{\eta} = [\eta_1, \ldots, \eta_{n_{\text{mat}}}]^\top$..

With a suitable initial estimate of elasticities and viscosities, the root-finding problem can be easily solved using methods like Newton's method or Levenberg-Marquardt revealing the physical parameter values. We initialize our estimation process by setting $E_1 = \varepsilon(0)/\sigma(0)$—or the mean value over a set of n_{trial} data from experimental trials—and by choosing $E_l = \eta_l = 1$ with $l \in \{2, \ldots, n_{\text{mat}}\}$. Further, we require corresponding elastic and viscous parameters to be of the

same sign such that their relaxation time $\tau_l = \eta_l / E_l > 0$ for any elastic and viscous modulus. Care needs to be taken in the numeric values obtained in this manner for these are not unique see e.g., relaxation time $\tau_l = \eta_l / E_l$, but also the ability to swap parameters of two viscoelastic elements.

5.3 Results

First, we estimate the stress-strain dynamics defined through the ODE as stated in Eq. (5.4a), respectively the transfer function from Eq. (5.3) with a near strain-step input. With the system dynamics estimated, we obtain numerical values of elasticity and viscosity from the coefficients. Data from several trials are then combined and provide an averaged cable stress-strain model which we will use to predict i.e., simulate the dynamics under an arbitrary strain input motion.

5.3.1 Parameter Estimation

Ultimately, we desire a stress-strain model that covers well the main dynamics of UHMWPE fiber cables over a wide range of motion i.e., for both slow and fast excitation as well as small and large deflection. In order to obtain such a model, we physically excite the cable with varying strain input trajectories for this will be the ultimate use case of the proposed model. Results presented in this section are all obtained with a fixed unstrained cable length of $L_\mathrm{o} = 2.783\,\mathrm{m}$ composed of material Dyneema® SK78 Liros D-Pro. Results of Young's modulus or elastic modulus are given in Pa rather than a specific stiffness of the cable, usually given in Pa m with respect to an unstrained length[42]. Similarly, the viscous modulus will be given in Pa s rather than as specific viscosity expressed in Pa m s. In fact, stiffness is commonly associated to the properties of a structure, whereas

[42] It may be clear to the experienced reader that a cable with longer unstrained length features an elasticity smaller than the same cable of shorter unstrained length.

Table 5.2: Values of estimated elastic and viscous parameters of the GMW material model with $n_{\mathrm{MW}} \in \{2, 3, 4\}$. Data are obtained from the estimated strain step responses graphed in Fig. 5.10.

	$n_{\mathrm{MW}} = 2$		$n_{\mathrm{MW}} = 3$		$n_{\mathrm{MW}} = 4$	
Element l	E_l/GPa	η_l/GPa s	E_l/GPa	η_l/GPa s	E_l/GPa	η_l/GPa s
1	7.252	∞	7.196	∞	7.135	∞
2	0.848	9.894	1.025	1.011	0.897	0.283
3	—	—	0.613	12.694	0.581	2.171
4	—	—	—	—	0.484	17.153

Young's modulus is related to the intrinsic mechanical properties of a material i.e., independent of its geometry.

5.3.1.1 Impact of Number of Elements

While Maxwell-chain material models comprise multiple elastic and viscous components, the number of MW material elements marks the only independent parameter for representing a physical viscoelastic material response. In fact, each MW material can be parametrized by a single parameter, its relaxation time $\tau_l = \eta_l / E_l$, showing us that elasticity and viscosity are proportional to each other and may not be chosen uniquely without incorporating further data. Since each MW material reflects stress relaxation occurring at a given time instance τ_l and vanishes before then i.e., vanishes for $t < \tau_l$, the number of elements can be chosen from strain-step response given infinite observation of stress. However, from a practical perspective, such very slow relaxation is not of major interest for the latter use of the proposed model since cable robots will not remain steady for long terms.

It is clear from Fig. 5.2 that a single spring is not sufficiently covering the relaxing strain-step behavior. As such, we investigate a Maxwell-chain material model with $n_{\mathrm{mat}} \in \{2, 3, 4\}$ such that at least one MW material is included. Incorporating one component, we see instantaneous relaxation as the strain-step ends, as well as the anticipated stress relaxation during constant strain (see Fig. 5.11). However, the instantaneous peak of stress at $t = 45\,\mathrm{s}$ as anticipated by the estimated transfer function does not reach the same

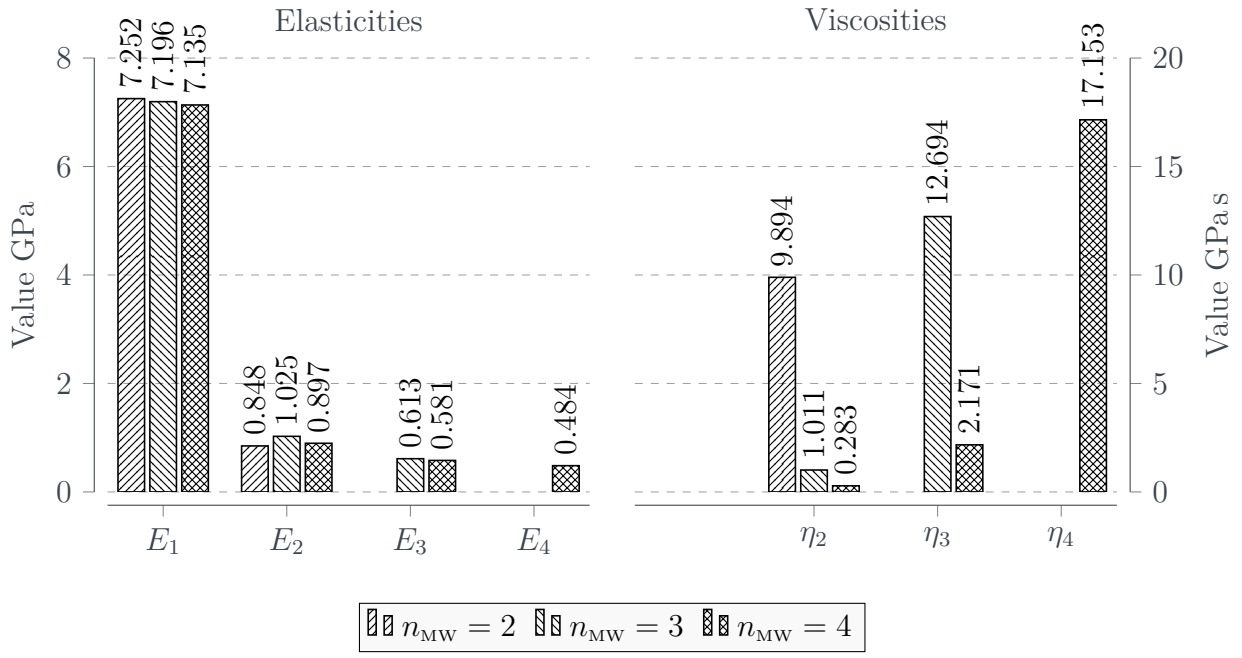

Figure 5.10: Elastic and viscous parameters of GMW material model estimated over $n_{\mathrm{trial}} = 10$ trials for $n_{\mathrm{MW}} \in \{2, 3, 4\}$. Purely elastic behavior, parametrized solely by E_1 is estimated to $E_1 \approxeq 7\,\mathrm{GPa}$, conforming with manufacturers' data sheets. Further mechanical parameters E_l and η_l $(l \in \{2, 3, 4\})$ are not available in data sheets. Numeric values are given in Table 5.2. Note the first MW material element contains no damper, which can be expressed by $\eta_1 = \infty$.

absolute values—the error between measurement and model maximizes up to $\Delta f = 53.800\,\mathrm{N} \approxeq 10.374\,\%$. On the other hand, during instantaneous relaxation at $t = 90\,\mathrm{s}$, the model predicts the cable force at a maximum error of $\Delta f = -1.646\,\mathrm{N} \approxeq -41.088\,\%$, which is a non-negligible underestimation of the cable force. Increasing the number of MW material components to $n_{\mathrm{MW}} = 3$ we obtain smooth approximation of the stress relaxation, in particular the dogleg after strain increase gets smoothed noticeably, decreasing the error of approximation and improving goodness of fit from 95.700 % to 98.100 %. Further increasing the number of MW material elements does not improve goodness of fit noticeably, which is expected as the duration of the strain plateau is kept reasonably short with only $t_{\mathrm{plateau}} = 45\,\mathrm{s}$. With longer plateau times, the cable will tend to relax farther with an asymptotic response that will ultimately converge toward the initial tension implicating MW material components with very low relaxation times $\tau_l = \eta_l / E_l$.

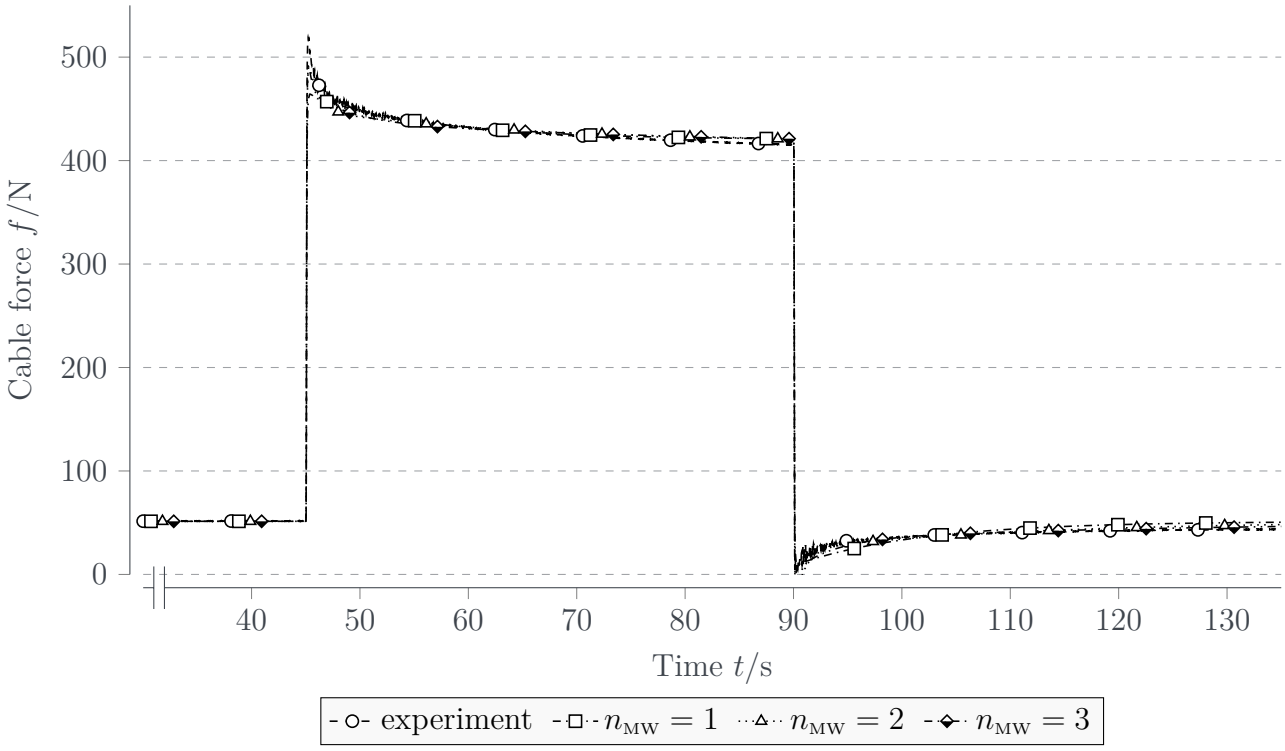

Figure 5.11: Estimated strain-step response of Dyneema® SK78 cable with number of MW material varying from $n_{\mathrm{MW}} = 2$ to $n_{\mathrm{MW}} = 4$. Increasing the number of MW material elements smooths the instantaneous step-response of the material at $t_{\mathrm{step}} = 45\,\mathrm{s}$. Numerical values of parameters obtained from estimation are given in Table 5.2.

Comparing numerical values of elasticity and viscosity given in Table 5.2 with those by the manufacturer is doomed to fail due to the manufacturer providing only yield strengths and maximum strain under high load. Since these values are obtained under different conditions and different scenarios—tensile strength and maximum strain are provided at break—their transferability seems very underhanded. Results presented by other research groups like Piao et al. (2017), Sanborn et al. (2015), Vlasblom et al. (2006), Lv et al. (2017), O'Masta (2014), Rost (2013), and Takata et al. (2018), though partially obtained with cables of different diameter, show both elastic and viscous parameters are within 8 % of the data obtained in aforementioned contributions.

5.3.1.2 Variation of Mechanical Properties

In Section 5.3.1.1, we Estimated viscoelastic material parameters of elasticity and viscosity over a set of $n_{\text{trial}} = 10$ trials i.e., estimation solved the least-squares problem minimizing the least squares problem from Eq. (5.9). As such, the result is the best fit to a set of data implying averaged well fit. In this section, we will focus on the constancy of mechanical properties by performing estimation on each of the $n_{\text{trial}} = 10$ trials one trial at a time. If we find out that spread / standard deviation of mechanical parameters is comparatively low among trials we can conclude that only few experiments are needed to obtain a consistently parametrized model, whereas a large standard deviation would imply the opposite. Further, small standard deviation in the mechanical parameters are favorable for on-line parameter estimation enabling us to incorporate an on-line estimation process like ARMAX into the robot. ARMAX is a model for statistical analysis of time series based on autoregressive–moving-average models (ARMA models) extending it by including also models with exogenous inputs model—in some software algorithms, exogenous inputs are also called independent inputs (Whittle 1953; Hannan 1970; Whittle 1983). With ARMA and ARMAX models, time-series of data are regressed on their own past values (AR component) in order to understand or predict future values in the series and linear modeling of the error term at coetaneous and previous time values (MA component).

Instantaneous elasticity with median $\tilde{E}_1 \approxeq 7.239\,\text{Pa}$ and small 25th and 75th percentile emerge, indicating very closely lying estimates of the purely elastic element even for every single trial (data are tabulated in Tables C.1 to C.3, mean values are visualized in Fig. 5.10). Variance $\sigma^2_{E_1}$ does not increase significantly when adding more elements to the model indicating what is to be assumed: the instantaneous stress response is captured by a purely elastic response of the cable material. With increasing number of elements, the median of the second elasticity E_2 does not change significantly, however, its variance increases as we go from a 2-element GMW material to a 4-element GMW material. Since the measured stress response is the superposed relaxation of every single MW

material element, it makes distinguishing two elements more convoluted when only relatively short-in-time data are available. We can similarly argue for the third elasticity E_3 for a GMW material with $n_{\text{MW}} = 3$ and $n_{\text{MW}} = 4$ elements. What needs to be pointed out though is the near-constancy of elastic components throughout adding more MW material elements to the model. In fact, a decay in elasticity E_2 is to be expected with increasing number of MW material elements since each element represents a single relaxation time. With more elements added, more stress relaxation transients can be approximated allowing for each element to converge closer to its specific relaxation time rather than being the least-squares fit over multiple relaxation times.

Viscous parameters η_l, on the other hand, show larger spread of data, which is to be anticipated since viscous parameters more largely affect the stress relaxation times $\tau_l = \eta_l / E_l$. With increasing number of MW material elements, we observe a decrease in the second MW material element's viscosity η_2, corresponding well with the model's assumption. Assuming only one MW material element, the material's stress relaxation has to be captured by a single relaxation time, which will ultimately, due to the estimation algorithm, lead to the parameter of viscosity being the least squares fit over all physical relaxations. When more elements are added, further stress relaxations can be captured e.g., for a two-MW material element material, the first MW material element may be characteristic for instantaneous stress relaxation, whereas the second MW material element is responsible for short-term stress relaxation. Consequently, adding more MW material elements allow for capturing more unique stress relaxations and preceding viscous parameters will decrease in their value.

Combining data from elastic and viscous parameters, we can confirm our assumptions that a material model with more MW material elements allows for better approximation of multiple unique stress relaxations compared to a material model with fewer MW material elements. In the data given, for the $n_{\text{MW}} = 4$ GMW material, we can see a decrease in the elastic parameters of each MW material element while the viscous parameters increase for each MW material element. Recalling stress relaxation time of element l is defined

through $\tau_l = \eta_l / E_l$, a decreasing elastic and increasing viscous parameter relates to an increasing relaxation time.

5.3.1.3 Conclusions

Conventional stress-strain description for cable robot cables is based either on a simple viscoelastic model composed of a linear spring in parallel to a linear damper resulting in reasonable approximation of the dynamics from stress to strain. However, the inverse dynamics formulation i.e., from strain to stress, with its use case in cable force control and forward dynamics simulation, cannot be described in this way due to missing causality. In addition, the conventional cable stress-strain model cannot describe effects like stress relaxation when under constant strain (see Fig. 5.2).

When experimentally assessing the stress-strain dynamics, we experience obvious stress-relaxation at constant strain that is dependent on the previous change of strain. To more concisely capture this behavior in a model, we apply the theory of viscoelastic materials to satisfying account and combine several serial linear spring-damper elements in parallel to obtain a model capable of predicting stress-relaxation. This mechanics approach provides approximation of experimental data used for identification at up to 98.200 % goodness-of-fit, well capturing the features of interest (instantaneous stress relaxation during tensing and relaxing).

It may further be pointed out that the stress-strain model derived in this thesis may likewise be used for the inverse direction of dynamics i.e., from stress to strain by simply inverting the estimated transfer function. This procedure is often used for feed-forward control and would allow us to feed the necessary strain trajectory into the system to achieve a desired cable stress along a trajectory.

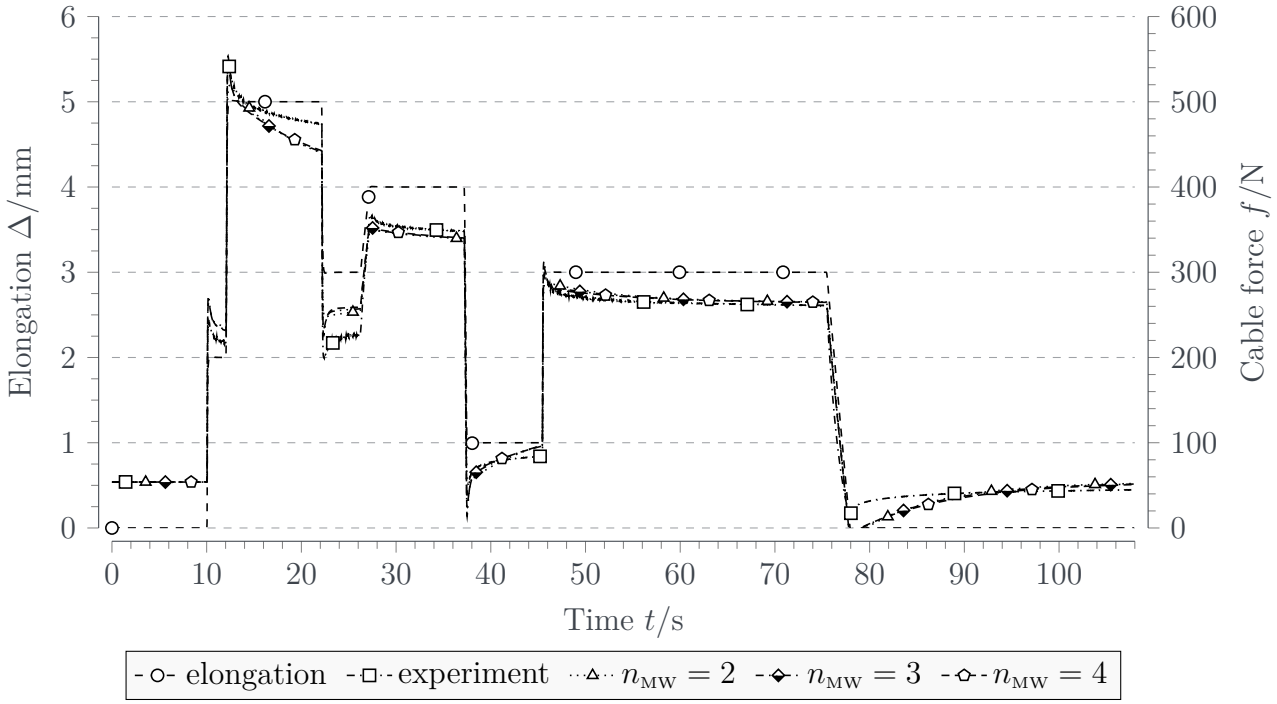

Figure 5.12: Validation results of the stress-strain dynamics over a trajectory of cable force plateaus with varying flank times and plateau times using parameters from Table 5.2. Cable material with $n_{\mathrm{mat}} = 4$ MW material components yields an overall goodness of fit of 92.3 % with noticeable deviation during the first two plateaus; yet all models drastically error after the last relaxation where the predicted cable force becomes negative whereas experimentally obtained cable force stays positive.

5.3.2 Stress-Strain Prediction

The goal of a physically more prevalent stress-strain model in mind, we aim for predicting or anticipating the stress response of Dyneema® cables after having obtained a well-parametrized model. From theory of linear time-invariant systems, we can infer that it suffices to obtain the system's response to a step-input; then performing estimation of the transfer of suitable order—in our case with $n_{\mathrm{pole}} = n_{\mathrm{zeros}} \in \{2, 3, 4\}$ poles and zeros, respectively—yields a good approximation of the overall system dynamics.

Let us thus choose the elastic and viscous parameters obtained in Section 5.3.1 and presented in Table 5.2. We choose to take the parameters averaged over all $n_{\mathrm{trial}} = 10$ trials to obtain the multi-trial best-fit transfer function.

The cable model with only one MW material component i.e., $n_{\text{mat}} = 2$ again yields only a good first-order approximation of the overall stress-strain dynamics covering qualitatively the cable's stress relaxation. Adding a second MW material in parallel to the material allows to better cover the instantaneous stress relaxation after strain is kept constant, yet only a three-MW material model ($n_{\text{mat}} = 4$) reduces the error of the instantaneous stress relaxation. In addition, with three separate relaxation elements represented by three MW material, short, medium, and long-term stress relaxation can be covered well, as anticipated by the validation experiment.

5.4 Conclusions

Stress-strain dynamics of UHMWPE fiber cables can experimentally be shown to behave dissimilar to a perfect solid i.e., to not obey Hooke's law. Given a strain-step input, asymptotic and exponential stress relaxation can be identified composed of multiple relaxations, each with its respective relaxation time. Such behavior may be modeled by means of polynomial fitting of the error between perfect solid and the observed stress-strain behavior. However, the cable material also keeps track of the history of strain inputs resulting in different hysteretic behavior when being operated on different levels of axial pretension (see Fig. 5.1). Polynomial fitting can only describe part of the cable's actual physical response since it does not consider the mechanics and kinematics of the underlying material but describes a purely phenomenological observation.

The stress-strain model provided in this chapter for the stress-strain dynamics of UHMWPE Dyneema® fiber cables is based on a mechanical description of the underlying mechanics—though still largely simplified for we consider the overall cable kinematics and not kinematics of each fiber strand and its interaction with shielding fibers. Based on viscoelastic theory, a generic model based on the generalized Maxwell material (GMW material) is proposed which is composed of an arbitrary number of serial linear spring-damper elements placed in parallel to a purely elastic spring. By means of this model, we can describe the ODE

underlying the dynamics from strain input to stress output—the main interest for control of cable robots and for force control algorithms. In particular, the proposed model's only free parameter are the number of elements in use, which must be experimentally obtained from the strain-step response.

We experimentally investigated the dynamics of a Dyneema® SK78 cable by fitting the transfer function obtained from the GMW material using an iterative S-K algorithm. A simple two-element MW material model already matches experimentally data better, in fact the instantaneous overshoot after a strain-step is evident in the simulation data. Further adding of MW material components, instantaneous stress-relaxation is captured more closely and gets smoother with every serial linear spring-damper element added. With three MW material parallel to a linear spring, goodness of fit of the transfer function plateaus at 98.200 %, as further stress-relaxation occurs slower than the experimental trial duration.

Lastly, numerical results obtained of elasticities and viscosities of the material model have to be trusted, from a purely theoretical point of view, through conformance with experimental data. Since the manufacturer's data sheet only provide for linear elasticity in a constant stress setup after sufficient relaxation time, only the purely elastic component can be verified with other data; in which case the estimated elasticity lies closely to data found in the manufacturer's data sheets. Further mechanical parameters used in the model are obtained from solving a nonlinear root-finding problem linking the transfer function's numerator and denominator coefficients to the elastic and viscous parameters.

Further steps in deepening findings of the theoretic-experimental work conducted in this thesis must include more extensive and long-term estimation procedures. Particularly influence of external environmental parameters such as temperature and light, but also the guiding and winding process of the cable are not yet linked to the new findings of the stress-strain dynamics[43]. In addition,

[43] Kraus et al. have conducted research on pulley friction, yet under the assumption of linear elastic cables, which is true for the static case of cable robot operation which is qualified through the investigations in this thesis.

linearity of elasticity and viscosity in the unstrained cable length must further be verified—or for that matter falsified since this is another crucial factor when it comes to cable force control.

Chapter 6

Summary

6.1 Conclusions

Previously unaccounted for in cable robot kinematics and dynamics, cables can now be considered using the cable model proposed in this thesis which is based on elastica theory typified by the Cosserat rod theory. By assuming cables very slender and thin rods of linear elasticity and flexibility, we can now formulate internal strain and bending deformations causing both elongation and sagging. This allows us to provide for a complete formulation of the multibody system cable robot with its mobile platform in conjunction with the cables. Numerical validation of the cable model itself shows close match with analytically obtained natural frequencies with a suitable selection of $n_\mathrm{s} = 10$ segments and a local polynomial degree $p = 4$. Also, the static cable shape lies in close proximity to the catenary cable shape by Irvine, affirming the model validity for cables and rods with much lower flexural rigidity.

We incorporated the cable model into a multibody simulation framework for cable robots that works well for different cable robot configurations like CoGiRo and IPAnema and can cover a wide range of cable robot dimensions. In the static case, the simulation framework converges quickly and consistently toward the kinetostatic equilibrium and provides force distributions close to what conventional force distribution algorithms determine. In particular, while the advanced closed form force distribution by Pott can fail or provide inconsistent data for cable robots like CoGiRo, the framework resulting from this thesis can handle these systems just as well. The obtained simulation model is composed of a single rigid body and m flexible bodies resulting in a flexible multibody

simulation formulation. Conventionally available solvers for such DAE are not capable of handling such systems due to their high numerical stiffness, which is why we propose, besides the flexible multibody formulation of cable robots, using an energy-conservative numerical time-integration scheme. While its current implementation in MATALB is computationally not very efficient, we are able to obtain energy-conservative simulation results at sampling rates of 1 ms without numerical instabilities. With the cable robot multibody simulation framework at hand, comprehensive simulation of the dynamics of interacting components of a cable robot are now possible allowing for better understanding of cable robot behavior. Feasibility and scalability of the multibody cable robot model is demonstrated.

On the topic of axial stress-strain dynamics, existing methods to describing such dynamics mechanically are applied to Dyneema® fiber cables. Experimental data shows hysteretic behavior during tensing and relaxing as well as stress relaxation when under constant strain. The mechanical model's dynamics were successfully used for estimation of the mechanical parameters of elasticity and viscosity using the S-K algorithm. Validation of the stress-relaxation and hysteresis with the material parametrized through experiments shows validity of the selected model type as well as its quantitative parameters.

6.2 Outlook

On the side of simulation, we should desire faster numerical integration of the dynamics of a cable robot as formulated in this thesis. This may either be very easily obtained by converting the MATLAB-based simulation framework into a C/C++-based framework, while keeping its modularity in mind. It may, however, also be obtained by using numerically more efficient root-finding problems compared to the rather simple Newton's method used in finding the results in presented in this thesis. While the number of iterations has never outreached the self-set limit of 100 iterations, Newton's method's constant step size hinders the root-finding from making larger steps along the gradient—this

may easily be remedied by using a trust-region-reflective algorithm or Levenberg-Marquardt with adaptive step size. While the iterative integration schemes has several advantages over conventional ODE-solver, it inherently results in a nonlinear residual function needing evaluation. That is, other than conventional ODE-solver solving for the state's derivative and integrating over time, this formulation will inherently always remain slower. It remains to be seen how much speed improvement can be gained.

Our multibody cable robot simulation framework was initially implemented using constraint-violation handling based on GGL, which allows for solving for the accelerations, yet introduces an additional level of constraints on the velocity level. Due to numerical issues of stability and small time-step sizes, we transitioned to the mechanical integrator by Betsch which does not feature these shortcomings, yet requires iteratively solving a system of nonlinear equations in the next-state estimates. There are other numerical integration schemes specifically designed for multibody systems of largely varying stiffness or incorporating beams or cables like the projective dynamics methods used by Soler et al. (2018). These integrators also provide force and momentum-consistent integration while not requiring solving nonlinear root-finding problems at every time-step. From the numerical point of view, there is room for improvement, requiring however good knowledge of numerical integration schemes and the mechanics behind the system.

The cable model based on the well-established Cosserat rod theory can be transferred to describing a full cable robot system, despite it primarily addressing beams and rods. However, it currently lacks viscous dynamics and as such any oscillation remains undamped. It is possible to incorporate viscous components into the Cosserat rod by means of conventional KV material elements (Lacarbonara et al. 2008; Lang et al. 2013). This will render the cable model more realistic, however, also more challenging to parametrize as further mechanical properties needs to be identified.

Results obtained from cable axial stress-strain dynamics identification can now be used in order to better evaluate cable force control or to implement

model-based control on the force level. Since the dynamics formulation comprise a linear ODE rather than nonlinear compensation methods, it is possible to use the resulting transfer function in feed-forward control or model-based creep compensation. This remedies having to tune cable force controller with large safety margins due to stability concerns.

Experimental observations give the delusive impression that a purely spring-damper based kinematic cable is insufficient with regards to short-term dynamics. This impression stems from cables showing some memory effect when being continuously excited and then kept at constant strain. Such behavior cannot be modeled through springs or dampers, but by means of fractional derivatives (Mainardi et al. 2011). Using fractional derivatives, external excitation on the cable like contact with pulleys or the winch can be modeled too, as these affect the stress-strain propagation in dependence of the direction of excitation (Sun et al. 2015). Following this direction requires though more deeper knowledge and understanding of material rheology, which may be out of the scope of any roboticist.

The most challenging open task resulting from the two findings of this thesis—a flexible multibody simulation framework and the stress-strain dynamics of fiber cables—is the incorporation of the latter in the former. We propose a spatial cable model based on purely linear elasticity, while on the other hand showing that physical fiber cables behave anything but that. However, while the stress-strain dynamics of fiber cables remains largely uncharted territory, its incorporation into the Cosserat rod-based cable remains to-be-completed. Extensions of the Cosserat rod with viscoelastic elements can be done, however, the stress-strain cable model we presented is more complex than a simple spring-damper element requiring the fourth-order derivative of strain and stress. To attain continuity of the cable shape in itself, the polynomial degree must be raised. Another major challenge arising from this task lies in a mechanically consistent formulation of internal energies and forces using a 4th-order ODE on stress and strain. Without profound knowledge in continuum mechanics and possibly even viscoelastic materials, this task must remain open for the time being.

Lastly, as is the case with any modeling and simulation, obtaining mechanical parameters in order to parametrize the model is as vital as is a sufficient model. Most of the parameters for the cable model presented in this thesis can be obtained rather straightforward like cross-section area, diameter, unit weight, or length. However, obtaining values for the parameters specifically impacting dynamics like elastic modulus, shear modulus, or viscous modulus, is not straightforward. With the experimental identification of the stress-strain dynamics, we presented a methodology for obtaining numerical values of elasticity and viscosity, yet other values remain unknown. If we are interested in physically meaningful parameter values of our cable robot model, then experimental parameter identification of unknown parameters have to be made. If all we are interested in is a realistically behaving cable robot model, then physically meaningful values may no be of interest and we can choose to use optimization methods matching simulation data with experimental data to find the right parameter set. Consequently, experimental validation of the spatial cable model presented in this thesis is necessary and ought be the next step.

Bibliography

(RIA) 1999 (RIA), Robotic Industries Association, 1999. *American National Standard for Industrial Robots and Robot Systems: Safety Requirements*. ANSI/RIA R15.06-1999. Robotic Industries Association (RIA) and American National Standards Institute Inc. (ANSI). Ann Arbor, MI, USA. URL: https://webstore.ansi.org/standards/ria/ansiriar15061999.

Abdolshah et al. 2015 Abdolshah, Saeed; Barjuei, Erfan Shojaei, 2015. Linear Quadratic Optimal Controller for Cable-Driven Parallel Robots. *Frontiers of Mechanical Engineering* **10** (4), pp. 344–351. ISSN: 2095-0233. DOI: 10.1007/s11465-015-0364-8.

Abramowitz et al. 1972 Abramowitz, Milton; Stegun, Irene A., 1972. *Handbook of Mathematical Functions*. With Formulas, Graphs, and Mathematical Tables. 9th ed. Vol. 55. Applied Mathematics Series. New York, NY, USA: United States Department of Commerce, National Bureau of Standards and Dover Publications. ISBN: 978-0-486-61272-0. DOI: 10.1119/1.1972842.

Adamiec-Wójcik et al. 2014 Adamiec-Wójcik, Iwona; Awrejcewicz, Jan; Brzozowska, Lucyna; Drąg, Łukasz, 2014. Modelling of Ropes With Consideration of Large Deformations and Friction by Means of the Rigid Finite Element Method. In: Jan Awrejcewicz, (ed.). *Applied Non-Linear Dynamical Systems*. Vol. 93. Springer Proceedings in Mathematics & Statistics. Cham, Switzerland: Springer, pp. 115–137. ISBN: 978-3-319-08265-3. DOI: 10.1007/978-3-319-08266-0_9.

Adamiec-Wójcik et al. 2015 Adamiec-Wójcik, Iwona; Brzozowska, Lucyna; Drąg, Łukasz, 2015. An Analysis of Dynamics of Risers During Vessel Motion by Means of the Rigid Finite Element Method. *Ocean Engineering* **106**, pp. 102–114. ISSN: 0029-8018. DOI: 10.1016/j.oceaneng.2015.06.053.

Adamiec-Wójcik et al. 2013 Adamiec-Wójcik, Iwona; Brzozowska, Lucyna; Wojciech, Stanisław, 2013. Modification of the Rigid Finite Element Method in Modeling Dynamics of Lines and Risers. *Archive of Mechanical Engineering* **60** (3), pp. 409–429. ISSN: 0004-0738. DOI: 10.2478/meceng-2013-0026.

Albus et al. 1992 Albus, James S.; Bostelman, Roger V.; Dagalakis, Nicholas G., 1992. The NIST ROBOCRANE: Originally published as "The NIST SPIDER, A Robot Crane". *Journal of Research of the National Institute of Standards and Technology* **97** (3), pp. 373–385. DOI: 10.6028/jres.097.016. URL: https://ws680.nist.gov/publication/get_pdf.cfm?pub_id=820409.

Alikhani et al. 2011 Alikhani, Alireza; Vali, Mehdi, 2011. Modeling and Robust Control of a New Large Scale Suspended Cable-Driven Robot Under Input Constraint. In: *Ubiquitous Robots and Ambient Intelligence: Proceedings of the 2011 IEEE International Conference on*. 2011 IEEE International Conference on Ubiquitous Robots and Ambient Intelligence. IEEE, pp. 238–243. ISBN: 978-1-4577-0722-3. DOI: 10.1109/urai.2011.6145969.

Altschuler 1998 Altschuler, Daniel R., 1998. The National Astronomy and Ionosphere Center's (NAIC) Arecibo Observatory in Puerto Rico: Particle Physics and Cosmology. In: José F. Nieves, (ed.). *Particle Physics and Cosmology and the Second Latin American Symposium on High Energy Physics: First Tropical Workshop on*. First Tropical Workshop on Particle Physics and Cosmology and the Second Latin American Symposium on High Energy Physics. San Juan, Puerto Rico, USA, Apr. 1–11, 1998. Vol. 444. 1. American Institute of Physics (AIP), pp. 563–570. ISBN: 1-56396-775-8. DOI: 10.1063/1.56603.

Altschuler 2002 Altschuler, Daniel R., 2002. The National Astronomy and Ionosphere Center's (NAIC) Arecibo Observatory in Puerto Rico. In: Sneśzana Stanimirović; Daniel Altschuler; Peter B. Goldsmith; Chris Salter, (eds.). *Single-Dish Radio Astronomy: Techniques and Applications*. San Francisco, CA, USA.

Vol. 278. Astronomical Society of the Pacific Conference Series 1. National Radio Astronomy Observatory (NRAO) et al. Astronomical Society of the Pacific, pp. 1–24. ISBN: 1-58381-120-6. URL: https://ui.adsabs.harvard.edu/abs/2002aspc..278....1a.

Antman 2005 Antman, Stuart S., 2005. *Nonlinear Problems of Elasticity*. Applied Mathematical Sciences. New York, NY, USA: Springer-Verlag. ISBN: 0-387-20880-1. DOI: 10.1007/0-387-27649-1.

Ardema 2005 Ardema, Mark D., 2005. *Analytical Dynamics: Theory and Applications*. New York, NY, USA: Kluwer Academic/Plenum Publishers. ISBN: 0-306-48681-4. DOI: 10.1007/b116020.

Arnold 2004 Arnold, Martin, 2004. *Simulation Algorithms in Vehicle System Dynamics*. Tech. rep. 27. Department of Mathematics and Computer Science, Martin-Luther-University Halle. URL: http://www.mathematik.uni-halle.de/reports/sources/2004/04-27report.pdf.

Ayala Cuevas et al. 2017 Ayala Cuevas, Jorge Ivan; Laroche, Édouard; Piccin, Olivier, 2017. Assumed-Mode-Based Dynamic Model for Cable Robots With Non-Straight Cables. In: Clément M. Gosselin; Philippe Cardou; Tobias Bruckmann; Andreas Pott, (eds.). *Cable-Driven Parallel Robots: Proceedings of the Third International Conference on Cable-Driven Parallel Robots*. Mechanisms and Machine Science 53. Cham, Switzerland: Springer, pp. 15–25. ISBN: 978-3-319-61431-1. DOI: 10.1007/978-3-319-61431-1_2.

Babaei et al. 2016 Babaei, Behzad; Davarian, Ali; Pryse, Kenneth M.; Elson, Elliot L.; Genin, Guy M., 2016. Efficient and Optimized Identification of Generalized Maxwell Viscoelastic Relaxation Spectra. *Journal of the Mechanical Behavior of Biomedical Materials* **55**, pp. 32–41. DOI: 10.1016/j.jmbbm.2015.10.008. eprint: 2652-3785.

Baraff 1996 Baraff, David, 1996. Linear-Time Dynamics Using Lagrange Multipliers. In: *Computer Graphics and Interactive Techniques: Proceedings of the 1996 Annual Conference on*. Pittsburg, PA, USA. COMPUTERGRAPHICS Annual Conference Series CMU-RI-TR-95-44. The Robotics Institute, Carnegie Mellon University. ACM Press. DOI: 10.1145/237170.237226. URL: https://ri.cmu.edu/pub_files/pub2/baraff_david_1996_1/baraff_david_1996_1.pdf.

Baumgarte 1972 Baumgarte, Joachim W., 1972. Stabilization of Constraints and Integrals of Motion in Dynamical Systems. *Computer Methods in Applied Mechanics and Engineering* **1** (1), pp. 1–16. ISSN: 0045-7825. DOI: 10.1016/0045-7825(72)90018-7.

Bedoustani et al. 2008 Bedoustani, Yousef Babazadeh; Bigras, Pascal; Taghirad, Hamid D.; Aref, Mohammad M., 2008. Dynamics Analysis of a Redundant Parallel Manipulator Driven by Elastic Cables. In: *Control, Automation, Robotics and Vision: Proceedings of the 2008 IEEE International Conference on*. 2008 IEEE International Conference on Control, Automation, Robotics and Vision. Hanoi, Vietnam. Institute of Electrical and Electronics Engineers (IEEE). IEEE, pp. 536–542. DOI: 10.1109/icarcv.2008.4795575.

Bedoustani et al. 2011 Bedoustani, Yousef Babazadeh; Bigras, Pascal; Taghirad, Hamid D.; Bonev, Ilian A., 2011. Lagrangian Dynamics of Cable-Driven Parallel Manipulators: A Variable Mass Formulation. *Transactions of the Canadian Society for Mechanical Engineering* **35** (4), pp. 529–542. ISSN: 0315-8977. DOI: 10.1139/tcsme-2011-0032.

Behzadipour et al. 2006 Behzadipour, Saeed; Khajepour, Amir, 2006. Stiffness of Cable-Based Parallel Manipulators With Application to Stability Analysis. *Journal of Mechanical Design* **128** (1), pp. 303–310. ISSN: 1050-0472. DOI: 10.1115/1.2114890.

Bellucci 2014 Bellucci, Michael A., 2014. *On the Explicit Representation of Orthonormal Bernstein Polynomials*. URL: http://arxiv.org/pdf/1404.2293v2.

Bensoam 2013 Bensoam, Joel, 2013. Differential Geometry Applied to Acoustics: Non Linear Propagation in Reissner Beams. In: Frank Nielsen; Frédéric Barbaresco, (eds.). *Geometric Science of Information*. Vol. 8085. Lecture Notes in Computer Science (LNCS) and Image Processing, Computer Vision, Pattern Recognition, and Graphics (LNIP). Berlin, Germany and Heidelberg, Germany: Springer, pp. 641–649. ISBN: 978-3-642-40019-3. DOI: 10.1007/978-3-642-40020-9_71.

Berti et al. 2017 Berti, Alessandro; Gouttefarde, Marc; Carricato, Marco, 2017. Dynamic Recovery of Cable-Suspended Parallel Robots After a Cable Failure. In: Jadran Lenarčič; Jean-Pierre Merlet, (eds.). *Advances in Robot Kinematics 2016*. Vol. 4. Springer Proceedings in Advanced Robotics 4. Cham, Switzerland: Springer, pp. 331–339. ISBN: 978-3-319-56802-7. DOI: 10.1007/978-3-319-56802-7_35.

Berti et al. 2012 Berti, Alessandro; Merlet, Jean-Pierre; Carricato, Marco, 2012. Solving the Direct Geometrico-Static Problem of 3-3 Cable-Driven Parallel Robots by Interval Analysis: Preliminary Results. In: Tobias Bruckmann; Andreas Pott, (eds.). *Cable-Driven Parallel Robots*. Mechanisms and Machine Sciences 12. Berlin, Germany and Heidelberg, Germany: Springer, pp. 251–268. ISBN: 978-3-642-31987-7. DOI: 10.1007/978-3-642-31988-4_16.

Berti et al. 2015 Berti, Alessandro; Merlet, Jean-Pierre; Carricato, Marco, 2015. Solving the Direct Geometrico-Static Problem of Underconstrained Cable-Driven Parallel Robots by Interval Analysis. *The International Journal of Robotics Research* **35** (6), pp. 723–739. ISSN: 0278-3649. DOI: 10.1177/0278364915595277.

Betsch 2005 Betsch, Peter, 2005. The Discrete Null Space Method for the Energy Consistent Integration of Constrained Mechanical Systems. *Computer Methods in Applied Mechanics and Engineering* **194** (50-52), pp. 5159–5190. ISSN: 0045-7825. DOI: 10.1016/j.cma.2005.01.004.

Betsch 2006 Betsch, Peter, 2006. Energy-Consistent Numerical Integration of Mechanical Systems With Mixed Holonomic and Nonholonomic Constraints. *Computer Methods in Applied Mechanics and Engineering* **195** (50-51), pp. 7020–7035. ISSN: 0045-7825. DOI: 10.1016/j.cma.2005.01.027.

Bhatti et al. 2007 Bhatti, M. Idrees; Bracken, Paul, 2007. Solutions of Differential Equations in a Bernstein Polynomial Basis. *Journal of Computational and Applied Mathematics* **205** (1), pp. 272–280. ISSN: 0377-0427. DOI: 10.1016/j.cam.2006.05.002.

Birdsall et al. 1991 Birdsall, Charles K.; Langdon, A. Bruce, 1991. *Plasma Physics via Computer Simulation*. Series in Plasma Physics. IOP Publishing Ltd. ISBN: 978-0-070-05371-7. DOI: 10.1887/0750301171.

Bishop 1975 Bishop, Richard L., 1975. There Is More Than One Way to Frame a Curve. *The American Mathematical Monthly* **82** (3), p. 246. ISSN: 0002-9890. DOI: 10.2307/2319846.

Blajer 2011 Blajer, Wojciech, 2011. Methods for Constraint Violation Suppression in the Numerical Simulation of Constrained Multibody Systems: A Comparative Study. *Computer Methods in Applied Mechanics and Engineering* **200** (13-16), pp. 1568–1576. ISSN: 0045-7825. DOI: 10.1016/j.cma.2011.01.007.

Blanchet et al. 2014 Blanchet, Laurent; Merlet, Jean-Pierre, 2014. Interference Detection for Cable-Driven Parallel Robots (CDPRs). In: *Advanced Intelligent Mechatronics: Proceedings of the 2014 IEEE/ASME International Conference on*. 2014 IEEE/ASME International Conference on Advanced Intelligent Mechatronics. Besacon, France, July 8–11, 2014. Institute of Electrical and Electronics Engineers (IEEE).

Bokaian 1990 Bokaian, Alireza R., 1990. Natural Frequencies of Beams Under Tensile Axial Loads. *Journal of Sound and Vibration* **142** (3), pp. 481–498. ISSN: 0022-460X. DOI: 10.1016/0022-460x(90)90663-k.

Boor 1978 Boor, Carl de, 1978. *A Practical Guide to Splines*. Vol. 27. Applied Mathematical Sciences. New York, NY, USA, Berlin, Germany, and Heidelberg, Germany: Springer New York. ISBN: 978-3-540-90356-7. DOI: 10.1007/978-1-4612-6333-3. URL: http://d-nb.info/790067706/04.

Borgstrom et al. 2009 Borgstrom, Per Henrik; Jordan, Brett L.; Sukhatme, Guarav S.; Batalin, Maxim A.; Kaiser, William J., 2009. Rapid Computation of Optimally Safe Tension Distributions for Parallel Cable-Driven Robots. *IEEE Transactions on Robotics* **25** (6), pp. 1271–1281. DOI: 10.1109/tro.2009.2032957.

Bosscher et al. 2007 Bosscher, Paul; Williams, Robert L.; Bryson, L. Sebastian; Castro-Lacouture, Daniel, 2007. Cable-Suspended Robotic Contour Crafting System. *Automation in Construction* **17** (1), pp. 45–55. ISSN: 0926-5805. DOI: 10.1016/j.autcon.2007.02.011.

Bostelman et al. 1994 Bostelman, Roger V.; Albus, James S.; Dagalakis, Nicholas G.; Jacoff, Adam; Gross, John, 1994. Applications of the NIST ROBOCRANE. In: *Robotics and Manufacturing: Proceedings of the 1994 ASME International Symposium on*. 1994 ASME International Symposium on Robotics and Manufacturing. Maui, HI, USA. American Society of Mechanical Engineers (ASME). ASME, pp. 403–410.

Box 1976 Box, George E. P., 1976. Science and Statistics. *Journal of the American Statistical Association* **71** (356), pp. 791–799. ISSN: 0162-1459. DOI: 10.1080/01621459.1976.10480949.

Boyer et al. 2011 Boyer, Frédéric; Nayer, Guillaume de; Leroyer, Alban; Visonneau, Michel, 2011. Geometrically Exact Kirchhoff Beam Theory: Application to Cable Dynamics. *Computer Methods in Applied Mechanics and Engineering* **6** (4), p. 041004. ISSN: 0045-7825. DOI: 10.1115/1.4003625.

Brinson et al. 2008 Brinson, Hal F.; Brinson, L. Catherine, 2008. *Polymer Engineering Science and Viscoelasticity*. Boston, MA, USA: Springer US. ISBN: 978-0-387-73860-4. DOI: 10.1007/978-0-387-73861-1.

Briot et al. 2007 Briot, Sébastien; Bonev, Ilian, 2007. Are Parallel Robots More Accurate Than Serial Robots? *CSME Transactions* **31** (4), pp. 445–456. DOI: 10.1139/tcsme-2007-0032. URL: https://hal.archives-ouvertes.fr/hal-00362500.

Bruckmann et al. 2008 Bruckmann, Tobias; Mikelsons, Lars; Brandt, Thorsten; Hiller, Manfred; Schramm, Dieter, 2008. Wire Robots Part I: Kinematics, Analysis & Design. In: Jee-Hwan Ryu, (ed.). *Parallel Manipulators, New Developments*. I-Tech Education and Publishing. ISBN: 978-3-902613-20-2. DOI: 10.5772/5365.

Bruckmann et al. 2006 Bruckmann, Tobias; Pott, Andreas; Hiller, Manfred, 2006. Calculating Force Distributions for Redundantly Actuated Tendon-Based Stewart Platforms. In: Jadran Lenarčič; Bernard Roth, (eds.). *Advances in Robot Kinematics: Proceedings of the 2006 International Conference on*. Dordrecht, Netherlands: Springer, pp. 403–412. ISBN: 978-1-4020-4940-8. DOI: 10.1007/978-1-4020-4941-5_44.

Bulín et al. 2017 Bulín, Radek; Hajžman, Michal; Polach, Pavel, 2017. Complex Modelling and Dynamical Analysis of Parallel Cable Mechanisms. In: Joao Carlos Mendes Carvalho; Daniel Martins; Roberto Simoni; Henrique Simas, (eds.). *Multibody Mechatronic Systems*. Vol. 54. Mechanisms and Machine Science. Cham, Switzerland: Springer, pp. 193–202. ISBN: 978-3-319-67566-4. DOI: 10.1007/978-3-319-67567-1_18.

Cao et al. 2008 Cao, Deng-Qing; Tucker, Robin W., 2008. Nonlinear Dynamics of Elastic Rods Using the Cosserat Theory: Modelling and Simulation. *International Journal of Solids and Structures* **45** (2), pp. 460–477. ISSN: 0020-7683. DOI: 10.1016/j.ijsolstr.2007.08.016.

Carricato et al. 2010 Carricato, Marco; Merlet, Jean-Pierre, 2010. Geometrico-Static Analysis of Under-Constrained Cable-Driven Parallel Robots. In: Jadran Lenarčič; Michael M. Stanisic, (eds.). *Advances in Robot Kinematics: Motion in Man and Machine*. Dordrecht, Netherlands: Springer, pp. 309–319. ISBN: 978-90-481-9261-8. DOI: 10.1007/978-90-481-9262-5_33.

Caverly et al. 2014 Caverly, Ryan James; Forbes, James Richard, 2014. Dynamic Modeling and Noncollocated Control of a Flexible Planar Cable-Driven Manipulator. *IEEE Transactions on Robotics* **30** (6), pp. 1386–1397. ISSN: 1552-3098. DOI: 10.1109/tro.2014.2347573.

Caverly et al. 2015a Caverly, Ryan James; Forbes, James Richard, 2015. Maintaining Positive Cable Tensions During Operation of a Single Degree of Freedom Flexible Cable-Driven Parallel Manipulator. In: *2015 American Control Conference (ACC): Proceedings of the*. Chicago, IL, USA. IEEE, pp. 1205–1210. DOI: 10.1109/acc.2015.7170897.

Caverly et al. 2015b Caverly, Ryan James; Forbes, James Richard; Mohammadshahi, Donya, 2015. Dynamic Modeling and Passivity-Based Control of a Single Degree of Freedom Cable-Actuated System. *IEEE Transactions on Control Systems Technology* **23** (3), pp. 898–909. DOI: 10.1109/tcst.2014.2347807.

Chellal et al. 2015 Chellal, Ryad; Cuvillon, Loïc; Laroche, Édouard, 2015. A Kinematic Vision-Based Position Control of a 6-DoF Cable-Driven Parallel Robot. In: Andreas Pott; Tobias Bruckmann, (eds.). *Cable-Driven Parallel Robots*. Vol. 32. Mechanisms and Machine Sciences. Cham, Switzerland: Springer, pp. 213–225. ISBN: 978-3-319-09488-5. DOI: 10.1007/978-3-319-09489-2_15.

Chellal et al. 2014 Chellal, Ryad; Laroche, Édouard; Cuvillon, Loïc, 2014. An $\mathcal{H}_\infty$ Methodology for Position Control of 6-DoF Cable-Driven Parallel Robots. In: *Control Conference (ECC): Proceedings of the 2014 European*. IEEE, pp. 358–363. ISBN: 978-3-9524269-1-3. DOI: 10.1109/ecc.2014.6862431.

Chellal et al. 2012 Chellal, Ryad; Laroche, Edouard; Cuvillon, Loïc; Gangloff, Jacques, Sept. 2012. An Identification Methodology for 6-DoF Cable-Driven Parallel Robots Parameters Application to the INCA 6D Robot. In: Tobias Bruckmann; Andreas Pott, (eds.). *Cable-Driven Parallel Robots*. Mechanisms and Machine Sciences 12. Berlin, Germany and Heidelberg, Germany: Springer, pp. 301–317. ISBN: 978-3-642-31987-7. DOI: 10.1007/978-3-642-31988-4_19.

Choi et al. 2017 Choi, Sung-Hyun; Park, Jong-Oh; Park, Kyoung-Su, 2017. Tension Analysis of a 6-Degree-Of-Freedom Cable-Driven Parallel Robot Considering Dynamic Pulley Bearing Friction. *Advances in Mechanical Engineering* **9** (8). ISSN: 1687-8132. DOI: 10.1177/1687814017714981.

Collard et al. 2011 Collard, Jean-François; Lamaury, Johann; Gouttefarde, Marc, 2011. Dynamics Modelling of Large Suspended Parallel Cable-Driven Robots. In: *Multibody Dynamics: 2011 ECCOMAS Thematic Conference on*. Thematic Conference on Multibody Dynamics. Brussels, Belgium. European Community on Computational Methods in Applied Sciences (ECCOMAS), pp. 01–13. URL: https://hal-lirmm.ccsd.cnrs.fr/lirmm-00737241.

Collings 2016 Collings, David, 2016. Multiple-Span Suspension Bridges: State of the Art. *Proceedings of the Institution of Civil Engineers: Bridge Engineering* **169** (3), pp. 215–231. DOI: 10.1680/jbren.15.00035.

Cone 1985 Cone, Lawrence L., 1985. Skycam, an Aerial Robotic Camera System. In: *Byte Magazine*. Vol. 10. 10, pp. 122–132.

Costello 1990 Costello, George A., 1990. *Theory of Wire Rope*. Mechanical Engineering Series. New York, NY, USA: Springer US. ISBN: 978-1-4684-0352-7. DOI: 10.1007/978-1-4684-0350-3.

Cubero 2006 Cubero, Sam, (ed.), 2006. *Industrial Robotics: Theory, Modelling and Control*. Pro Literatur Verlag, Germany and ARS, Austria. ISBN: 3-86611-285-8. DOI: 10.5772/44.

Dadkhah 2015 Dadkhah, Mahmood, 2015. Solving Linear Time Varying Systems by Orthonormal Bernstein Polynomials. *Science Journal of Applied Mathematics and Statistics* **3** (4), pp. 194–198. DOI: 10.11648/j.sjams.20150304.15.

Dagalakis et al. 1989 Dagalakis, Nicholas G.; Albus, James S.; Goodwin, Kenneth R.; Lee, James D.; Tsai, Tsung-Ming; Abrishamian, Hoosh; Bastelman, Roger, 1989. *Robot Crane Technology: Final Report*. Tech. rep. Gaithersburg, CO, USA: National Institute of Standards and Technology (NIST). DOI: 10.6028/nist.tn.1267.

Dahl 1968 Dahl, P. R., 1968. *A Solid Friction Model*. Tech. rep. TOR-158(3107-18). El Segundo, CA, USA: The Aerospace Corporation. DOI: 10.21236/ada041920.

Dallej et al. 2012 Dallej, Tej; Gouttefarde, Marc; Andreff, Nicolas; Dahmouche, Redwan; Martinet, Philippe, 2012. Vision-Based Modeling and Control of Large-Dimension Cable-Driven Parallel Robots. In: *Intelligent Robots and Systems: Proceedings of the 2012 IEEE/RSJ International Conference on*. IEEE, pp. 1581–1586. ISBN: 978-1-4673-1737-5. DOI: 10.1109/iros.2012.6385504.

Davis 1975 Davis, Philip J., 1975. *Interpolation and Approximation*. 1st ed. Vol. 7. New York, NY, USA: Dover Publications. ISBN: 978-0-486-62495-2.

Diao et al. 2009 Diao, Xiumin; Ma, Ou, 2009. Vibration Analysis of Cable-Driven Parallel Manipulators. *Multibody System Dynamics* **21** (4), pp. 347–360. ISSN: 1384-5640. DOI: 10.1007/s11044-008-9144-0.

Dietmaier 1998 Dietmaier, Peter, 1998. The Stewart-Gough Platform of General Geometry Can Have 40 Real Postures. In: *Advances in Robot Kinematics: Analysis and Control*. Dordrecht, Netherlands: Springer, pp. 7–16. DOI: 10.1007/978-94-015-9064-8_1.

Dokken et al. 1990 Dokken, Tor; Daehlen, Morten; Lyche, Tom; Mørken, Knut, 1990. Good Approximation of Circles by Curvature-Continuous Bézier Curves. *Computer Aided Geometric Design* **7** (1), pp. 33–41. ISSN: 0167-8396. DOI: 10.1016/0167-8396(90)90019-n.

Dreyer et al. 1984 Dreyer, T. P.; Murray, Daniel M., 1984. The Comparison of Modelling Approaches and Numerical Solution Procedures for Segmented Representations of Cable Shape. *Mathematical Modelling* **5** (4), pp. 223–241. ISSN: 0270-0255. DOI: 10.1016/0270-0255(84)90002-2.

Drmač et al. 2015 Drmač, Zlatko; Gugercin, Serkan; Beattie, Christopher A., 2015. Quadrature-Based Vector Fitting for Discretized $\mathcal{H}_2$ Approximation. *SIAM Journal on Scientific Computing* **37** (2), A625–A652. ISSN: 1064-8275. DOI: 10.1137/140961511.

Du et al. 2015 Du, Jingli; Agrawal, Sunil K., 2015. Dynamic Modeling of Cable-Driven Parallel Manipulators With Distributed Mass Flexible Cables. *Journal of Vibration and Acoustics* **137** (2), p. 021020. ISSN: 0739-3717. DOI: 10.1115/1.4029486.

Du et al. 2012 Du, Jingli; Bao, Hong; Cui, Chuanzhen; Duan, Xuechao, 2012. Nonlinear PD Control of a Long-Span Cable-Supporting Manipulator in Quasi-Static Motion. *Journal of Dynamic Systems, Measurement, and Control* **134** (1), p. 11022. ISSN: 0022-0434. DOI: 10.1115/1.4004784.

Duan et al. 2010 Duan, Qingjuan; Du, Jingli; Duan, Baoyan; Tang, Aofei, 2010. Deployment/Retrieval Modeling of Cable-Driven Parallel Robot. *Mathematical Problems in Engineering* **2010**, pp. 1–10. ISSN: 1024-123X. DOI: 10.1155/2010/909527.

Duan et al. 2011 Duan, Qingjuan; Duan, Xuechao, 2011. Analysis of Cable-Actuated Parallel Robot With Variable Length and Velocity Cable. *Procedia Engineering* **15**, pp. 2732–2737. ISSN: 1877-7058. DOI: 10.1016/j.proeng.2011.08.514.

Eade 2017 Eade, Ethan, 2017. *Lie Groups for 2d and 3d Transformations*. Tech. rep. Cambridge, England, United Kingdom: University of Cambridge. URL: http://ethaneade.org/lie.pdf.

Edelsbrunner et al. 2008 Edelsbrunner, Herbert; Kobbelt, Leif; Polthier, Konrad; Farouki, Rida T., 2008. *Pythagorean-Hodograph Curves: Algebra and Geometry Inseparable*. Vol. 1. Berlin, Germany and Heidelberg, Germany: Springer. ISBN: 978-3-540-73397-3. DOI: 10.1007/978-3-540-73398-0.

Eich 1993 Eich, Edda, 1993. Convergence Results for a Coordinate Projection Method Applied to Mechanical Systems With Algebraic Constraints. *SIAM Journal on Numerical Analysis* **30** (5), pp. 1467–1482. ISSN: 0036-1429. DOI: 10.1137/0730076.

Fabritius et al. 2019 Fabritius, Marc; Martin, Christoph; Pott, Andreas, 2019. Calculation of the Cable-Platform Collision-Free Total Orientation Workspace of Cable-Driven Parallel Robots. In: Andreas Pott; Tobias Bruckmann, (eds.). *Cable-Driven Parallel Robots: Proceedings of the Fourth International Conference on Cable-Driven Parallel Robots*. Vol. 74. Advances in Mechanism and Machine Science 74. Cham, Switzerland: Springer, pp. 137–148. DOI: 10.1007/978-3-030-20751-9_12.

Farouki 2012 Farouki, Rida T., 2012. The Bernstein Polynomial Basis: A Centennial Retrospective. *Computer Aided Geometric Design* **29** (6), pp. 379–419. ISSN: 0167-8396. DOI: 10.1016/j.cagd.2012.03.001.

Farouki et al. 2003 Farouki, Rida T.; Goodman, Tim N. T.; Sauer, Thomas, 2003. Construction of Orthogonal Bases for Polynomials in Bernstein Form on Triangular and Simplex Domains. *Computer Aided Geometric Design* **20** (4), pp. 209–230. ISSN: 0167-8396. DOI: 10.1016/s0167-8396(03)00025-6.

Faugère et al. 2006 Faugère, Jean-Charles; Merlet, Jean-Pierre; Rouillier, Fabrice, 2006. *On Solving the Direct Kinematics Problem for Parallel Robots*. Research rep. RR-5923. Sophia-Antipolis, France: Institut National de Recherche en Informatique et en Automatique (INRIA). URL: https://hal.inria.fr/inria-00072366v2.

Featherstone 2008 Featherstone, Roy, 2008. *Rigid Body Dynamics Algorithms*. New York, NY, USA: Springer US. ISBN: 978-0-387-74314-1. DOI: 10.1007/978-1-4899-7560-7.

Findley et al. 1976 Findley, William N.; Lai, James S.; Onaran, Kasif, 1976. *Creep and Relaxation of Nonlinear Viscoelastic Materials: With an Introduction to Linear Viscoelasticity*. North-Holland Series in Applied Mathematics and Mechanics. New York, NY, USA: Dover Publications Inc. 400 pp. ISBN: 978-0-486-66016-5.

Flores 2014 Flores, Paulo, 2014. A New Approach to Eliminate the Constraints Violation at the Position and Velocity Levels in Constrained Mechanical Multibody Systems. In: Paulo Flores; Fernando Viadero, (eds.). *New Trends in Mechanism and Machine Science: From Fundamentals to Industrial Applications*. Mechanisms and Machine Science 24. Cham, Switzerland: Springer, pp. 385–393. DOI: 10.1007/978-3-319-09411-3_41.

Fritzkowski et al. 2013 Fritzkowski, Pawel; Kamiński, Henryk, 2013. Non-Linear Dynamics of a Hanging Rope. *ACM Transactions on Mathematical Software* **10** (1), pp. 81–90. ISSN: 0098-3500. DOI: 10.1590/s1679-78252013000100008.

Funaro 1992 Funaro, Daniele, 1992. *Polynomial Approximation of Differential Equations*. Vol. 8. Berlin, Germany and Heidelberg, Germany: Springer. ISBN: 978-3-540-55230-7. DOI: 10.1007/978-3-540-46783-0.

Gagliardini et al. 2014 Gagliardini, Lorenzo; Caro, Stéphane; Gouttefarde, Marc; Wenger, Philippe; Girin, Alexis, 2014. A Reconfigurable Cable-Driven Parallel Robot for Sandblasting and Painting of Large Structures. In: Andreas Pott; Tobias Bruckmann, (eds.). *Cable-Driven Parallel Robots*. Vol. 32. Mechanisms and Machine Sciences. Cham, Switzerland: Springer, pp. 275–291. ISBN: 978-3-319-09488-5. DOI: 10.1007/978-3-319-09489-2_20.

García-Fernández et al. 2011 García-Fernández, Ignacio; Pla-Castells, Marta; Gamón, Miguel A.; Martínez-Durá, Rafael J., 2011. New Developments in Simulation-Based Harbour Crane Training. *International Journal of Simulation and Process Modelling* **6** (4), p. 274. ISSN: 1740-2123. DOI: 10.1504/ijspm.2011.048009.

García-Fernández et al. 2008 García-Fernández, Ignacio; Pla-Castells, Marta; Martínez-Durá, Rafael J., 2008. Elevation Cable Modeling for Interactive Simulation of Cranes. In: M. Gross; D. James, (eds.). *Computer Animation: Proceedings of the 2008 Symposium on*. 2008 Symposium on Computer Animation. Paris, France, July 11–13, 2018. The Eurographics Association. DOI: 10.2312/sca/sca08/173-181.

García-Fernández et al. 2007 García-Fernández, Ignacio; Pla-Castells, Marta; Martínez-Durá, Rafael J.; Simos, Theodore E.; Psihoyios, George; Tsitouras, Ch., 2007. A Mixed Model for Real-Time, Interactive Simulation of a Cable Passing Through Several Pulleys. In: *AIP Conference Proceedings: Numerical Analysis and Applied Mathematics*. 2007 International Conference of Numerical Analysis and Applied Mathematics. Corfu, Greece, Sept. 16–20, 2007. Vol. 936. 1. American Institute of Physics (AIP), pp. 212–215. ISBN: 978-0-7354-0447-2. DOI: 10.1063/1.2790111.

Garnier et al. 2003 Garnier, Hugues; Mensler, Michel; Richard, Alain, 2003. Continuous-Time Model Identification From Sampled Data: Implementation Issues and Performance Evaluation. *International Journal of Control* **76** (13), pp. 1337–1357. ISSN: 0020-7179. DOI: 10.1080/0020717031000149636.

El-Ghazaly et al. 2014 El-Ghazaly, Gamal; Gouttefarde, Marc; Creuze, Vincent, 2014. Adaptive Terminal Sliding Mode Control of a Redundantly-Actuated Cable-Driven Parallel Manipulator: CoGiRo. In: Andreas Pott; Tobias Bruckmann, (eds.). *Cable-Driven Parallel Robots*. Vol. 32. Mechanisms and Machine Sciences. Cham, Switzerland: Springer, pp. 179–200. ISBN: 978-3-319-09488-5. DOI: 10.1007/978-3-319-09489-2_13.

Gil et al. 2007 Gil, Amparo; Segura, Javier; Temme, Nico M., 2007. *Numerical Methods for Special Functions*. Philadelphia, PA, USA: Society for Industrial & Applied Mathematics. ISBN: 978-0-89871-634-4. DOI: 10.1137/1.9780898717822.

Godbole et al. 2017 Godbole, Harsh Atul; Caverly, Ryan James; Forbes, James Richard, 2017. Modelling of Flexible Cable-Driven Parallel Robots Using a Rayleigh-Ritz Approach. In: Clément M. Gosselin; Philippe Cardou; Tobias Bruckmann; Andreas Pott, (eds.). *Cable-Driven Parallel Robots: Proceedings of the Third International Conference on Cable-Driven Parallel Robots*. Mechanisms and Machine Science 53. Cham, Switzerland: Springer, pp. 3–14. ISBN: 978-3-319-61431-1. DOI: 10.1007/978-3-319-61431-1_1.

Gonzalez 1996 Gonzalez, Oscar, 1996. Time Integration and Discrete Hamiltonian Systems. *Journal of Nonlinear Science* **6** (5), pp. 449–467. ISSN: 0938-8974. DOI: 10.1007/bf02440162.

Gorbatsevich et al. 1993 Gorbatsevich, Vladimir V.; Onishchik, Arkady L.; Vinberg, Ernest B., 1993. *Lie Groups and Lie Algebras I: Foundations of Lie Theory Lie Transformation Groups*. Arkady L. Onishchik (ed.)trans. by Theodore T. Kozlowski. Vol. 20. Berlin, Germany and Heidelberg, Germany: Springer. ISBN: 978-3-540-61222-3. DOI: 10.1007/978-3-642-57999-8.

Gosselin et al. 2011 Gosselin, Clément M.; Grenier, Martin, 2011. On the Determination of the Force Distribution in Overconstrained Cable-Driven Parallel Mechanisms. *Meccanica* **46** (1), pp. 3–15. ISSN: 0025-6455. DOI: 10.1007/s11012-010-9369-x.

Gough 1962 Gough, V. Eric, 1962. Universal Tyre Test Machine. *Proceedings of the Institution of Mechanical Engineers* **117**, pp. 117–137. URL: https://ci.nii.ac.jp/naid/10016629296/en/.

Gouttefarde et al. 2012 Gouttefarde, Marc; Collard, Jean-François; Riehl, Nicolas; Baradat, Cédric, 2012. Simplified Static Analysis of Large-Dimension Parallel Cable-Driven Robots. In: *Robotics and Automation: Proceedings of the 2012 IEEE International Conference on*. Saint Paul, MN, USA. Institute of Electrical and Electronics Engineers (IEEE). IEEE, pp. 2299–2305. DOI: 10.1109/icra.2012.6225159.

Gouttefarde et al. 2008 Gouttefarde, Marc; Krut, Sebastien; Company, Olivier; Pierrot, François; Ramdani, Nacim, 2008. On the Design of Fully Constrained Parallel Cable-Driven Robots. In: *Advances in Robot Kinematics (ARK): Analysis and Design*. Dordrecht, Netherlands: Springer, pp. 71–78. DOI: 10.1007/978-1-4020-8600-7_8. URL: http://hal-lirmm.ccsd.cnrs.fr/lirmm-00322375/en/.

Gouttefarde et al. 2015 Gouttefarde, Marc; Lamaury, Johann; Reichert, Christopher; Bruckmann, Tobias, 2015. A Versatile Tension Distribution Algorithm for n-DoF Parallel Robots Driven by $n+2$ Cables. *IEEE Transactions on Robotics* **31** (6), pp. 1444–1457. ISSN: 1552-3098. DOI: 10.1109/tro.2015.2495005.

Gouttefarde et al. 2007 Gouttefarde, Marc; Merlet, Jean-Pierre; Daney, David, 2007. Wrench-Feasible Workspace of Parallel Cable-Driven Mechanisms. In: *Robotics and Automation: Proceedings of the 2007 IEEE International Conference on*. 2007 IEEE International Conference on Robotics and Automation. Roma, Italy. IEEE, pp. 1492–1497. DOI: 10.1109/robot.2007.363195.

Greenstein 1965 Greenstein, David S., 1965. Interpolation and Approximation (Philip J. Davis). *SIAM Review* **7** (1), pp. 151–152. ISSN: 0036-1445. DOI: 10.1137/1007028.

Haghighipanah et al. 2015 Haghighipanah, Mohammad; Li, Yangming; Miyasaka, Muneaki; Hannaford, Blake, 2015. Improving Position Precision of a Servo-Controlled Elastic Cable Driven Surgical Robot Using Unscented Kalman Filter. In: *Intelligent Robots and Systems: Proceedings of the 2015 IEEE/RSJ International Conference on*. 2015 IEEE/RSJ International Conference on Intelligent Robots and Systems. Hamburg, Germany. IEEE Robotics and Automation Society (IEEE/RAS). IEEE, pp. 2030–2036. DOI: 10.1109/iros.2015.7353646.

Hajžman et al. 2011 Hajžman, Michal; Polach, Pavel, 2011. Modelling of Cables for Application in Cable-Based Manipulators Design. In: *Multibody Dynamics: 2011 ECCOMAS Thematic Conference on*. ECCOMAS Thematic Conference on Multibody Dynamics. Brussels, Belgium. European Community on Computational Methods in Applied Sciences (ECCOMAS).

Hamed et al. 2006 Hamed, Ehab; Frostig, Yeoshua, 2006. Natural Frequencies of Bonded and Unbonded Prestressed Beams: Prestress Force Effects. *Journal of Sound and Vibration* **295** (1–2), pp. 28–39. ISSN: 0022-460X. DOI: 10.1016/j.jsv.2005.11.032.

Hannan 1970 Hannan, Edward J., 1970. *Multiple Time Series*. Edward J. Hannan (ed.). Hoboken, NJ, USA: John Wiley & Sons, Inc. ISBN: 978-0-470-31642-9. DOI: 10.1002/9780470316429.

Hao et al. 2005 Hao, Fang; Merlet, Jean-Pierre, 2005. Multi-Criteria Optimal Design of Parallel Manipulators Based on Interval Analysis. *Mechanism and Machine Theory* **40** (2), pp. 157–171. ISSN: 0094-114X. DOI: 10.1016/j.mechmachtheory.2004.07.002.

Hiller et al. 2005 Hiller, Manfred; Fang, Shiqing; Mielczarek, Sonja; Verhoeven, Richard; Franitza, Daniel, 2005. Design, Analysis and Realization of Tendon-Based Parallel Manipulators. *Mechanism and Machine Theory* **40** (4), pp. 429–445. ISSN: 0094-114X. DOI: 10.1016/j.mechmachtheory.2004.08.002.

Howell 1992 Howell, Christopher Todd, 1992. Investigation of the Dynamics of Low-Tension Cables. Cambridge, MA, United States. Woods Hole Oceanographic Institution, Massachusetts Institute of Technology, Cambridge, MA, United States, PhD thesis, 1992. hdl: 1721.1/13170.

Hussein et al. 2018 Hussein, Hussein; Santos, Joao Cavalcanti; Gouttefarde, Marc, 2018. Geometric Optimization of a Large Scale CDPR Operating on a Building Facade. In: *2018 IEEE/RSJ International Conference on Intelligent Robots and Systems*. 2018 IEEE/RSJ International Conference on Intelligent Robots and Systems. Madrid, Spain, Oct. 1–May 10, 2018. IEEE Robotics Society of Japan (IEEE/RSJ). Institute of Electrical and Electronics Engineers (IEEE), pp. 5117–5124. ISBN: 978-1-5386-8094-0. DOI: 10.1109/iros.2018.8593900.

Huston et al. 1982 Huston, Ronald L.; Kamman, James W., 1982. Validation of Finite Segment Cable Models. *Computers & Structures* **15** (6), pp. 653–660. ISSN: 0045-7949. DOI: 10.1016/s0045-7949(82)80006-0.

Husty 1996 Husty, Manfred L., 1996. An Algorithm for Solving the Direct Kinematic of Stewart-Gough-Type Platforms. *Mechanism and Machine Theory* **31** (4), pp. 365–380. ISSN: 0094-114X.

Husty et al. 2002 Husty, Manfred L.; Mielczarek, Sonja; Hiller, Manfred, 2002. A Redundant Spatial Stewart-Gough Platform With Maximal Forward Kinematics Solution Set. In: *Advances in Robot Kinematics: Proceedings of the 2002 International Conference on*. Dordrecht, Netherlands: Springer, pp. 147–154. DOI: 10.1007/978-94-017-0657-5_16.

Ibrahimbegović 1995 Ibrahimbegović, Adnan, 1995. On Finite Element Implementation of Geometrically Nonlinear Reissner's Beam Theory: Three-Dimensional Curved Beam Elements. *Computer Methods in Applied Mechanics and Engineering* **122** (1-2), pp. 11–26. ISSN: 0045-7825. DOI: 10.1016/0045-7825(95)00724-f.

Irvine 1974 Irvine, H. Max, 1974. Studies in the Statics and Dynamics of Simple Cable Systems. Pasadena, CA, USA: California Institute of Technology. California Institute of Technology, Pasadena, Pasadena, CA, USA, PhD thesis, 1974. URL: http://resolver.caltech.edu/CaltechEERL:1974.DYNL-108.

Izard et al. 2018 Izard, Jean-Baptiste; Gouttefarde, Marc; Hussein, Hussein; Martin, Christoph; Kraus, Werner; Pott, Andreas; Rodriguez, Mariola, 2018. Cable-Driven Parallel Robots: Principle and Applications of an Advanced Crane System. In: *Architectural Envelopes (ICAE 2018): Proceedings of the 2018 International Congress on*. San Sebastian-Donostia, Spain. URL: https://hal-lirmm.ccsd.cnrs.fr/lirmm-01898808.

Izard et al. 2012 Izard, Jean-Baptiste; Gouttefarde, Marc; Michelin, Micaël; Tempier, Olivier; Baradat, Cédric, 2012. A Reconfigurable Robot for Cable-Driven Parallel Robotic Research and Industrial Scenario Proofing. In: Tobias Bruckmann; Andreas Pott, (eds.). *Cable-Driven Parallel Robots*. Mechanisms and Machine Sciences 12. Berlin, Germany and Heidelberg, Germany: Springer, pp. 135–148. ISBN: 978-3-642-31987-7. DOI: 10.1007/978-3-642-31988-4_9.

Ji et al. 2019 Ji, Yongcheng; Kim, Yail J., 2019. State-Of-The-Art Review of Bridges Under Rail Transit Loading. *Proceedings of the Institution of Civil Engineers: Structures and Buildings* **172** (6), pp. 451–466. ISSN: 0965-0911. DOI: 10.1680/jstbu.18.00005.

Jung et al. 2018 Jung, Woo-Tai; Kim, Yail J.; Kang, Jae-Yoon; Park, Jong-Sup, 2018. State-Of-The-Practice of Constructed Bridges in Korea. *Proceedings of the Institution of Civil Engineers: Structures and Buildings* **171** (9), pp. 705–718. DOI: 10.1680/jstbu.16.00165.

Kawamura et al. 1995a Kawamura, Sadao; Choe, Won; Tanaka, Satoshi; Pandian, Shunmugham R., 1995. Development of an Ultrahigh Speed Robot FALCON Using Wire Drive System. In: *Robotics and Automation: Proceedings of the 1995 IEEE International Conference on*. 1995 IEEE International Conference on Robotics and Automation. IEEE, pp. 1764–1850. DOI: 10.1109/robot.1995.525288.

Kawamura et al. 1995b Kawamura, Sadao; Ida, Mizuto; Wada, Takahiro; Wu, Jing-Long, 1995. Development of a Virtual Sports Machine Using a Wire Drive System: A Trial of Virtual Tennis. In: *Intelligent Robots and Systems: Proceedings of the 1995 IEEE/RSJ International Conference on*. 1995 IEEE/RSJ International Conference on Intelligent Robots and Systems. Vol. 1. IEEE Robotics Society of Japan (IEEE/RSJ). IEEE Computer Society Press, pp. 111–116. DOI: 10.1109/iros.1995.525783.

Khosravi et al. 2014 Khosravi, Mohammad A.; Taghirad, Hamid D., 2014. Dynamic Modeling and Control of Parallel Robots With Elastic Cables: Singular Perturbation Approach. *IEEE Transactions on Robotics* **30** (3), pp. 694–704. ISSN: 1552-3098. DOI: 10.1109/tro.2014.2298057.

Khosravi et al. 2013 Khosravi, Mohammad A.; Taghirad, Hamid D.; Oftadeh, Reza, 2013. A Positive Tensions PID Controller for a Planar Cable Robot: An Experimental Study. In: *Robotics and Mechatronics (ICRoM): Proceedings of the 2013 RSI/ISM International Conference on*. Sharif University of Technology, Tehran, Iran, Feb. 13–15, 2013. Robotics Society of Iran (RSI) and Academy of Sciences of Islamic Republic of Iran (ISM)). IEEE, pp. 325–330. ISBN: 978-1-4673-5809-5. DOI: 10.1109/icrom.2013.6510127.

Korayem et al. 2011 Korayem, Moharam Habibnejad; Tourajizadeh, H., 2011. Maximum DLCC of Spatial Cable Robot for a Predefined Trajectory Within the Workspace Using Closed Loop Optimal Control Approach. *Journal of Intelligent & Robotic Systems* **63** (1), pp. 75–99. ISSN: 0921-0296. DOI: 10.1007/s10846-010-9521-9.

Korayem et al. 2017 Korayem, Moharam Habibnejad; Yousefzadeh, Mehrdad; Beyranvand, B., 2017. Dynamics and Control of a 6-DoF Cable-Driven Parallel Robot With Visco-Elastic Cables in Presence of Measurement Noise. *Journal of Intelligent and Robotic Systems* **88** (1), pp. 73–95. ISSN: 0921-0296. DOI: 10.1007/s10846-017-0546-1.

Kozak et al. 2006 Kozak, Kris; Zou, Qian; Wang, Jinsong, 2006. Static Analysis of Cable-Driven Manipulators With Non-Negligible Cable Mass. *IEEE Transactions on Robotics* **22** (3), pp. 425–433. ISSN: 1552-3098. DOI: 10.1109/tro.2006.870659.

Kraus 2015 Kraus, Werner, 2015. Force Control of Cable-Driven Parallel Robots. Stuttgart, Germany: Fraunhofer Verlag. Stuttgarter Beiträge zur Produktionsforschung 49. Institute for Control Engineering of Machine Tools and Manufacturing Units ISW, University of Stuttgart, Stuttgart, Germany, PhD thesis, 2015. ISBN: 978-3-8396-0979-8. DOI: 10.18419/opus-6899. urn: urn:nbn:de:bsz:93-opus-105511.

Kraus et al. 2015a Kraus, Werner; Kessler, Michael; Pott, Andreas, 2015. Pulley Friction Compensation for Winch-Integrated Cable Force Measurement and Verification on a Cable-Driven Parallel Robot. In: *Robotics and Automation: Proceedings of the 2015 IEEE International Conference on*. 2015 IEEE International Conference on Robotics and Automation. Seattle, WA, USA, May 26–30, 2015. Institute of Electrical and Electronics Engineers (IEEE). IEEE, pp. 1627–1632. DOI: 10.1109/icra.2015.7139406.

Kraus et al. 2015b Kraus, Werner; Mangold, Alexander; Ho, Wei Yang; Pott, Andreas, 2015. Haptic Interaction With a Cable-Driven Parallel Robot Using Admittance Control. In: Andreas Pott; Tobias Bruckmann, (eds.). *Cable-Driven Parallel Robots*. Mechanisms and Machine Sciences. Cham, Switzerland: Springer, pp. 201–212. ISBN: 978-3-319-09488-5. DOI: 10.1007/978-3-319-09489-2_14.

Kraus et al. 2015c Kraus, Werner; Miermeister, Philipp; Schmidt, Valentin; Pott, Andreas, 2015. Hybrid Position/Force Control of a Cable-Driven Parallel Robot With Experimental Evaluation. In: Paulo Flores; Fernando Viadero, (eds.). *New Trends in Mechanism and Machine Science*. Mechanisms and Machine Sciences. Cham, Switzerland: Springer, pp. 553–561. ISBN: 978-3-319-09410-6. DOI: 10.1007/978-3-319-09411-3_59.

Kraus et al. 2014 Kraus, Werner; Schmidt, Valentin; Rajendra, Puneeth; Pott, Andreas, 2014. System Identification and Cable Force Control for a Cable-Driven Parallel Robot With Industrial Servo Drives. In: *Robotics and Automation: Proceedings of the 2014 IEEE International Conference on*. 2014 IEEE International Conference on Robotics and Automation. Hong Kong, China. Institute of Electrical and Electronics Engineers (IEEE). IEEE, pp. 5921–5926. DOI: 10.1109/icra.2014.6907731.

Labuschagne et al. 2009 Labuschagne, Antoinette; Rensburg, Nicolaas F. J. van; Merwe, Alna J. van der, 2009. Comparison of Linear Beam Theories. *Mathematical and Computer Modelling* **49** (1-2), pp. 20–30. ISSN: 0895-7177. DOI: 10.1016/j.mcm.2008.06.006.

Lacarbonara et al. 2008 Lacarbonara, Walter; Pacitti, Arnaud, 2008. Nonlinear Modeling of Cables With Flexural Stiffness. *Mathematical Problems in Engineering* **2008** (3), pp. 1–21. ISSN: 1024-123X. DOI: 10.1155/2008/370767.

Lalo 2013 Lalo, Wildan, 2013. Ein Beitrag zur Entwicklung von Assistenzsystemen für Serielle und Parallele Roboter am Beispiel von Autobetonpumpen und Seilbasierten Regalbediengeräten. Duisburg, Germany. University of Duisburg-Essen, Duisburg, Germany, PhD thesis, 2013. urn: urn:nbn:de:hbz:464-20140305-150014-7.

Lamaury et al. 2012 Lamaury, Johann; Gouttefarde, Marc, 2012. A Tension Distribution Method With Improved Computational Efficiency. In: Tobias Bruckmann; Andreas Pott, (eds.). *Cable-Driven Parallel Robots*. Mechanisms and Machine Sciences 12. Berlin, Germany and Heidelberg, Germany: Springer, pp. 71–85. DOI: 10.1007/978-3-642-31988-4_5.

Lambert 2006 Lambert, Casey Marcel, 2006. Dynamics and Control of a Multi-Tethered Aerostat Positioning System. Ottawa, Canada: Library and Archives Canada. McGill University, Ottawa, Canada, PhD thesis, 2006. ISBN: 978-0-494-32203-1. oai: oai:digitool.library.mcgill.ca:102994.

Lambert et al. 2007 Lambert, Casey Marcel; Nahon, Meyer; Chalmers, Dean, 2007. Implementation of an Aerostat Positioning System With Cable Control. *IEEE/ASME Transactions on Mechatronics* **12** (1), pp. 32–40. DOI: 10.1109/tmech.2006.886251.

Lambert 1991 Lambert, John Denholm, 1991. *Numerical Methods for Ordinary Differential Systems*. ISBN: 0-471-92990-5.

Lang et al. 2013 Lang, Holger; Leyendecker, Sigrid; Linn, Joachim, 2013. Numerical Experiments for Viscoelastic Cosserat Rods With Kelvin–Voigt Damping.

Lang et al. 2009 Lang, Holger; Linn, Joachim, 2009. *Lagrangian Field Theory in Space and Time for Geometrically Exact Cosserat Rods*.

Lang et al. 2011 Lang, Holger; Linn, Joachim; Arnold, Martin, 2011. Multi-Body Dynamics Simulation of Geometrically Exact Cosserat Rods. *Multibody System Dynamics* **25** (3), pp. 285–312. ISSN: 1384-5640. DOI: 10.1007/s11044-010-9223-x.

Laroche et al. 2012 Laroche, Édouard; Chellal, Ryad; Cuvillon, Loïc; Gangloff, Jacques, 2012. A Preliminary Study for $\mathcal{H}_\infty$ Control of Parallel Cable-Driven Manipulators. In: Tobias Bruckmann; Andreas Pott, (eds.). *Cable-Driven Parallel Robots*. Mechanisms and Machine Sciences 12. Berlin, Germany and Heidelberg, Germany: Springer, pp. 353–369. ISBN: 978-3-642-31987-7. DOI: 10.1007/978-3-642-31988-4_22.

Li 2015 Li, Hui, 2015. On the Static Stiffness of Incompletely Restrained Cable-Driven Robot. In: Andreas Pott; Tobias Bruckmann, (eds.). *Cable-Driven Parallel Robots*. Vol. 32. Mechanisms and Machine Sciences. Cham, Switzerland: Springer, pp. 55–69. ISBN: 978-3-319-09488-5. DOI: 10.1007/978-3-319-09489-2_5.

Li et al. 2008 Li, Hui; Nan, Rendong; Kärcher, Hans J.; Zhu, Wenbai; Sun, Jinghai; Lazanowski, Markus; Kern, Simon; Strah, Bruno; Wamba, Francis Fomi; Jin, Chengjin, 2008. Working Space Analysis and Optimization of the Main Positioning System of FAST Cabin Suspension. In: *Ground-Based and Airborne Telescopes Ii: Radio Telescopes and Their Technology*. SPIE Astronomical Telescopes + Instrumentation. Marseille, France, June 23, 2008. Vol. 7012. SPIE Proceedings. SPIE, pp. 1–11. DOI: 10.1117/12.790537.

Li et al. 2012 Li, Hui; Zhang, Xinyu; Yao, Rui; Sun, Jinghai; Pan, Gaofeng; Zhu, Wenbai, 2012. Optimal Force Distribution Based on Slack Rope Model in the Incompletely Constrained Cable-Driven Parallel Mechanism of FAST Telescope. In: Tobias Bruckmann; Andreas Pott, (eds.). *Cable-Driven Parallel Robots*. Mechanisms and Machine Sciences 12. Berlin, Germany and Heidelberg, Germany: Springer, pp. 87–102. ISBN: 978-3-642-31987-7. DOI: 10.1007/978-3-642-31988-4_6.

Li et al. 2011 Li, Hui; Zhu, Wenbai; Pan, Gaofeng, 2011. Equilibrium Analysis of FAST Rope-Drive Parallel Manipulator Based on Rope Force Optimization. *Engineering Mechanics* **28** (4), pp. 185–193.

Liu et al. 2009 Liu, Pan; Zhang, Lixun; Wang, Keyi; Zhang, Jinyu, 2009. Dynamics Analysis and Control of Wire-Driven Rehabilitative Robot. *Zhongguo Jixie Gongcheng/China Mechanical Engineering* **20** (11), pp. 1335–1339. ISSN: 1004-132X.

Liu et al. 2013 Liu, Zhihua; Tang, Xiaoqiang; Shao, Zhufeng; Wang, Liping; Tang, Lewei, 2013. Research on Longitudinal Vibration Characteristic of the Six-Cable-Driven Parallel Manipulator in FAST. *Advances in Mechanical Engineering* **5** (0), p. 547416. ISSN: 1687-8132. DOI: 10.1155/2013/547416.

Lü et al. 2002 Lü, Yonggang; Wang, Guozhao; Yang, Xunnian, 2002. Uniform Hyperbolic Polynomial B-Spline Curves. *Computer Aided Geometric Design* **19** (6), pp. 379–393. ISSN: 0167-8396. DOI: 10.1016/s0167-8396(02)00092-4.

Lubich et al. 1995 Lubich, Christian; Engstler, Christian; Nowak, Ulrich; Pöhle, Uwe, 1995. Numerical Integration of Constrained Mechanical Systems Using Mexx*. *Mechanics of Structures and Machines* **23** (4), pp. 473–495. ISSN: 0890-5452. DOI: 10.1080/08905459508905248.

Lunze 2010 Lunze, Jan, 2010. *Regelungstechnik 1*. 10th ed. Berlin, Germany and Heidelberg, Germany: Springer. ISBN: 978-3-642-29532-4. DOI: 10.1007/978-3-642-29533-1.

Luo et al. 2001 Luo, Y. F.; Deng, C. G.; Li, Guoqiang; He, Y. M., 2001. Structural Analysis of FAST Reflector Supporting System. *Astrophysics and Space Science* **278** (1/2), pp. 231–236. ISSN: 0004-640X. DOI: 10.1023/a:1013131502739.

Lv et al. 2017 Lv, Fei; Chen, Xiaowei; Wan, Caixia; Su, Fengmei; Ji, Youxin; Lin, Yuanfei; Li, Xueyu; Li, Liangbin, 2017. Deformation of Ultrahigh Molecular Weight Polyethylene Precursor Fiber: Crystal Slip With or Without Melting. *Macromolecules* **50** (17), pp. 6385–6395. ISSN: 0024-9297. DOI: 10.1021/acs.macromol.7b01153.

Mainardi et al. 2011 Mainardi, Francesco; Spada, Giorgio, 2011. Creep, Relaxation and Viscosity Properties for Basic Fractional Models in Rheology. *The European Physical Journal Special Topics* **193** (1), pp. 133–160. ISSN: 1951-6355. DOI: 10.1140/epjst/e2011-01387-1.

Mao et al. 2015 Mao, Ying; Jin, Xin; Gera Dutta, Geetanjali; Scholz, John P.; Agrawal, Sunil K., 2015. Human Movement Training With a Cable Driven Arm Exoskeleton (CaReX). *IEEE Transactions on Neural Systems and Rehabilitation Engineering* **23** (1), pp. 84–92. ISSN: 1534-4320. DOI: 10.1109/tnsre.2014.2329018.

Marques et al. 2012 Marques, Severino P. C.; Creus, Guillermo J., (eds.), 2012. *Computational Viscoelasticity*. SpringerBriefs in Applied Sciences and Technology and SpringerBriefs in Computational Mechanics. Berlin, Germany and Heidelberg, Germany: Springer. ISBN: 978-3-642-25310-2. DOI: 10.1007/978-3-642-25311-9.

McCarthy 1990 McCarthy, J. Michael, 1990. *Introduction to Theoretical Kinematics*. Cambridge, MA, USA: MIT Press. ISBN: 0-262-13252-4.

Merlet 1990 Merlet, Jean-Pierre, 1990. *An Algorithm for the Forward Kinematics of General 6 D.o.f. Parallel Manipulators*. Research rep. RR-1331. Sophia-Antipolis, France: Institut National de Recherche en Informatique et en Automatique (INRIA), p. 27.

Merlet 2000 Merlet, Jean-Pierre, 2000. *Parallel Robots*. Solid Mechanics and Its Application. Dordrecht, Netherlands: Kluwer Academic Publishers. DOI: 10.1007/978-94-010-9587-7.

Merlet 2010 Merlet, Jean-Pierre, 2010. MARIONET, A Family of Modular Wire-Driven Parallel Robots. In: Jadran Lenarčič; Michael M. Stanisic, (eds.). *Advances in Robot Kinematics: Motion in Man and Machine*. Vol. 97. Dordrecht, Netherlands: Springer, pp. 53–61. ISBN: 978-90-481-9261-8. DOI: 10.1007/978-90-481-9262-5_6.

Merlet 2014 Merlet, Jean-Pierre, 2014. The Influence of Discrete-Time Control on the Kinematico-Static Behavior of Cable-Driven Parallel Robot With Elastic Cables. In: Jadran Lenarčič; Oussama Khatib, (eds.). *Advances in Robot Kinematics*. Cham, Switzerland: Springer, pp. 113–121. ISBN: 978-3-319-06697-4. DOI: 10.1007/978-3-319-06698-1_13.

Merlet 2015a Merlet, Jean-Pierre, 2015. On the Real-Time Calculation of the Forward Kinematics of Suspended Cable-Driven Parallel Robots. In: *Proceedings of the 14th IFToMM World Congress*. 14th IFToMM World Congress. Taipei, Taiwan, Oct. 25–30, 2015. Vol. 2. International Federation for the Promotion of Mechanism and Machine Science (IFToMM), pp. 276–285. ISBN: 978-986-04-6098-8. DOI: 10.6567/iftomm.14th.wc.os2.020.

Merlet 2015b Merlet, Jean-Pierre, 2015. On the Redundancy of Cable-Driven Parallel Robots. In: Paulo Flores; Fernando Viadero, (eds.). *New Trends in Mechanism and Machine Science*. Vol. 24. Mechanisms and Machine Sciences. Cham, Switzerland: Springer, pp. 31–39. ISBN: 978-3-319-09410-6. DOI: 10.1007/978-3-319-09411-3_4.

Merlet 2015c Merlet, Jean-Pierre, 2015. The Kinematics of Cable-Driven Parallel Robots With Sagging Cables: Preliminary Results. In: *IEEE International Conference on Robotics and Automation*. Seattle, WA, USA, pp. 1593–1598. DOI: 10.1109/icra.2015.7139401.

Merlet 2016 Merlet, Jean-Pierre, 2016. A New Generic Approach for the Inverse Kinematics of Cable-Driven Parallel Robot With 6 Deformable Cables. In: Jadran Lenarčič; Jean-Pierre Merlet, (eds.). *Advances in Robotik Kinematics 2016*. Vol. 4. Springer Proceedings in Advanced Robotics 4. Cham, Switzerland: Springer, pp. 209–216. ISBN: 978-3-319-56802-7. DOI: 10.1007/978-3-319-56802-7_22.

Merlet et al. 2015 Merlet, Jean-Pierre; Alexandre-dit-Sandretto, Julien, 2015. The Forward Kinematics of Cable-Driven Parallel Robots With Sagging Cables. In: Andreas Pott; Tobias Bruckmann, (eds.). *Cable-Driven Parallel Robots*. Vol. 32. Mechanisms and Machine Sciences. Cham, Switzerland: Springer, pp. 3–15. ISBN: 978-3-319-09488-5. DOI: 10.1007/978-3-319-09489-2_1.

Merlet et al. 2008 Merlet, Jean-Pierre; Gosselin, Clément M., 2008. Parallel Mechanisms and Robots. In: Bruno Siciliano; Oussama Khatib, (eds.). *Springer Handbook of Robotics*. Berlin, Germany and Heidelberg, Germany: Springer Science+Business Media. ISBN: 978-3-540-30301-5. DOI: 10.1007/978-3-540-30301-5_13.

Michelin et al. 2015 Michelin, Micaël; Baradat, Cédric; Nguyen, Dinh Quan; Gouttefarde, Marc, 2015. Simulation and Control With Xde and Matlab/Simulink of a Cable-Driven Parallel Robot (Cogiro). In: Andreas Pott; Tobias Bruckmann, (eds.). *Cable-Driven Parallel Robots*. Vol. 32. Mechanisms and Machine Sciences. Cham, Switzerland: Springer, pp. 71–83. ISBN: 978-3-319-09488-5. DOI: 10.1007/978-3-319-09489-2_6.

Miermeister 2010 Miermeister, Philipp, 2010. Dynamic Modeling and Hardware-In-The-Loop Simulation of the Parallel Cable Robot IPAnema Including 3D Visualization. Stuttgart, Germany. Institute for Control Engineering of Machine Tools and Manufacturing Units ISW, University of Stuttgart, Stuttgart, Germany, Cand. thesis, 2010.

Miermeister et al. 2015 Miermeister, Philipp; Kraus, Werner; Lan, Tian; Pott, Andreas, 2015. An Elastic Cable Model for Cable-Driven Parallel Robots Including Hysteresis Effects. In: Andreas Pott; Tobias Bruckmann, (eds.). *Cable-Driven Parallel Robots*. Vol. 32. Mechanisms and Machine Sciences. Cham, Switzerland: Springer, pp. 17–28. ISBN: 978-3-319-09488-5. DOI: 10.1007/978-3-319-09489-2_2.

Miermeister et al. 2016 Miermeister, Philipp; Lachele, Maria; Boss, Rainer; Masone, Carlo; Schenk, Christian; Tesch, Joachim; Kerger, Michael; Teufel, Harald; Pott, Andreas; Bulthoff, Heinrich H., 2016. The Cablerobot Simulator Large Scale Motion Platform Based on Cable Robot Technology. In: *2016 IEEE/RSJ International Conference on Intelligent Robots and Systems*. 2016 IEEE/RSJ International Conference on Intelligent Robots and Systems. Daejeon, South Korea. Institute of Electrical and Electronics Engineers (IEEE), pp. 3024–3029. ISBN: 978-1-5090-3762-9. DOI: 10.1109/iros.2016.7759468.

Miermeister et al. 2010a Miermeister, Philipp; Pott, Andreas, 2010. Modelling and Real-Time Dynamic Simulation of the Cable-Driven Parallel Robot IPAnema. In: Doina Pisla; Marco Ceccarelli; Manfred L. Husty; Burkhard Corves, (eds.). *New Trends*

in Mechanism Science. Dordrecht, Netherlands: Springer, pp. 353–360. ISBN: 978-90-481-9688-3. DOI: 10.1007/978-90-481-9689-0_41.

Miermeister et al. 2010b Miermeister, Philipp; Pott, Andreas; Verl, Alexander, 2010. Dynamic Modeling and Hardware-In-The-Loop Simulation for the Cable-Driven Parallel Robot IPAnema. In: *International Symposium on Robotics and German Conference on Robotics: Proceedings of the 2010*. International Symposium on Robotics and German Conference on Robotics. Munich, Germany, June 7–9, 2010, pp. 1–8. ISBN: 978-3-8007-3273-9.

Mikelsons et al. 2008 Mikelsons, Lars; Bruckmann, Tobias; Schramm, Dieter; Hiller, Manfred, 2008. A Real-Time Capable Force Calculation Algorithm for Redundant Tendon-Based Parallel Manipulators. In: *IEEE International Conference on Robotics and Automation, 2008*. Pasadena, CA, USA. Institute of Electrical and Electronics Engineers (IEEE). DOI: 10.1109/robot.2008.4543805.

Ming et al. 1994 Ming, Aiguo; Higuchi, Toshiro, 1994. Study on Multiple Degree-Of-Freedom Positioning Mechanism Using Wires (Part 1): Concept, Design and Control. *International Journal of the Japan Society for Precision Engineering* **28** (2), pp. 131–138.

Miranda et al. 1997 Miranda, Mario J.; Fackler, Paul R., 1997. *Numerical Integration*. Boston, MA, USA: Boston College. DOI: 10.1201/9781315137650-3. URL: http://fmwww.bc.edu/ec-p/software/miranda/default.html.

Miyasaka et al. 2016 Miyasaka, Muneaki; Haghighipanah, Mohammad; Li, Yangming; Hannaford, Blake, 2016. Hysteresis Model of Longitudinally Loaded Cable for Cable Driven Robots and Identification of the Parameters. In: *Robotics and Automation: 2016 IEEE International Conference on*. 2016 IEEE International Conference on Robotics and Automation. Stockholm, Sweden, May 16–21, 2016. Institute of Electrical and Electronics Engineers (IEEE), pp. 4051–4057. DOI: 10.1109/icra.2016.7487596.

Miyasaka et al. 2015 Miyasaka, Muneaki; Matheson, Joseph; Lewis, Andrew; Hannaford, Blake, 2015. Measurement of the Cable-Pulley Coulomb and Viscous Friction for a Cable-Driven Surgical Robotic System. In: *Intelligent Robots and Systems: Proceedings of the 2015 IEEE/RSJ International Conference on*. 2015 IEEE/RSJ International Conference on Intelligent Robots and Systems. Hamburg, Germany. IEEE Robotics Society of Japan (IEEE/RSJ), pp. 804–810. DOI: 10.1109/iros.2015.7353464.

Mladenova 1999 Mladenova, Clementina D., 1999. Applications of Lie Group Theory to the Modeling and Control of Multibody Systems. *Multibody System Dynamics* **3**, pp. 367–380. ISSN: 1384-5640.

Mousavi et al. 2018 Mousavi, Mohammad Reza; Ghanbari, Masoud; Moosavian, S. Ali A.; Zarafshan, Payam, 2018. Explicit Dynamics of Redundant Parallel Cable Robots. *Nonlinear Dynamics* **13** (1), p. 66. ISSN: 0924-090X. DOI: 10.1007/s11071-018-4476-7.

Nahon 1999 Nahon, Meyer, 1999. Dynamics and Control of a Novel Radio Telescope Antenna. In: *Modeling and Simulation Technologies Conference and Exhibit*. Modeling and Simulation Technologies Conference and Exhibit. Portland, OR, USA, Aug. 9–11, 1999. American Institute of Aeronautics and Astronautics. DOI: 10.2514/6.1999-4120.

Nan et al. 2011 Nan, Rendong; Li, Di; Jin, Chengjin; Wang, Qiming; Zhu, Lichun; Zhu, Wenbai; Zhang, Haiyan; Yue, Youling; Qian, Lei; Nan, Rendong; Jin, Chengjin; Wang, Qiming; Zhu, Lichun; Zhu, Wenbai; Zhang, Haiyan; Yue, Youling, 2011. The Five-Hundred Meter Aperture Spherical Radio Telescope (FAST) Project. *International Journal of Modern Physics D* **20** (6), pp. 989–1024. DOI: 10.1142/s0218271811019335. URL: https://arxiv.org/ftp/arxiv/papers/1105/1105.3794.pdf.

Nan et al. 2003 Nan, Rendong; Ren, Gexue; Zhu, Wenbai; Lu, Yingjie., 2003. Adaptive Cable-Mesh Reflector for the FAST. (44). J. L. Han; X. H. Sun; J. Yang; R. Wielebinski (ed.), pp. 13–18. ISSN: 1874-1029.

Nikravesh 2008 Nikravesh, Parviz E., 2008. Newtonian-Based Methodologies in Multi-Body Dynamics. *Proceedings of the Institution of Mechanical Engineers, Part K: Journal of Multi-Body Dynamics* **222** (4), pp. 277–288. ISSN: 1464-4193. DOI: 10.1243/14644193jmbd152.

O'Masta 2014 O'Masta, Mark R., 2014. Mechanisms of Dynamic Deformation and Failure in Ultra-High Molecular Weight Polyethylene Fiber-Polymer Matrix Composites. Charlottesville, VA, USA. School of Engineering and Applied Science, University of Virginia, Charlottesville, VA, USA, PhD thesis, 2014. DOI: 10.18130/V3M243. URL: http://www.virginia.edu/ms/research/wadley/thesis/omastaphd.pdf.

Oh et al. 2004 Oh, So-Ryeok; Agrawal, Sunil Kumar, 2004. Nonlinear Sliding Mode Control and Feasible Workspace Analysis for a Cable Suspended Robot With Input Constraints and Disturbances. In: *American Control Conference: Proceedings of the 2004 IEEE*. 2004 IEEE American Control Conference. Boston, MA, USA, June 30–July 2, 2004. Vol. 5. Institute of Electrical and Electronics Engineers (IEEE), pp. 4631–4636. ISBN: 0-7803-8335-4. DOI: 10.23919/acc.2004.1384041.

Omelyan 1999 Omelyan, Igor P., 1999. A New Leapfrog Integrator of Rotational Motion: The Revised Angular-Momentum Approach. *Molecular Simulation* **22** (3), pp. 213–236. ISSN: 0892-7022. DOI: 10.1080/08927029908022097.

Omelyan et al. 2002 Omelyan, Igor P.; Mryglod, Ihor M.; Folk, Reinhard, 2002. Optimized Forest–Ruth And Suzuki-Like Algorithms for Integration of Motion in Many-Body Systems. *Computer Physics Communications* **146** (2), pp. 188–202. ISSN: 0010-4655. DOI: 10.1016/s0010-4655(02)00451-4.

Oprea 2007 Oprea, John, 2007. *Differential Geometry and Its Applications*. 2nd ed. Washington, DC, USA and Cambridge: Mathematical Association of America and Cambridge University Press. ISBN: 978-0-883-85748-9.

Palli et al. 2012 Palli, Gianluca; Borghesan, Gianni; Melchiorri, Claudio, 2012. Modeling, Identification, and Control of Tendon-Based Actuation Systems. *IEEE Transactions on Robotics* **28** (2), pp. 277–290. ISSN: 1552-3098. DOI: 10.1109/tro.2011.2171610.

Paul 1981 Paul, Richard P., 1981. *Robot Manipulators: Mathematics, Programming, and Control: The Computer Control of Robot Manipulators*. The MIT Press Series in Artificial Intelligence. Cambridge, MA, USA and London, England, United Kingdom: MIT. ISBN: 978-0-262-16082-7.

Phillips 2003 Phillips, George M., 2003. *Interpolation and Approximation by Polynomials*. New York, NY, USA: Springer New York. ISBN: 978-0-387-00215-6. DOI: 10.1007/b97417.

Piao et al. 2018 Piao, Jinlong; Jin, XueJun; Choi, Eunpyo; Park, Jong-Oh; Kim, Chang-Sei; Jung, Jinwoo, 2018. A Polymer Cable Creep Modeling for a Cable-Driven Parallel Robot in a Heavy Payload Application. In: Clément M. Gosselin; Philippe Cardou; Tobias Bruckmann; Andreas Pott, (eds.). *Cable-Driven Parallel Robots: Proceedings of the Third International Conference on Cable-Driven Parallel Robots*. Mechanisms and Machine Science 53. Cham, Switzerland: Springer, pp. 62–72. ISBN: 978-3-319-61431-1.

Piao et al. 2017 Piao, Jinlong; Jin, XueJun; Jung, Jinwoo; Choi, Eunpyo; Park, Jong-Oh; Kim, Chang-Sei, 2017. Open-Loop Position Control of a Polymer Cable-Driven Parallel Robot via a Viscoelastic Cable Model for High Payload Workspaces. *Advances in Mechanical Engineering* **9** (12), pp. 1–12. ISSN: 1687-8132. DOI: 10.1177/1687814017737199.

Piegl et al. 1997 Piegl, Les; Tiller, Wayne, 1997. *The NURBS Book*. Berlin, Germany and Heidelberg, Germany: Springer. ISBN: 978-3-540-61545-3. DOI: 10.1007/978-3-642-59223-2.

Pott 2010 Pott, Andreas, 2010. An Algorithm for Real-Time Forward Kinematics of Cable-Driven Parallel Robots. In: Jadran Lenarčič; Michael M. Stanisic, (eds.). *Advances in Robot Kinematics: Motion in Man and Machine*. Dordrecht, Netherlands: Springer, pp. 529–538. ISBN: 978-90-481-9261-8. DOI: 10.1007/978-90-481-9262-5_57.

Pott 2012 Pott, Andreas, 2012. Influence of Pulley Kinematics on Cable-Driven Parallel Robots. In: *Latest Advances in Robot Kinematics*. Dordrecht, Netherlands: Springer, pp. 197–204. DOI: 10.1007/978-94-007-4620-6_25.

Pott 2013 Pott, Andreas, 2013. An Improved Force Distribution Algorithm for Over-Constrained Cable-Driven Parallel Robots. In: Federico Thomas; Alba Perez Gracia, (eds.). *Computational Kinematics: Proceedings of the 6th International Workshop on Computational Kinematics*. Berlin, Germany and Heidelberg, Germany: Springer, pp. 139–146. ISBN: 978-94-007-7214-4. DOI: 10.1007/978-94-007-7214-4_16.

Pott 2018 Pott, Andreas, 2018. *Cable-Driven Parallel Robots: Theory and Application*. Vol. 120. Cham, Switzerland: Springer. ISBN: 978-3-319-76137-4. DOI: 10.1007/978-3-319-76138-1.

Pott et al. 2012 Pott, Andreas; Mütherich, Hendrik; Kraus, Werner; Schmidt, Valentin; Miermeister, Philipp; Verl, Alexander, 2012. IPAnema: A Family of Cable-Driven Parallel Robots for Industrial Applications. In: Tobias Bruckmann; Andreas Pott, (eds.). *Cable-Driven Parallel Robots*. Mechanisms and Machine Sciences 12. Berlin, Germany and Heidelberg, Germany: Springer, pp. 119–134. ISBN: 978-3-642-31987-7. DOI: 10.1007/978-3-642-31988-4_8.

Pott et al. 2015 Pott, Andreas; Schmidt, Valentin, 2015. On the Forward Kinematics of Cable-Driven Parallel Robots. In: *2015 IEEE/RSJ International Conference on Intelligent Robots and Systems*. 2015 IEEE/RSJ International Conference on Intelligent Robots and Systems. Hamburg, Germany. Institute of Electrical and Electronics Engineers

(IEEE), pp. 3182–3187. ISBN: 978-1-4799-9994-1. DOI: 10.1109/iros.2015.7353818.

Pott et al. 2019 Pott, Andreas; Tempel, Philipp; Verl, Alexander; Wulle, Frederik, 2019. Design, Implementation and Long-Term Running Experiences of the Cable-Driven Parallel Robot CaRo Printer. In: Andreas Pott; Tobias Bruckmann, (eds.). *Mechanisms and Machine Science: Proceedings of the Fourth International Conference on Cable-Driven Parallel Robots*. Vol. 74. Advances in Mechanism and Machine Science 74. Cham, Switzerland: Springer, pp. 379–390. DOI: 10.1007/978-3-030-20751-9_32.

Qian 2007 Qian, Hongliang, 2007. Theoretical and Experimental Research on Supporting Structure of FAST Reflector. Harbin, Heilongjiang, People's Republic of China. Harbin Instiue of Technology, Harbin, Heilongjiang, People's Republic of China, PhD thesis, 2007.

Quisenberry et al. 2006 Quisenberry, Johnny; Arena, Andrew, 2006. Discrete Cable Modeling and Dynamic Analysis. In: *Aerospace Sciences Meeting and Exhibit: Proceedings of the 2006 44th AIAA*. Reno, NV, USA, Jan. 9–12, 2006. American Institute of Aeronautics and Astronautics (AIAA). DOI: 10.2514/6.2006-424.

Vu-Quoc et al. 1995 Vu-Quoc, Loc; Li, Shenghu, 1995. Dynamics of Sliding Geometrically-Exact Beams: Large Angle Maneuver and Parametric Resonance. *Computer Methods in Applied Mechanics and Engineering* **120** (1-2), pp. 65–118. ISSN: 0045-7825. DOI: 10.1016/0045-7825(94)00051-n.

Raghavan 1993 Raghavan, Mala, 1993. The Stewart Platform of General Geometry Has 40 Configurations. *Journal of Mechanical Design* **115** (2), pp. 277–282. ISSN: 1050-0472. DOI: 10.1115/1.2919188.

Ramadour et al. 2014 Ramadour, Remy; Merlet, Jean-Pierre, 2014. Computing Safe Trajectories for an Assistive Cable-Driven Parallel Robot by Selecting the Cables Under Tension and Using Interval Analysis. In: *IEEE/ASME International Conference on Advanced Intelligent Mechatronics (AIM), 2014*, pp. 1349–1354. DOI: 10.1109/aim.2014.6878270.

Reichert et al. 2015 Reichert, Christopher; Müller, Katharina; Bruckmann, Tobias, 2015. Robust Internal Force-Based Impedance Control for Cable-Driven Parallel Robots. In: Andreas Pott; Tobias Bruckmann, (eds.). *Cable-Driven Parallel Robots*. Mechanisms and Machine Sciences. Cham, Switzerland: Springer, pp. 131–143. ISBN: 978-3-319-09488-5. DOI: 10.1007/978-3-319-09489-2_10.

Riehl et al. 2010 Riehl, Nicolas; Gouttefarde, Marc; Baradat, Cédric; Pierrot, François, 2010. On the Determination of Cable Characteristics for Large Dimension Cable-Driven Parallel Mechanisms. In: *Robotics and Automation: Proceedings of the 2010 IEEE International Conference on*. 2010 IEEE International Conference on Robotics and Automation. Anchorage, AK, USA. Institute of Electrical and Electronics Engineers (IEEE), pp. 4709–4714. DOI: 10.1109/robot.2010.5509887.

Rolland 2005 Rolland, Luc, 2005. Certified Solving of the Forward Kinematics Problem With an Exact Algebraic Method for the General Parallel Manipulator. *Advanced Robotics* **19** (9), pp. 995–1025. ISSN: 0169-1864. DOI: 10.1163/156855305774307004.

Romanyk et al. 2013 Romanyk, Dan L.; Melenka, Garrett W.; Carey, Jason P., 2013. Modeling Stress-Relaxation Behavior of the Periodontal Ligament During the Initial Phase of Orthodontic Treatment. *Journal of Biomechanical Engineering* **135** (9), p. 91007. ISSN: 1528-8951. DOI: 10.1115/1.4024631.

Rosati et al. 2007 Rosati, Giulio; Andreolli, Mattia; Biondi, Andrea; Gallina, Paolo, 2007. Performance of Cable Suspended Robots for Upper Limb Rehabilitation. In: *Rehabilitation Robotics: Proceedings of the 2007 IEEE International Conference on*. 2007 IEEE International Conference on Rehabilitation Robotics. Noordwijk, Netherlands, June 13–15, 2007. Institute of Electrical and Electronics Engineers (IEEE). Institute of Electrical and Electronics Engineers (IEEE), pp. 385–392. ISBN: 978-1-4244-1319-5. DOI: 10.1109/icorr.2007.4428454.

Rosati et al. 2005 Rosati, Giulio; Gallina, Paolo; Masiero, Stefano; Rossi, Aldo, 2005. Design of a New 5 D.o.f. Wire-Based Robot for Rehabilitation, pp. 430–433. DOI: 10.1109/icorr.2005.1501135.

Rosati et al. 2008 Rosati, Giulio; Seccoli, Riccardo; Zanotto, Damiano; Rossi, Aldo; Boschetti, Giovanni, 2008. Planar Robotic Systems for Upper-Limb Post-Stroke Rehabilitation. In: *Mechanical Engineering Congress and Exposition: Proceedings of the 2008 ASME International*. 2008 ASME International Mechanical Engineering Congress and Exposition. American Society of Mechanical Engineers (ASME). DOI: 10.1115/imece2008-67273.

Rost 2013 Rost, Arne, 2013. Untersuchung von Antrieben mit Kunststoff-Faserseilen für den Einsatz in Leichtbau-Gelenkarmrobotern. Stuttgart, Germany: Fraunhofer Verlag. Stuttgarter Beiträge zur Produktionsforschung 13. Institut für Steuerungstechnik der Werkzeugmaschinen und Fertigungseinrichtungen, Universität Stuttgart, Germany, Stuttgart, Germany, PhD thesis, 2013. ISBN: 978-3-8396-0568-4. DOI: 10.18419/opus-4545. urn: urn:nbn:de:bsz:93-opus-86109.

Roylance 2001 Roylance, David, 2001. *Engineering Viscoelasticity*. Cambridge, MA, USA: Department of Materials Science and Engineering, Massachusetts Institute of Technology. URL: https://web.mit.edu/course/3/3.11/www/modules/visco.pdf.

Sanathanan et al. 1963 Sanathanan, C. K.; Koerner, Judith, 1963. Transfer Function Synthesis as a Ratio of Two Complex Polynomials. *IEEE Transactions on Automatic Control* **8** (1), pp. 56–58. ISSN: 0018-9286. DOI: 10.1109/tac.1963.1105517.

Sanborn et al. 2015 Sanborn, Brett; DiLeonardi, Ann Mae; Weerasooriya, Tusit, 2015. Tensile Properties of Dyneema Sk76 Single Fibers at Multiple Loading Rates Using a Direct Gripping Method. *Journal of Dynamic Behavior of Materials* **1** (1), pp. 4–14. ISSN: 2199-7446. DOI: 10.1007/s40870-014-0001-3.

Sandretto et al. 2013 Sandretto, Julien Alexandre dit; Daney, David; Gouttefarde, Marc; Baradat, Cedric, 2013. *Calibration of a Fully-Constrained Parallel Cable-Driven Robot*. Research Centre Sophia Antipolis-Mdeiterranee. DOI: 10.1007/978-3-7091-1379-0_10.

Sauter 2003 Sauter, Daniel, 2003. Modeling the Dynamic Characteristics of Slack Wire Cables in Stockbridge Dampers. Darmstadt, Germany. Department of Mechanics, Technische Universität Darmstadt, Germany, Darmstadt, Germany, PhD thesis, 2003. urn: urn:nbn:de:tuda-tuprints-4176.

Schenk et al. 2015 Schenk, Christian; Bulthoff, Heinrich H.; Masone, Carlo, 2015. Robust Adaptive Sliding Mode Control of a Redundant Cable Driven Parallel Robot. In: *19th International Conference on System Theory, Control and Computing (Icstcc), 2015*. Cheile Gradistei, Romania, pp. 427–434. DOI: 10.1109/icstcc.2015.7321331.

Schenk et al. 2016 Schenk, Christian; Masone, Carlo; Miermeister, Philipp; Bulthoff, Heinrich H., 2016. Modeling and Analysis of Cable Vibrations for a Cable-Driven Parallel Robot. In: *2016 IEEE International Conference on Information and Automation*. 2016 IEEE International Conference on Information and Automation. Ningbo, China, Jan. 8–Mar. 8, 2016. Institute of Electrical and Electronics Engineers (IEEE), pp. 454–461. ISBN: 978-1-5090-4102-2. DOI: 10.1109/icinfa.2016.7831867.

Schmidt 2016 Schmidt, Valentin, 2016. Modeling Techniques and Reliable Real-Time Implementation of Kinematics for Cable-Driven Parallel Robots Using Polymer Fiber Cables. Stuttgart, Germany: Fraunhofer Verlag. Stuttgarter Beiträge zur Produktionsforschung 33. Institute for Control Engineering of Machine Tools and Manufacturing Units ISW, University of Stuttgart, Stuttgart, Germany, PhD thesis, 2016. ISBN: 978-3-8396-1168-5. DOI: 10.18419/opus-9085. urn: urn:nbn:de:bsz:93-opus-ds-91021.

Schmidt et al. 2014 Schmidt, Valentin; Müller, Bertram; Pott, Andreas, 2014. Solving the Forward Kinematics of Cable-Driven Parallel Robots With Neural Networks and Interval Arithmetic. In: Federico Thomas; Alba Perez Gracia, (eds.). *Computational Kinematics*. Vol. 15. Mechanisms and Machine Sciences. Dordrecht, Netherlands: Springer, pp. 103–110. ISBN: 978-94-007-7213-7. DOI: 10.1007/978-94-007-7214-4_12.

Schröppel et al. 2016 Schröppel, Christian; Wackerfuß, Jens, 2016. Introducing the Logarithmic Finite Element Method: A Geometrically Exact Planar Bernoulli Beam Element. *Advanced Modeling and Simulation in Engineering Sciences* **3** (1), p. 85. DOI: 10.1186/s40323-016-0074-8.

Siciliano et al. 2008 Siciliano, Bruno; Khatib, Oussama, 2008. *Springer Handbook of Robotics*. Berlin, Germany and Heidelberg, Germany: Springer. ISBN: 978-3-540-23957-4. DOI: 10.1007/978-3-540-30301-5.

Soler et al. 2018 Soler, Carlota; Martin, Tobias; Sorkine-Hornung, Olga, 2018. Cosserat Rods With Projective Dynamics. *Eurographics Symposium on Computer Animation* **37** (8).

Spak et al. 2014 Spak, Kaitlin; Agnes, Gregory; Inman, Daniel, 2014. Cable Parameters for Homogenous Cable-Beam Models for Space Structures. In: Fikret Necati Catbas, (ed.). *Dynamics of Civil Structures, Volume 4*. Conference Proceedings of the Society for Experimental Mechanics Series. Cham, Switzerland: Springer, pp. 7–18. ISBN: 978-3-319-04545-0. DOI: 10.1007/978-3-319-04546-7_2.

Stewart 1965 Stewart, D., 1965. A Platform With Six Degrees of Freedom. *Proceedings of the Institution of Mechanical Engineers* **180** (1), pp. 371–386. DOI: 10.1243/pime_proc_1965_180_029_02.

Stoer et al. 2002 Stoer, Josef; Bulirsch, Roland, 2002. *Introduction to Numerical Analysis*. New York, NY, USA: Springer New York. ISBN: 978-1-4419-3006-4. DOI: 10.1007/978-0-387-21738-3.

Stribeck 1903 Stribeck, R., 1903. *Die Wesentlichen Eigenschaften der Gleit- und Rollenlager*. Berlin, Germany: Springer.

Sun et al. 2008 Sun, Jinghai; Nan, Rendong; Zhu, Wenbai; Kärcher, Hans J.; Li, Hui; Angeli, George Z.; Cullum, Martin J., 2008. Simulation Model of FAST Focus Cabin for Pointing Accuracy Analysis. In: *Astronomical Telescopes and Instrumentation: Synergies Between Ground and Space*. Marseille, France, June 23, 2008. Vol. 7017. SPIE Proceedings. SPIE, pp. 70171L-1-70171L-10. DOI: 10.1117/12.787804.

Sun et al. 2015 Sun, Limin; Chen, Lin, 2015. Free Vibrations of a Taut Cable With a General Viscoelastic Damper Modeled by Fractional Derivatives. *Journal of Sound and Vibration* **335**, pp. 19–33. ISSN: 0022-460X. DOI: 10.1016/j.jsv.2014.09.016.

Surdilovic et al. 2007 Surdilovic, Dragoljub; Zhang, Jinyu; Bernhardt, Rolf, 2007. STRING-MAN: Wire-Robot Technology for Safe, Flexible and Human-Friendly Gait Rehabilitation. In: *Rehabilitation Robotics: Proceedings of the 2007 IEEE International Conference on*. 2007 IEEE International Conference on Rehabilitation Robotics. Noordwijk, Netherlands, June 13–15, 2007. Institute of Electrical and Electronics Engineers (IEEE). Institute of Electrical and Electronics Engineers (IEEE), pp. 446–453. ISBN: 978-1-4244-1319-5. DOI: 10.1109/icorr.2007.4428463.

Szczotka 2010 Szczotka, Marek, 2010. Pipe Laying Simulation With an Active Reel Drive. *Ocean Engineering* **37** (7), pp. 539–548. ISSN: 0029-8018. DOI: 10.1016/j.oceaneng.2010.02.009.

Takata et al. 2018 Takata, Atsushi; Endo, Gen; Suzumori, Koichi; Nabae, Hiroyuki; Mizutani, Yoshihiro; Suzuki, Yoshiro, 2018. Modeling of Synthetic Fiber Ropes and Frequency Response of Long-Distance Cable-Pulley System. *IEEE Robotics and Automation Letters*, p. 1. ISSN: 2377-3766. DOI: 10.1109/lra.2018.2803204.

Tang et al. 2009 Tang, Aofei; Qiu, Yuan-Ying; Mi, Jianwei; Kong, Lingfei, 2009. On Similarity of the Abnormal Model of a Wire Driven Parallel Robot. *Yingyong Jichu Yu Gongcheng Kexue Xuebao/Journal of Basic Science and Engineering* **17** (3), pp. 452–460. ISSN: 1005-0930.

Tang 2014 Tang, Xiaoqiang, 2014. An Overview of the Development for Cable-Driven Parallel Manipulator. *Advances in Mechanical Engineering* **2014** (10), pp. 1–9. ISSN: 1687-8132. DOI: 10.1155/2014/823028.

Tang et al. 2014 Tang, Xiaoqiang; Liu, Zhihua; Shao, Zhufeng; Wang, Liping, 2014. Self-Excited Vibration Analysis for the Feed Support System in FAST. *International Journal of Advanced Robotic Systems* **11** (4), p. 63. ISSN: 1729-8806. DOI: 10.5772/58521.

Tempel et al. 2019 Tempel, Philipp; Lee, Dongwon; Trautwein, Felix; Pott, Andreas, 2019. Modeling of Elastic-Flexible Cables With Time-Varying Length for Cable-Driven Parallel Robots. In: Andreas Pott; Tobias Bruckmann, (eds.). *Cable-Driven Parallel Robots: Proceedings of the Fourth International Conference on Cable-Driven Parallel Robots*. International Conference on Cable-Driven Parallel Robots. Krakow, Poland, July 1–4, 2019. Vol. 74. Advances in Mechanism and Machine Science 74. Cham, Switzerland: Springer, pp. 295–306. DOI: 10.1007/978-3-030-20751-9_25.

Tempel et al. 2015a Tempel, Philipp; Miermeister, Philipp; Lechler, Armin; Pott, Andreas, 2015. Modelling of Kinematics and Dynamics of the IPAnema 3 Cable Robot for Simulative Analysis. *Applied Mechanics and Materials* **794**, pp. 419–426. ISSN: 1662-7482. DOI: 10.4028/www.scientific.net/amm.794.419.

Tempel et al. 2015b Tempel, Philipp; Miermeister, Philipp; Pott, Andreas, 2015. Kinematics and Dynamics Modeling for Real-Time Simulation of the Cable-Driven Parallel Robot IPAnema 3. In: *Proceedings of the 14th IFToMM World Congress*. 14th IFToMM World Congress. Taipei, Taiwan. Vol. 2. International Federation for the Promotion of Mechanism and Machine Science (IFToMM), pp. 117–123. ISBN: 978-986-04-6098-8. DOI: 10.6567/iftomm.14th.wc.os4.020.

Tempel et al. 2015c Tempel, Philipp; Pott, Andreas, 2015. *Stuttgarter Simulationsforscher bei Expo 2015 in Mailand: Simulation Technology Success Stories*. Stuttgart, Germany: SimTech Cluster of Excellence.

Tempel et al. 2017 Tempel, Philipp; Schmidt, Andreas; Haasdonk, Bernard; Pott, Andreas, 2017. Application of the Rigid Finite Element Method to the Simulation of Cable-Driven Parallel Robots. In: Saïd Zeghloul; Lotfi Romdhane; Med Amine Laribi, (eds.). *Computational Kinematics*. Mechanisms and Machine Sciences 50. Cham, Switzerland: Springer, pp. 198–205. ISBN: 978-3-319-60867-9. DOI: 10.1007/978-3-319-60867-9_23.

Tempel et al. 2015d Tempel, Philipp; Schnelle, Fabian; Pott, Andreas; Eberhard, Peter, 2015. Design and Programming for Cable-Driven Parallel Robots in the German Pavilion at the Expo 2015. *Machines* **3** (3), pp. 223–241. ISSN: 2075-1702. DOI: 10.3390/machines3030223.

Tempel et al. 2018 Tempel, Philipp; Trautwein, Felix; Pott, Andreas, 2018. Experimental Identification of Stress-Strain Material Models of UHMWPE Fiber Cables for Improving Cable Tension Control Strategies. In: Jadran Lenarčič; Vincenzo Parenti-Castelli, (eds.). *Advances in Robot Kinematics 2018*. Vol. 8. 8. Cham, Switzerland: Springer, pp. 258–265. ISBN: 978-3-319-93187-6. DOI: 10.1007/978-3-319-93188-3_30.

Tibshirani 2015 Tibshirani, Ryan, 2015. *Newton's Method: Machine Learning 10-725 and Statistics 36-725*. Carnegie Mellon University. URL: http://www.stat.cmu.edu/~ryantibs/convexopt-s15/lectures/14-newton.pdf, visited on: 03/14/2017.

Verhoeven 2004 Verhoeven, Richard, 2004. Analysis of the Workspace of Tendon-Based Stewart Platforms. Duisburg, Germany. Universität Duisburg-Essen, Duisburg, Germany, PhD thesis, 2004. urn: urn:nbn:de:hbz:464-20061017-114435-6.

Vlasblom et al. 2006 Vlasblom, Martin P.; Bosman, Rigo L. M., 2006. Predicting the Creep Lifetime of HMPE Mooring Rope Applications. In: *OCEANS 2006*. Boston, MA, USA. Marine Technology Society (MTS), Institute of Electrical, and Electronics Engineers (IEEE). IEEE, pp. 1–10. DOI: 10.1109/oceans.2006.307013.

Voorhoeve et al. 2014 Voorhoeve, Robbert; Oomen, Tom; Herpen, Robbert van; Steinbuch, Maarten, 2014. On Numerically Reliable Frequency-Domain System Identification: New Connections and a Comparison of Methods. *IFAC Proceedings Volumes* **47** (3), pp. 10018–10023. ISSN: 1474-6670. DOI: 10.3182/20140824-6-za-1003.02264.

Wehage et al. 1982 Wehage, Roger A.; Haug, Edward J., 1982. Generalized Coordinate Partitioning for Dimension Reduction in Analysis of Constrained Dynamic Systems. *Journal of Mechanical Design* **104** (1), p. 247. ISSN: 1050-0472. DOI: 10.1115/1.3256318.

Whittle 1953 Whittle, Peter, 1953. Estimation and Information in Stationary Time Series. *Arkiv för Matematik* **2** (5), pp. 423–434. ISSN: 0004-2080. DOI: 10.1007/bf02590998.

Whittle 1983 Whittle, Peter, 1983. *Prediction and Regulation by Linear Least-Square Methods*. 2nd ed. Minneapolis, MI, USA: University of Minnesota Press. ISBN: 0-8166-1147-5. DOI: 10.5749/j.ctttsphx.

Yan 2016 Yan, Yuong, 2016. Developments in Fibers for Technical Nonwovens. In: *Advances in Technical Nonwovens*. Elsevier, pp. 19–96. ISBN: 978-0-081-00575-0. DOI: 10.1016/b978-0-08-100575-0.00002-4.

Yoshida 1990 Yoshida, Haruo, 1990. Construction of Higher Order Symplectic Integrators. *Physics Letters A* **150** (5-7), pp. 262–268. ISSN: 0375-9601. DOI: 10.1016/0375-9601(90)90092-3.

Young 2014 Young, Peter, 2014. *The Leapfrog Method and Other "Symplectic" Algorithms for Integrating Newton's Laws of Motion*. Physics Department, UC Santa Cruz.

Zarebidoki et al. 2011a Zarebidoki, Mahmoud; Lotfavar, Amir; Fahham, Hamid Reza, 2011. Dynamic Modeling and Robust Passivity-Based Control of a Cable-Suspended Robot. In: *Control, Instrumentation and Automation: Proceedings of the 2011 IEEE 2nd International Conference on*. 2011 IEEE 2nd International Conference on Control, Instrumentation, and Automation. Shiraz, Iran, Dec. 27–29, 2011. Institute of Electrical and Electronics Engineers (IEEE), pp. 923–928. ISBN: 978-1-4673-1689-7. DOI: 10.1109/icciautom.2011.6356785.

Zarebidoki et al. 2011b Zarebidoki, Mahmoud; Lotfavar, Amir; Fahham, Hamid Reza, 2011. Effectiveness of Adaptive Passivity-Based Trajectory Tracking Control of a Cable-Suspended Robot. In: *Trends in Mechanical and Industrial Engineering: Proceedings of the 2011 International Conference on*. International Conference on Trends in Mechanical and Industrial Engineering. Bangkok, Thailand, Dec. 23–24, 2011.

Zhang et al. 2016 Zhang, Guodong; Alberdi, Ryan; Khandelwal, Kapil, 2016. Analysis of Three-Dimensional Curved Beams Using Isogeometric Approach. *Engineering Structures* **117**, pp. 560–574. ISSN: 0141-0296. DOI: 10.1016/j.engstruct.2016.03.035.

Zohoor et al. 2013 Zohoor, Hassan; Kakavand, Farshad, 2013. Timoshenko Versus Euler–Bernoulli Beam Theories for High Speed Two-Link Manipulator. *Scientica Iranica* **20** (1), pp. 172–178. DOI: 10.1016/j.scient.2012.12.016.

Zohoor et al. 2008 Zohoor, Hassan; Khorsandijou, S. Mahdi; Abedinnasa, Mohammad H., 2008. Modified Nonlinear 3D Euler Bernoulli Beam Theory. *Journal of System Design and Dynamics* **2** (5), pp. 1170–1182. DOI: 10.1299/jsdd.2.1170.

Appendices

Appendix A

Robot Configurations

A.1 CoGiRo

Frame and Platform Dimension

Table A.1: Spatial positions of frame anchors and platform anchors give in respective local coordinate systems on cable robot CoGiRo.

	Frame anchor			Platform anchor		
Cable	$\boldsymbol{a}_{i,x}$/m	$\boldsymbol{a}_{i,y}$/m	$\boldsymbol{a}_{i,z}$/m	$\boldsymbol{b}_{i,x}$/m	$\boldsymbol{b}_{i,y}$/m	$\boldsymbol{b}_{i,z}$/m
1	−7.1197	5.4726	5.4106	0.4961	0.3561	0.9996
2	7.5056	5.0789	5.4182	0.4998	−0.3404	0.9991
3	7.1435	−5.5416	5.3975	−0.5045	−0.3463	0.9977
4	−7.4786	−5.1544	5.4009	−0.5097	0.3508	0.9976
5	−7.4083	5.1914	5.3987	−0.5032	−0.2700	0.0000
6	7.2243	5.3689	5.4080	−0.5032	0.4928	0.0000
7	7.4288	−5.2613	5.3878	0.5021	0.2750	−0.0007
8	−7.1967	−5.4398	5.3928	0.5032	−0.4928	0.0000

Platform

Table A.2: Inertial properties of mobile platform of cable robot CoGiRo.

Property	Variable	Value	Unit
Mass	m	90	kg
Inertia tensor	J_{xx}	36.598	$\mathrm{kg\,m^2}$
	J_{xy}	−0.453	$\mathrm{kg\,m^2}$
	J_{xz}	3.012	$\mathrm{kg\,m^2}$
	J_{yx}	−0.453	$\mathrm{kg\,m^2}$
	J_{yy}	35.982	$\mathrm{kg\,m^2}$
	J_{yz}	−1.539	$\mathrm{kg\,m^2}$
	J_{zx}	3.012	$\mathrm{kg\,m^2}$
	J_{zy}	−1.539	$\mathrm{kg\,m^2}$
	J_{zz}	25.439	$\mathrm{kg\,m^2}$

Cables

Table A.3: Mechanical properties of cables used on cable robot CoGiRo. Poisson's ratio inferred from (Yan 2016).

Property	Variable	Value	Unit
Diameter	d	9	mm
Cross-Section	A	63.617	$\mathrm{mm^2}$
Moment of Area	I	20.129	$\mathrm{mm^4}$
Unit Density	ϱ	2970.892	$\mathrm{kg\,m^{-3}}$
Young's Modulus	E	200	GPa
Poisson's Ratio	ν	0.290	−
Shear Modulus	G	77.519	GPa

A.2 COPacabana

Frame and Platform Dimension

Table A.4: Spatial positions of frame anchors and platform anchors give in respective local coordinate systems on cable robot COPHandling.

	Frame anchor			Platform anchor		
Cable	$\boldsymbol{a}_{i,x}$/m	$\boldsymbol{a}_{i,y}$/m	$\boldsymbol{a}_{i,z}$/m	$\boldsymbol{b}_{i,x}$/m	$\boldsymbol{b}_{i,y}$/m	$\boldsymbol{b}_{i,z}$/m
1	−1.5242	1.2804	2.8440	−0.1456	0.2158	−0.4964
2	1.9942	1.3167	2.8614	0.1431	0.2139	−0.4983
3	2.2960	−1.2262	2.6711	0.1481	−0.2162	−0.5051
4	−1.8156	−1.2737	2.6427	−0.1519	−0.2175	−0.5047
5	−1.5212	1.0751	−0.5077	−0.2214	0.1529	0.4987
6	2.2113	1.0425	−0.5109	0.2214	0.1469	0.4983
7	2.5490	−0.8643	−0.5075	0.2208	−0.1534	0.4956
8	−1.6108	−0.8378	−0.5128	−0.2214	−0.1469	0.4974

Table A.5: Spatial positions of frame anchors and platform anchors give in respective local coordinate systems on cable robot COPInspection.

	Frame anchor			Platform anchor		
Cable	$\boldsymbol{a}_{i,x}$/m	$\boldsymbol{a}_{i,y}$/m	$\boldsymbol{a}_{i,z}$/m	$\boldsymbol{b}_{i,x}$/m	$\boldsymbol{b}_{i,y}$/m	$\boldsymbol{b}_{i,z}$/m
1	2.1651	1.0844	3.0296	−0.4241	0.3489	−0.1491
2	1.8293	−1.8199	3.0400	0.4230	0.3517	−0.1493
3	−1.5096	−1.9808	3.0158	0.4247	−0.3479	−0.1549
4	−1.9176	1.0277	3.0004	−0.4230	−0.3517	−0.1537
5	2.2214	1.3171	−0.1470	−0.3510	0.4214	0.1509
6	2.2006	−1.5590	−0.1485	0.3497	0.4232	0.1493
7	−1.4759	−1.6728	−0.1458	0.3560	−0.4267	0.1514
8	−1.7874	1.2167	−0.1688	−0.3510	−0.4268	0.1554

Platform

Table A.6: Inertial properties of mobile platform of cable robot COPHandling.

Property	Variable	Value	Unit
Mass	m	10	kg
Inertia tensor	J_{xx}	2.041	$\mathrm{kg\,m^2}$
	J_{xy}	-9.400×10^{-5}	$\mathrm{kg\,m^2}$
	J_{xz}	-0.006	$\mathrm{kg\,m^2}$
	J_{yx}	-9.400×10^{-5}	$\mathrm{kg\,m^2}$
	J_{yy}	2.036	$\mathrm{kg\,m^2}$
	J_{yz}	0.002	$\mathrm{kg\,m^2}$
	J_{zx}	-0.006	$\mathrm{kg\,m^2}$
	J_{zy}	0.002	$\mathrm{kg\,m^2}$
	J_{zz}	0.044	$\mathrm{kg\,m^2}$

Table A.7: Inertial properties of mobile platform of cable robot COPInspection.

Property	Variable	Value	Unit
Mass	m	15	kg
Inertia tensor	J_{xx}	2.041	$\mathrm{kg\,m^2}$
	J_{xy}	-9.400×10^{-5}	$\mathrm{kg\,m^2}$
	J_{xz}	-0.006	$\mathrm{kg\,m^2}$
	J_{yx}	-9.400×10^{-5}	$\mathrm{kg\,m^2}$
	J_{yy}	2.036	$\mathrm{kg\,m^2}$
	J_{yz}	0.002	$\mathrm{kg\,m^2}$
	J_{zx}	-0.006	$\mathrm{kg\,m^2}$
	J_{zy}	0.002	$\mathrm{kg\,m^2}$
	J_{zz}	0.044	$\mathrm{kg\,m^2}$

Cables

Table A.8: Mechanical properties of cables used on COPacabana cable robots. Poisson's ratio inferred from (Yan 2016).

Property	Variable	Value	Unit
Diameter	d	6	mm
Cross-Section	A	28.274	mm^2
Moment of Area	I	3.976	mm^4
Unit Density	ϱ	813.459	$\mathrm{kg\,m}^{-3}$
Young's Modulus	E	12.200	GPa
Poisson's Ratio	ν	0.460	–
Shear Modulus	G	4.178	GPa

A.3 Expo

Frame and Platform Dimension

Table A.9: Spatial positions of frame anchors and platform anchors give in respective local coordinate systems on cable robot Expo.

	Frame anchor			Platform anchor		
Cable	$\boldsymbol{a}_{i,x}$/m	$\boldsymbol{a}_{i,y}$/m	$\boldsymbol{a}_{i,z}$/m	$\boldsymbol{b}_{i,x}$/m	$\boldsymbol{b}_{i,y}$/m	$\boldsymbol{b}_{i,z}$/m
1	6.1540	−3.1130	7.0440	0.2210	−0.4400	1.1449
2	6.5810	2.1500	7.0650	0.2260	0.4320	1.1483
3	−6.9300	2.0260	7.0810	−0.2180	0.4330	1.1499
4	−6.1700	−3.2290	7.0490	−0.2220	−0.4410	1.1470
5	6.1060	−3.1570	6.0450	0.4340	−0.6760	0.2660
6	6.8460	2.2180	6.0700	0.4390	0.6820	0.2724
7	−6.9190	2.0990	6.0800	−0.4360	0.6810	0.2750
8	−6.1280	−3.2720	6.0440	−0.4360	−0.6770	0.2695

Platform

Table A.10: Inertial properties of mobile platform of cable robot Expo.

Property	Variable	Value	Unit
Mass	m	150	kg
Inertia tensor	J_{xx}	32.852	$\mathrm{kg\,m^2}$
	J_{xy}	0	$\mathrm{kg\,m^2}$
	J_{xz}	0	$\mathrm{kg\,m^2}$
	J_{yx}	0	$\mathrm{kg\,m^2}$
	J_{yy}	19.336	$\mathrm{kg\,m^2}$
	J_{yz}	0	$\mathrm{kg\,m^2}$
	J_{zx}	0	$\mathrm{kg\,m^2}$
	J_{zy}	0	$\mathrm{kg\,m^2}$
	J_{zz}	32.656	$\mathrm{kg\,m^2}$

Cables

Table A.11: Mechanical properties of cables used on cable robot Expo.

Property	Variable	Value	Unit
Diameter	d	7	mm
Cross-Section	A	38.485	$\mathrm{mm^2}$
Moment of Area	I	7.366	$\mathrm{mm^4}$
Unit Density	ϱ	5144.927	$\mathrm{kg\,m^{-3}}$
Young's Modulus	E	200	GPa
Poisson's Ratio	ν	0.360	–
Shear Modulus	G	73.529	GPa

A.4 IPAnema Mini

Frame and Platform Dimension

Table A.12: Spatial positions of frame anchors and platform anchors give in respective local coordinate systems on cable robot IPAnema Mini.

	Frame anchor			Platform anchor		
Cable	$\boldsymbol{a}_{i,x}$/m	$\boldsymbol{a}_{i,y}$/m	$\boldsymbol{a}_{i,z}$/m	$\boldsymbol{b}_{i,x}$/m	$\boldsymbol{b}_{i,y}$/m	$\boldsymbol{b}_{i,z}$/m
1	−0.5000	0.3780	0.4470	−0.0220	0.0400	−0.0825
2	0.5000	0.3775	0.4470	0.0220	0.0400	−0.0825
3	0.5000	−0.3775	0.4470	0.0220	−0.0400	−0.0825
4	−0.5000	−0.3780	0.4470	−0.0220	−0.0400	−0.0825
5	−0.5315	0.3445	−0.4470	−0.0220	0.0400	0.0825
6	0.5315	0.3445	−0.4770	0.0220	0.0400	0.0825
7	0.5315	−0.3445	−0.4470	0.0220	−0.0400	0.0825
8	−0.5315	−0.3445	−0.4470	−0.0220	−0.0400	0.0825

Platform

Table A.13: Inertial properties of mobile platform of cable robot IPAnema Mini.

Property	Variable	Value	Unit
Mass	m	0.897	kg
Inertia tensor	J_{xx}	0.003	$\mathrm{kg\,m^2}$
	J_{xy}	0	$\mathrm{kg\,m^2}$
	J_{xz}	0	$\mathrm{kg\,m^2}$
	J_{yx}	0	$\mathrm{kg\,m^2}$
	J_{yy}	0.002	$\mathrm{kg\,m^2}$
	J_{yz}	0	$\mathrm{kg\,m^2}$
	J_{zx}	0	$\mathrm{kg\,m^2}$
	J_{zy}	0	$\mathrm{kg\,m^2}$
	J_{zz}	0.001	$\mathrm{kg\,m^2}$

Cables

Table A.14: Mechanical properties of cables used on cable robot IPAnema Mini. Poisson's ratio inferred from (Yan 2016).

Property	Variable	Value	Unit
Diameter	d	1.500	mm
Cross-Section	A	1.767	mm^2
Moment of Area	I	0.016	mm^4
Unit Density	ϱ	735.650	$\mathrm{kg\,m}^{-3}$
Young's Modulus	E	12.200	GPa
Poisson's Ratio	ν	0.460	–
Shear Modulus	G	4.178	GPa

A.5 IPAnema 3

Frame and Platform Dimension

Table A.15: Spatial positions of frame anchors and platform anchors give in respective local coordinate systems on cable robot IPAnema 3.

	Frame anchor			Platform anchor		
Cable	$\boldsymbol{a}_{i,x}$/m	$\boldsymbol{a}_{i,y}$/m	$\boldsymbol{a}_{i,z}$/m	$\boldsymbol{b}_{i,x}$/m	$\boldsymbol{b}_{i,y}$/m	$\boldsymbol{b}_{i,z}$/m
1	−8.5440	5.4630	3.2020	−0.0700	0.6480	−0.2600
2	8.1840	5.6920	3.2360	0.0600	0.6480	−0.2620
3	8.2240	−5.4920	3.2500	0.0600	−0.6510	−0.2620
4	−8.4910	−5.3220	3.2210	−0.0700	−0.6510	−0.2600
5	−8.1920	5.6480	−0.5890	−0.0850	0.7480	0.2610
6	7.2080	6.4630	−0.5480	0.0950	0.7490	0.2600
7	7.8690	−5.5570	−0.5270	0.0950	−0.7450	0.2600
8	−8.2700	−5.5450	−0.5820	−0.0850	−0.7460	0.2610

Platform

Table A.16: Inertial properties of mobile platform of cable robot IPAnema 3.

Property	Variable	Value	Unit
Mass	m	25	kg
Inertia tensor	J_{xx}	5.226	$\mathrm{kg\,m^2}$
	J_{xy}	0	$\mathrm{kg\,m^2}$
	J_{xz}	0	$\mathrm{kg\,m^2}$
	J_{yx}	0	$\mathrm{kg\,m^2}$
	J_{yy}	0.637	$\mathrm{kg\,m^2}$
	J_{yz}	0	$\mathrm{kg\,m^2}$
	J_{zx}	0	$\mathrm{kg\,m^2}$
	J_{zy}	0	$\mathrm{kg\,m^2}$
	J_{zz}	4.724	$\mathrm{kg\,m^2}$

Cables

Table A.17: Mechanical properties of cables used on cable robot IPAnema 3. Poisson's ratio inferred from (Yan 2016).

Property	Variable	Value	Unit
Diameter	d	6	mm
Cross-Section	A	28.274	$\mathrm{mm^2}$
Moment of Area	I	3.976	$\mathrm{mm^4}$
Unit Density	ϱ	813.459	$\mathrm{kg\,m^{-3}}$
Young's Modulus	E	12.200	GPa
Poisson's Ratio	ν	0.460	–
Shear Modulus	G	4.178	GPa

Appendix B

Natural Frequencies

Table B.1: First 20 natural frequenices of B-spline cable for local polynomial degree $p = 3$ over number of segments $n_\mathrm{s} \in \{1, 5, 10, 20\}$.

	$n_\mathrm{s} = 1$		$n_\mathrm{s} = 5$		$n_\mathrm{s} = 10$		$n_\mathrm{s} = 20$		Reference
Mode l	$\omega_l/\mathrm{rad\,s^{-1}}$	$e_{\omega_l}/\%$	$\omega_l/\mathrm{rad\,s^{-1}}$	$e_{\omega_l}/\%$	$\omega_l/\mathrm{rad\,s^{-1}}$	$e_{\omega_l}/\%$	$\omega_l/\mathrm{rad\,s^{-1}}$	$e_{\omega_l}/\%$	$\bar{\omega}_l/\mathrm{rad\,s^{-1}}$
1	414.698e−3	10.99	374.749e−3	0.30	373.866e−3	0.06	373.670e−3	0.01	373.630e−3
2	1.900	27.16	1.505	0.69	1.498	0.21	1.495	0.04	1.495
3	—	—	3.410	1.40	3.375	0.37	3.366	0.08	3.363
4	—	—	6.129	2.53	6.011	0.55	5.986	0.13	5.978
5	—	—	9.934	6.35	9.423	0.89	9.358	0.19	9.341
6	—	—	15.784	17.35	13.645	1.44	13.484	0.24	13.451
7	—	—	—	—	18.715	2.23	18.366	0.32	18.308
8	—	—	—	—	24.812	3.76	24.014	0.43	23.912
9	—	—	—	—	32.520	7.46	30.441	0.58	30.264
10	—	—	—	—	42.256	13.10	37.666	0.81	37.363
11	—	—	—	—	51.102	13.04	45.713	1.12	45.209
12	—	—	—	—	—	—	54.614	1.51	53.803
13	—	—	—	—	—	—	64.428	2.03	63.143
14	—	—	—	—	—	—	75.275	2.79	73.231
15	—	—	—	—	—	—	87.374	3.93	84.067
16	—	—	—	—	—	—	101.031	5.63	95.649
17	—	—	—	—	—	—	116.515	7.91	107.979
18	—	—	—	—	—	—	133.739	10.48	121.056
19	—	—	—	—	—	—	151.659	12.44	134.880
20	—	—	—	—	—	—	167.697	12.21	149.452

Table B.2: First 20 natural frequenices of B-spline cable for local polynomial degree $p = 4$ over number of segments $n_\mathrm{s} \in \{1, 5, 10, 20\}$.

	$n_\mathrm{s} = 1$		$n_\mathrm{s} = 5$		$n_\mathrm{s} = 10$		$n_\mathrm{s} = 20$		Reference
Mode l	$\omega_l/\mathrm{rad\,s^{-1}}$	$e_{\omega_l}/\%$	$\omega_l/\mathrm{rad\,s^{-1}}$	$e_{\omega_l}/\%$	$\omega_l/\mathrm{rad\,s^{-1}}$	$e_{\omega_l}/\%$	$\omega_l/\mathrm{rad\,s^{-1}}$	$e_{\omega_l}/\%$	$\bar{\omega}_l/\mathrm{rad\,s^{-1}}$
1	373.740e−3	0.03	373.935e−3	0.08	373.715e−3	0.02	373.645e−3	0.00	373.630e−3
2	1.900	27.16	1.500	0.34	1.496	0.08	1.495	0.02	1.495
3	4.990	48.39	3.391	0.83	3.369	0.18	3.364	0.03	3.363
4	—	—	6.075	1.63	5.998	0.34	5.982	0.06	5.978
5	—	—	9.535	2.08	9.396	0.59	9.349	0.09	9.341
6	—	—	13.911	3.42	13.565	0.85	13.468	0.13	13.451
7	—	—	20.707	13.11	18.507	1.09	18.342	0.19	18.308
8	—	—	—	—	24.248	1.41	23.975	0.26	23.912
9	—	—	—	—	30.817	1.83	30.370	0.35	30.264
10	—	—	—	—	38.517	3.09	37.528	0.44	37.363
11	—	—	—	—	48.813	7.97	45.449	0.53	45.209
12	—	—	—	—	59.865	11.27	54.138	0.62	53.803
13	—	—	—	—	—	—	63.615	0.75	63.143
14	—	—	—	—	—	—	73.909	0.92	73.231
15	—	—	—	—	—	—	85.050	1.17	84.067
16	—	—	—	—	—	—	97.096	1.51	95.649
17	—	—	—	—	—	—	110.251	2.10	107.979
18	—	—	—	—	—	—	125.030	3.28	121.056
19	—	—	—	—	—	—	142.155	5.39	134.880
20	—	—	—	—	—	—	161.665	8.17	149.452

Table B.3: First 20 natural frequenices of B-spline cable for local polynomial degree $p = 5$ over number of segments $n_\mathrm{s} \in \{1, 5, 10, 20\}$.

	$n_\mathrm{s} = 1$		$n_\mathrm{s} = 5$		$n_\mathrm{s} = 10$		$n_\mathrm{s} = 20$		Reference
Mode l	$\omega_l/\mathrm{rad\,s^{-1}}$	$e_{\omega_l}/\%$	$\omega_l/\mathrm{rad\,s^{-1}}$	$e_{\omega_l}/\%$	$\omega_l/\mathrm{rad\,s^{-1}}$	$e_{\omega_l}/\%$	$\omega_l/\mathrm{rad\,s^{-1}}$	$e_{\omega_l}/\%$	$\bar{\omega}_l/\mathrm{rad\,s^{-1}}$
1	373.740e−3	0.03	373.850e−3	0.06	373.690e−3	0.02	373.642e−3	0.00	373.630e−3
2	1.501	0.42	1.498	0.22	1.495	0.06	1.495	0.01	1.495
3	4.990	48.39	3.380	0.51	3.367	0.13	3.364	0.03	3.363
4	10.449	74.79	6.040	1.03	5.992	0.24	5.981	0.05	5.978
5	—	—	9.541	2.14	9.377	0.39	9.347	0.07	9.341
6	—	—	13.786	2.49	13.533	0.61	13.465	0.10	13.451
7	—	—	18.869	3.07	18.485	0.97	18.334	0.14	18.308
8	—	—	26.147	9.34	24.244	1.39	23.959	0.19	23.912
9	—	—	—	—	30.758	1.63	30.341	0.25	30.264
10	—	—	—	—	38.044	1.82	37.486	0.33	37.363
11	—	—	—	—	46.127	2.03	45.405	0.43	45.209
12	—	—	—	—	56.526	5.06	54.106	0.56	53.803
13	—	—	—	—	69.833	10.59	63.592	0.71	63.143
14	—	—	—	—	—	—	73.851	0.85	73.231
15	—	—	—	—	—	—	84.870	0.96	84.067
16	—	—	—	—	—	—	96.669	1.07	95.649
17	—	—	—	—	—	—	109.287	1.21	107.979
18	—	—	—	—	—	—	122.764	1.41	121.056
19	—	—	—	—	—	—	137.319	1.81	134.880
20	—	—	—	—	—	—	153.869	2.96	149.452

Table B.4: First 20 natural frequenices of B-spline cable for local polynomial degree $p = 6$ over number of segments $n_\mathrm{s} \in \{1, 5, 10, 20\}$.

	$n_\mathrm{s} = 1$		$n_\mathrm{s} = 5$		$n_\mathrm{s} = 10$		$n_\mathrm{s} = 20$		Reference
Mode l	$\omega_l/\mathrm{rad\,s^{-1}}$	$e_{\omega_l}/\%$	$\omega_l/\mathrm{rad\,s^{-1}}$	$e_{\omega_l}/\%$	$\omega_l/\mathrm{rad\,s^{-1}}$	$e_{\omega_l}/\%$	$\omega_l/\mathrm{rad\,s^{-1}}$	$e_{\omega_l}/\%$	$\bar{\omega}_l/\mathrm{rad\,s^{-1}}$
1	373.630e−3	0.00	373.762e−3	0.04	373.669e−3	0.01	373.638e−3	0.00	373.630e−3
2	1.501	0.42	1.497	0.15	1.495	0.04	1.495	0.01	1.495
3	3.420	1.70	3.374	0.34	3.366	0.10	3.363	0.02	3.363
4	10.449	74.79	6.019	0.68	5.989	0.18	5.980	0.04	5.978
5	19.247	106.06	9.454	1.21	9.368	0.30	9.346	0.06	9.341
6	—	—	13.770	2.38	13.511	0.45	13.463	0.09	13.451
7	—	—	18.842	2.92	18.430	0.67	18.330	0.12	18.308
8	—	—	24.665	3.15	24.152	1.00	23.951	0.16	23.912
9	—	—	32.131	6.17	30.746	1.59	30.328	0.21	30.264
10	—	—	—	—	38.142	2.08	37.463	0.27	37.363
11	—	—	—	—	46.244	2.29	45.363	0.34	45.209
12	—	—	—	—	54.930	2.10	54.034	0.43	53.803
13	—	—	—	—	65.397	3.57	63.489	0.55	63.143
14	—	—	—	—	80.719	10.22	73.754	0.71	73.231
15	—	—	—	—	—	—	84.850	0.93	84.067
16	—	—	—	—	—	—	96.756	1.16	95.649
17	—	—	—	—	—	—	109.410	1.33	107.979
18	—	—	—	—	—	—	122.775	1.42	121.056
19	—	—	—	—	—	—	136.896	1.49	134.880
20	—	—	—	—	—	—	151.809	1.58	149.452

Appendix C

Stress Strain Estimation Results

Table C.1: Estimated viscoelastic material parameters of elasticity and viscosity over $n_{\text{trial}} = 10$ trials for $n_{\text{mat}} = 2$ GMW material elements. Data shown includes median $\tilde{x}$, standard deviation σ_x, lower 25th percentile $p_{25\,\%}$ and upper 75th percentile $p_{75\,\%}$ of data.

	Elasticities		Viscosities	
Trial	E_1/GPa	E_2/GPa	η_2/GPa	g/%
1	7.211	0.868	11.423	97.229
2	7.222	0.837	9.909	97.403
3	7.253	0.890	9.214	97.481
4	7.225	0.840	9.740	97.399
5	7.216	0.834	10.116	97.425
6	7.221	0.837	11.053	97.390
7	7.272	0.849	10.539	97.396
8	7.313	0.849	8.754	97.468
9	7.318	0.850	7.963	97.517
10	7.253	0.844	11.161	97.372
Statistical Analysis				
$\tilde{x}$	7.239	0.846	10.012	97.401
σ_x	$3.970 \cdot 10^{-2}$	$1.720 \cdot 10^{-2}$	1.115	$7.822 \cdot 10^{-2}$
$p_{25\,\%}$	7.221	0.837	9.214	97.390
$p_{75\,\%}$	7.272	0.850	11.053	97.468

Table C.2: Estimated viscoelastic material parameters of elasticity and viscosity over $n_{\text{trial}} = 10$ trials for $n_{\text{mat}} = 3$ GMW material elements. Data shown includes median $\tilde{x}$, standard deviation σ_x, lower 25th percentile $p_{25\,\%}$ and upper 75th percentile $p_{75\,\%}$ of data.

	Elasticities			Viscosities		
Trial	E_1/GPa	E_2/GPa	E_3/GPa	η_2/GPa	η_3/GPa	g/%
1	7.173	1.139	0.738	0.553	13.264	97.505
2	7.170	1.014	0.621	0.888	12.445	98.014
3	7.222	1.183	0.706	0.608	10.387	98.012
4	7.173	1.017	0.617	0.904	12.221	98.017
5	7.178	1.626	0.684	0.596	11.876	97.728
6	7.150	0.976	0.616	0.822	12.178	98.102
7	7.266	1.134	0.825	0.798	10.793	97.527
8	7.268	1.024	0.609	0.847	10.652	98.042
9	7.289	1.454	0.662	0.558	9.016	97.881
10	7.185	1.011	0.627	0.784	12.107	98.082
Statistical Analysis						
$\tilde{x}$	7.181	1.103	0.644	0.728	12.048	98.013
σ_x	$4.990 \cdot 10^{-2}$	9.045	$6.997 \cdot 10^{-2}$	0.284	2.008	0.225
$p_{25\,\%}$	7.173	1.014	0.617	0.558	10.652	97.728
$p_{75\,\%}$	7.266	1.626	0.706	0.904	13.264	98.042

Table C.3: Estimated viscoelastic material parameters of elasticity and viscosity over $n_{\text{trial}} = 10$ trials for $n_{\text{mat}} = 4$ GMW material elements. Data shown includes median $\tilde{x}$, standard deviation σ_x, lower 25th percentile $p_{25\,\%}$ and upper 75th percentile $p_{75\,\%}$ of data.

	Elasticities				Viscosities			
Trial	E_1/GPa	E_2/GPa	E_3/GPa	E_4/GPa	η_2/GPa	η_3/GPa	η_4/GPa	g/%
1	7.051	0.868	0.634	0.543	0.267	2.415	23.824	98.050
2	7.107	0.785	0.587	0.482	0.245	2.132	16.948	98.127
3	7.200	0.924	0.586	0.456	0.256	1.069	11.250	98.070
4	7.105	0.647	0.614	0.470	0.175	2.305	17.190	98.093
5	7.094	0.771	0.593	0.488	0.254	2.189	18.289	98.181
6	7.023	0.798	0.632	0.537	0.279	2.630	28.981	98.243
7	7.109	0.792	0.621	0.503	0.271	2.557	22.995	98.201
8	7.226	0.722	0.584	0.455	0.218	1.925	12.904	98.115
9	7.254	0.701	0.547	0.454	0.198	1.629	10.252	98.085
10	6.956	0.998	0.650	0.591	0.307	3.208	45.652	98.239
Statistical Analysis								
$\tilde{x}$	7.106	0.788	0.603	0.485	0.255	2.360	17.740	98.121
σ_x	$9.261 \cdot 10^{-2}$	0.105	$3.093 \cdot 10^{-2}$	$4.579 \cdot 10^{-2}$	$3.959 \cdot 10^{-2}$	2.852	11.953	$7.054 \cdot 10^{-2}$
$p_{25\,\%}$	7.051	0.722	0.586	0.456	0.218	2.132	12.904	98.085
$p_{75\,\%}$	7.200	0.868	0.632	0.537	0.271	2.630	23.824	98.201

Appendix D

Quadrature

The basic problem of numerical integration lies in finding a definite integral of a smooth function $f(x)$ on the interval $x \in [a, b]$ such that we obtain

$$\int_a^b f(x)\ \mathrm{d}x$$

to a given accuracy. The basic principle of numerical integration lies in collecting a weighted sum of the integrand evaluated at discrete points within the interval. Depending on the desired accuracy and the method in use for intergration, the integration points and their weights vary. In its very basic form, a constant interpolating function is formed at the point $a + b/2$ giving $f(a + b/2)$, usually referred to as the midpoint rule, which gives us

$$\int_a^b f(x)\ \mathrm{d}x = (b - a)\, f\Big(\frac{a + b}{2}\Big)\,.$$

With the degree of the interpolating function increasing—the most common ones are linear or quadratic polynomials–, also the quality of approximation increasing yielding better results i.e., lower integration errors. One may then improve approximation accuracy, by splitting the interval $[a, b]$ into n_{qp} subintervals for each of which the integral approximation is calculated. This yields the composite rule of numerical integration of e.g., the interval $[a + l\,h, a + (l + 1)\,h] \subseteq [a, b]$ with $h = (b - a)/n_{\mathrm{qp}}$ and $l \in \{0, \ldots, n_{\mathrm{qp}}\}$. If the intervals are equally spaced i.e., there exist only one interval step size h, then we obtain Newton-Cotes formulas or Simpson's rule. On the other hand, if the subintervals are unevenly spaced we obtain the Gaussian quadrature formulae, which are more accurate than Newton-Cotes formulas with f being smooth i.e., sufficiently differentiable.

Due to higher accuracy than Newton-Cotes formulas for smooth functions, Gaussian quadrature rule is employed to approximate the integrals of forces and energies of the cable. This formulation, named after Carl Friedrich Gauss, is

Table D.1: Abscissae and weights for Gaussian quadrature rule on interval $[-1, 1]$ for different number of quadrature points n_{qp}.

Point	$n_{\mathrm{qp}} = 1$		$n_{\mathrm{qp}} = 2$		$n_{\mathrm{qp}} = 3$		$n_{\mathrm{qp}} = 4$		$n_{\mathrm{qp}} = 5$	
l	x_l	w_l	x_l	w_l	x_l	w_l	x_l	w_l	x_l	w_l
1	0	2	-0.577	1	-0.775	0.556	-0.861	0.348	-0.906	0.237
2	—	—	0.577	1	0	0.889	-0.340	0.652	-0.538	0.479
3	—	—	—	—	0.775	0.556	0.340	0.652	0	0.569
4	—	—	—	—	—	—	0.861	0.348	0.538	0.479
5	—	—	—	—	—	—	—	—	0.906	0.237

stated for any function $f(x)$ on the interval $[a, b]$ with quadrature weights w_l. Gaussian quadrature rule is exact for polynomials of degree $p \leq 2\,n_{\mathrm{qp}} - 1$ if the nodes x_l and their corresponding weights w_l are chosen suitably. The bases functions used in Gaussian quadrature are Legendre polynomials of degree n_{qp} denoted $P_{n_{\mathrm{qp}}}(x)$, with the n_{qp}-th polynomial normalized to give $P_{n_{\mathrm{qp}}}(1) = 1$. Then, the l-th Gauss node x_l is the l-th root of $P_{n_{\mathrm{qp}}}$ and the weights are given by the formula (see Abramowitz et al. (1972))

$$w_l = \frac{2}{\left(1 - x_l^2\right)^2 \left[P'_{n_{\mathrm{qp}}}(x_l)\right]^2}\,.$$

The l-th root of $P_{n_{\mathrm{qp}}}$ can be determined in different ways depending on the desired accuracy on the value using e.g., Newton's method for solving $P_{n_{\mathrm{qp}}}(x_l) = 0$ using an asymptotic formula (Abramowitz et al. 1972), or by means of the Golub-Welsch algorithm (Gil et al. 2007). Values for lower-order quadrature rules up to $n_{\mathrm{qp}} = 5$ over interval $[-1, 1]$ are given in Table D.1.

For a more general formulation of functions defined on an interval $[a, b]$, the integral must be recast to $[0, 1]$ before applying Gaussian quadrature rule. With a linear function $g\colon x \in [a, b] \to [0, 1] \ni \tilde{x}\colon x \mapsto x\,\frac{b-a}{2} + \frac{a+b}{2}$ this can be expressed straightforward as

$$\int_a^b f(x)\;\mathrm{d}x = \frac{b-a}{2} \sum_{l=1}^{n_{\mathrm{qp}}} w_l\, f\!\left(x_l\,\frac{b-a}{2} + \frac{a+b}{2}\right).$$

Appendix E

Root-Finding Problem

Root-finding is the problem of finding the real or complex valued number x of a continuous function $f\colon \mathbb{R} \to \mathbb{R}$, $x \mapsto f(x)$, for which holds $f(x) \equiv 0$. While sometimes roots can be expressed in closed form, in the most general case it is not possible to compute exactly the root of a function—let alone due to numerical rounding precision. One can also apply the root-finding problem to cases, where one wants to find equality of two functions—usually functions nIinear in one or more variables—for number x. That is, we can rewrite $f(x) = g(x)$ to read $h(x) = f(x) - g(x)$, for which we can now apply the root-finding problem to $h(x)$ w.r.t. x. It must be noted that there may be cases where root-finding algorithms do not find a root which, however, does not state there exist no root.

In most cases, root-finding algorithms are iterative procedures, using a start point or initial guess to provide a sequence of numbers that converge toward the root. During each iteration, the algorithm ideally proceeds closer and closer to the root and provides increasingly more accurate approximations of the root. Eventually, the iteration has to be stopped due to rounding precision, perfect equality of $f(x) \equiv 0$ can never be achieved. Therefore, every root-finding algorithm provides only an approximation, not the exact root solution.

E.1 Bracketing Methods

As the name implies, bracketing methods determine increasingly smaller brackets (intervals) containing the root. With the intervall smaller than a given threshold, a root has been found. Bracketing methods observe the sign of $f(x)$ on the interval boundaries, which can be used to determine if there is a root inside the interval or not.

If f is a continuous function and there is an interval $[a, b]$ for which $f(a)$ and $f(b)$ have opposite signs, then for the midpoint $c = \frac{a+b}{2}$ it must hold that

Algorithm 1 Pseudo-algorithm of the bisection iteration algorithm.

```
k ← 0                                              ▷ Iteration count
c ← false                                          ▷ Flag if converged or not
while k < k_max ∧ ∼ c do
    x_k ← (a+b)/2
    if |a − x_k| ≤ ϵ_s ∨ |f(x_k)| ≤ ϵ_r then       ▷ Check interval too narrow or
                                                     residual below tolerance
        c ← true                                   ▷ Algorithm has converged
    else
        if f(x_k) f(a) < 0 then
            b ← x_k
        else
            a ← x_k
        end if
    end if
    k ← k + 1                                      ▷ Update iteration counter
end while
```

either

$$\operatorname{sgn}(f(a)) = -\operatorname{sgn}(f(c))\,,$$

or

$$\operatorname{sgn}(f(b)) = -\operatorname{sgn}(f(c))\,,$$

is true, unless c is the exact root, then $f(c) \equiv 0$. One then updates the interval boundaries and sets $b = c$ or $a = c$, respectively, and repeats this process until some stopping criterion is fulfilled—usually until the interval is sufficiently small i.e., $|b - a| \leq \epsilon_{\text{res}}$. The iterative procedure of the Bisection method is given in Algorithm 1.

E.2 Iterative Methods

Even though above presented bracketing methods are also iterative root-finding algorithms, a proper iterative root-finding algorithm uses, per defintion, an auxiliary function applied to the last computed approximation of the root to get a new or closer approximation. This iteration stops when a fixed point—within numerical bounds—of the auxiliary function is reached i.e., the computed value is sufficiently close to the preceding ones.

E.2.1 Newton's Method

The most often used numerical root-finding algorithm is Newton's method (or Newton-Raphson), which finds successively better approximations to the roots of a real-valued scalar or vector function $f(x)$ or $\boldsymbol{f}(\boldsymbol{x})$, respectively. We present Newton's method for the scalar-valued case, but it can be extended to the vector-valued case in a straightforward manner.

Let $f\colon [a,b] \to \mathbb{R}$ be a smooth scalar function defined on interval $[a,b]$. To use Newton's method, one starts with an initial guess x_0 in close proximity to the actual root x^*. Then, we can perform linearization of f around x^* giving us

$$f(x_0 = x^* + \Delta x) = f(x^*) + f'(x^*)\,\Delta x$$

The function is thus approximated by its tangent, for which the x-intercept of the tangent is calculated

$$y = 0 = f'(x_k)\,(x^* - x_k) + f(x_k)$$

typically providing a better approximation to the function's root. This iteration process is then repeated until certain termination conditions are met. We can rewrite the iterative algorithm to yield the next approximate of the root x_{k+1}.

Newton's method can be directly extended to higher dimensions for either $\boldsymbol{x} \in \mathbb{R}^m$ with $\boldsymbol{f}(x)\colon \mathbb{R} \to \mathbb{R}^n$ or $\boldsymbol{f}(\boldsymbol{x})\colon \mathbb{R}^n \to \mathbb{R}^m$ by using the Jacobian of $\boldsymbol{f}(\boldsymbol{x})$ at $\boldsymbol{x}_k$ yielding

$$\begin{aligned} \Delta\boldsymbol{x} &= \mathrm{D}\,\boldsymbol{f}^{-1}(\boldsymbol{x}_k)\,\boldsymbol{f}(\boldsymbol{x}_k)\,, \\ \boldsymbol{x}_{k+1} &= \boldsymbol{x}_k - \Delta\boldsymbol{x}\,. \end{aligned}$$

Stopping criteria for Newton's method are simply given through either a small residual $\|\boldsymbol{f}(x_k)\| \leq \epsilon_{\text{res}}$, small step size $\|\Delta\boldsymbol{x}\| \leq \epsilon_{\Delta}$, or exceeded iteration count $k > k_{\max}$.

E.2.2 Improved Newton's Method

Improved versions of the conventional Newton's method have been introduced as the algorithm can get into trouble when the increment $\Delta\boldsymbol{x}$ gets too large. One way to mitigate this problem is a softened or damped iteration method by

means of which the increment $\Delta \boldsymbol{x}$ is scaled such that

$$\boldsymbol{x}_{k+1} = \boldsymbol{x}_k - \alpha \, \Delta \boldsymbol{x} = \boldsymbol{x}_k - \alpha \, \mathrm{D}\, \boldsymbol{f}(\boldsymbol{x}_k)^{-1} \, \boldsymbol{f}(\boldsymbol{x}_k) \,,$$

where α is a small number with $\alpha \leq 1$. Damping by a constant factor like $\alpha = 1/2$ can improve initial iterations, but destroys the quadratic convergence. Besides that, it is difficult to determine how to select the damping factor a priori. However, we can adjust damping such that it vanishes as iteration converges by setting

$$\alpha = \frac{1}{1 + \beta \, \|\Delta \boldsymbol{x}\|} \,,$$

where a good practice is to set $\beta \equiv 10$ (Tibshirani 2015).

Since finding a suitable value for β is still involved and depends on many different factors, another strategy is to choose α adaptively, so that the objective function almost always decreases on each iteration. This additional adaptive selection of α introduces a second loop inside each Newton iteration loop. Starting with a full Newton step, we check this step reduces the objective function. If it does not, step size is halved and we repeat this procedure until we find a step size that reduces the residual, or until a maximum number of halving have been performed e.g., 10. Newton's damped method is especially powerful when Newton's method would otherwise oscillate around the root due to too tight tolerances. In this case, the reduced step size almost always allows for satisfying the residual or step size tolerances without drastically increasing the iteration count. A pseudo algorithm of the adaptive damped Newton's method is given in Algorithm 2.

E.2.3 Secant Method / Broyden's method

By replacing the derivative in Newton's method with a finite difference, one implements the Secant method for scalar-valued functions or Broyden's Method for higher dimensions. This method is benefitial if the derivative cannot be determined analytically or if it can not be computed. However, the speed of convergence is slower.

Algorithm 2 Pseudo-algorithm of the adaptive damped Newton's method.

```
k ← 0                                                    ▷ Iteration count
d ← false                                                ▷ Flag if newton step converged or not
while k < k_max ∧ ¬d do                                  ▷ Start Newton loop
    Δx ← D f(x_k)^{-1} f(x_k)                            ▷ Calculate step size
    α ← 1                                                ▷ Init damping factor
    c ← false                                            ▷ Flag if damped newton converged
    while α >= 1/1024 ∧ ¬c do                            ▷ Start damped Newton loop
        x̃_{k+1} ← x_k − α Δx                             ▷ Trial update
        if ‖f(x̃_{k+1})‖ ≤ ‖f(x_k)‖ then                  ▷ Decrease in residual
            x_{k+1} ← x̃_{k+1}
            c ← true
        else
            α ← α/2                                      ▷ Residual not smaller, decrease step size
        end if
    end while                                            ▷ End damped Newton loop
    if ‖α Δx‖ ≤ ε_Δ ∧ ‖f(x_{k+1})‖ ≤ ε_res then          ▷ Termination checks
        d ← true
    else
        x_k = x_{k+1}
    end if
    k ← k + 1                                            ▷ Update iteration counter
end while                                                ▷ Outer Newton loop
```

We start with the initial interval $[a_0, b_0]$, the end points of which we use to construct a line of the form

$$y = \frac{f(b_0) - f(a_0)}{b_0 - a_0} (x - b_0) + f(b_0) \,,$$

of which we find the root i.e., $y = 0$ giving us

$$x = b_0 - f(b_0) \frac{b_0 - a_0}{f(b_0) - f(a_0)} \,.$$

We then set $a_1 = b_1$ and $b_1 = x$, and repeat above formula giving us the iterative formulation

$$\begin{aligned} x_{k+1} &= b_k - f(b_k) \frac{b_k - a_k}{f(b_k) - f(a_k)} \,, \\ a_{k+1} &= b_k \,, \\ b_{k+1} &= x_{k+1} \,, \end{aligned}$$

until close convergence of the interval around the function's root is found.

One drawback of the secant method is possible failure to converge as it does not require the root to be within the initial interval $[a_k, b_k]$ at every step which can be observed from the update procedure. Conversely, the false position (regula falsi) method iterates on the interval with changing its change-of-sign behavior. A small change to the interval boundary updating procedure ensures that regula falsi method will always converge. At iteration step k, the signs of $f(a_k)$ and $f(x_{k+1})$ are compared and if they have same signs i.e., $f(a_k)\, f(x_{k+1}) \geq 0$, then interval boundaries are updated to

$$[a_{k+1}, b_{k+1}] = [x_{k+1}, b_k]\,,$$

else to

$$[a_{k+1}, b_{k+1}] = [a_k, x_{k+1}]\,.$$

Broyden's method is the multi-dimensional generalization of the Secant method where the Jacobian matrix $\mathrm{D}\,\boldsymbol{f}_k$ is determined iteratively at iteration step k using the finite-difference approximation

$$\mathrm{D}\,\boldsymbol{f}_k\,(\boldsymbol{x}_k - \boldsymbol{x}_{k-1}) \simeq \boldsymbol{f}(\boldsymbol{x}_k) - \boldsymbol{f}(\boldsymbol{x}_{k-1})$$

or equivalently

$$\mathrm{D}\,\boldsymbol{f}_k\,\Delta\boldsymbol{x}_k = \Delta\boldsymbol{f}_k$$

if we use $\Delta\boldsymbol{x}_k = \boldsymbol{x}_k - \boldsymbol{x}_{k-1}$ and likeweise $\Delta\boldsymbol{f}_k = \boldsymbol{f}(\boldsymbol{x}_k) - \boldsymbol{f}(\boldsymbol{x}_{k-1})$. This equation, however, is underdetermined in the multi-dimensional case, which is why Broyden's method uses the current estimate of the Jacobian matrix $\mathrm{D}\,\boldsymbol{f}_{k-1}$ and update it by taking the solution to the secant equation

$$\mathrm{D}\,\boldsymbol{f}_k = \mathrm{D}\,\boldsymbol{f}_{k-1} + \frac{\Delta\boldsymbol{f}_k - \mathrm{D}\,\boldsymbol{f}_{k-1}\,\Delta\boldsymbol{x}_k}{\|\Delta\boldsymbol{x}_k\|^2}\,\Delta\boldsymbol{x}_k^\top\,,$$

which allows us to perform a typical Newton step

$$\boldsymbol{x}_{k+1} = \boldsymbol{x}_k - \mathrm{D}\,\boldsymbol{f}_k^{-1}\,\boldsymbol{f}(\boldsymbol{x}_k)\,.$$

To directly update the inverse Jacobian matrix, we may use Sherman–Morrison formula

$$\mathrm{D}\,\boldsymbol{f}_k^{-1} = \mathrm{D}\,\boldsymbol{f}_{k-1}^{-1} + \frac{\Delta\boldsymbol{x}_k - \mathrm{D}\,\boldsymbol{f}_{k-1}^{-1}\,\Delta\boldsymbol{f}_k}{\boldsymbol{x}_k^\top\,\mathrm{D}\,\boldsymbol{f}_{k-1}^{-1}\,\Delta\boldsymbol{f}_k}\,\Delta\boldsymbol{x}_k^\top\,\mathrm{D}\,\boldsymbol{f}_{k-1}^{-1},$$

which may be favorable when computing the inverse Jacobian is computationally too expensive since only the initial inverse Jacobian $\mathrm{D}\,\boldsymbol{f}_0^{-1}$ has to be calculated.

Appendix F

Solving DAEs

Solving differential-algebraic equations is an involved task that requires more sophisticated approaches than integration of conventional ODEs since not only does the vector of states $\boldsymbol{y}$ have to follow the dynamics given through the ODE, but constraints have to be fulfilled at every step of integration, too.

In general, a DAE is given in the form

$$\begin{aligned} \boldsymbol{y}'(t) &= \boldsymbol{f}(\boldsymbol{y}(t), t)\,, \\ \mathbb{0} &= \boldsymbol{g}(\boldsymbol{y}(t), t)\,, \\ \boldsymbol{y}(t_0) &= \boldsymbol{y}_0\,. \end{aligned}$$

where $\boldsymbol{y}$ is the state vector, $\boldsymbol{y}'$ its derivative, $\boldsymbol{f}(\boldsymbol{y}(t), t)$ defines the differential equation of $\boldsymbol{y}'$, and $\boldsymbol{g}(\boldsymbol{y}(t), t)$ defines the algebraic constraints. This formulation also holds for higher order differential equations e.g., in $\boldsymbol{y}''$ which may be rewritten with new states ${}^z\boldsymbol{y} = [\boldsymbol{y}, \boldsymbol{y}']^\top$ and ${}^z\boldsymbol{y}' = [\boldsymbol{y}', \boldsymbol{y}'']^\top$, then reading for ${}^z\boldsymbol{y}'(t) = \boldsymbol{f}({}^z\boldsymbol{y}, t)$.

It can be seen directly that the algebraic constraints are only given on the position value of $\boldsymbol{y}(t)$ which makes solving the DAE for $\boldsymbol{y}'(t)$ more involved. Without giving explicit details on how to numerically integrate ODEs using methods like forward or backward Euler, it may be inferred from secondary literature that these integrators cannot satisfy algebraic constraints at the same time, cf. e.g., Miranda et al. (1997). It remains an open field of research to find appropriate description for DAEs that will allow for explicit integration of the underlying ODE while also enforcing minimum constraint violation on the underlying algebraic level. Since mechanical systems are very often composed of multiple coupled bodies interacting with each other, numerically solving DAEs is a very dominant part in finding the time response of a mechanical system given an initial value. Many different approaches to both handling constraint violation and to integration schemes are available in the literature, some of which will be briefly summarized in this chapter.

F.1 Constraint Violation Handling

Assume a constrained mechanical system with its second-order dynamics ODE as given by

$$\boldsymbol{M}(\boldsymbol{q})\,\ddot{\boldsymbol{q}} = \boldsymbol{\gamma}(\boldsymbol{q},\dot{\boldsymbol{q}}) + \mathrm{D}\,\boldsymbol{g}(\boldsymbol{q})\,\boldsymbol{\lambda}(t)\,, \tag{F.1a}$$

under the constraints

$$\mathbb{0} = \boldsymbol{g}(\boldsymbol{q},t)\,, \tag{F.1b}$$

where $\boldsymbol{g}(\boldsymbol{q},t)$ is the vector of n_g position-level constraints on the mechanical system. For the sake of brevity, we omit nonholonomic constraints of the form $\mathbb{0} = \boldsymbol{A}\,\dot{\boldsymbol{q}}$ and focus solely on holonomic constraints. However, constraints Eq. (F.1b) imply additional restrictions on the state variables $\boldsymbol{q}$, $\dot{\boldsymbol{q}}$, and $\boldsymbol{\lambda}$. These implicit constraints can be inferred from twofold time-derivation of the positional constraints

$$\frac{\mathrm{d}\boldsymbol{g}}{\mathrm{d}t} = \frac{\partial \boldsymbol{g}}{\partial \boldsymbol{q}}\,\dot{\boldsymbol{q}} + \frac{\partial \boldsymbol{g}}{\partial t} = \mathrm{D}\,\boldsymbol{g}\,\dot{\boldsymbol{q}} + \mathrm{D}_t\,\boldsymbol{g} \equiv \mathbb{0}\,, \tag{F.2a}$$

$$\frac{\mathrm{d}^2\boldsymbol{g}}{\mathrm{d}t^2} = \mathrm{D}_{\boldsymbol{q}}(\mathrm{D}\,\boldsymbol{g}\,\dot{\boldsymbol{q}})\,\dot{\boldsymbol{q}} + 2\;\mathrm{D}\,\boldsymbol{g}\,\dot{\boldsymbol{q}} + \mathrm{D}\,\boldsymbol{g}\,\ddot{\boldsymbol{q}} + \mathrm{D}_t^2\,\boldsymbol{g} \equiv \mathbb{0}\,. \tag{F.2b}$$

Rearranging Eq. (F.2b) for $\mathrm{D}\,\boldsymbol{g}\,\ddot{\boldsymbol{q}}$ such that

$$\mathrm{D}\,\boldsymbol{g}\,\ddot{\boldsymbol{q}} = -\,\mathrm{D}_{\boldsymbol{q}}(\mathrm{D}\,\boldsymbol{g}\,\dot{\boldsymbol{q}})\,\dot{\boldsymbol{q}} - 2\;\mathrm{D}\,\boldsymbol{g}\,\dot{\boldsymbol{q}} - \mathrm{D}_t^2\,\boldsymbol{g} =: \boldsymbol{\zeta}$$

yields the hidden acceleration constraints which we can then place in parallel to Eq. (F.1a) yielding the corrected ODE

$$\boldsymbol{M}(\boldsymbol{q})\,\ddot{\boldsymbol{q}} = \boldsymbol{\gamma}(\boldsymbol{q},\dot{\boldsymbol{q}}) + \mathrm{D}\,\boldsymbol{g}^{\top}\,\boldsymbol{\lambda}\,, \tag{F.3a}$$

$$\mathrm{D}\,\boldsymbol{g}\,\ddot{\boldsymbol{q}} = \boldsymbol{\zeta}(\boldsymbol{q},\dot{\boldsymbol{q}},t), \tag{F.3b}$$

Equivalently, we may state Eq. (F.3) in vector-matrix notation reading

$$\begin{bmatrix} \boldsymbol{M}(\boldsymbol{q},\dot{\boldsymbol{q}},t) & -\,\mathrm{D}\,\boldsymbol{g}^{\top} \\ \mathrm{D}\,\boldsymbol{g} & \mathbb{0} \end{bmatrix} \cdot \begin{bmatrix} \ddot{\boldsymbol{q}} \\ \boldsymbol{\lambda} \end{bmatrix} = \begin{bmatrix} \boldsymbol{\gamma}(\boldsymbol{q},\dot{\boldsymbol{q}},t) \\ \boldsymbol{\zeta}(\boldsymbol{q},\dot{\boldsymbol{q}},t) \end{bmatrix}\,. \tag{F.4}$$

Given in Eq. (F.4) is the full DAE that can numerically be solved simultaneously for the accelerations $\ddot{\boldsymbol{q}}$ and Lagrange multipliers $\boldsymbol{\lambda}$ in order to obtain the constraint respecting system response. This method is generally referred to as the standard Lagrange multipliers method (SLM) (Flores 2014). When using SLM, indefinite growth of constraint violation occurs over time and, as such, will produce unacceptable results due to integration of numerical errors implying constraint violation where there physically would be none. In fact, the constraints Eq. (F.1b) are no longer considered explicitly in conjunction with the system dynamics Eq. (F.1a) but only implicitly through their first and second total derivative w.r.t. time. Ultimately, constraint violation handling methods are necessary for correcting the systems state ensuring both minimal to no constraint violation as well as correct result propagation[44]. Several methods for handling the constraint violation exist, some of which will be presented to show their complexity, procedural implementation, and their applicability to simulation of cable robots.

F.1.1 Baumgarte Stabilization Method

BSM allows for minor violation of the constraints before introducing corrective forces (Baumgarte 1972; Blajer 2011) Its implementation for the control of constraint violation is one of the simplest making it the most commonly used constraint violation handling method and the first choice for simulation of any dynamical system. However, its simplicity comes at the price of ambiguous selection of parameters.

BSM introduces a corrective feedback term on the constraints Eq. (F.4) such that they obey to

$$\ddot{\boldsymbol{g}} + 2\,\boldsymbol{\alpha}\,\dot{\boldsymbol{g}} + \boldsymbol{\beta}^2\,\boldsymbol{g} = \mathbb{0}\,, \tag{F.5}$$

where matrices $\boldsymbol{\alpha} = \operatorname{diag}(\alpha_1, \alpha_2, \ldots, \alpha_{n_g})$ and $\boldsymbol{\beta} = \operatorname{diag}(\beta_1, \beta_2, \ldots, \beta_{n_g})$ are $(n_g \times n_g)$ matrices of stabilization parameters of the feedback term. One can read these parameters as being the natural frequency $\boldsymbol{\omega}_0 = \boldsymbol{\beta}$ and damping $\boldsymbol{D} = \boldsymbol{\beta}^{-1}\,\boldsymbol{\alpha}$ of a normalized mass-spring-damper system. Selection of the parameter values is arbitrary, however, the stability of the general solution for linear dynamical

[44] A "correct result propagation" implies energy conservative integration of the DAE i.e., the constraint violation handling/compensation must not introduce energy into the system where it may physically be not possible.

systems is guaranteed if they are chosen as positive definite matrices or positive definite constants in the scalar case. However, since most mechanical multibody systems are nonlinear, their numerical stability cannot be guaranteed a priori. One option is to set $\boldsymbol{\alpha} = \boldsymbol{\beta}$ to achieve critical damping in the constraint violation, as pointed out by Baumgarte himself (Baumgarte 1972). In any other case, numerical experiments are needed to find suitable choices for $\boldsymbol{\alpha}$ and $\boldsymbol{\beta}$.

Appending Eq. (F.5) to the DAE from Eq. (F.4) yields the constraint corrected DAE as

$$\begin{bmatrix} \boldsymbol{M}(\boldsymbol{q}) & -\mathrm{D}\,\boldsymbol{g}^{\top} \\ \mathrm{D}\,\boldsymbol{g} & \mathbb{0} \end{bmatrix} \begin{bmatrix} \ddot{\boldsymbol{q}} \\ \boldsymbol{\lambda} \end{bmatrix} = \begin{bmatrix} \boldsymbol{\gamma}(\boldsymbol{q}, \dot{\boldsymbol{q}}) \\ \boldsymbol{\zeta}(\boldsymbol{q}, \dot{\boldsymbol{q}}) - 2\,\boldsymbol{\alpha}\,\dot{\boldsymbol{g}} - \boldsymbol{\beta}^2\,\boldsymbol{g} \end{bmatrix} . \tag{F.6}$$

F.1.2 Penalty Method

penalty method (PM) handles constraint violation differently than BSM as it introduces constraint violation handling into the equations of motion in a different manner. The PM-based DAE is based on the unconstrained system of bodies

$$\boldsymbol{M}(\boldsymbol{q})\,\ddot{\boldsymbol{q}} = \boldsymbol{\gamma}(\boldsymbol{q}, \dot{\boldsymbol{q}})\,, \tag{F.7}$$

for which the constraint violation at all levels of position, velocity, and acceleration are considered a second-order ODE of the form

$$\boldsymbol{m}_{\mathrm{PM}}\,\ddot{\boldsymbol{g}} + \boldsymbol{d}_{\mathrm{PM}}\,\dot{\boldsymbol{g}} + \boldsymbol{k}_{\mathrm{PM}}\,\boldsymbol{g} = \mathbb{0}\,, \tag{F.8}$$

where $\boldsymbol{m}_{\mathrm{PM}}$, $\boldsymbol{d}_{\mathrm{PM}}$, and $\boldsymbol{k}_{\mathrm{PM}}$ are some constant, positive diagonal matrices giving the equation physical meaning by turning it into the equivalent of a mass-spring-damper system. After some mathematical manipulations of Eq. (F.8) and introducing it in Eq. (F.7), the new ODE may be retrieved as

$$(\boldsymbol{M} + \boldsymbol{\alpha}\;\mathrm{D}\,\boldsymbol{g}^{\top}\;\mathrm{D}\,\boldsymbol{g})\,\ddot{\boldsymbol{q}} = \boldsymbol{\gamma} - \boldsymbol{\alpha}\;\mathrm{D}\,\boldsymbol{g}^{\top}\,(\dot{\mathrm{D}}\,\boldsymbol{g}\,\dot{\boldsymbol{q}} + 2\,\boldsymbol{\mu}\,\boldsymbol{\omega}\,\dot{\boldsymbol{g}} + \boldsymbol{\omega}^2\,\boldsymbol{g})\,, \tag{F.9}$$

where $\boldsymbol{\omega} = \boldsymbol{m}_{\mathrm{PM}}^{-1}\,\boldsymbol{k}_{\mathrm{PM}}$, $\boldsymbol{\mu} = (2\,\boldsymbol{\omega}\,\boldsymbol{m}_{\mathrm{PM}})^{-1}\,\boldsymbol{d}_{\mathrm{PM}}$, and $\boldsymbol{\alpha} = \boldsymbol{m}_{\mathrm{PM}}$.

With the PM being very similar to the SLM, it also suffers from problems arising from introducing new arbitrary parameters $\boldsymbol{\alpha}$, $\boldsymbol{\mu}$, and $\boldsymbol{\omega}$ into the system dynamics. The benefit of PM comes from reducing the number of equations that need to be solved since Eq. (F.9) poses a system of only n equations. PM

provides good control over constraint violation with $\boldsymbol{\alpha} \to \infty$, typical values are $\boldsymbol{\alpha} = 1 \times 10^{17}\,\mathbb{1}$, $\boldsymbol{\omega} = 10\,\mathbb{1}$, and $\boldsymbol{\mu} = 1\,\mathbb{1}$ (Nikravesh 2008). However, the parameter choice still remains ambiguous and numerical stability can only be guaranteed for linear dynamical systems.

F.1.3 Augmented Lagrangian Formulation

augmented Lagrangian formulation (ALF) is a revised formulation of the PM trying to remove ambiguity of choosing $\boldsymbol{\alpha}$, $\boldsymbol{\omega}$ and $\boldsymbol{\mu}$ by iteratively solving the system of equations for the accelerations. The iterative process at a given time step $t \equiv t_{\text{eval}}$ with iteration index $k = 0$ is initialized for the unconstrained system

$$\boldsymbol{M}(\boldsymbol{q})\,\ddot{\boldsymbol{q}}_k = \boldsymbol{\gamma}(\boldsymbol{q}, \dot{\boldsymbol{q}})\,. \tag{F.10}$$

The iterative process continues with evaluating

$$(\boldsymbol{M} + \boldsymbol{\alpha}\ \mathrm{D}\boldsymbol{g}^{\top}\ \mathrm{D}\boldsymbol{g})\,\ddot{\boldsymbol{q}}_{k+1} = \boldsymbol{M}\ddot{\boldsymbol{q}}_k + \cdots \tag{F.11}$$

$$- \boldsymbol{\alpha}\ \mathrm{D}\boldsymbol{g}^{\top}\left(\dot{\mathrm{D}}\boldsymbol{g}\,\dot{\boldsymbol{q}} + 2\,\boldsymbol{\mu}\,\boldsymbol{\omega}\,\dot{\boldsymbol{g}} + \boldsymbol{\omega}^2\,\boldsymbol{g}\right), \tag{F.12}$$

for $\ddot{\boldsymbol{q}}_{k+1}$ until satisfying

$$\|\ddot{\boldsymbol{q}}_{k+1} - \ddot{\boldsymbol{q}}_k\| \leq \epsilon\,, \tag{F.13}$$

where ϵ is a specified level of error tolerance on the error of generalized accelerations. Using ALF, no iterative root-finding algorithm like Newton's method is needed as Eq. (F.12) can be understood as finding the solution to the linear equation $\boldsymbol{A}\boldsymbol{x} = \boldsymbol{b}$ for which efficient numerical methods exist.

F.1.4 Coordinate Partitioning Method

As its name implies, coordinate partitioning method (CPM) requires partitioning the generalized coordinates into two sets of 1) independent coordinates $\boldsymbol{q}^{(\text{ind})}$,

and 2) dependent coordinates $\boldsymbol{q}^{(\mathrm{dep})}$:

$$\boldsymbol{q} \Rightarrow \begin{Bmatrix} \boldsymbol{q}^{(\mathrm{ind})} \\ \boldsymbol{q}^{(\mathrm{dep})} \end{Bmatrix},$$

for which the number of independent coordinates $\boldsymbol{q}^{(\mathrm{ind})}$ equals the number of DOF of the system (Wehage et al. 1982). Similarly, the system velocities and accelerations are also partitioned.

Finally, the integration process is revised to consider only the independent variables such that

$$\int \ddot{\boldsymbol{q}}^{(\mathrm{ind})} = \dot{\boldsymbol{q}}^{(\mathrm{ind})},$$
$$\int \dot{\boldsymbol{q}}^{(\mathrm{ind})} = \boldsymbol{q}^{(\mathrm{ind})}.$$

All dependent coordinates $\boldsymbol{q}^{(\mathrm{dep})}$ and independent velocities $\dot{\boldsymbol{q}}^{(\mathrm{ind})}$ are then calculated from the corresponding constraint equations. One drawback of the CPM is their poor numerical efficiency stemming from the iterative solution for dependent generalized coordinates.

F.1.5 Direct Correction Approach

Constraint violation handling methods are set up to ensure no violation of the coordinate level constraints. We may, as such, consider the final constraint satisfying coordinates as coordinates obtained through numerical integration corrected by a correction term as

$$\boldsymbol{q}_{\mathrm{cor}} = \boldsymbol{q}_{\mathrm{unc}} + \delta\boldsymbol{q},$$

where subscript $(\cdot)_{\mathrm{cor}}$ and $(\cdot)_{\mathrm{unc}}$ denote corrected and uncorrected coordinates, respectively, and $\delta\boldsymbol{q}$ is the vector of coordinate corrections to ensure constraint violation. Similarly, we may rewrite the constraint equations as

$$\boldsymbol{g}(\boldsymbol{q}_{\mathrm{cor}}) = \boldsymbol{g}(\boldsymbol{q}_{\mathrm{unc}}) + \delta\boldsymbol{g} = \mathbb{0}, \tag{F.14}$$

where $\delta \boldsymbol{g}$ is the variation of the constraint equations

$$\delta \boldsymbol{g} = \frac{\partial \boldsymbol{g}}{\partial \boldsymbol{q}_1}\delta \boldsymbol{q}_1 + \frac{\partial \boldsymbol{g}}{\partial \boldsymbol{q}_2}\delta \boldsymbol{q}_2 + \cdots + \frac{\partial \boldsymbol{g}}{\partial \boldsymbol{q}_n}\delta \boldsymbol{q}_n = \mathrm{D}\,\boldsymbol{g}\,\delta \boldsymbol{q}\,,$$

which we can use to rewrite Eq. (F.14) to yield

$$\delta \boldsymbol{q} = -\,\mathrm{D}\,\boldsymbol{g}^{-1}\,\boldsymbol{g}(\boldsymbol{q}_{\mathrm{unc}})\,. \tag{F.15}$$

In general, the constraint Jacobian $\mathrm{D}\,\boldsymbol{g}$ is rectangular, thus the inverse $\mathrm{D}\,\boldsymbol{g}^{-1}$ does not exist. We may, however, apply the concept of the Moore-Penrose inverse matrix, yielding

$$(\mathrm{D}\,\boldsymbol{g})^{+} = \mathrm{D}\,\boldsymbol{g}^{\mathsf{H}}\left(\mathrm{D}\,\boldsymbol{g}\,\mathrm{D}\,\boldsymbol{g}^{\mathsf{H}}\right)^{-1},$$

in which $\mathrm{D}\,\boldsymbol{g}^{\mathsf{H}}$ is the conjugate transpose of matrix $\mathrm{D}\,\boldsymbol{g}$. Using this, we can rewrite Eq. (F.15) to read

$$\delta \boldsymbol{q} = -\mathrm{D}\,\boldsymbol{g}^{\mathsf{H}}\left(\mathrm{D}\,\boldsymbol{g}\,\mathrm{D}\,\boldsymbol{g}^{\mathsf{H}}\right)^{-1}\boldsymbol{g}(\boldsymbol{q}_{\mathrm{unc}})\,. \tag{F.16}$$

Finally, we obtain the equation that represents the corrected generalized coordinates $\boldsymbol{q}_{\mathrm{cor}}$ in each time step as

$$\boldsymbol{q}_{\mathrm{cor}} = \boldsymbol{q}_{\mathrm{unc}} - \mathrm{D}\,\boldsymbol{g}^{\mathsf{H}}\big(\mathrm{D}\,\boldsymbol{g}\,\mathrm{D}\,\boldsymbol{g}^{\mathsf{H}}\big)^{-1}\boldsymbol{g}(\boldsymbol{q}_{\mathrm{unc}})\,. \tag{F.17}$$

Similarly, the generalized velocities are corrected by

$$\dot{\boldsymbol{q}}_{\mathrm{cor}} = \dot{\boldsymbol{q}}_{\mathrm{unc}} + \delta \dot{\boldsymbol{q}}\,,$$

which must satisfy the velocity constraints

$$\dot{\boldsymbol{g}}(\boldsymbol{q}_{\mathrm{cor}}, \dot{\boldsymbol{q}}_{\mathrm{cor}}) = \dot{\boldsymbol{g}}(\boldsymbol{q}_{\mathrm{cor}}, \dot{\boldsymbol{q}}_{\mathrm{unc}}) + \delta \dot{\boldsymbol{g}} = \mathbb{0}\,,$$

for which $\delta \dot{\boldsymbol{g}}$ represents the variation of the velocity constraints reading

$$\delta \dot{\boldsymbol{g}} = \frac{\partial \dot{\boldsymbol{g}}}{\partial \boldsymbol{q}}\,\delta \boldsymbol{q} + \frac{\partial \dot{\boldsymbol{g}}}{\partial \dot{\boldsymbol{q}}}\,\delta \dot{\boldsymbol{q}}\,.$$

With the generalized coordinates already being corrected i.e., $\delta \boldsymbol{q} \equiv \mathbb{0}$, and introducing $\mathrm{D}\dot{\boldsymbol{g}}$ as the Jacobian of the velocity constraints, we obtain

$$\delta \dot{\boldsymbol{g}} = \mathrm{D}\dot{\boldsymbol{g}}\, \delta \dot{\boldsymbol{q}}\,,$$

resulting in

$$\dot{\boldsymbol{g}}(\boldsymbol{q}_{\mathrm{cor}}, \dot{\boldsymbol{q}}_{\mathrm{unc}}) + \mathrm{D}\dot{\boldsymbol{g}}\, \delta \dot{\boldsymbol{q}} = \mathbb{0}\,,$$

which may be rewritten in terms of $\delta \dot{\boldsymbol{q}}$ to read

$$\begin{aligned} \delta \dot{\boldsymbol{q}} &= -(\mathrm{D}\dot{\boldsymbol{g}})^{+}\, \dot{\boldsymbol{g}}(\boldsymbol{q}_{\mathrm{cor}}, \dot{\boldsymbol{q}}_{\mathrm{unc}}) \\ &= -(\mathrm{D}\dot{\boldsymbol{g}})^{\mathsf{H}} \left(\mathrm{D}\dot{\boldsymbol{g}}\ \mathrm{D}\dot{\boldsymbol{g}}^{\top}\right)^{-1} \dot{\boldsymbol{g}}(\boldsymbol{q}_{\mathrm{cor}}, \dot{\boldsymbol{q}}_{\mathrm{unc}})\,. \end{aligned}$$

Ultimately, we obtain the equation for the corrected velocities at every integration time step as

$$\dot{\boldsymbol{q}}_{\mathrm{cor}} = \dot{\boldsymbol{q}}_{\mathrm{unc}} - \mathrm{D}\dot{\boldsymbol{g}}^{\mathsf{H}}\, (\mathrm{D}\dot{\boldsymbol{g}}\ \mathrm{D}\dot{\boldsymbol{g}}^{\top})^{-1}\, \dot{\boldsymbol{g}}(\boldsymbol{q}_{\mathrm{cor}}, \dot{\boldsymbol{q}}_{\mathrm{unc}}).$$

F.1.6 Gear-Gupta-Leimkuhler

From a numerical point of view, coordinate partitioning methods like the one presented in Appendix F.1.4 are less favorable because they select only a subset of linearly independent generalized coordinates computing the remaining dependent generalized coordinates by solving the system of nonlinear equations Eq. (F.1b). It is more favorable to keep *all* coordinates in the system dynamics described through Eq. (F.1). This can be achieved by either index reduction or projection, where projection techniques are state-of-the-art to avoid any drift effects in the numerical solving procedure (Eich 1993; Lubich et al. 1995). The constraint residual $\|\boldsymbol{g}(\boldsymbol{q}_k, t_k)\|$ at time step $t = t_k$ is monitored, and, when breaching through a user-defined error threshold $\epsilon > 0$, projected onto the manifold $\{\, \boldsymbol{\eta} \colon \boldsymbol{g}(\boldsymbol{\eta}, t_k) \equiv \mathbb{0} \,\}$. Mathematically, this can be defined as a minimization problem of the form

$$\hat{\boldsymbol{q}}_k = \min_{\{\, \boldsymbol{\eta} \colon\, \boldsymbol{g}(\boldsymbol{\eta}, t_k) \equiv \mathbb{0} \,\}} \|\boldsymbol{\eta} - \boldsymbol{q}_k\|$$

which may be solved efficiently by Newton iterations to find the projected new state $\hat{\boldsymbol{q}}_n$. The implementation of explicit projection methods for both $\boldsymbol{q}_n$ and $\dot{\boldsymbol{q}}_n$ can help avoid drift in the constraints, however, using such methods is restricted to Runga-Kutta and other one-step solvers as the implementation in advanced backward differentiation formulae (BDF) solvers is nontrivial. Knowing that, a reformulation of Eq. (F.1) in ways that it implicitly includes the projection onto the constraint manifold may be found as described by GGL. By introducing a new auxiliary state $\boldsymbol{v} = \dot{\boldsymbol{q}}$ with $\dot{\boldsymbol{v}} = \frac{\mathrm{d}\boldsymbol{v}}{\mathrm{d}t}$ and consideration of Eqs. (F.1b) and (F.2a) simultaneously, GGL defines the extended dynamical DAE-system as

$$\begin{aligned} \dot{\boldsymbol{q}}(t) &= \boldsymbol{v} - \mathrm{D}\,\boldsymbol{g}^{\top}(\boldsymbol{q}, t)\,\boldsymbol{\mu}\,, \\ \boldsymbol{M}(\boldsymbol{q})\,\dot{\boldsymbol{v}}(t) &= \boldsymbol{\gamma}(\boldsymbol{q}, \boldsymbol{v}, t) - \mathrm{D}\,\boldsymbol{g}^{\top}\,\boldsymbol{\lambda}\,, \\ \mathbb{0} &= \boldsymbol{g}(\boldsymbol{q}, t)\,, \\ \mathbb{0} &= \mathrm{D}\,\boldsymbol{g}(\boldsymbol{q}, t)\,\boldsymbol{v} + \dot{\boldsymbol{g}}(\boldsymbol{q}, t)\,. \end{aligned} \tag{F.18}$$

F.2 Numerical Integrators for Mechanical Systems

Conventionally, one may use any integrator for first-order DAE as long as they can handle singular mass matrices $\boldsymbol{M}$[45]. This can very often be achieved by implicit solvers[46], however, one needs to to take into account the system's specificity. Since commercially available solvers generally integrate a first-order ODE using a variable step size, their error bounds—both absolute and relative error on the forward integrated state—can be very restrictive and do not consider the physical quantities of the states. A cogent example may be given when considering a system with two translation and one rotational DOF. Generally, rotations are parametrized in radian, the rate of change of which may be significantly larger than that of translational states parametrized in meter. With a constrained mechanical system, the free body's dynamics are impacted by the constraint forces which generally are a function of the state of the system. Since the constraint forces / Lagrange multipliers are now part of the state of integration, their rate of change is tracked by the solver's error calculation. However, there usually is no need to bound errors on the constraint forces as

[45] Singular mass matrices emerge with the matrix formulation of a DAE where the mass matrix rank decreases and as such the matrix cannot be inverted.

[46] In MATLAB `ode15s` for linearly implicit systems (see Eq. (F.4)) and `ode15i` for fully implicit systems.

we would want them to be unconstrained in that sense as that they will always make sure the constraints are satisfied.

It may be possible to separately specify bounds of constraint forces states, however, the rate of change of these states will always be monitored by the solver eventually leading to termination of integration when bounds can no longer be satisfied, not even with decreasing step size. If the mechanical system now also is governed by nonholonomic constraints, then the impact of error-bound controlled variable step-size solvers becomes more prominent. To the rescue come integrators that are not based on pure mathematics of differential equations, but are based on meta knowledge from the mechanical system under integration. In principle, since we are concerned with integrating a mechanical system which we have obtained from either Newton-Euler's method, Lagrangian mechanics, or Hamiltonian dynamics, we can integrate properties like energy and momentum conservation into the integration process.

F.2.1 Leapfrog

Leapfrog algorithm considers the dynamics in the Hamiltonian description such that we do not obtain a single, second-order differential equation, but merely two coupled, first-order differential equations (Young 2014). The algorithm was first introduced by Yoshida (1990) and Birdsall et al. (1991) and later used as base for improved integrators of motion in mult-body systems by Omelyan et al. (2002). We rewrite $\ddot{x} = F(x,t)$ to read[47]

$$\begin{aligned} \frac{\mathrm{d}x(t)}{\mathrm{d}t} &= v(t)\,, \\ a(t) = \frac{\mathrm{d}v(t)}{\mathrm{d}t} &= F(x(t)) = -\frac{\mathrm{d}U(x(t))}{\mathrm{d}x}\,. \end{aligned}$$

where we use the auxiliary state of velocities $v(t)$ and the potential $U(x(t))$ of the forces $F(x(t))$. If we perform Taylor expansion of $x(t)$ at time step t_k with step size h, we obtain

$$x(t_k + h) = x(x_k) + h\,v(t_k) + \frac{1}{2}\,h^2\,a(t_k) + O(h^3)\,,$$

[47] Without loss of generality we state only the scalar form of the Leapfrog integrator. Transfer to the vectorial case is left to the reader.

with $v(t_k) = \frac{\mathrm{d}x(t_k)}{\mathrm{d}t}$ and $a(t_k) = \frac{\mathrm{d}^2x(t_k)}{\mathrm{d}t^2}$; while we obtain for the Taylor expansion of the velocity $\frac{\mathrm{d}x(t_k)}{\mathrm{d}t}$ at time $t_k + h$

$$v(t_k + h) = v(t_k) + \frac{1}{2}\, h\, a(t_k) = v(t_{k+\frac{h}{2}})\,.$$

Substituting this equation into the Taylor expansion of $x(t_k + h)$ gives

$$x(t_k + h) = x(t_k) + h\, v(t_k + \frac{h}{2}) + O(h^3)\,.$$

This gives the standard Leapfrog algorithm for time step k

$$\begin{aligned} v_{k+\frac{1}{2}} &= v_{k-\frac{1}{2}} + h\, a_k\,, \\ x_{k+1} &= x_k + h\, v_{k+\frac{1}{2}}\,. \end{aligned}$$

Despite this algorithm numerically integrating mechanical systems with a step size error of $O(h^4)$, it is not often very practical as it does not synchronize the velocities—position values are available at full-integer time values k, whilst velocity values are only available at half-integer time values either $k - \frac{1}{2}$ or $k + \frac{1}{2}$. However, the equations can be expressed in a form that allows for obtaining velocities and positions at full-integer values giving the re-arranged and synchronized "kick-drift-kick" form

$$\begin{aligned} v_{k+\frac{1}{2}} &= v_k + \frac{h}{2}\, a_k\,, \\ x_{k+1} &= x_k + h\, v_{k+1/2}\,, \\ v_{k+1} &= v_{k+\frac{1}{2}} + \frac{h}{2}\, a_{k+1}\,. \end{aligned}$$

Above formulation is favorable for variable step size integration as the separation of velocities and accelerations to the start and end of the algorithm requires only one extra—possibly expensive—calculation of accelerations when halving the step size $h \to h/2$. In addition, the leapfrog algorithm also allows for considering dissipative forces during integration, even though the algorithm then becomes slightly more involved. In this case, the accelerative forces are

split into two parts such that the accelerations read

$$a(x, v, t) = F(x, t) - G(v)\,.$$

In a first step, we consider the approximation of the accelerations to be given through

$$a_k = F_k - G_{k-\frac{1}{2}}$$

giving us

$$\begin{aligned}\hat{v}_{k+\frac{1}{2}} &= v_{k-\frac{1}{2}} + h\,F_k - h\,G_{k-\frac{1}{2}}\,,\\ \hat{x}_{k+1} &= x_k + h\,\hat{v}_{k+\frac{1}{2}}\,.\end{aligned}$$

Then, a second step approximation yields the current velocities

$$v_k = \frac{\hat{x}_{k+1} - x_{k-1}}{2\,h}\,,$$

which we can then use to continue with the conventional leapfrog algorithm. In the end, the leapfrog algorithm for systems with velocity-dependent forces reads

$$\begin{aligned}\hat{v}_{k+\frac{1}{2}} &= v_{k-\frac{1}{2}} + h\,F_k - h\,G_{k-\frac{1}{2}}\,,\\ \hat{x}_{k+1} &= x_k + h\,\hat{v}_{k+\frac{1}{2}}\,,\\ v_k &= \frac{\hat{x}_{k+1} - x_{k-1}}{2\,h}\,,\\ v_{k+\frac{1}{2}} &= v_{k-\frac{1}{2}} + h\,a_k\,,\\ x_{k+1} &= x_k + h\,v_{k+\frac{1}{2}}\,.\end{aligned}$$

Since the leapfrog algorithm provides an explicit solution for the next state, geometric constraints can be incorporated straightforward by solving the system of (non)linear constraint equations of the next step simultaneously with the constraint forces (Omelyan 1999).

F.2.2 Energy-Momentum Conserving Integrator

We again consider a mechanical system subject to holonomic and hon-holonomic constraints. The motion of the system is governed by the set of differential-algebraic equations reading

$$\begin{aligned} \boldsymbol{M}\,\ddot{\boldsymbol{q}} + \mathrm{D}\,U(\boldsymbol{q}) &= \mathrm{D}\,\boldsymbol{g}^{\top}(\boldsymbol{q})\,\boldsymbol{\lambda} + \mathrm{D}\,\boldsymbol{G}^{\top}(\boldsymbol{q})\,\boldsymbol{\mu}\,, \\ \boldsymbol{g}(\boldsymbol{q}) &= \mathbb{0}\,, \\ \boldsymbol{G}(\boldsymbol{q},\dot{\boldsymbol{q}}) &= \mathbb{0}\,. \end{aligned}$$

Holonomic constraints are given by n_g constraint functions $\boldsymbol{g}(\boldsymbol{q}) \in \mathbb{R}^{n_g}$ which restrict possible motions of the system through constraint forces with relative magnitude given through $\boldsymbol{\lambda} \in \mathbb{R}^{n_g}$. Nonholonomic constraints are given by n_G constraint functions $\boldsymbol{G}(\boldsymbol{q},\dot{\boldsymbol{q}}) \in \mathbb{R}^{n_G}$ restricting motion through constraint forces with relative magnitude given through $\boldsymbol{\mu} \in \mathbb{R}^{n_G}$. The approach revisited here and originally presented by Betsch (2006) restricts to systems with potential function $U(\boldsymbol{q}) \in \mathbb{R}$ resulting in forces $\mathrm{D}\,U(\boldsymbol{q})$, and constant mass matrix $\boldsymbol{M} \in \mathbb{R}^{n\times n}$.

Betsch proposes a new mechanical integrator for energy-consistent integration of mechanical systems subjected to kinematic and geometric constraints. We consider a time interval $T_k = [t_k, t_{k+1}]$ with given positions $\boldsymbol{q}_k$ and velocities $\boldsymbol{v}_k$ at time t_k. By defining the mid-point value similar to the leapfrog algorithm as $(\cdot)_{k+\frac{1}{2}} = ((\cdot)_k + (\cdot)_{k+1})/2$, the one-step time-integration scheme with $h = t_{k+1} - t_k$ then reads

$$\begin{aligned} \boldsymbol{q}_{k+1} - \boldsymbol{q}_k &= h\,\boldsymbol{v}_{k+\frac{1}{2}}\,, \\ \boldsymbol{M}(\boldsymbol{v}_{k+1} - \boldsymbol{v}_k) &= -h\,\overline{\nabla} U(\boldsymbol{q}_k, \boldsymbol{q}_{k+1}) + \cdots \\ &\quad + h\,\overline{\nabla}\boldsymbol{g}(\boldsymbol{q}_k, \boldsymbol{q}_{k+1})^{\top}\,\bar{\boldsymbol{\lambda}} + \cdots \\ &\quad + h\,\overline{\nabla}\boldsymbol{G}(\boldsymbol{q}_k, \boldsymbol{q}_{k+1})^{\top}\,\bar{\boldsymbol{\mu}}\,, \\ \mathbb{0} &= \overline{\nabla}\boldsymbol{g}(\boldsymbol{q}_k, \boldsymbol{q}_{k+1})\,\boldsymbol{v}_{k+\frac{1}{2}}\,, \\ \mathbb{0} &= \overline{\nabla}\boldsymbol{G}(\boldsymbol{q}_k, \boldsymbol{q}_{k+1})\,\boldsymbol{v}_{k+\frac{1}{2}}\,. \end{aligned} \tag{F.20}$$

The nominal constraint forces $\boldsymbol{\lambda}(t)$, $\boldsymbol{\mu}(t)$ are assumed constant within each time step i.e., $\boldsymbol{\lambda}(t_k) \approxeq \bar{\boldsymbol{\lambda}}$, $\boldsymbol{\mu}(t_k) \approxeq \bar{\boldsymbol{\mu}}$. In Eq. (F.20), $\overline{\nabla}$ refers to the discrete derivative of its argument (Gonzalez 1996) (see the following section).

Discrete Derivative

For a scalar-valued function $f\colon \mathbb{R}^n \to \mathbb{R}$, $\boldsymbol{q} \mapsto f(\boldsymbol{q})$ and two points $\boldsymbol{x}, \boldsymbol{y} \in \mathbb{R}^n$, Gonzalez defines the discrete derivative similar to the continuous derivative as

$$\begin{aligned} \overline{\nabla} f(\boldsymbol{x}, \boldsymbol{y}) &= \frac{\partial f(\boldsymbol{z})}{\partial \boldsymbol{q}} - \frac{f(\boldsymbol{y}) - f(\boldsymbol{x}) - \frac{\partial f(\boldsymbol{z})}{\partial \boldsymbol{q}} \boldsymbol{v}}{\|\boldsymbol{v}\|} \boldsymbol{v}^\top , \\ \boldsymbol{v} &= \boldsymbol{y} - \boldsymbol{x} , \\ \boldsymbol{z} &= \frac{1}{2} (\boldsymbol{x} + \boldsymbol{y}) , \end{aligned} \tag{F.21}$$

with its two properties of directionality

$$\begin{aligned} \overline{\nabla} f(\boldsymbol{x}, \boldsymbol{y})\, \boldsymbol{v} &= \left(\frac{\partial f(\boldsymbol{z})}{\partial \boldsymbol{q}} - \frac{f(\boldsymbol{y}) - f(\boldsymbol{x}) - \frac{\partial f(\boldsymbol{z})}{\partial \boldsymbol{q}} \boldsymbol{v}}{\|\boldsymbol{v}\|} \boldsymbol{v}^\top \right) \boldsymbol{v} , \\ &= f(\boldsymbol{y}) - f(\boldsymbol{x}) , \end{aligned} \tag{F.22a}$$

and of consistency

$$\overline{\nabla} f(\boldsymbol{x}, \boldsymbol{y}) = \frac{\partial f(\boldsymbol{z})}{\partial \boldsymbol{q}} , \tag{F.22b}$$

for $\|\boldsymbol{y} - \boldsymbol{x}\| \to 0$, which can be shown using the Taylor expansion of $f(\boldsymbol{x})$ and $f(\boldsymbol{y})$ up to order 4.

Equation (F.21) can be extended to vector-valued functions $\boldsymbol{f}\colon \mathbb{R}^n \mapsto \mathbb{R}^m$ for which the partial derivative $\frac{\partial \boldsymbol{f}(\boldsymbol{z})}{\partial \boldsymbol{q}} = \mathrm{D}\, \boldsymbol{f}$ represents the Jacobian matrix.

Constrained Scheme

Betsch highlights some key properties of this constrained schemed as

1. Conservation of energy. It can be shown for the energy function

$$E(\boldsymbol{q}_k, \boldsymbol{v}_k) = \frac{1}{2} \boldsymbol{v}_k \boldsymbol{M} \boldsymbol{v}_k + U(\boldsymbol{q}_k) ,$$

the integrator algorithmically conserves energy within the integration interval i.e.,

$$E(\boldsymbol{q}_{k+1}, \boldsymbol{v}_{k+1}) - E(\boldsymbol{q}_k, \boldsymbol{v}_k) \equiv 0\,.$$

2. Satisfaction of geometric constraints at time t_{k+1}. This follows straight from Eq. (F.20)$_3$ taking into account Eq. (F.20)$_1$ and the directionality property of the discrete derivative Eq. (F.22a).
3. Velocity constraints are satisfied only for mid-point velocities $\boldsymbol{v}_{k+\frac{1}{2}}$.

System motion can now be solved iteratively for the unknowns $(\boldsymbol{q}_{k+1}, \boldsymbol{v}_{k+1})$ and $\bar{\boldsymbol{\lambda}}$, $\bar{\boldsymbol{\mu}}$ employing the scheme given in Eq. (F.20) such that we first eliminate the unknown velocities $\boldsymbol{v}_{k+1}$

$$\boldsymbol{v}_{k+1} = \frac{2}{h}\,(\boldsymbol{q}_{k+1} - \boldsymbol{q}_k) - \boldsymbol{v}_k\,, \tag{F.23a}$$

which, substituted into Eq. (F.20), gives

$$\begin{aligned}
\mathbb{0} &= \frac{2}{h}\,\boldsymbol{M}\,(\boldsymbol{q}_{k+1} - \boldsymbol{q}_k) - 2\,\boldsymbol{M}\,\boldsymbol{v}_k + \overline{\nabla} U(\boldsymbol{q}_k, \boldsymbol{q}_{k+1}) + \cdots \\
&\quad + h\,\overline{\nabla}\boldsymbol{g}(\boldsymbol{q}_k, \boldsymbol{q}_{k+1})^\top\,\bar{\boldsymbol{\lambda}} + h\,\overline{\nabla}\boldsymbol{G}(\boldsymbol{q}_k, \boldsymbol{q}_{k+1})^\top\,\bar{\boldsymbol{\mu}}\,, \qquad \text{(F.23b)} \\
\mathbb{0} &= \boldsymbol{g}(\boldsymbol{q}_{k+1})\,, \qquad \text{(F.23c)} \\
\mathbb{0} &= \boldsymbol{G}(\boldsymbol{q}_{k+\frac{1}{2}})\,(\boldsymbol{q}_{k+1} - \boldsymbol{q}_k) \qquad \text{(F.23d)}
\end{aligned}$$

This system of nonlinear equations can be solved by applying Newton's method as presented in Appendix E.2.1. For this, we state the Jacobian matrix w.r.t. $\boldsymbol{q}_{k+1}$ at Newton's step l of the residual function as given in Eq. (F.23)

$$\mathrm{D}\,\boldsymbol{e}(\boldsymbol{q}_{k+1}^{(l)}) = \begin{bmatrix} \boldsymbol{k}_1 & h\,\overline{\nabla}\boldsymbol{g}(\boldsymbol{q}_k, \boldsymbol{q}_{k+1}^{(l)}) & h\,\overline{\nabla}\boldsymbol{G}(\boldsymbol{q}_{k+\frac{1}{2}}^{(l)}) \\ \boldsymbol{k}_2 & \mathbb{0} & \mathbb{0} \\ \boldsymbol{k}_3 & \mathbb{0} & \mathbb{0} \end{bmatrix},$$

with

$$\boldsymbol{k}_1 = \frac{2}{h}\,\boldsymbol{M} + \frac{\partial \overline{\nabla} U(\boldsymbol{q}_k, \boldsymbol{q}_{k+1})}{\partial \boldsymbol{q}_{k+1}} + \cdots$$

$$
\begin{aligned}
&+ h \sum_{r=1}^{n_g} \boldsymbol{\lambda}_r \frac{\partial \overline{\nabla} \boldsymbol{g}_r(\boldsymbol{q}_k, \boldsymbol{q}_{k+1}^{(l)})}{\partial \boldsymbol{q}_{k+1}} + \cdots \\
&+ h \sum_{r=1}^{n_G} \boldsymbol{\mu}_r \frac{\partial \overline{\nabla} \boldsymbol{G}_r(\boldsymbol{q}_{k+\frac{1}{2}})}{\partial \boldsymbol{q}_{k+1}} \\
\boldsymbol{k}_2 &= \mathrm{D}\, \boldsymbol{g}(\boldsymbol{q}_{k+1}^{(l)})\,, \\
\boldsymbol{k}_3 &= \mathrm{D}\, \boldsymbol{G}(\boldsymbol{q}_{k+\frac{1}{2}}) + \begin{bmatrix} (\boldsymbol{q}_{k+1} - \boldsymbol{q}_k)^\top \frac{\partial \boldsymbol{G}_1(\boldsymbol{q}_{k+\frac{1}{2}}^{(l)})}{\partial \boldsymbol{q}_{k+1}} \\ \vdots \\ (\boldsymbol{q}_{k+1} - \boldsymbol{q}_k)^\top \frac{\partial \boldsymbol{G}_{n_G}(\boldsymbol{q}_{k+\frac{1}{2}}^{(l)})}{\partial \boldsymbol{q}_{k+1}} \end{bmatrix},
\end{aligned}
$$

in which the partial derivative w.r.t. $\boldsymbol{y}$ of the discrete derivative $\frac{\partial \overline{\nabla} \boldsymbol{f}(\boldsymbol{x},\boldsymbol{y})}{\partial \boldsymbol{y}}$ of a vector-valued function $\boldsymbol{f}(\boldsymbol{q})$ is given through

$$
\begin{aligned}
\frac{\partial \overline{\nabla} f(\boldsymbol{x}, \boldsymbol{y})}{\partial \boldsymbol{y}} &= \frac{\partial^2 \boldsymbol{f}(\boldsymbol{z})}{\partial \boldsymbol{q}^2} + \cdots \\
&\quad + \frac{\boldsymbol{v}}{\|\boldsymbol{v}\|} \left(\frac{\partial \boldsymbol{f}(\boldsymbol{y})}{\partial \boldsymbol{q}} - \boldsymbol{v}^\top \frac{\partial^2 \boldsymbol{f}(\boldsymbol{z})}{\partial \boldsymbol{q}^2} - \frac{\partial \boldsymbol{f}(\boldsymbol{z})}{\partial \boldsymbol{q}} \right) + \cdots \\
&\quad + \left(\frac{\mathbb{1}_n}{\|\boldsymbol{v}\|} + 2 \frac{\boldsymbol{v}\, \boldsymbol{v}^\top}{\|\boldsymbol{v}\|^2} \right) \left(\boldsymbol{f}(\boldsymbol{y}) - \boldsymbol{f}(\boldsymbol{x}) - \frac{\partial \boldsymbol{f}(\boldsymbol{z})}{\partial \boldsymbol{q}}\, \boldsymbol{v} \right),
\end{aligned}
$$

again with

$$
\begin{aligned}
\boldsymbol{v} &= \boldsymbol{y} - \boldsymbol{x}\,, \\
\boldsymbol{z} &= \frac{1}{2} (\boldsymbol{x} + \boldsymbol{y})\,.
\end{aligned}
$$

Aufgrund der geringen Steifigkeit der in parallelen Seilrobotern verwendeten Seile kommt es unweigerlich zu Schwingungen. Die Beschreibung dieser Schwingungen stellt sich bei parallelen Seilrobotern aufgrund ihrer kinematischen Redundanz als besonders herausfordernd dar. Diese Arbeit bietet einen grundlegend neuen Ansatz zur Modellierung dieser Art von Roboter und verwendeter Seile auf Basis elastischer Mehrkörper. Basierend auf der Balkentheorie nach Cosserat wird ein niedrig dimensionales Seilmodell unter Verwendung von B-splines als Menge der Ansatzfunktionen formuliert. Die anschließende numerische Integration des steifen Mehrkörpersystems erfolgt unter Nutzung eines energie- und impulserhaltenden numerischen Integrators.

Ebenso bietet diese Arbeit Einblick in das Kraftdehnungsverhalten von polyethylenbasierten Faserseilen. Die experimentellen Untersuchungen geben Aufschluss über das Kurz- und Langzeitdehnungsverhalten der Seile und einen darauf basierenden Modellierungsansatz.

ISBN 978-3-8396-1536-2

9 783839 615362

FRAUNHOFER VERLAG